UNIVERSITY OF SOUTHAMPTON

FACULTY OF NATURAL AND ENVIRONMENTAL SCIENCES

School of Chemistry

The Role of Additives in Fischer-Tropsch Reactions

by

Michal Perdjon-Abel

Thesis for the degree of Doctor of Philosophy

August 2011

UNIVERSITY OF SOUTHAMPTON

ABSTRACT

FACULTY OF NATURAL AND ENVIRONMENTAL SCIENCES
SCHOOL OF CHEMISTRY

Doctor of Philosophy

THE ROLE OF ADDITIVES IN FISCHER-TROPSCH REACTIONS

by Michal Perdjon-Abel

The Fischer-Tropsch Synthesis (FTS) is an alternative route to produce liquid fuels from a variety of carbon feedstocks including coal and biomass. Typically iron and cobalt based catalysts have been used for the FTS reaction, in which a mixture of CO and H_2 (syn-gas) reacts to form hydrocarbons. Enhanced performance has been reported for iron-based systems doped with alkali metals and chalcogenides. Sulfides are considered a poison for most catalytic processes, but sulfur in the form of sulfates (S^{VI}) is found to enhance the performance of iron based catalysts towards the FTS when present at low levels.

In this study a wide range of iron based catalysts was prepared under varying synthesis conditions and with different dopants. The standard methods of preparation used were co-precipitation and incipient wetness impregnation. A structural study of a wide range of iron based catalysts was carried out using characterisation methods such as X-ray Absorption Fine Structure (XAFS) spectroscopy, X-ray Photoelectron Spectroscopy (XPS), Powder X-ray Diffraction (PXRD), Scanning Electron Microscopy (SEM), Energy Dispersive X-ray (EDX) and Brunner-Emmett-Taller surface area determination (BET). The characterisation was performed before and after reduction of the catalysts (under H_2) to form the catalytically active materials.

Before reduction, PXRD, XPS and quantitative analysis identified a haematite iron oxide structure (α-Fe_2O_3) for all samples. The crystallinity of the iron oxide materials varied between samples prepared in various conditions. The highest crystallinity was observed for the samples synthesised at pH7, fast titrant addition rate, at room temperature. The same techniques revealed changes in the iron oxide structure after reduction. The catalysts activated at 400 ^oC were mainly composed of Fe_3O_4 and those activated at 450 ^oC were a mixture of Fe^{2+}, Fe^{3+} oxides and metallic iron Fe^0. Moreover, the study of the role of alkali metals showed that some of the alkali promoters (K, Rb) may decrease the effective iron oxide reduction temperature. The nitrogen adsorption experiment was used to establish that iron oxide doped with different promoters had a mesoporous structure with a narrow pore size distribution. The SEM analysis indicated two different types of surface: irregularly shaped agglomerates with smaller round edged particles attached to their surface and homogenous agglomerates surfaces with sharp edges for the samples with different promoters. The most homogenous were the samples with Rb. All samples had small particles attached to the surface of larger agglomerates.

An increase of the alkali metals on the surface after the activation process and migration of the alkalis to the surface with rising reduction temperature were observed using bulk and surface techniques (XRF, EDX and XPS). The differences in K K-edge shape of the XANES spectrum indicated changes in the local structure of K corresponding to changes of coordination number around K^+ during activation. It was also observed that reduction influenced the sulfur species in iron oxide catalyst. For all the samples prior to reduction sulfates (SO_4^{2-}) were detected by XPS and XAFS. After the reduction at 400 ^oC and 450 ^oC, characteristic XPS S 2p peaks for both sulfate and sulfide, were noticed. The sulfate/sulfide ratio was higher for the catalyst samples reduced at the lower temperature.

Acknowledgments

I would like to offer my sincerest gratitude to my supervisors Prof. John Evans and Prof. Moniek Tromp, who with patience, knowledge and experience in many fields of chemistry have supported me throughout my thesis. Thank you for your encouragement during my time at the university. I appreciate that I had opportunity to work in an environment of many excellent scientists, and I would like to especially acknowledge the advice and guidance one of them, my advisor - Dr Andrew Hector.

I gratefully acknowledge the financial support from my sponsor the Sasol Technology R&D, Sasolburg, South Africa, and members of the company Dr Johan Labuschagne, Dr Paul Webb and Prof. Bob Tooze for the meetings and advice.

I also thank University staff for support, cooperation and the friendly environment, especially Mrs. Jill Queen, Mrs. Beverley Price, Mrs. Beverley Macey, Mrs. Chun Borodzicz, Ms. Mary Smith, Mrs. Sally Dady, Dr David Kinnison, Mr. Karl Hagon, Mr. Przemyslaw Tryc and Mrs. Pat Dear for the best tea in the world.

I am very grateful for the opportunity to meet and work with the cheerful and friendly members of my group: Peter, Sarah, Rowena, Stuart, Khaled, Richard, Sam, Ania, Ewa, Otello and Sergio.
Warm thanks to all my friends for joyful moments: Ala, Karol, Pietro, Sara, Ola, Ross, Angie, Thomas, Peri, Miriam, Javier, Rute, Theo, Imran, ThaoNguyen, Simon, Biniam, Ricardo and Francesco.

I would like especially to thank my parents Halina and Wojciech Perdjon for their unconditional love and support during all of the years of my education. I would like to thank my wife, Magdalena and my daughter Michelle who have supported, encouraged and waited for me for long months.

DECLARATION OF AUTHORSHIP

I Michal Perdjon-Abel declare that the thesis entitled The Role of Additives in Fischer-Tropsch Reactions and the work presented in the thesis are both my own, and have been generated by me as the result of my own original research. I confirm that:

- this work was done wholly or mainly while in candidature for a research degree at this University;
- where any part of this thesis has previously been submitted for a degree or any other qualification at this University or any other institution, this has been clearly stated;
- where I have consulted the published work of others, this is always clearly attributed;
- where I have quoted from the work of others, the source is always given. With the exception of such quotations, this thesis is entirely my own work;
- I have acknowledged all main sources of help;
- where the thesis is based on work done by myself jointly with others, I have made clear exactly what was done by others and what I have contributed myself;
- none of this work has been published before submission

Signed: ……..

Date:…….

Chapter 1

Introduction

1. Introduction

The most significant energy sources from the beginning of the industrial civilization have been crude oil, coal, natural gas, nuclear electricity and hydro-electricity. Crude oil extraction is fundamental as a source of energy in industry and for most of the forms of transport. However, there are concerns that consumption of the crude oil in some countries, like for example USA, China, Japan, India, etc., is higher than the production of the oil[1-3].

There are many prognoses e.g. the Hubbert (1949), Campbell and Laherrere (1998) "Peak Oil" theory about deficit of the crude oil[4-7]. The "Peak Oil" is a hypothesis which holds that the oil production will reach a maximum when around half of the existing resources have been extracted[8]. It is possible that cheap oil used for transport and cheap gas used for example for buildings heating will run out in our lifetime. Thus it is important to seek alternative energy sources[9]. The oil production curve, as originally suggested by Hubbert in 1956[10], is presented below, Figure 1.1.

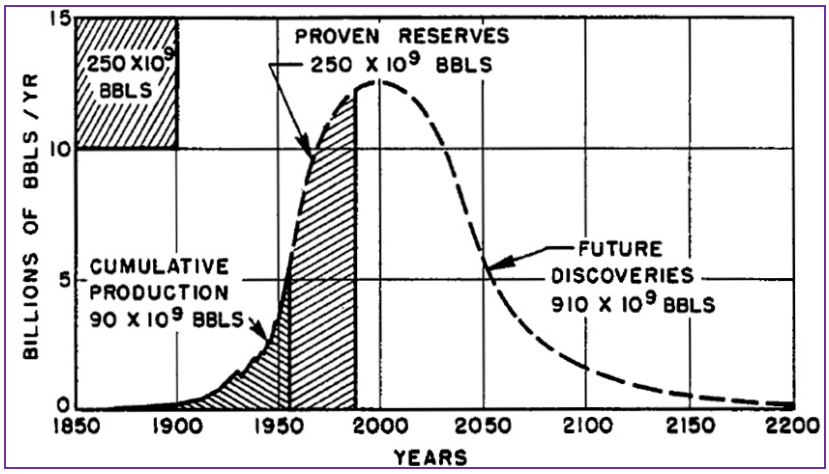

Fig. 1.1 World Crude oil production based upon initial reserves of 250 billion barrels[10] .

There are many theories like for example one based on so-called "abiotic" oil formation, which is more optimistic but, unfortunately, more controversial than already disputed "peak oil" theory based on biogenic theory. The abiotic theory states that crude oil is created in non-biological processes, while the biogenic theory claims that petroleum derives from biological matter. There is scientific evidence for both theories; however,

there are more proofs for the theory that claims biological origins of petroleum. Both theories, regardless of the controversy, are significant for the study of the genesis of crude oil and in oil exploration[8,11]. The rising concerns regarding the deficit of non-renewable energy sources, mainly crude oil, natural gas and uranium, has motivated many scientists to work on renewable energy sources. There have been, for many years, working alternatives to the non-renewable, renewable sources of energy like e.g. biofuels, wind mills, fuel cell systems.

However, the percentage of renewable energy sources explored is and will, for a long time, be lower than the non-renewable ones, like for example coal. Figure 1.2 below shows a chart of current world net electricity generation by fuel and a prognosis until 2035[12].

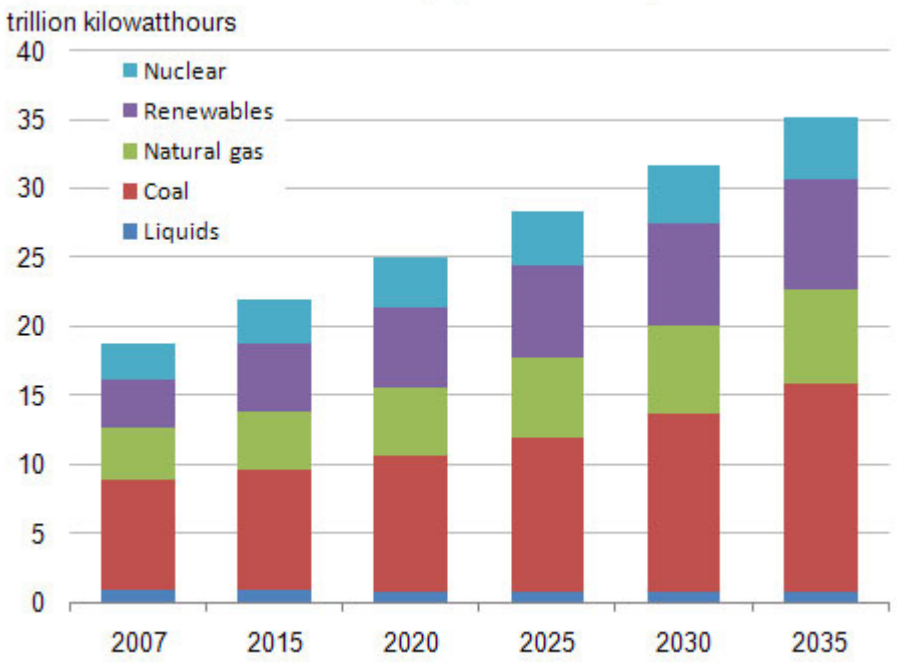

Fig. 1.2 World net electricity generation by fuel, 2007-2035 (trillion kilowatt hours).

The Fischer Tropsch (FT) process uses coal or natural gas to produce synthetic fuel and can be a viable alternative when the prices of fuel from crude oil rise. The reserves of coal and natural gas are larger than those of crude oil[13-16]. Thus the FT process may supply fuel in the world market for a longer period than the refinement of crude oil.

The Fischer-Tropsch (FT) reaction is a heterogeneous catalysis process during which the components of synthesis gas, CO and H_2, react to form hydrocarbons. The reaction between CO and H_2 was discovered by Franz Fischer, from the Max-Planck Institute, and Hans Tropsch, a co-worker of Fischer and professor of chemistry in Prague (Czech Republic), Mülheim (Germany) and Chicago (USA), in 1922[17,18,19]. The most common active metals used to produce paraffins and olefins in the FT process are Fe, Co, Ni and Ru. The consumption of active metals in the FT process varies significantly and depends on their catalytic properties, efficiency and price. To improve the catalyst activity and selectivity promoters are used, for example alkali metals. The active metals and their promoters will be described below.

The synthesis gas (syngas) used in the FT process is usually generated from coal or methane. The method of production depends mainly on the price of methane and coal and their availability. The synthetic fuel produced in the FT process can compete with refined crude when the price of the crude oil is of about 20 $ per barrel[20-22]. Thus it is very important for the fuels produced via FT from methane that there is a low and stable price of that source.

The synthesis of the fuels via the FT process may also compete with the fuels produced from crude oils as a more environmentally friendly method. The FT gasoline and diesel are S and N free and low in aromatics. However, twice as much CO_2 is emitted into the atmosphere in the FT process in comparison to the fuels produced from the crude oil. It needs to be noted that around one-third of the coal is used to raise steam and the remaining two-thirds are used into gasifiers, where half of the coal is burnt (emission of CO_2) to give necessary energy for the highly endothermic gasification reaction.
The production of fuel from syngas via the FT process is the third largest commercial use of syngas after the production of hydrogen and methanol[23]. The three main sources from which syngas can be obtained produce different ratios of H_2/CO.
From natural gas:

$CH_4 + H_2O \leftrightarrow 3H_2 + CO$ $\Delta H = +49.0$ kcal mol^{-1} [23] (1.1)

From oil reactions:

$-CH_2- + H_2O \leftrightarrow 2H_2 + CO$ $\Delta H = +36.1$ kcal mol^{-1} (1.2)

From coal:

$C + H_2O \leftrightarrow H_2 + CO$ $\Delta H = +31.1$ kcal mol^{-1} (1.3)

Some other ways in which syngas can be obtained or used are illustrated in Fig.1.3.

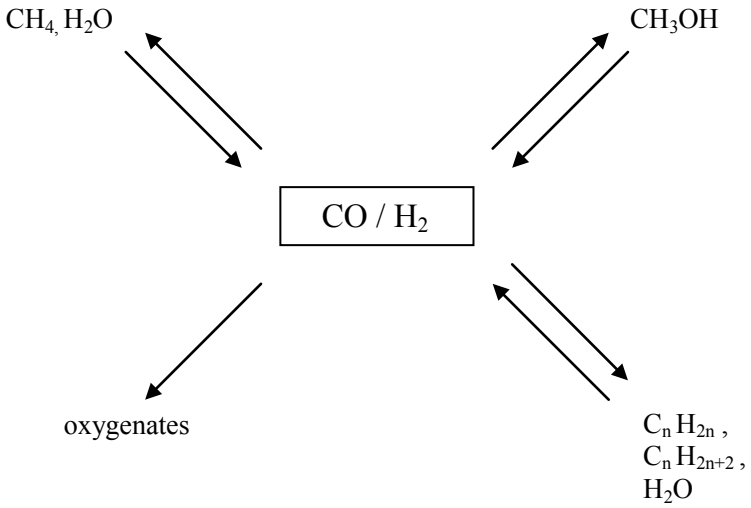

Fig.1.3 Reactions of synthesis gas,[24]

The production of syngas from natural gas or coal is highly endothermic and the most expensive stage in the whole FT process. Methane is generally thermally or catalytically converted to syngas with steam and oxygen. Coal is usually converted to syngas in non-catalytic fluidized or moving bed types gasifiers. Moreover, the overall cost of production of the syngas increases due to the high degree of sulfur purification of the syngas required due to its poisoning effect. The conversion of carbon sources to syngas constitutes about 60 - 70% of the total cost because of purification and high-energy input required to run the process[25].

1.1 The Fischer –Tropsch synthesis

The FT reaction can be presented in two main equations:

$n\ CO + (2n+1)\ H_2 \rightarrow C_nH_{2n+2} + n\ H_2O \quad \Delta H < 0$, (exothermic) (1.1.1)

$n\ CO + 2n\ H_2 \rightarrow C_nH_{2n} + n\ H_2O \quad \Delta H < 0$, (exothermic) (1.1.2)

Examples of the CH_4 and C_4H_8, formation enthalpies:

$CO + 3H_2 \rightarrow CH_4 + H_2O \quad \Delta H = -206$ kJ/mol[26]

$4CO + 8H_2 \rightarrow C_4H_8 + 4H_2O \quad \Delta H = -525$ kJ/mol[26]

Equations 1.1 and 1.2 describe the synthesis of paraffins and olefins respectively. Both reactions are strongly exothermic[27,28]. As reported by Schulz[29], the desorption of a paraffin from an FT catalyst surface is much less probable than the desorption of an olefin. There is in the Fischer-Tropsch synthesis a wide variety of products, with different lengths of carbon chain and different number of carbon-carbon double bonds, depending on the catalytically active metal and the pressure of the reaction.

There are very important side reactions in the FT process:

$CO + H_2O \rightarrow CO_2 + H_2 \quad \Delta H\ (298\ K) = -41.2$ kJ/mol [33] (1.1.3)

$2CO \rightarrow CO_2 + C \quad \Delta H\ (298\ K) = -172$ kJ/mol [30] (1.1.4)

The water gas shift (WGS) conversion reaction is presented in equation 1.3. The WGS conversion is important because it increases the H_2/CO ratio. The WGS is exothermic reaction where CO conversion is limited by a thermodynamic equilibrium limitation (ΔH (298 K) = - 41.2 kJ/mol).[31,32,33]. The reaction in equation (1.4) takes place on the active metal surface, and results in the conversion of carbon monoxide into carbon dioxide leaving carbon behind on the surface. This highly exothermic reaction is known as the Boudouard reaction, and leads to deactivation of the catalyst by carbon $C_{(s)}$ deposition (the result of spontaneous cracking), which blocks the active sites of the catalyst[33].

1.2. Iron catalysts in Fischer Tropsch Synthesis

1.2.1 Why iron?

Fe-based catalysts are an attractive complement to the commonly used Co-based catalysts, due to relatively low cost, high WGS reaction activity and higher selectivity to hydrocarbons[34]. The mechanisms of reactions occurring at the surface, and the interaction between syngas and the catalyst, vary with respect to the kind of the active metal in the catalyst, its speciation and their interaction with the promoters. All of the metals are Group 8-10 metals and some of the transition metals are active for FT synthesis; however, the choice of the active metals to be used in this process depends on the following factors: FT activity, WGS activity, hydrogenation activity and the price. Only the transition metals like Fe, Ni, Co and Ru have high enough FT activity for commercial application.

The absence of a dispersing support in FT catalysts runs the risk of sintering at high temperatures and thus giving a very low concentration of active sites. Unsupported iron-oxide catalysts are though very active and do not require a high surface area. Also, the absence of a support such as e.g. Al_2O_3, SiO_2, zeolites may not prevent sintering during high temperature processes carried out for long hours. The support would also influence the CO adsorption. Consequently, there may be difficulties in the characterization of promoters in the catalyst using some of the spectral methods like e.g. UV or IR, due to the high concentration of iron and the fact that iron oxides are not UV or IR transparent in the appreciable wavelength range of solid samples.

The process of dissociation of carbon monoxide by Fe and elements like Co, Ni, Ru, Rh occurs at slightly elevated temperatures (Fe 27 ^{o}C, Rh 197 ^{o}C). The syngas reduces oxides of these metals at temperatures around 197 ^{o}C, which is recommended for the FT synthesis. The reduction of the oxides of other metals like La, W, Cr, and Re is more difficult or not possible at temperatures at which the Fischer-Tropsch synthesis can produce acceptably long hydrocarbons. Metals like Cd, Zn, Cu, Ag, Au cannot be a catalyst for FT synthesis of hydrocarbons due to the fact that they do not adsorb CO strongly enough.

According to Dry (2002), if the price of scrap iron is 1.0, the estimated price of Ni will be 250, of Co 1000 and of Ru 50 000. The high price of Ru and its low availability restrict its application on a large scale. The FT process based on Ni catalysts generates too much CH_4[35]. This leaves Fe and Co as the only two metals which have a practical application in a FT synthesis.

Catalysts with Fe as the active metal, especially with alkali promoters, exhibit high WGS activity and can be applied in a process with low H_2/CO ratio obtained from coal or heavy oil gasification. The Fe-based FT catalyst is undesirable for synthesis with a high H_2/CO ratio usually obtained from natural gas[36,37]. However, the higher WGS activity can also be a disadvantage for Fe-based catalyst in comparison to those with Co. WGS activity increases the rate of water consumption and water inhibition phenomena are observed, resulting in a decrease in the catalyst activity[38]. In the FT process with a Co-based catalyst no water inhibition occurs. The Fe-based catalyst with a high density of the active sites used in low temperature FT processes may be used to produce heavy products and to low CO_2 selectivity. Furthermore, Fe-based FT catalysts might be more economically attractive than the Co-based ones.

There are two FT operating modes for Fe-based catalysts. The high temperature process (HTFT) is performed at temperatures between 300 - 350 °C and is used for the production of the light olefins and gasoline. The low temperature process (LTFT) is carried out at temperatures between 200 - 240 °C and is used for the production of waxes. One example of LTFT reactor is the Sasol Slurry Bed Reactor where syngas is going upwards through slurry containing the catalyst particles suspended in molten FT wax. In the LTFT the low temperature reduces the selectivity towards the undesired methane and increases wax production. The Sasol Advanced Synthol Reactor[39,40] is a high temperature process reactor in which the syngas flows through a fluidized bed of finely dispersed catalyst, as presented schematically in Figure 1.2.1. The gas throughput and hydrocarbon production rate are higher in HTFT reactors in comparison to these LTFT reactors due to the higher activity of the HTFT. The LTFT process has a big influence in the production of high quality diesel fuel[25,41].

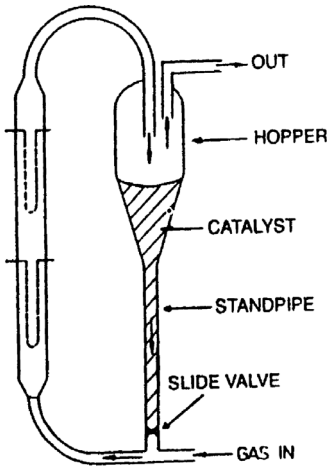

Fig. 1.2.1 Sasol Circulating Fluidized Bed reactor, (CFB).

1.2.2 Iron-based catalyst activation

The synthesis of the metal oxide catalyst is only part of the process of preparing a catalyst for the FT process. The metal oxide form is not usually active and the catalyst must undergo a reduction process before it can take part in the FT reaction. The activation of iron-based catalysts is usually carried out under hydrogen, carbon monoxide, or a mixture of both gases [42-44]. The FT Fe-based catalyst undergoes many transformations during the pretreatment as well as the main FT process. The FT effectiveness greatly depends on the form of the catalyst in each of the stages.

The first stage of the activation process is the reduction of haematite (α-Fe_2O_3) and leads to the production of magnetite (Fe_3O_4). The nature of the reduction process products present after activation relies on the activation gas used and conditions applied. The metal phases created after reduction depend on the time of exposure to the reductant, the reactor system, the pressure and temperature of the activation. Under CO gas or a mixture of CO and H_2 during pretreatment, iron carbide will be produced. There are many variations of the products present after pretreatment under CO. Some observed are iron carbides e.g. ε-Fe_2C, $\acute{\varepsilon}$-$Fe_{2.2}C$, Fe_xC and trigonal prismatic carbides, χ-$Fe_{2.5}C$ and θ-Fe_3C. However, activation carried out only under H_2 gives metallic iron (Fe^0). The Fe^0 will react in FT process with the syngas and iron carbide species will form at this stage[45].

According to Luo et al[46]. The reduction of Fe_2O_3 with CO and H_2 occurs in two steps; the reactions are presented below.

The reduction of Fe_2O_3 with CO:

$3Fe_2O_3 + CO \rightarrow 2Fe_3O_4 + CO_2$

$5Fe_3O_4 + 32CO \rightarrow 3Fe_5C_2 + 26CO_2$

The reduction of Fe_2O_3 with H_2:

$3Fe_2O_3 + H_2 \rightarrow 2Fe_3O_4 + H_2O$

$Fe_3O_4 + 4H_2 \rightarrow 3Fe + 4H_2O$

A variety of experiments have been conducted to characterise the iron phases present after the activation of iron-based catalysts in different atmospheres and at different conditions. For example Yang et al[47] found that the products of activation under syngas of an iron-based catalyst with a magnesium promoter depended on the magnesium content. The content of iron carbides in the activated catalysts first increases as a function of magnesium content and then goes through a maximum and decreases. Zhao et al. Shroff et al.[49] and Bukur et al. determined that the products of activation of a copper and potassium promoted iron-based catalyst under hydrogen were Fe_3O_4 and α-Fe; when the activation was performed in the atmosphere of carbon monoxide or syngas the catalyst consisted of Fe_3O_4 (mainly) and Fe_xC (carbides)[,48,49]. Li et al. characterized the products of activation of an iron-based catalyst, with an addition of manganese and potassium, under $H_2/CO = 1.2$ at 553 K and 0.1 MPa, to be χ-Fe_5C_2, and Fe^{2+} and Fe^{3+} ions. The examples of the possible structures of iron oxide before activation (α-Fe_2O_3) and those which may appear after the activation process (Fe_3O_4 and α-Fe) are presented in Figure 1.2.2.1.

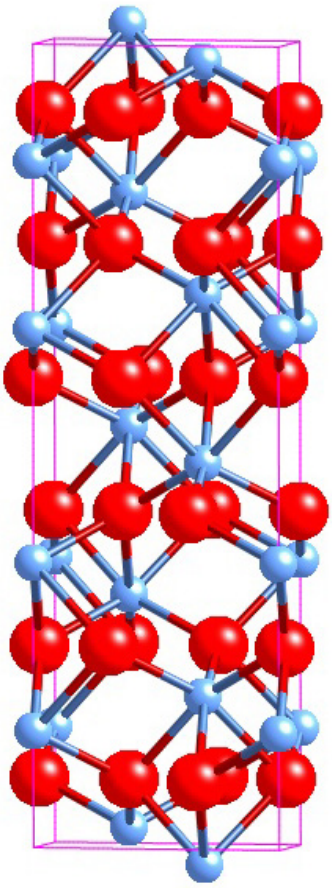

Fig.1.2.2.1 The hexagonal unit cell of haematite (α-Fe_2O_3). Fe^{3+} cations blue, O anions red sphere.

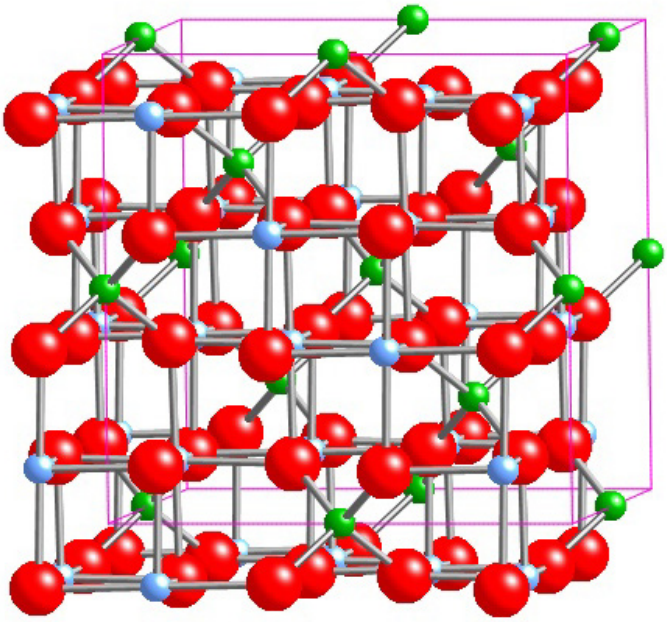

Fig. 1.2.2.2 Cubic structure of magnetite (blue spheres - octahedral $Fe^{2+/3+,}$ green – tetrahedral Fe^{3+} and red - oxygen).

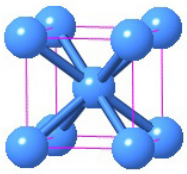

Fig. 1.2.2.3 Metallic Body-centred cubic-I lattice α-Fe

1.2.3 Catalyst surface – mechanisms of product formation

Different reactions can take place on a solid catalyst surface, e.g. adsorption of the reactants (physisorption and chemisorption), desorption of the products. The FT reaction involves the following main steps occurring at the catalyst surface:

- transport of reactants through the gas phase to the catalyst,
- the adsorption and dissociation of CO,
- the adsorption and dissociation of H_2,
- surface chemical reactions leading to alkyl chains (transfer of 2H to the oxygen to yield H_2O, desorption of H_2O, transfer of 2H to the carbon to yield CH_2, formation of a new C/C-bond),
- desorption of the final hydrocarbon products (primary products of the FT process),
- reactions taking place on the primary hydrocarbon products secondary reactions) like e.g. chain growth re-initiation[50,51].

However, there are many theories regarding these catalyst surface reactions and the order in which they take place. Schulz depicted some of the species that exist on the catalyst surface during the FT reaction, the examples are shown in Figure .1.2.3.1..

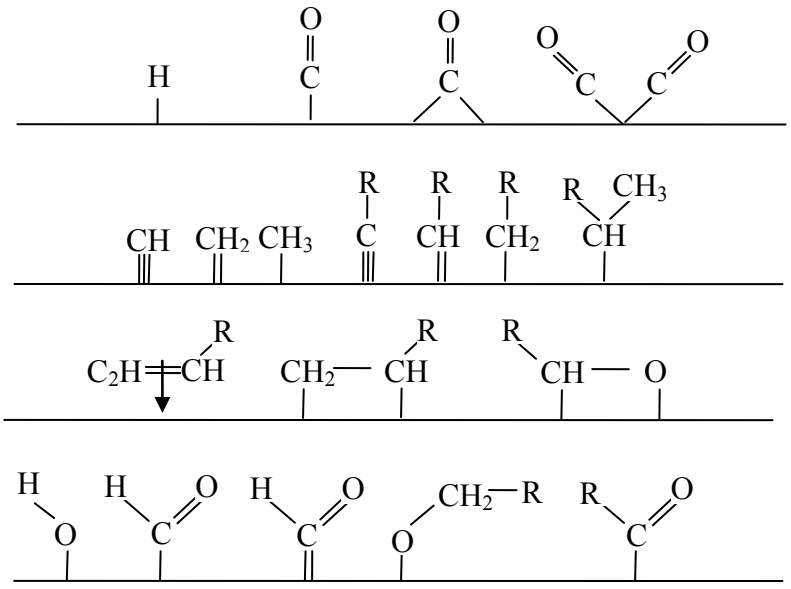

Fig. 1.2.3.1 Species that may exist on the catalyst surface during the FT reaction. [23,52].

There has been a large amount of research on the mechanism of the FT reaction. The earliest postulate was made by Fischer and Tropsch (1926), who suggested that carbon deposited from CO as a surface or bulk carbide eventually formed FT products. Pichler and Schulz[53] (1970) postulated a mechanism whereby CO was inserted into a metal-alkyl or metal-hydrogen bond. In 1979, Biloen et al. [54], presented evidence for the stepwise insertion of CH_x units produced from a syngas mixture. Brady and Pettit[55] (1981) supported the view that the principal FT mechanism involves a $–CH_2–$ stepwise polymerization.

One of the proposed FT mechanisms is postulated by Dry (1990)[56]. He also suggested that the first stage in the chain initiation is dissociation/chemisorption of CO, which might be bound to the surface of the catalyst in many different ways like for example in Figure 1.2.3.2:

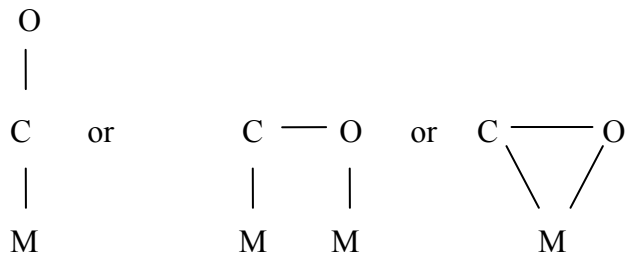

Fig. 1.2.3.2. The examples of CO bounding to the surface of the catalyst

The alcohols and aldehydes may be the primary compounds which appear on the surface, as a result of the insertion of CO into the chain. The -CH_2- group may also occur at this stage, Figure 1.2.3.3.

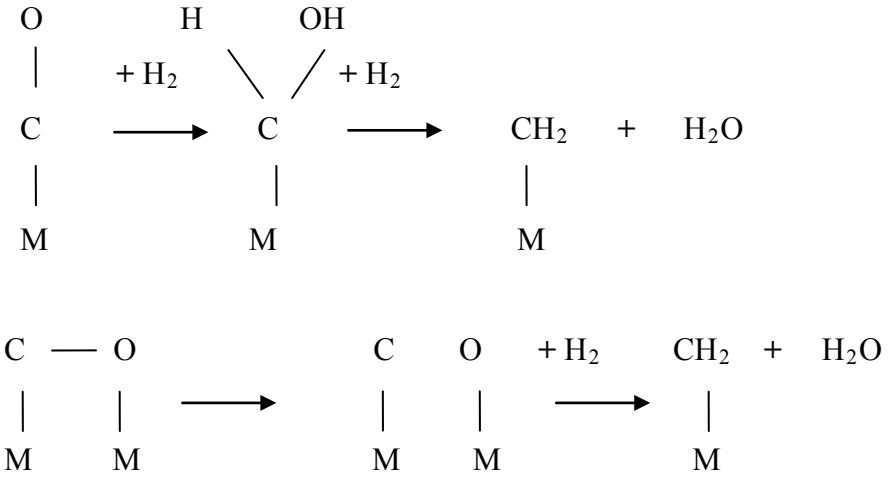

Fig. 1.2.3.3. Mechanism of the FTS; the chain initiation.

After the chain initiation and –CH_2- group formation the chain growth follows, Figure 1.2.3.4:

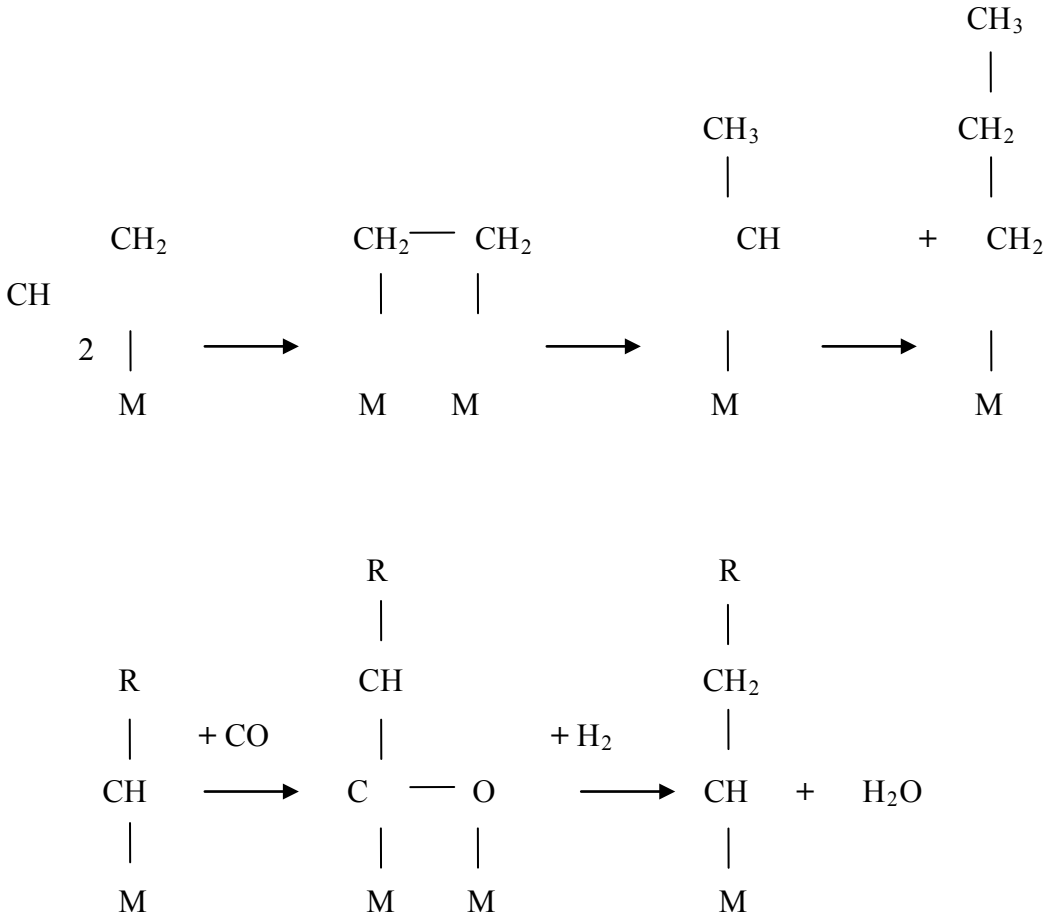

Fig. 1.2.3.4. Mechanism of the FTS; the chain growth.

After chain growth the chain termination follows and many different products may occur due to desorption, hydrogenation, insertion of oxygen and oxygenated species, Figure 1.2.3.5:

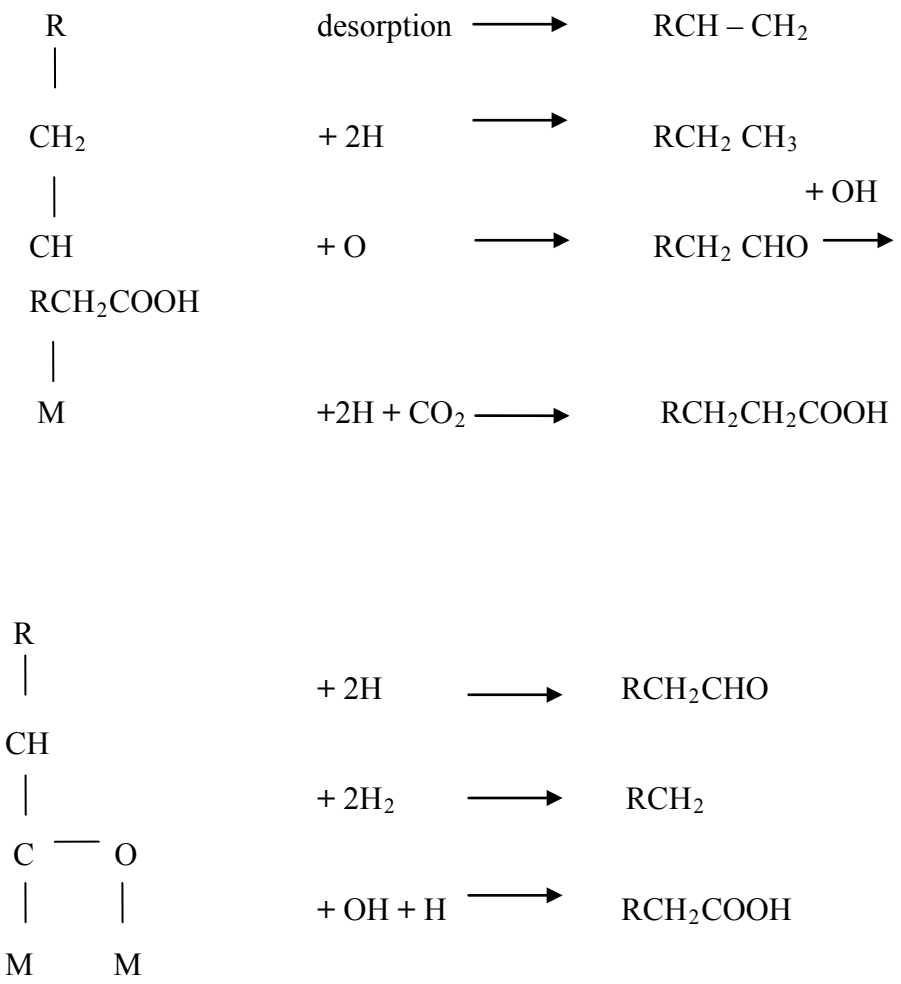

Fig. 1.2.3.5. Mechanism of the FTS; the chain termination.

In order to gain a better understanding of what occurs at the catalyst surface the bonding between CO and the catalyst should be mentioned. The multiple bond character of the metal-carbon bond occurs by formation of metal-CO π bonds by overlapping of metal dπ orbitals with empty anti-bonding CO orbitals, Figure 1.2.3.6.

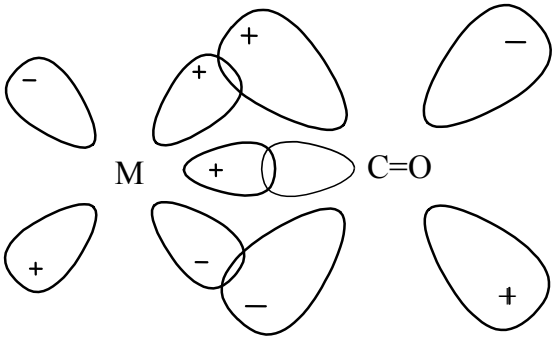

Fig. 1.2.3.6. Transition metal - carbon monoxide bond[23]

1.3 Sulfur in FT iron-based catalysts

Sulfur containing compounds are well known to exert an inhibiting or a poisoning effect in catalysts[57-61]. In solid catalysts sulfur generally forms several ordered structures, and with increasing coverage, it decreases or even suppresses the activity of the metal catalyst. The activation energy for the dissociation of H_2S on the iron surface is very low, thus the presence of H_2S in the feed may cause the deposition of atomic sulfur on the iron surface[57]. Sulfur is strongly chemisorbed by most of the catalytically active metals and in some cases even converts the metals into sulfides[58]. Therefore, the amount of sulfur in feedstock gases used in the FT process must be as low as possible. There are many important sulfur purification processes. The Rectisol process is employed in industry to reduce the sulfur content of coal-based feedstocks in the FT process to practical levels, even down to a level of 5 ppb.

1.3.1 S and CO dissociation on the catalyst surface

In the experiment presented by Curulla, the influence of sulfur on the dissociation of CO on a Fe-based catalyst surface in the FT process was studied. Two Fe-based catalyst surfaces were presented. Firstly, Fe (100) with one S atom per unit cell in a p(2x2) structure, ¼ ML coverage and the second with two S atoms per cell in a c(2x2) structure and ½ ML coverage. They were studied using density functional theory for the dissociation of CO and compared to a S-free Fe (100) catalyst surface. The dissociation of the CO on the Fe (100), which did not contain S was an exothermic process, but the same process occurring on the surface of the Fe-based catalyst with S (Fe(100)-S-p(2x2)) became endothermic. It was discovered that the activation energy for the dissociation of CO at the surface of Fe with S was slightly lower and also changed the sign of the reaction. Curulla et al. stated that the only stable adsorption site for atomic sulfur was the 4 – fold hollow site. In Figure 1.3.1, both Fe (100)-S-p (2x2) and Fe (100)-S-c (2x2) structures, are presented. For Fe (100)-S-c(2x2) CO adsorption at 4-fold hollow sites labelled (H) in the picture and on top sites labelled (T) is favoured. For Fe (100)-S-p(2x2) CO adsorbs at two distinct 4-fold hollow sites signed (H1) and (H2) and at the bridge sites (B).

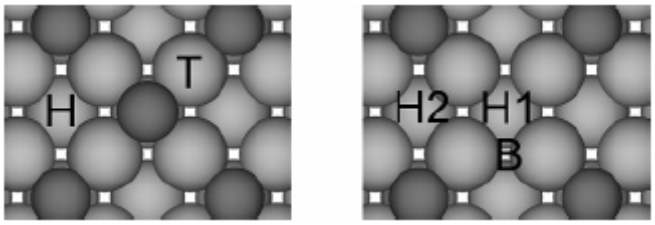

Fig. 1.3.1 Fe (100)-S-c(2x2) (Left) and Fe(100)-S-p(2x2) (Right) CO adsorption possibilities. Sulfur atoms are the dark circles.

According to the adsorption energies the interaction between CO and S on Fe(100) is short ranged (in the Curulla et al. experiment sulfur influences only the nearest surroundings). The sulfur itself does not cause any significant changes on the chemisorption geometry of CO.

1.3.2 Sulfur as a promoter, calcination and reduction process

It has been shown that sulfide species on the surface of the Fe-based catalyst are a poison. However, low sulfide loadings have also been reported to increase olefin/paraffin ratios. It was also reported[59-61] that a small amount of sulfate (SO_4^{2-}) may have a significant positive influence on an iron-based catalyst, acting as a promoter by increasing activity and heavier hydrocarbon selectivity.

Schulz[62], Flory[63] and Anderson[64] analysed the product distribution in many FTS. As a result the following equation for mass fraction based on statistical distributions was proposed:

$$W_n = n(1-\alpha)^2\,\alpha^{n-1} \quad (1.3.2.1)$$

where W_n is the weight percent of product containing n carbon atoms, and α the probability of chain growth.

The equation written in a logarithmic form is referred to as the Anderson-Schulz-Flory (ASF) equation:

$$\log\frac{W_n}{n} = n\log\alpha + \frac{(1-\alpha)^2}{\alpha} \quad (1.3.2.2)$$

where the α value may be calculated from the slope and the intercept. In the ASF equation all hydrocarbon products have well-defined maxima in allowed selectivity. For example, gasoline has α in the range between 0.7 and 0.8, diesels between 0.8 and 0.9, and waxes have an α factor greater than 0.9. According to Bromfield and Coville, a small amount of sulfur existing as SO_4^{2-} in the catalyst improves heavier hydrocarbons selectivity. In their experiment, the α factor was equal 0.78 for 500 ppm of sulfur in the catalyst, α = 0.83 for 2000 ppm of sulfur and α = 0.65 for the 5000 ppm of sulfur. The α factor for the catalyst with a very high concentration of sulfur (20 000 ppm) had an α value equal 0.53, which is typical for short chain hydrocarbons (C_3). Wu et al. confirmed the enhancement in diesel formation. However, they suggested a more complicated form of distribution with a three-parameter model of Huff and Satterfield[59,65]:

$$x_n = \beta(1-\alpha_1)\alpha_1^{n-1} + (1-\beta)(1-\alpha_2)\alpha_2^{n-1} \quad (1.3.2.3)$$

where α_1 is the chain growth factor of type 1 sites and α_2 is the chain growth factor of type 2 sites. The value of $\alpha_1 = 0.72$, $\alpha_1 = 0.92$ and $\beta = 0.60$.

Sulfur in Fe-based catalyst in FT reactions may be introduced from many different sources like $(NH_4)_2SO_3$, $(NH_4)_2SO_4$, $(NH_4)_2S$, Na_2S, and $FeSO_4 .xH_2O$, or deposited from H_2S. Bromfield and Coville discovered that a small amount of sulfide like Na_2S or $(NH_4)_2S$, added during the precipitation stage in the FT catalyst synthesis resulted in selectivity modifications and an activity enhancement. It was discovered that the catalysts with sulfide concentrations up to 500 ppm were around four times more active than the catalyst without sulfide. It was also found that high concentration of sulfur, above the level 20,000 ppm caused poisoning of the catalyst.

The calcination of the FT Fe-based catalyst cannot be performed at very high temperatures due to sintering and the consequent loss of active surface. The temperature

should not be lower than 200 ºC in order to effectively remove poisoning nitrates from the catalyst surface. As mentioned above, iron-based FT catalysts have to be activated before the FT process. Pre-treatment of the iron-based catalyst under hydrogen influences the formation of different iron species and the sulfur speciation at the surface.

Calcination and reduction conditions, time and temperature influence the transformation of S species on the surface of the Fe-based catalyst. The presence of S^{2-} species was discovered for low-level S-containing catalysts after calcination at 200 ºC and reduction at 300 ºC. However, after high temperature calcination (400 ºC) SO_4^{2-} species dominated. The high-level S-containing catalysts, on the other hand, calcined at 200 ºC and reduced at 300 ºC, exhibited the presence of both sulfide and sulfate species. Reduction at 400 ºC left only sulfide species on the surface. The occurrence of oxidized sulfur species, like sulfate in sulfided Fe-based catalyst in the Bromfield and Coville (1997) experiment, suggests a sequence of redox reactions taking place when reduction is carried out at higher temperatures.

The working Fe-based catalyst is composed of many phases like α-Fe, Fe_3O_4, Fe_xC and the answer to which of above phases is the most active is still being studied[61-68]. In low-level sulfided catalysts the presence of sulfates may suggest incomplete reduction of iron. [61,69-71]. However, a Fe-based FT catalyst with high concentration of sulfides added in the precipitation stage is reduced to metallic form more rapidly during activation. Wu et al. and others[60,72] also observed a decrease in the reduction temperature for the transformation of α-Fe_2O_3 to Fe_3O_4 for the catalyst synthesised with a small amount of sulfate. Wu et al. have also shown that the sulfate-containing catalyst has a higher surface area and more dispersed α-Fe_2O_3 phase than a sulfate-free catalyst. Thus, the surface area and reducibility of the Fe-based FT catalyst are strongly related to the levels of S^{2-} and SO_4^{2-}, which act as a potential promoter or poison in the FT reaction.

1.3.3. Sulfur and oxygen vacancies competition

Bromfield and Coville[61,73,74] observed that each sulfide atom at low coverage may poison even from 8 to 10 atoms of Fe and this leads to a decrease of catalyst activity. During the reduction process, it was discovered that sulfur may block the diffusion of oxygen on the catalyst surface. The S site competes with O according to a segregation mechanism occurring on the surface during reduction under hydrogen. Sulfur migration and oxygen depletion depend on the concentration of oxygen on the surface. When oxygen is abundant segregation of one atom of S is preceded by the removal of two atoms of O, until one O atom is substituted by one S atom. Figure 1.3.3. shows that, at elevated temperatures, bulk oxygen vacancies diffuse to the surface and they react with sulfur atoms. The S coverage may depend on the competition phenomena between desorption into a gas phase and filling of appearing new vacancies.

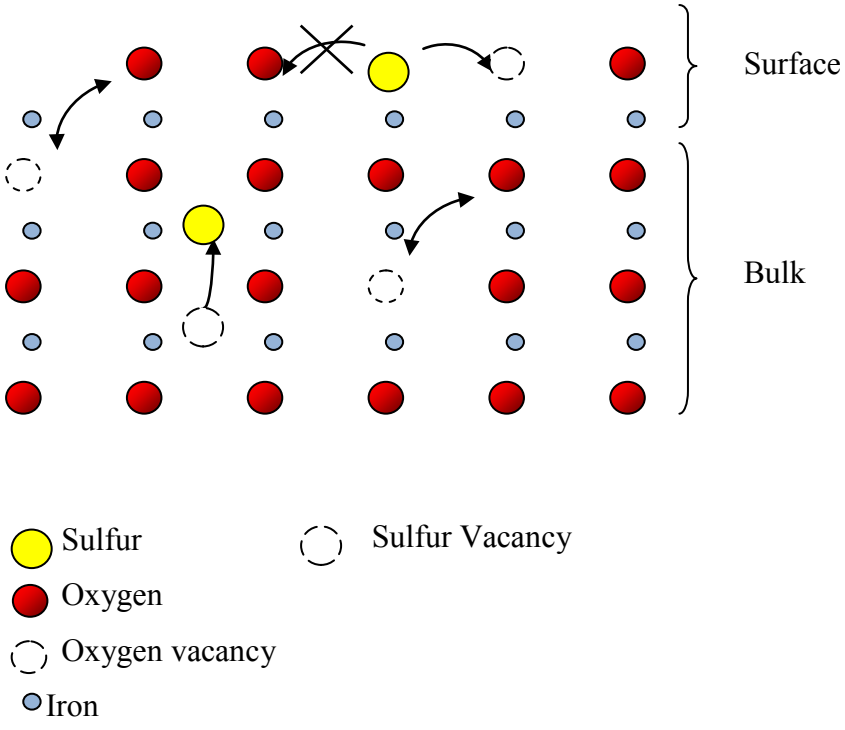

Fig. 1.3.3 The mechanism of the influence of bulk reduction state of iron oxide on the S desorption.

In this work, the surface of the Fe-based catalyst with low (500 ppm) concentrations of S at the surface was studied with the application of various spectroscopic techniques.

For better understanding of the migration effect of S, which can occur during activation, both surface and bulk techniques were applied. The techniques applied were XRF and XANES for bulk analysis and EDX and XPS as surface sensitive techniques. After analyzing the results from both technique types it was possible to evaluate the distribution of S in the Fe-based catalyst.

1.4 Alkali metals as promoters in FT catalysts

Metallic catalysts often contain chemical compounds which themselves are inactive but improve the activity, selectivity and stability of the catalyst - promoters. The iron oxide catalyst in the FT process is usually promoted by alkali metals. The most important roles of the alkali promoters for the FT process:

(1) enhance the CO and decrease the H_2 adsorption,[75 -81]
(2) enhance FTS activity[77,80,82,83 ,97]
(3) shift the selectivity in the FTS to higher hydrocarbons[76,77,80,84]
(4) favour the formation of unsaturated products [75,77,80,]
(5) suppress the hydrogenation of olefins[77,78,80,85]
(6) increase in activity for the WGS [77,81,86,87,]
(7) influence for the reduction process of iron oxide FT catalyst[97,75,77,80,88,89]

1.4.1 Alkali metals properties

The alkali metals, the Group 1 elements, are lithium, sodium, potassium, rubidium, caesium and francium. According to the very small occurrence in the nature and high radioactivity francium is not discussed. All alkali metals have atoms with one electron in the outermost electron shell; electron configuration ns^1. Therefore, they form simple positively charged ionic compounds when the outer electron shell gives up the electron to a more electronegative element. The alkali metals properties like e.g. electronegativity, first ionisation energy, lattice energies are homologous and decrease down the group and properties like reactivity, atomic and ionic radius, increase down the group[90] The exception is Li in Allred-Rochow electronegativities. However this

electronegativity scale may be useful for discussing the electron distribution in alkali metals. Selected properties are shown in a table 1.4.1.

Table 1.4.1 Properties of the Group 1 elements [90,91]

	Li	Na	K	Rb	Cs
Atomic radius (pm) [90]	152	186	231	244	262
Ionic radius (pm) [90]	60	95	133	148	169
Ionization energy (kJ mol^{-1})	519	494	418	402	376
Ionization potentials (kcal mol^{-1}) [91]	124	118	100	96	90
Lattice enthalpies of formation of alkali metals M_2O (kJ mol^{-1}) [91]	143.4	99.4	86.4	78.9	75.9
Allred-Rochow electronegativities	0.97	1.01	0.91	0.89	0.86

The alkali metal properties like e.g. the first ionization energy are influenced by the change in the atomic and ionic radius. The radii of the atoms of the Group 1 elements are related to the number of orbitals/shells around the nucleus and the electrostatic attraction of the outer electrons by the nucleus. The increase in atomic radii down the group leads to a decrease in energy needed to remove the electron from the outer shell (first ionization energy) in the process of creation of a cation. Another very important feature changing down the Group 1 is the reactivity of the alkali metals. The ability to form cations increases down the group due to the decrease of the ionization energy and consequently an increase in the reactivity of heavier atoms. The variation in atomic radius and first ionization energy of the elements of Group 1 is presented in Figure 1.4.1.

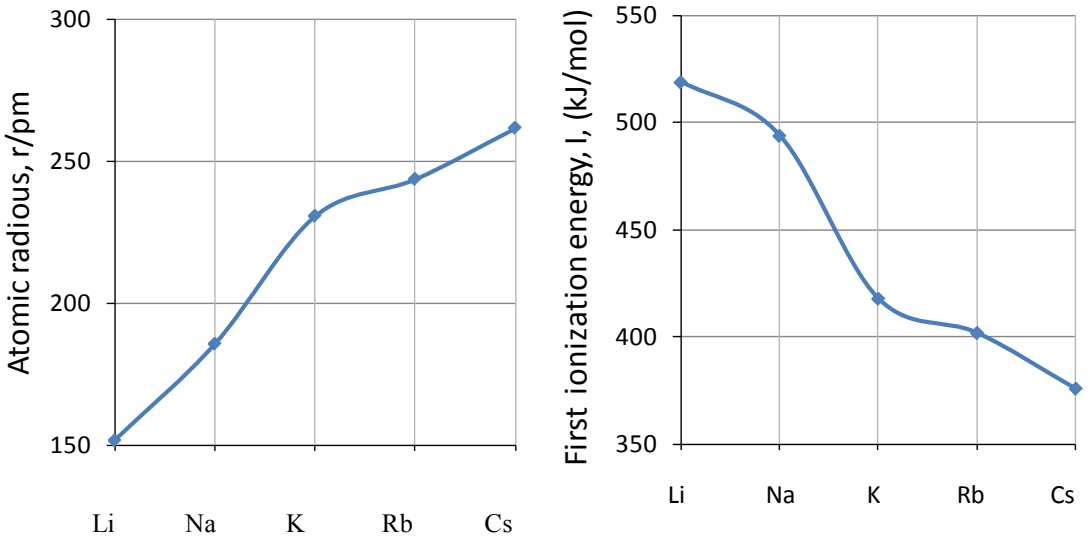

Fig. 1.4.1 The tendency in atomic radius (left) and first ionization energy of the elements of Group 1.

The small distance between nucleus and electron like e.g. in Li or Na is related to strong Coulombic attraction. The electronegativity – the power of the atom to attract electrons - is higher than for the atoms of the elements lower in the Group 1.

The electronegativity scale suggested by Allred and Rochow is based on the influence of electric field at the surface of an atom. According to it the Coulombic potential at the surface of the atom is proportional to the effective nuclear charge and radius ratio (Z_{eff}/r), and the electric field is proportional to the ratio of effective nuclear charge and radius squared (Z_{eff}/r^2). According to the Allred-Rochow definition alkalis with higher electronegativity have higher effective nuclear charge and smaller covalent radius. The values of electronegativities suggested by Allred-Rochow are given in the Table 1.4.1. Another characteristic property, which increases down the group, is polarizability. The larger and heavier atoms and ions of the alkali metals have characteristic closely separated frontier orbitals, this is why the atoms and ions from down the Group 1 are most polarisable.

1.4.2. Alkali metal ions in FT Fe Catalysts

The basic properties and trends of the alkali metals as discussed above are the introduction to a very important observation in FT catalysts with alkali promoters, which is the migration of the alkalis. The ionic transport should be considered from many perspectives. The mobility of the alkalis will be different on the surface and in the bulk of the iron oxide catalyst. The migration will change also during the reduction process, depending on the different structures which will occur during the activation process. The alkali metals will behave differently in α-Fe_2O_3, Fe_3O_4, and a Fe_3O_4/Fe mixture, they will interact/migrate in a different way in a rhombohedral, an octahedral and a tetrahedral structure. Both crystallographic and thermodynamic parameters may be related to the activation energy for migration of the alkalis[92]. The most important parameters which can explain that process are: the average metal-oxygen bond energy within the lattice, the mobile alkalis ion radius versus active metal oxide radius ratio, lattice polarizability towards ionic migration. The basic scheme for the migration of the alkali ions in the iron oxide catalyst towards the surface is presented below, Figure 1.4.2.1.

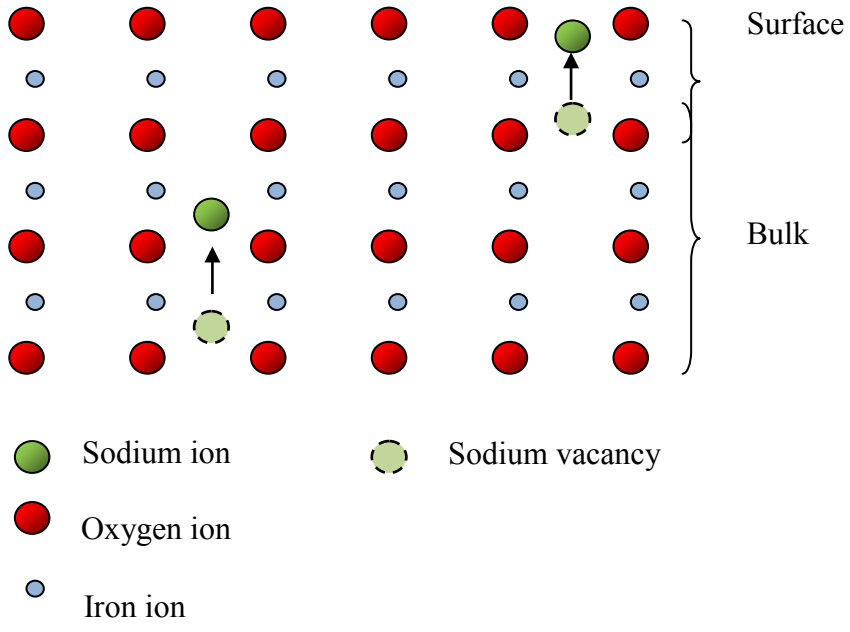

Fig. 1.4.2.1 Schematic migration process of the alkali metals ions in the iron oxide catalyst towards the surface.

An important parameter in considering the migration of alkali metals towards the surface in the iron oxide catalyst is the ionic radius of the alkali. The higher ability of migration towards the surface according to the alkali size would follow the order: Li > Na > K > Rb > Cs. However, the possible variations in migration in a crystal structure depending on size of the pores/cavities and size of their entrances, should be considered. Thus, due to the large size, Cs might remain at the entrance of the micropores and ability of migration, as suggested by Fierro (1990) may be even lower than K[93].

The migration of alkali metals on both sites on the Fe_3O_4 (111) surface was also examined in the previous study. It was found that migration of Li and Na from site-2 to site-1 needs more energy than for K, Rb, Cs, which had no energy barrier to migrate. The experiment led to the conclusion that negligible energy barriers of alkali metals may facilitate their migration ability on the Fe_3O_4(111) surface. The surface and two different adsorption sites for alkali metals in a p(1 x 1) unit cell of Fe_3O_4(111) are presented in Figure 1.4.2.2

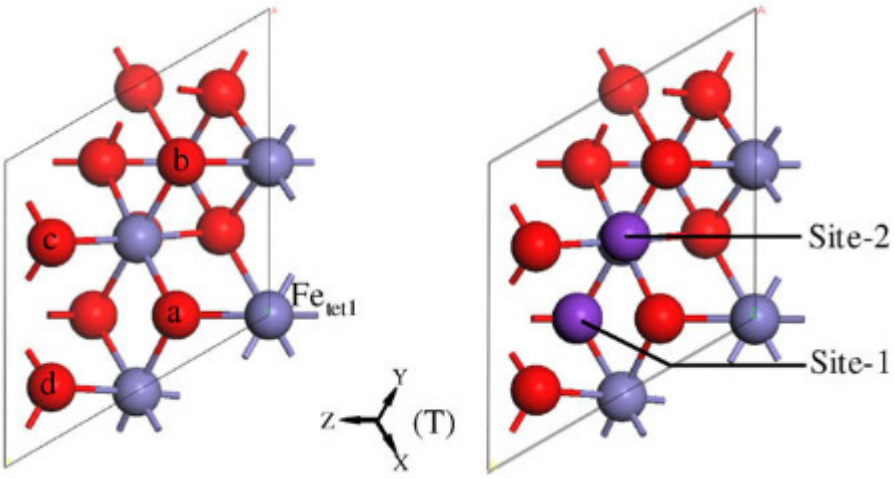

Fig. 1.4.2.2 Front view for a p(1 x 1) Fe_3O_4 (111) unit cell and two different adsorption sites of alkali metals. Fe atom – blue , O – red, alkali metal –purple.

The initial form of the alkali promoters used in this study are alkali carbonates like Na_2CO_3, K_2CO_3, Rb_2CO_3. The lattice energy of the carbonates, and their thermal decomposition temperature, decrease down the group[90,94]. Different lattice enthalpies explain different chemical properties like e.g. thermal stabilities of ionic solids. A good example might be the fact that the carbonates combined with large cations are more difficult to decompose thermally as large cations stabilize large anions[95]. The enthalpy

change for thermal decomposition of the Group 1 metal carbonates may be presented like:

$$M_2CO_3(s) \leftrightarrow M_2O(s) + CO_2(g)$$

$$\Delta H = X + H_L(M_2CO_3) - H_L(M_2O)$$

X – enthalpy input required for the gas phase decomposition of CO_3^{2-}:

$$CO_3^{2-}(g) = O^{2-}(g) + CO_2(g),$$

H_L – lattice enthalpies

The enthalpies change equations for thermal decomposition of the alkali metals which will be used in the experiment (Na, K and Rb), are presented below:

1) $Na_2CO_3(s) \leftrightarrow Na_2O(s) + CO_2(g)$ ΔH (298 K) = 321 kJ/mol

2) $K_2CO_3(s) \leftrightarrow K_2O(s) + CO_2(g)$ ΔH (298 K) = 394 kJ/mol

3) $Rb_2CO_3(s) \leftrightarrow Rb_2O(s) + CO_2(g)$ ΔH (298 K) = 416.5 kJ/mol

The decomposition temperature is lower for metal oxides that have relatively high lattice enthalpies compared with carbonates. Thermal decomposition of the alkali metal carbonates (M^+) will occur in higher temperature than higher charged alkaline earth carbonates (M^{2+}), where the difference in lattice enthalpy between MO and MCO_3 is also due to the larger charge on the cation.

It was previously discovered by Dry et al.[75] that the relative activity of FT catalysts with an alkali metal used as a promoter increases in the following order Li < Na ≈ Rb < K[96,75]. This trend was confirmed later by Yang et al., who used density functional theory (DFT) and computed the net charge for the interaction of alkali metals with the Fe_3O_4 (111) surface[97]. The order of electron donating by alkali metals to the surface Fe and O atoms studied by Yang was Li < Na < K ≈ Rb ≈ Cs. The alkali metals change the surface state of Fe 3d orbital during electron transfer from alkali metal to the Fe 3d

orbital. The differences in electron donating for alkalis are explained to the large extent of the amplitude of valence band for adsorbing K, Rb and Cs, which are very similar and larger than those of Na and Li.

1.4.3 The alkali metals and Fischer-Tropsch process activity

One of the most important role of the alkali promoters for the FT synthesis is to enhance the CO and decrease the H_2 adsorption. The increase of the CO adsorption phenomenon might be explained by a simple mechanism where alkali metal donates electrons to the iron. The electrons are next accepted by CO, which facilitates its chemisorption to the iron oxide site. The Fe-C bonding formation is competitive to Fe-H bond creation. Thus the presence of the alkali metals causes weakening of the Fe-H and C-O bonds and strengthening of the Fe-C bond[81,98].

The FTS activity enhancement is due to the electrostatic field of alkali promoter, which influences the behaviour in its vicinity. The electrostatic field can enhance or suppress the shifts of electrons associated with a chemisorption bond. The alkali promoter activates sites in neighbouring molecules, but always acts as a blocker of the site where is present, since the promoter itself is not active[99].

Potassium is a common promoter for iron catalysts in FTS for many years. It has been found that potassium promoters provide an increase in the alkene yield and a decrease in the fraction of methane that is produced. Potassium also increases the catalytic activity for FTS and WGS reactions[100]. However, potassium may be used as a promoter only with specific quantities. It was noticed[,100] that a very high potassium loading may lead to negative effects like coverage of part of the surface area of the iron catalyst which leads to a limitation of the promoting effect and decrease in the CO conversion. It was also observed[101-103] that potassium helps to form active sites during reduction of iron oxides. Moreover it was also shown that potassium promoter facilitates the reduction of iron oxide to metallic iron during hydrogen activation. It has been hypothesised that potassium may facilitate formation of nucleation sites and that resulting in the origination/creation of small carbide crystallites. An important property of potassium

may be resistance to sulfur deactivation of FT catalysts, as proposed by Anderson and others[69,104].

Another alkali metal used as a promoter in FTS is sodium. It was reported that residual sodium left during the synthesis of the catalyst acts as a textural inhibitor, resulting in bigger iron phase particles size and smaller surface area[105]. Sodium can weaken the dispersion of the α-Fe_2O_3 phase. Both sodium and potassium can reduce methane selectivity in iron catalysts. Iron catalysts with Na and K exhibit much higher WGS rate than other alkali promoted catalysts or unprompted catalysts[105-107].

Rubidium as a FTS promoter behaves similarly to the previously described alkali promoters and increases overall CO conversion and causes a decrease of methane selectivity. Moreover rubidium enhances the higher molecular weight fraction of hydrocarbons (C_{5+}) and improves olefins selectivity. It was also observed that a rubidium promoter in FTS might be less effective as a promoter, than for example potassium; the energies of the electronic transitions of rubidium facilitate study by XPS and XAFS techniques [108]. In general the effects of alkali promotion on iron FT catalysts are: suppression of hydrogenation capability, increase in CO dissociation, increase in formation of long-chain hydrocarbons, and decrease in the conversion activity of CO.

1.5 Conclusions

The FTS fuel will be a good alternative source of energy for a long time before renewable energy sources start to dominate. It is very important to study FTS to make the process more cost-efficient and economically advantageous. The development of the catalyst, the most important element in economizing FTS, may be the key to make the process a more competitive source of energy. The iron oxide FTS catalyst may be a cheaper option comparing to catalysts with other active metals including the commonly used cobalt catalyst in FTS. To improve the properties of iron oxide catalyst the study of additives and different synthesis methods and conditions will be carried out.

The main aim of this project is development of a series of iron-based FT catalysts with different dopants. Firstly, the behaviour of the iron oxide catalyst before activation and its transformation during activation will be examined. Then the influence of different types of alkali metals added will be investigated.

The influence of different synthesis parameters like temperature, pH and titration rates on the catalyst morphology and porosity as well as other physical and chemical properties will be studied. Moreover, in the project, the influence of the preparation method (co-precipitation, wetness incipient impregnation) on the FT catalyst properties will be determined. After alkali metal promoters, the influence of sulfur on the properties of the FT catalyst will be investigated.

Detailed characterization of the synthesized FT catalysts by means of Scanning Electron Microscopy (SEM), Energy Dispersive X-ray (EDX), Brunauer, Emmett and Teller surface area determination (BET), Powder X-ray diffraction (P-XRD), X-Ray Absorption Spectroscopy (XAS), X-ray Photoelectron Spectroscopy (XPS) and X-ray Fluorescence spectroscopy (XRF). The techniques used in the project will be described in the next chapter (Chapter 2).

1.6 References

1. PennWell Corporation, *Oil & Gas Journal*, 103 (2005) 1.
2. www.opec.org, 2011.
3. www.bp.com/statisticalreview, 2011.
4. Hubbert, M.K., *Science,* 109 (1949) 103.
5. Almeida P., Silva P., *Energy Policy,* 37 (2009) 1267.
6. Campbell C., Heapes S., *An Atlas of Oil and Gas Depletion,* Jeremy Mills Publishing, Lindley, Huddersfield, UK, 2008.
7. Campbell C., Laherrere J., *Sci. Am.,* 3 (1998) 78.
8. Hook M., Bardi U., Feng L., Pang X., *Mar. Petrol. Geol.,* 27 (2010) 1995.
9. MacKay D.J.C., *Sustainable Energy - without the hot air,* Cambridge University Press, Cambridge, UK, 2009.
10. Hubbert M., *Nuclear Energy and The Fossil Fuels,* Energy Bulletin, Santa Rosa, California, USA, 95 (1956) 1.
11. Peters K.E., Walters, C.C., Moldowan, J.M., *The Biomarker Guide*, Cambridge University Press, Cambridge, UK, 1 (2005) 1155.
12. www.eia.gov
13. Ning W., Koizumi N., Yamada M., *Catal. Commun.*, 8 (2007) 275.
14. Dry M.E., *Appl. Catal. A-Gen.,* 189 (1999) 185.
15. Schobert H.H., Song C.*, Fuel,* 81 (2002) 15.
16. Alpern B., Sousa M.J., *Int. J. Coal Geol.,* 50 (2002) 3.
17. Fischer F., Tropsch H., *Brennst-Chem*., 7 (1926) 97.
18. Morales F., Weckhuysen B. M., *Catalysis,* 19 (2006) 1.
19. www.Fischer–Tropsch.org, 2011.
20. Dry M.E., *Appl. Catal. A: Gen.*, 276 (2004) 1.
21. Jager B. *Proceedings of the 5th Natural Gas Conversion Symposium*, Taormina, Italy, 1998.
22. Demirbas A., Dincer K., *Sila Sci.,* 30 (2008) 1233.
23. Wender I., *Fuel Process. Technol.*, 48 (1996) 189.

24. Moulijn J.A., van Leeuwen P.W.N.M., Santen R.A., *Catalysis An Integrated Approach to Homogenous, Heterogeneous and Industrial Catalysis;* Elsevier Science Publishers B.V. Amsterdam, Netherlands, 79 (1993) 1.
25. Dry M.E., *Appl. Catal. A: Gen.*, 138 (1996) 319.
26. CRC Handbook of Chemistry and Physics, CRC Press, Taylor and Francis Group, 89th Edition, London, UK, 2008.
27. Kagan D. N., Lapidus A. L., Shpil'rain E. E., *Solid Fuel Chem.,* 42 (2008) 132.
28. Zhang Q, Kang J., Wang Y., *Chem. Cat. Chem.*, 2 (2010) 1030.
29. Shultz J. F., Hofer J. E., Cohn E. M., Stein K. C., Anderson R.B., US Government Printing Office, *Bur. Mines Bull*., 578 (1959) 139.
30. Iglesia E., Spivey J.J., Fleisch T. H., *Stud. Surf. Sci. Catal.*, 136 (2001) 1.
31. Sekine Y., Chihara T., Watanabe R., Sakamoto Y., Matsukata M., Kikuchi E., *Catal. Lett.*, 140 (2010) 184.
32. Natesakhawat S., Wang X., Zhang L., Ozkan U.S., *J. Mol. Catal. A-Chem.,* 260 (2006) 82.
33. F. R. van den Berg, *Zirconia-Supported Iron -Based Fischer-Tropsch Catalysts Influence of Pressure and Potassium on Structure and Catalytic Properties*, Universiteit Utrecht, 2001.
34. Wan H.-J., Wu B., Zhang C.-H., Teng B.-T., Tao Z.-C., Yang Y., Zhu Y.-L., Xiang H.-W., Li Y.-W., *Fuel* 85 (2006) 1371.
35. Dry M.E., *Catal. Today* 71 (2002) 227.
36. Schulz H., *App. Catal. A-Gen.,* 186 (1999) 3.
37. Li S., Krishnamoorthy S., Li A., Meitzner G.D., Iglesia E., *J. Catal.,* 206 (2002) 202.
38. Kim Y.H., Hwang D.-Y, Song S.H., Lee S.B., Park E.D., Park M.-J., *Korean J. Chem. Eng*., 26(2009)1591.
39. Duvenhage D.J., Shingles T., *Catal. Today,* 71 (2002) 301.
40. Jager B., Espinoza R., *Catal. Today*, 23 (1995) 17.
41. Espinoza R.L., Steynberg A.P., Jager B., Voslo A.C, *Appl. Catal. A: Gen.,* 186 (1999) 13.
42. Herranz T., Rojas S., Pérez-Alonso F.J., Ojeda M., Terreros P., Fierro J.L.G., *J. Catal.,* 243 (2006) 199.

43. Bukur D.B., Okabe K., Rosynek M.P., Li C., Wang D., Rao K.R.P.M., Huffman G.P., *J. Catal.*, 155 (1995) 353.
44. O'Brien R.J., Xu L., Spicer R.L., Davis B.H., *Energy Fuels 10* (1996) 921.
45. Schulz H., Schaub G., Claeys M., Riedel T., *Appl. Catal. A Gen.,* 186 (1999) 215.
46. Luo M., Davis B.H., *Fuel Process. Technol.,* 83 (2003) 49.
47. Yang J., Sun Y., Tang Y., Liu Y., Wang H., Tian L., Wang H., Zhang Z., Xiang H., Li Y., *J., Mol. Catal. A Chem.,* 245 (2006) 26.
48. Zhao R., Sudsakorn K., Goodwin Jr. J.G., Jothimurungesan K., Gangwal S. K., Spivey J.J., *Catal. Today,* 71 (2002) 319.
49. Shroff M.D., Kalakkad D.S., Coulter K.E., Köhler S.D., Harrington M.S., Jackson N.B., Sault A.G., Datye A.K., *J. Catal*., 156 (1995) 185.
50. Marales Cano, F., *Manganese Promotion in Titania-Supported Cobalt Fischer-Tropsch Catalysis,* Ponsen & Looijen, Wageningen, Netherlands, 2006.
51. Twigg M. V., *Catalyst Handbook*, Wolfe Publishing Ltd, Billingham, UK, 1989.
52. Schulz, H., *Mol. Chem.,* 1 (1985) 1.
53. Pichler, H., Schulz, H., *Chem.Ing.Tech.,* 42 (1970) 162.
54. Biloen P., Sachtler,W.M., *Adv. Catal.,* 30 (1981) 165.
55. Brady R.C., Pettit, R.,, *J. Am. Chem. Soc.,* 103 (1981) 1287.
56. Dry M.E., *Catal. Today*, 6 (1990) 183.
57. Curulla-Ferré D., Govender A., Bromfield T.C., Niemantsverdriet J.V., *J. Phys. Chem. B,* 110 (2006) 13897.
58. Cornils B., Herrmann W.A., Schlögl R., Wong C.H., *Catalysis from A to Z*, Wiley-VCH GmbH & Co., Weinheim, Germany, 2003.
59. Wu B.., Bai L., Xiang H., Li Y.-W., Zhang Z., Zhong B., *Fuel,* 83 (2004) 205.
60. Bromfield T., Coville N., *App. Surf. Sci.,* 119 (1997) 19.
61. Bromfield T., Coville N., *App. Catal. A-Gen.,* 186 (1999) 297.
62. Schulz G.V., *Z. Phys. Chem.,* 30 (1935) 379.
63. Flory P.J., *J. Am. Chem. Soc*., 58 (1936) 1877.
64. Friedel R.A., Anderson R.B., *J.Am.Chem.Soc.* 72 (1950) 2307.
65. Huff G.A., Satterfield C.N., J. Catal., 85 (1984) 370.
66. Reymond J.P., Meriaudeau P., Teichner S.J., *J.Catal.,* 75(1992) 39.

67. Shashkin D.P., Shiryaev P.A., Chichagov A.V., Morozova O.S., Krylov O.V., *Kin. Catal.,* 33 (1992) 744.
68. Duvenhage D.J., Espinoza R., Coville N.J., by Delmon B., G.F. Froment, *Catalyst Deactivation,* Elsevier Science Publishers B.V., Amsterdam, Netherlands, (1994) 351.
69. Shultz J.F., Hofer L.J.E., Karn F.S., Anderson R.B., *J. Phys. Chem.,* 66 (1962) 501.
70. Anderson B. B., Karn F. S., Kelly R. E., Shultz I. F., *Bur. Mines Bull*., 628, US Government Printing Office, Washington DC, USA, 1965.
71. Rapoport I.B., Muzovskaya O.A., *Khim. Tekhnol.,* 2 (1957) 18.
72. Curtis V., Nicolaides C.P., Coville N.J., Hildebrandt D., Glasser D., *Catal. Today,* 49 (1999) 33.
73. Bartholomew C.H., Agrawal P.K., Katzer J.R., *Adv. Catal.,* 31(1982) 135.
74. Kiskinova M.P., *Poisoning and Promotion in Catalysis based on Surface Science Concepts and Experiments*, Amsterdam, 1992.
75. Dry M. E., in: Anderson J. R., Boudard M., *Catalysis: Sci. Techn.,* 1 (1981) 155.
76. H. Kolbel,Giehring H., *Brennstoff-Chem.,* 44 (1963) 343.
77. Yang Y., Xiang H-W., Xu Y-Y., Bai L., Li Y-W., *Appl. Catal. A-Gen.,* 266 (2004) 181.
78. Henrici-Olive G., Olive S., *J. Molec. Catal*. 16 (1982) 187.
79. Dry M.E., Shingles T., Boshoff L.J. and Osthuizen G.J., *J. Catal.,* 15 (1969) 190.
80. Luo M., O'Brien R.J., Bao S., Davis B.H*., Appl. Catal. A-Gen.,* 239 (2003) 111.
81. Bukur D. B., Mukesh D., Patel S,A., *Ind. Eng. Chem. Res.* 29 (1990) 194.
82. Lee E.H., *Catal. Rev*., 8 (1973) 285.
83. Hirano T., *Appl. Catal.*, 26 (1986) 65.
84. Benzel H.P., Kerbs H.J., *Surf. Sci.*, 109 (1981) 527.
85. Ronald A.D., Bell A.T., *J. Catal.* 97 (1986) 121.
86. Dictor R. A., Bell A.T*., J. Catal.* 100 (1986) 533.
87. Miller D. G., Moskovits M., *J. Phys. Chem. Process Des. Dev.*, 22 (1983) 97.
88. Rankin J.L., Bartholomew C. H., *J. Catal.* 100 (1986) 533.
89. Jiang M., Koizumi N., Yamada M., *Appl. Catal*. A 204 (2000) 895.

90. Shriver D.F., Atkins P.W., et al., *Inorganic Chemistry*, Oxford University Press, Fourth Edition, Oxford, UK, 2006.
91. Johnson D.A., *Some thermodynamic aspects of inorganic chemistry*, Cambridge University Press, Cambridge, 1968.
92. Sammells A.F., Schwartz M., Mackay R.A., Barton T. F., Peterson D.R., *Catal. Today,* 56 (2000) 325.
93. Fierro J. L. G., Medina F., Salagre P., Sueiras J.E., *J.Molec. Catal.,* 61 (1990) 197.
94. Shchukarev A.V., Korolkov D.V*., Central. Eur. J. Chem* 2 (2004) 347.
95. Cox P.A., *Instant Notes Inorganic Chemistry*, Oxford, UK, 2004.
96. Ngantsoue-Hoc W., Zhang Y., J. O'Brien R., Luo M., Davis H. *Appl. Catal. A-Gen.* 236 (2002) 77.
97. Yang T., Wen X-D., Li Y-W., Wang J., Jiao H., *Surf. Sci.*, 603 (2009) 78.
98. Sarkar A., Jacobs G., Ji Y., Hamdeh H., Davis B.H., *Catal. Lett.,* 121 (2008) 1.
99. Bowker M., *The Basic and Applications of Heterogeneous Catalysis,* Oxford University Press, Oxford, UK, *53* (1998) 25.
100. Luo M., O'Brien R.J., Bao S., Davis B.H., *Appl. Catal. A-Gen.,* 239 (2003) 111.
101. Li S., Li A., Krishnamoorthy S., Iglesia E., *Catal. Lett.,* 77 (2001) 197.
102. Li S., Ding W., Meitzner G.D., Iglesia E., *J. Phys. Chem. B.* 106 (2002) 85.
103. Li S., Krishnamoorthy S., Li A., Meitzner G.D., Iglesia E., *J. Catal.*, 206 (2002) 202.
104. Madon, R. J., Shaw H., *Catal. Rev. Sci. Eng.*, 15 (1977) 69.
105. An X., Baoshan W., Hou W., Wan H., Tao Z., Li T., Zhang Z., Xiang H., Li Y., Xu B., Yi F., *J. Molec. Catal. A: Chem.,* 263 (2007) 266.
106. Xu Q. , He D., Fujiwara M., Tanaka M., Souma Y., Yamanaka H., *J. Molec. Catal. A: Chem.*,136 (1998) 16.
107. Ledakowicz S., Nettelhoff H., Kokuun R., Dekwer W.D., *Ind. Eng. Chem. Process Des. Dev.*, 24 (1985) 1043.
108. Doskocil E.J., Bordawekar S.V., Davis R.J., *J. Catal.*, 169 (1997) 327.

Chapter 2
Experimental Techniques

2.1 Scanning Electron Microscopy (SEM) and Energy Dispersive X-ray (EDX)

Scanning electron microscopy is a method used to determine the size and shape of catalyst particles revealing information about the composition of the particles. The interaction between the high energy electrons and the sample give many different detectable signals like diffracted electrons, secondary electrons, backscattered electrons, X-rays, transmitted electrons, Auger electrons[1], Figure 2.1.1.

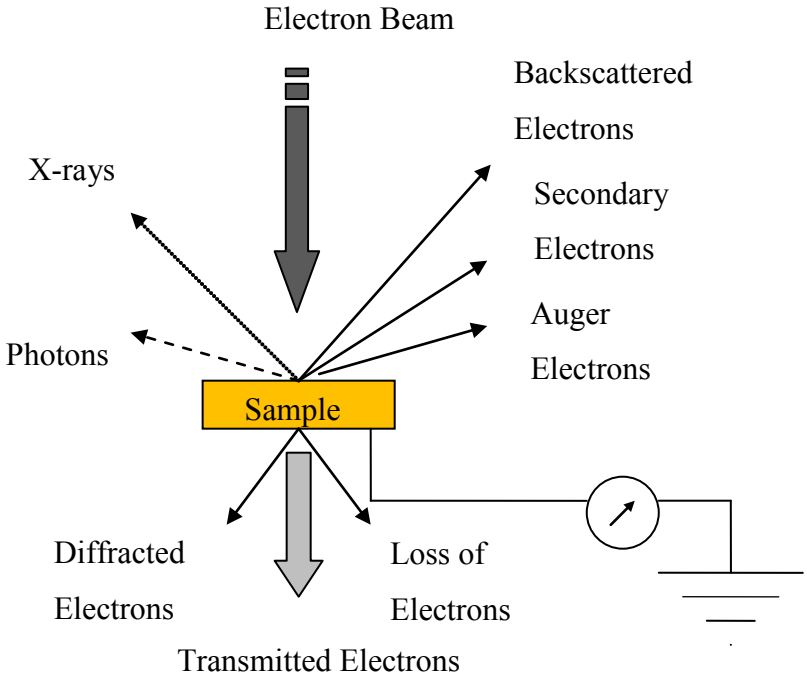

Fig.2.1.1 The interaction of the electron beam with a sample in electron microscopy.

The electrons are emitted from a small region at the tip usually of a heated tungsten filament and are accelerated towards the anode where the sample is placed. The field generated between the cathode and the anode is modified by the Wehnelt cylinder, which focuses the electron beam.

In the scanning electron microscope (SEM) the electrons are accelerated to an energy which is usually between 1 keV and 30 keV[2]. The electron energy for the SEM method is considerably lower than the high energy electrons in the transmission electron microscopy (TEM) method[1]. The scanning electron microscope is primarily used to study the surface and structure of bulk specimen. SEM and TEM employ a beam of electrons, Figure 2.1.2.

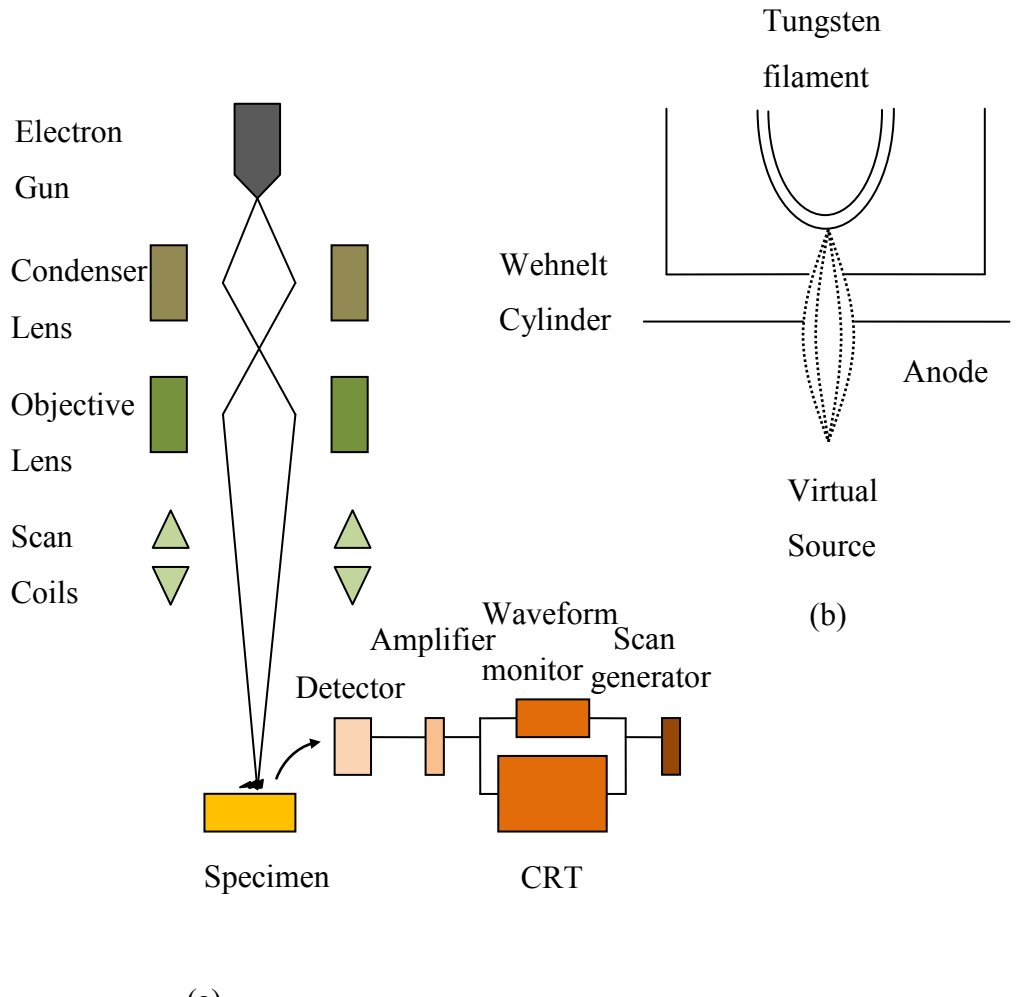

Fig.2.1.2. Scanning electron microscope (a) and electron gun (b).

The electron gun, condenser lenses, and vacuum system, are similar in both instruments but the ways in which the images are produced are different. Transmission electron microscopy gives additional information about the internal structure of thin specimens. The main difference between SEM and TEM is that SEM sees contrast due to the

topology of a surface, whereas TEM projects all information in a two-dimensional image.

The electron microscope offers additional possibilities for analyzing samples. Energy-dispersive X-ray spectroscopy (EDX) allows the determination of the elemental composition of the sample[1]. The EDX may be in the same SEM system which is then called SEM-EDX. When the incident beam excites an electron from an inner shell (core shell orbital) of an atom, and the electron from a higher-energy shell fills in the vacancy, an X-ray with the energy equal to the difference of the two orbitals is emitted at the same time, Figure 2.1.3. The emitted X-rays are characteristic for each element and allow the determination of the chemical composition of a selected part of the sample. In the experiment, the SEM topographical images are formed from low-energy secondary electrons. The secondary electron appears due to the incident electrons beam which excites them from the core electrons of the sample. They move towards the surface causing elastic and inelastic collisions and consequently with loss of the energy, until they reach the continuum, Figure 2.1.3. The intensity or area of a peak in an EDX spectrum is proportional to the concentration of the corresponding element in the specimen.

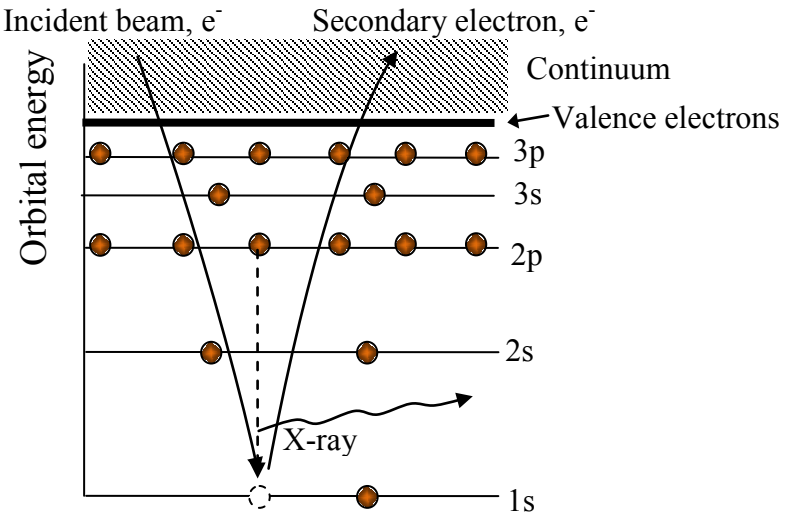

Fig. 2.1.3. Schematic atomic energy level distribution diagram, showing electronic transition in SEM-EDX technique.

It is also possible that the difference in energies during the transition causes the ejection of photoelectrons, or a third electron in an outer shell is ejected (Auger electron). The signal in a form of photoelectrons can be measured by X-ray photoelectron spectroscopy and provides information about the surface of the analysed samples. The technique will be described further in subchapter 2.5.

In this work a JSM 5910 scanning electron microscope with combined energy dispersive X-ray microanalysis (Oxford Inca 300) was employed. The JSM 5910 system has a characteristic accelerating voltage range from 0.3 to 30 kV, magnification up to 300,000 and resolution of 3.0 nm at 30 kV. The equipment can be used for secondary electron and backscattered electron imaging and Auger radiation detection.

2.2 Specific surface area determination (BET)

The specific surface area of a synthesized material can be determined by interpreting measurements of volume of gas adsorbed on the surface with regard to pressure at a constant temperature. The most common type of isotherm equation for powdered materials corresponds to that describing a multilayer surface adsorption[3].

Brunauer, Emmett and Teller showed how to extend Langmuir's monolayer approach to multilayer adsorption. The basic assumption is that the Langmuir equation applies to each adsorbed layer, with the added postulate that the heat of adsorption for the first layer energy may have one specific value, whereas for succeeding layers it is equal to the heat of condensation of the liquid adsorbate, H_e[4]. The Langmuir equation is presented below:

$$k_1 S_1 = k_2 p S_0 = k_2 p \left(S - S_1 \right)$$

$$\theta = \frac{bp}{1+bp} \qquad \text{where} \quad b = \frac{k_2}{k_1}$$

where,

θ – surface coverage,

b – ratio of rate of adsorption to rate of evaporation onto/from surface,

p – pressure.

For this equation it was assumed that the surface consists of a certain number of sites and that adsorbed molecules do not interact with each other.

Brunauer, Emmett and Teller derived an equation that yields the average heat of adsorption in the first layer and the volume of gas required to form a monolayer on the adsorbent. The Brunauer – Emmett – Teller (BET) equation can be put in the form:

$$\frac{x}{n(1-x)} = \frac{1}{cn_m} + \frac{(c-1)x}{cn_m} \qquad x = \frac{p}{p_0}$$

where,

n_m – adsorbed moles per gram of material,

c – constant.

so that n_m and c can be obtained from the slope and intercept of the straight line best fitting the plot of $x/n(1-x)$ *vs* x.

The specific surface area can be obtained through the equation:

$$n_m = \Sigma \ / N_A \sigma^0$$

where,

Σ – specific surface area,

N_A – Avogadro's constant (6.022×10^{23} mol^{-1})

σ^0 – area of site or molecule of adsorbate (for N_2 its value is 16.2 $Å^2$ mol^{-1})

The BET equation is the standard one for practical surface area determinations, usually with nitrogen at 77 K as the adsorbate.

In the experiments described in this thesis the Micromeritics Gemini surface area analyzer and the Micromeritics Sample Degas System were used. The Gemini system has two gas reservoirs, presented in Figure 2.2.1 (1) filled with equal volumes of the nitrogen (adsorptive). The nitrogen gas is dosed into the sample in the sample tube and in the balance tube. The system of transducers (2) and (4) with valves (3) and (5) are responsible for balancing and keeping constant pressure in both tubes. There is also third volume adsorbed transducer (6) between reservoirs which monitors the pressure between them and determines the amount of gas adsorbed by the sample. The dosing and accounting of the gas uptake is possible because the sample and the balance tube are identical and have the same conditions within, and the only difference is the presence of the analysed sample in the first tube[5]. Before the experiment all of the samples were pretreated in nitrogen at 150 ^{o}C for 3 hours in order to remove any moisture adsorbed on the catalyst surface. The Micromeritics Gemini surface area analyzer is presented in the Figure 2.2.1 (below).

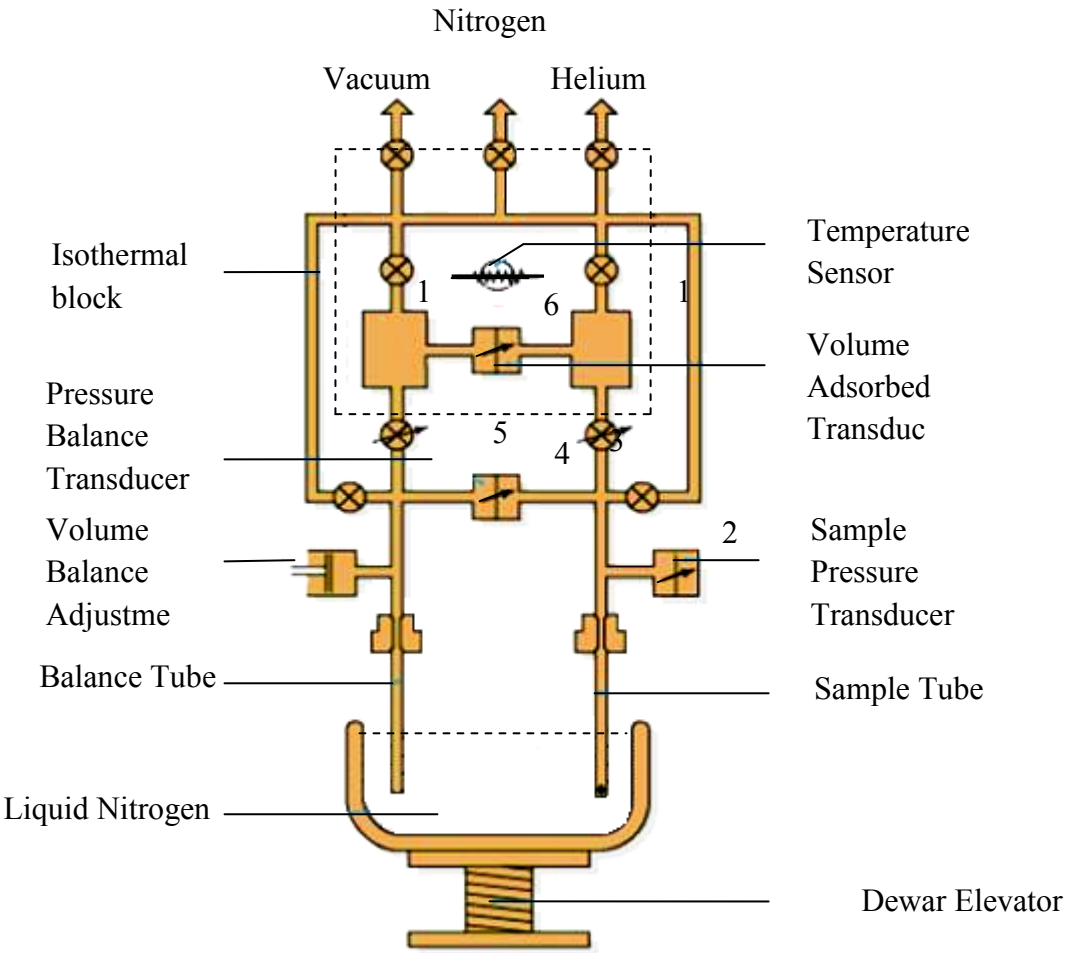

Fig.2.2.1. The elements of the Micromeritics Gemini surface area analyzer.

2.3 Powder X-ray diffraction

Powder X-ray diffraction is an X-ray scattering technique based on observing the scattered intensity of an X-ray beam interacting with a sample as a function of incident and scattered angle, wavelength, energy or polarization. X-rays are scattered by the atoms, and diffraction can occur from a periodic array of scattering centres separated by distances with a length similar to the wavelength of the radiation (~1 Å), such as exists in a crystal[6]. The scattering is equivalent to reflection from adjacent parallel planes separated by a distance *d,* Figure 2.3.1. The angle at which constructive interference occurs between waves of wavelength λ is given by the Bragg equation (below).

$$2d\sin\theta = n\lambda$$

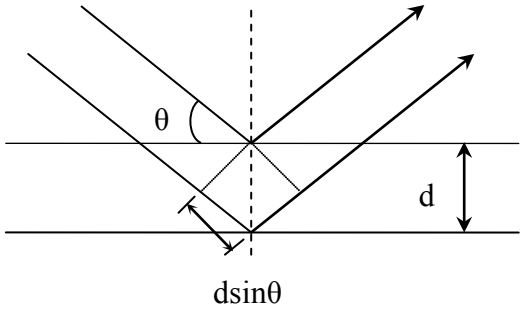

Fig.2.3.1. The Bragg equation is derived by treating layers of atoms as reflecting planes; X-rays interfere constructively when the additional path length $2d\sin\theta$ is equal to.

where d – distance between planes,
θ – angle of incidence and reflection of incident ray,
n – an integer,
λ – wavelength of incident ray.

Each possible family of planes in a lattice is characterized by its own distance between planes (interplanar spacing), so that[7]:

$$d_{nh,nk,nl} = \frac{d_{hkl}}{n}$$

where h,k,l – plane indices;
hence the Bragg equation is generally given as

$$2d_{hkl}\sin\theta_{hkl} = \lambda$$

Rearrangement of the equation gives:

$$\sin\theta_{hkl} = \left(\frac{\lambda}{2}\right)\times\left(\frac{1}{d_{hkl}}\right)$$

The Bragg equation is the basis for all methods for obtaining the unit cell geometry from the measured geometry of the diffraction pattern[8].

In the powder X-ray diffraction method the materials studied are usually in polycrystalline form, consisting of thousands of small crystallites, typically from 0.1 to 10 μm in size and of random orientation. When the X-ray beam interacts with the crystallites the X-rays with characteristic wavelengths are produced. The diffracted X-rays are detected and counted. The sample is scanned through a range of 2θ angles thus all possible diffraction directions of the lattice should be obtained for the random orientation of the powdered material. Each of the analysed samples has a set of unique d-spacing and conversion of the diffraction peaks to d-spacing allows identification of the analysed material.

The PXRD patterns in the experiment were recorded in the 10 -110^{o} *2θ* range in the scan mode (0.02^{o}, 0.12 s) using a Siemens D5000 XRD diffractometer. The diffraction instrument was equipped with goniometer with *θ/2θ* geometry. The instrument operating in reflection geometry using $CuK_{\alpha 1}$ radiation, λ = 1.54056 Å, focused by a Ge crystal primary monochromator. The Cu tube is working at 40 mA and 40 kV with supplied water-cooling system. The slit arrangement is a 2 mm pre-sample slit, 2 mm post-sample slit and a 0.2 mm detector slit.

2.4 X-Ray Absorption Spectroscopy (XAS)

X-ray absorption fine structure (XAFS) observed in XAS has been used as part of this project to obtain information about the structural properties of the catalysts prepared by different methods, especially about the coordination chemistry and oxidation state[9]. In the XAFS technique, the X-rays absorbed by an atom at energies near and above the core-level binding energies are used to give information about the chemical state and local atomic structure for a selected atomic species.

Since the crystallinity of the sample is not required it is a very helpful technique to determine the local structure in a broad range of materials: XAFS can be used in different systems including amorphous materials, solutions and is also broadly applied for heterogeneous catalysis[9-11]. It is a bulk technique in which X-rays are penetrating deep in matter (depth depending on energy used). XAFS is complementary to other

techniques and in combination with other surface sensitive techniques can provide a complete set of information on the studied iron catalyst.

The technique, especially the x-ray absorption near edge structure (XANES) part of the spectra, has been used for direct measurement of the oxidation state and geometry of diluted sulfur species and alkali promoters, using references, in iron catalysts prepared in a variety of methods.

2.4.1 X-ray-absorption near edge structure (XANES)

In general XAS can be divided into two parts: the near-edge spectra called X-ray Absorption Near Edge Structure (XANES) – typically within 50 eV of the main absorption edge, and the Extended X-ray Absorption Fine Structure (EXAFS), Figure 2.4.1, (below).

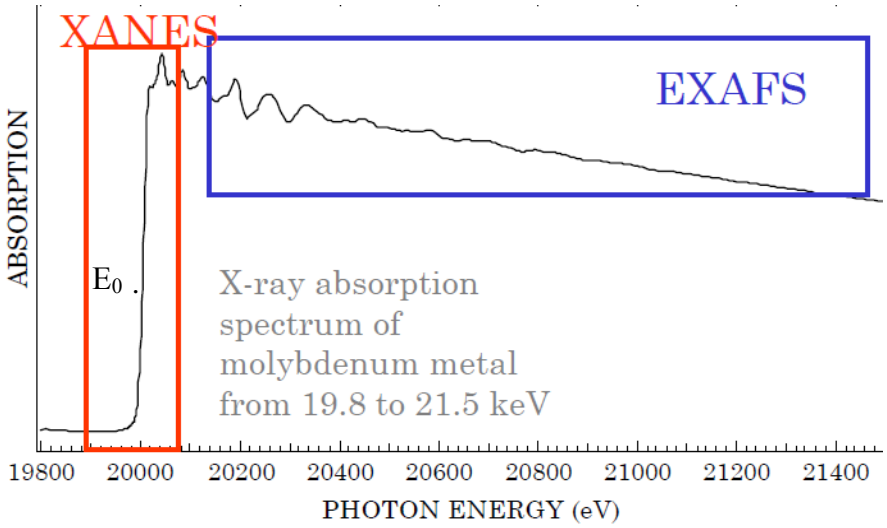

Fig. 2.4.1.1. The XANES and EXAFS regions of XAS, figure from presentation of Bare, UOP (2005).

The XANES technique provides information about the formal oxidation state (energy position of edge), the electronic properties (energy position of the pre edges and the edge), the coordination geometry of the absorbing atom (presence and absence of pre

edge features), and band-structure (density of available, i.e. empty, electronic states). The EXAFS data is used to determine the distances, coordination number, and type of neighbouring species of the absorbing atom, including their disorder[11- 15].
In this work, XANES is used as a fingerprinting technique, where the shift of the edge position is applied to determine the oxidation state by comparing to measured known reference materials. The heights and positions of edge peaks were used to assess oxidation states and coordination geometry of elements of interest in a sample.

The pre-edge region originates from partially allowed transitions, like quadrupolar or orbitals hybridised with p or d orbitals. Quadrupole transitions may not be strongly visible because the transition Hamiltonian contains small terms that are non dipolar[16]. The main edge is the dipole allowed transitions from the core level to the higher unfilled or half-filled orbitals (e. g. s → p, or p → d). The features in the XANES region depend on hybridisation, and geometry of the compound. The increase in absorption occurs due to the high probability of such transitions. The pre-edge transition and the main K-edge are presented in a Figure 2.4.1.2. A further consequence, of photoelectron scattering on neighbouring atoms, will be presented in Figure 2.4.1.3.

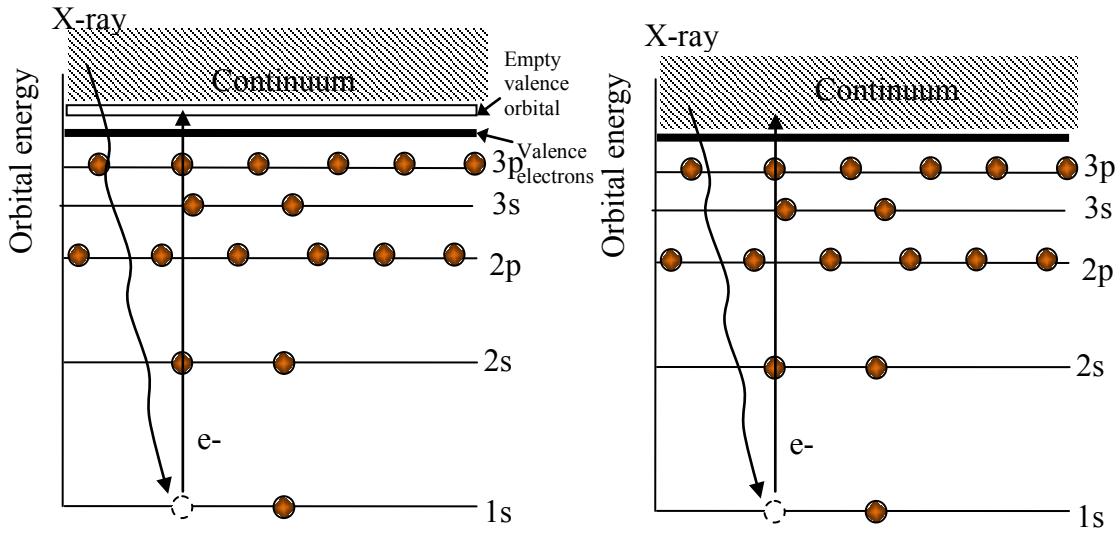

Fig.2.4.1.2. Atomic energy level distribution showing electronic transitions a) XANES pre-edge transition, b) XANES absorption K-edge.

The energy of the incident x-ray beam of the pre-edge region is lower than the binding energy (E_0), where ($E < E_0$), Figure 2.4.1.1. The energy of the XANES region is between the edge and (E_0) and, the region where the electron wavelength equals the distance from the adsorbing atom to its nearest neighbours, about 30 eV ($E = E_0 \pm 30$ eV)[9,11]. At energies above the absorption edge, i.e. binding energy E_0, the photoelectron obtains kinetic energy $E_{kin,}$ ($E_{kin} = h\nu - E_0$).

In the XANES the electron's kinetic energy is low and the scattering resonance phenomenon of the neighbouring atoms is strong. However when the electron's kinetic energy is higher in the EXAFS region the effect of multiple scattering becomes smaller (weaker and more regular vibrations)[17]. Both XANES and EXAFS scattering effects are presented in Figure 2.4.1.3.

One of the perturbation methods applied to scattering by an extended body is the Born approximation. The estimation is accurate if the scattered field is small, compared to the incident field, in the scatterer[18,19]. Because the Born-like scattering is divergent and because the large number of effects in the electron shell (many-body interaction, particle-hole interaction and multiple scattering) the XANES characterization might be complicated.

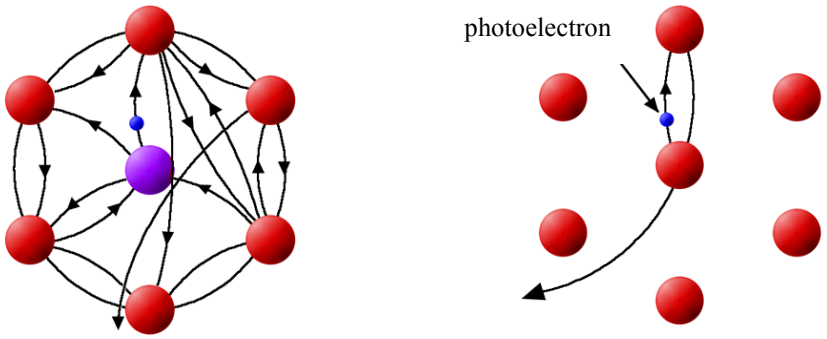

Fig.2.4.1.3. Schematic view of photoelectron scattering on neighbour atoms, determining the resonances in XANES (left) and EXAFS oscillations[19].

The XANES part of XAFS provides information about the geometry of the local structure using the multiple scattering phenomenon, while EXAFS gives information about the bond distances and coordination numbers, from the interference in the single scattering process of the electron scattered by surrounding atoms. One of the advantages of the XANES in comparison to EXAFS is that technique has a larger signal than EXAFS, and the measurement may be carried out with a lower concentration of the analysed elements. Thus the technique may be used also for the study of the catalysts with low concentration of the sulfur dopants. The XANES analyses and its interpretations are still being developed. Thus the references used as a fingerprint are considered to be very useful information for most XANES analyses.

2.4.2 General information about XAFS

When X-radiation interacts with the sample, there are many different effects observed, such as absorption, Compton scattering and Rayleigh scattering. During absorption an electronic transition (photoelectric effect) is observed. The excited state created can relax by emitting energetic electrons and a photon of longer wavelength. Electron of higher orbital falls down to fill a core hole. The energy which is emitted corresponds to energy difference between to levels. XAS measures the absorption of X-rays as a function of X-ray energy *E*. The X-ray absorption coefficient is obtained from the decay in the X-ray beam intensity I with distance x, Figure 2.4.2.1.

$$\mu(E) = -d\ln I/dx$$

According to the Beer-Lambert's Law after the X-rays travel a distance x into the sample the intensity reduces to:

$$I = I_0 e^{-\mu x}$$

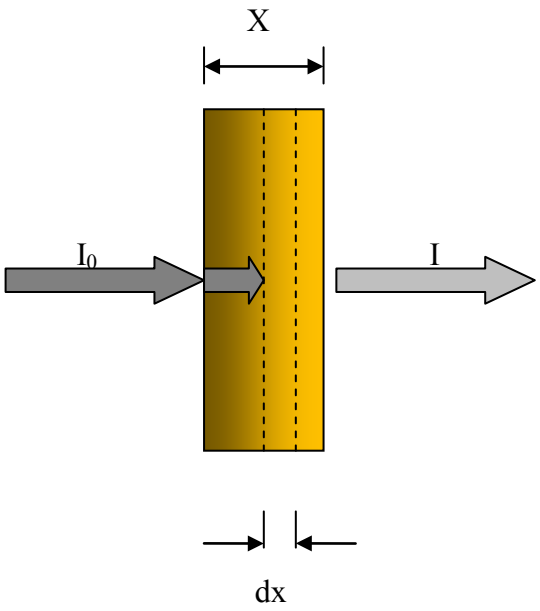

Fig.2.4.2.1. X-ray absorption by a sample according to Beer-Lambert's law.

where μ is the linear absorption coefficient, I is the intensity transmitted through the sample, I_0 is the X-ray intensity incident on a sample and x is the sample thickness.
The absorption coefficient depends strongly on the X-ray energy E, atomic number Z, on density ρ and atomic mass A:

$$\mu \approx \rho Z^4/AE^3$$

If the absorption coefficient is plotted as a function of the incident photon energy we can observe three main features (Figure 2.4.2.2). The first one shows a general decrease in X-ray absorption with increasing energy.

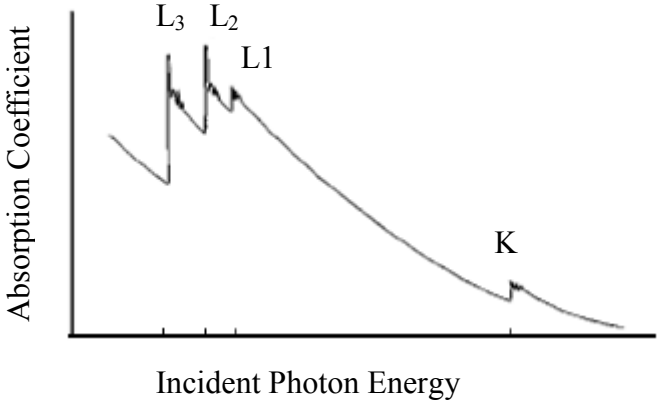

Fig. 2.4.2.2. X-ray absorption coefficient as a function of incident photon energy.

The next features present are sharp rises at certain energies which are called the edges. The energy positions of the edges are specific to a given absorption atom and reflect the excitation energy of inner-shell electrons. After the edges we can observe oscillations modulating the absorption. This is due to photo-electrons scattered from a neighbouring atom. The scattered photo-electron can return to the absorbing atom, modulating the amplitude of the photo-electron wave-function at the absorbing atom. The oscillatory wiggles are evident where the XANES features fall away form the EXAFS[9,14], as in Figure 2.4.1.1.

Every absorption edge is correlated with a specific atom that absorbs the X-ray. The energies of the edges (ionization energies) are characteristic of the atomic species present in a sample. That is because excitation of core electron is related to binding energy and thus is element specific. The transition proceeds to an unoccupied state (above the Fermi energy level), which leaves behind a core hole. When ionization occurs the core hole left behind is unstable and will be filled by an electron of higher orbital. The decay of the excited atomic state can take place in two ways. One is fluorescence. In this case, a higher energy core-level electron relaxes into the deeper core hole and ejects an X-ray of characteristic energy. The fluorescence energies emitted in this way are well-defined and can be used to identify the atoms in a system. The second mechanism for the decay of the excited atomic state is the Auger effect. In this process an electron from a higher energy core-level fills the lower energy core-level, which results in another (third) electron being ejected into the continuum. Both effects are presented in a Figure 2.4.2.3., below.

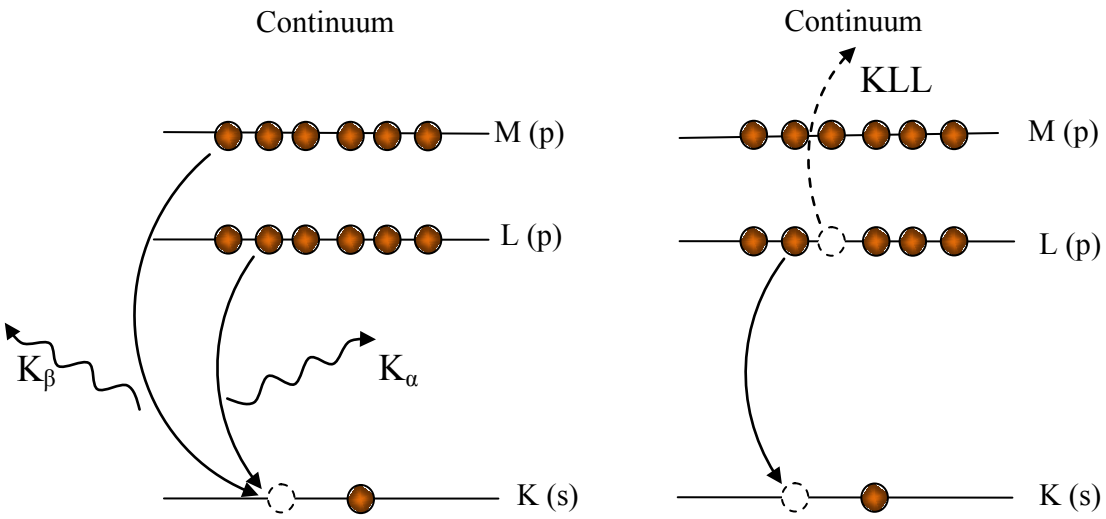

Fig. 2.4.2.3 Decay of the excited state. X-ray fluorescence effect (left) and the Auger radiation effect (right).

2.4.3. Fluorescence experiments and electron yield geometries

XAFS can be measured in transmission, fluorescence or electron yield geometries. The energy dependence of the absorption coefficient μ (E) in transmission is a logarithmic function of the quotient of X-ray intensity incident on a sample over intensity transmitted through the sample, as:

$$\mu(E) = \log(I_0/I)$$

However, in the X-ray fluorescence the energy dependence of the absorption coefficient is equal to the quotient of the monitored intensity of a fluorescence line over X-ray intensity incident on a sample, as below:

$$\mu(E) \approx I_f / I_0$$

For samples with a very low concentration of the element of interest the absorbance could be too low for a transmission mode experiment to be carried out. In a fluorescence

XAFS measurement, the X-rays emitted from the sample will include the fluorescence line of interest, fluorescence lines from other elements in the sample, and both elastically and inelastically (Compton) scattered X-rays.

The simple scheme of the fluorescence X-ray absorption system and beam angles are presented in Figure 2.4.3.1.

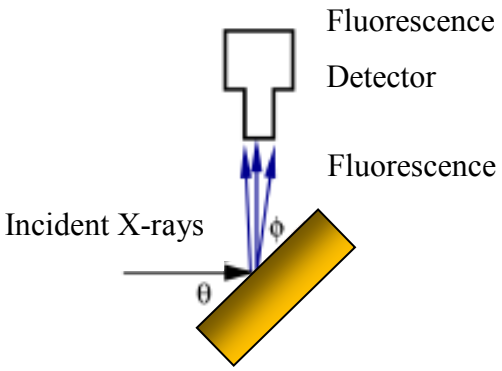

Fig. 2.4.3.1 Fluorescence X-ray absorption spectroscopy measurements, the incident angle (θ), exit angle (Φ).

The Auger electrons are emitted as part of the relaxation process when a higher-orbital electron fills the hole after photoelectron. The penetration ranges of the Auger electrons emitted from the absorbing atoms determine the sampling depth in the total-electron-yield technique. The LMM Auger electrons for example, have ranges of hundreds of angstroms and KLL Auger electrons have ranges of thousands of angstroms[20]. The electron yield may be used to improve the surface sensitivity.

2.4.4 Elements of a beamline

Sulfur, sodium and potassium K-edges XANES spectra were recorded at Lucia beamline, Swiss Light Source (SLS) and on I18 station in Diamond Light Source, Oxford.

2.4.4.1 Lucia XAS beamline

On the LUCIA beamline, the light source is provided by an undulator. An undulator is a periodic structure of dipole magnets which causes an oscillation in the electron path. Each oscillation produced its own light source and these interfere with each other to create intense harmonics. The energy of the harmonics is a function of electron energy, the period of the magnetic array and the magnetic field. The energy of the harmonics is changed by varying the effective magnetic field at the electron beam by choosing the distance between the poles of the magnet.

The next element, a spherical mirror, focuses the beam onto adjustable slits. The high-order harmonics sent by the undulator are minimized by two flat, water cooled mirrors located behind the spherical mirror. The planar mirrors serve as filters and also decrease the thermal load which is received on the next element, the monochromator, Figure 2.4.4.1. Because of the energy range of the beamline available at Lucia a double crystal monochromator is used. There are five kinds of crystals used in the Lucia beamline: Si(111), InSb(111), YB_{66}(400), $KTiOPO_4$(011) and beryl(10$\underline{1}$0). In the experiment with the Na K edge, a beryl (1010) crystal monochromator was used and for sulfur a Si(111) monochromator.

The last focusing elements of the beam are high quality mirrors made of Si coated by nickel (Kirkpatrick-Baez (KB) system). They give a high flux over a wide energy range, which gives a stable beam position on the sample during the scan and a relatively long working distance.

XAS spectra were collected in fluorescence (Si drift diode dead time < 15%) and electron yield mode. Through the mono-element energy dispersive silicon drift diode (SDD) it was possible to detect fluorescence of lighter elements (down to the carbon) including sulfur and sodium, important in this work[21].

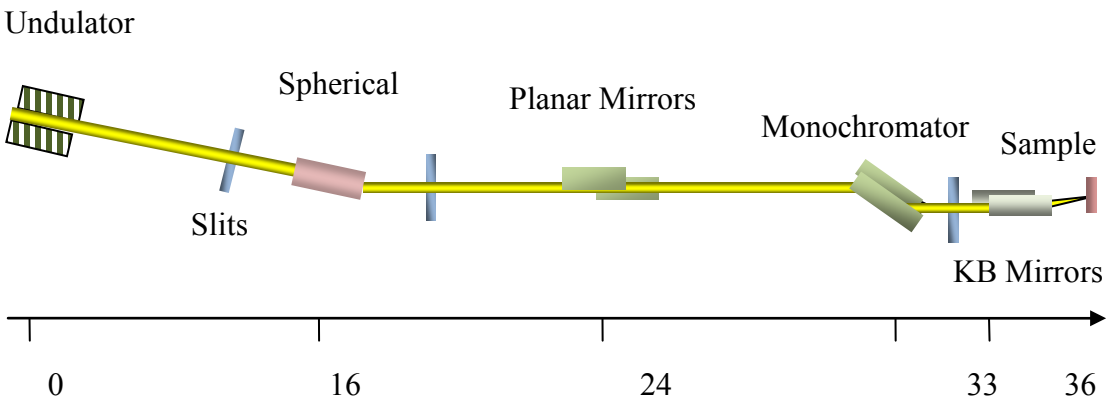

Fig. 2.4.4.1 General layout of the Lucia beam line.

2.4.4.2 Station I18 at Diamond Light Source (DLS)

The first element on the station I18 DLS beamline, similarly like it was for the Lucia beamline is an undulator. A selected peak output reaches a beryllium window where IR-UV and soft X-rays are reduced. Beryllium serves as a low-energy cut-off. The beam subsequently reaches slits which reduce the beam size. The beam is then led from the primary slits to a monochromator by means of highly planar silicon crystal mirrors. They act as a cut-off filter, extracting the harmonics and also as a focusing element.
The first element of the mirror system has a special toroidal shape to provide a highly

parallel beam to the crystal monochromator, Fig.2.4.4.2. In the I18 station there was a choice of five kinds of crystals: Si(311), Si(220), Si(111), Ge(111), InSb(111). In this work the Si (111) based monochromator was used for the study of samples with a low concentration of potassium.

Behind the monochromator the secondary slits can be found, then another system of mirrors and a last pair of tertiary slits. Similarly to the Lucia beam line, the last focusing element of the beam are KB mirrors which provide highly focussed monochromatic radiation for spectroscopic analysis[22,23].

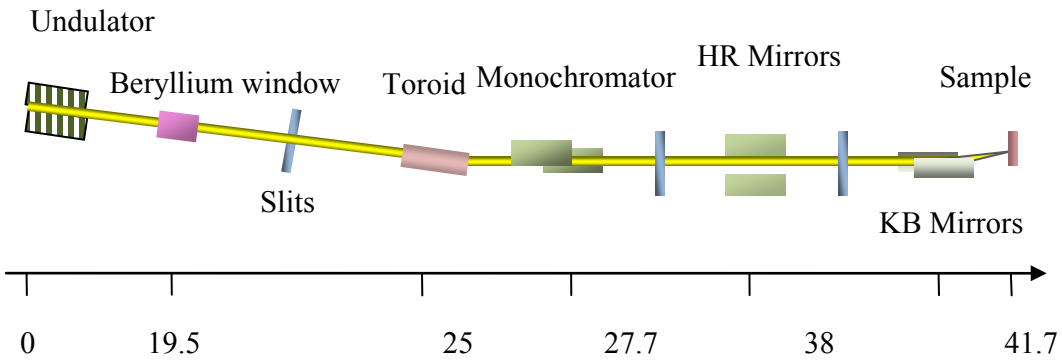

Fig.2.4.4.2. The X-ray spectroscopy beamline on I18 at Diamond[22,23].

2.5 X-ray Photoelectron Spectroscopy (XPS)

X-ray Photoelectron Spectroscopy (XPS) is one of the ionization-based techniques which measures the kinetic energy (E_K) of photoelectrons generated through ionization when the measured material is exposed to the high-energy radiation or particles. There are two main types of photo-ionization techniques according to the type of the radiation and its target. The first one is ultraviolet photoelectron spectroscopy (UPS), which is used to determine the kinetic energy of the valence electrons and UV radiation corresponding to the ejection of the electron. The second technique, which was employed in this experiment, is X-ray photoelectron spectroscopy (XPS) in which high-energy X-rays are used to expel core electrons, Figure 2.5.1.

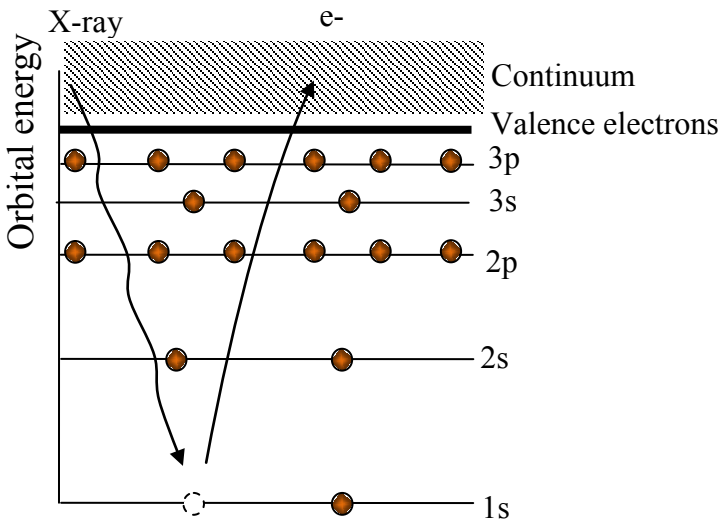

Fig. 2.5.1. Schematic diagram of the ejected photoelectron from the core level to continuum in X-ray photoelectron spectroscopy.

Electrons penetrate solids to the depth of around 1 nm, thus XPS is a measurement favourable for surface elemental analysis. The XPS technique in the experiment is used for determining the elemental composition of the surface, especially the oxidation state of elements of interest. The comparison of the elemental composition by the use of surface sensitive techniques such as XPS together with bulk techniques is a good source of information for describing the migration process of the promoters like sulfates or cations of the alkali metals in the iron oxide catalysts.

The XPS technique is applied to measure kinetic energies (E_K) of photoelectrons emitted through irradiation used to determine band structures of solids. The kinetic energy of the photoelectrons is related to the binding energy (E_B) of electrons in their orbitals by the following relationship:

$$E_K = h\nu - \varphi - E_B$$

E_K - kinetic energy of electron (eV),
E_B - electron binding energy (eV),
h - Planck's constant (eV · s),
υ -frequency of incident X-rays (s^{-1}),
φ -surface work function (eV)

Each element has a unique set of energy levels and a unique set of binding energies and for electrons present on these levels, XPS can be used to identify and determine the concentration of the elements on the surface. Moreover, the calculated E_B gives information about the oxidation state and bonding of the atoms, due to the chemical shifts, which depend on the differences in the chemical potential and polarizability of the examined compounds. The peaks recorded in a measurement are named after the core level from which the photoelectrons were rejected. The peaks indicate the relative probabilities of different ionisation processes. Therefore, there will be one single peak visible for the ionization of the *s* orbital. After ionization of *p* or *d* orbitals, split peaks will be observed related to the presence of vacancies in the $p_{1/2}$, $p_{3/2}$, $d_{3/2}$, $d_{5/2}$, states. Thus usually two peaks in the XPS spectra after ionization of the p, d orbitals will be exposed[24]. The XPS technique is a surface sensitive technique because the emitted photoelectrons have relatively low kinetic energies and they undergo inelastic collisions with the material.

The electrons from inner layers may collide with these from the upper orbitals, lose kinetic energy and usually contribute to the noise signal of the spectrum, Figure 2.5.2. The electrons from near the surface have higher probability of being released and detected. The XPS spectrum provides useful information depending on the kind of specimen and the angle of the incident beam from the outermost layer of the analysed samples[25,26].

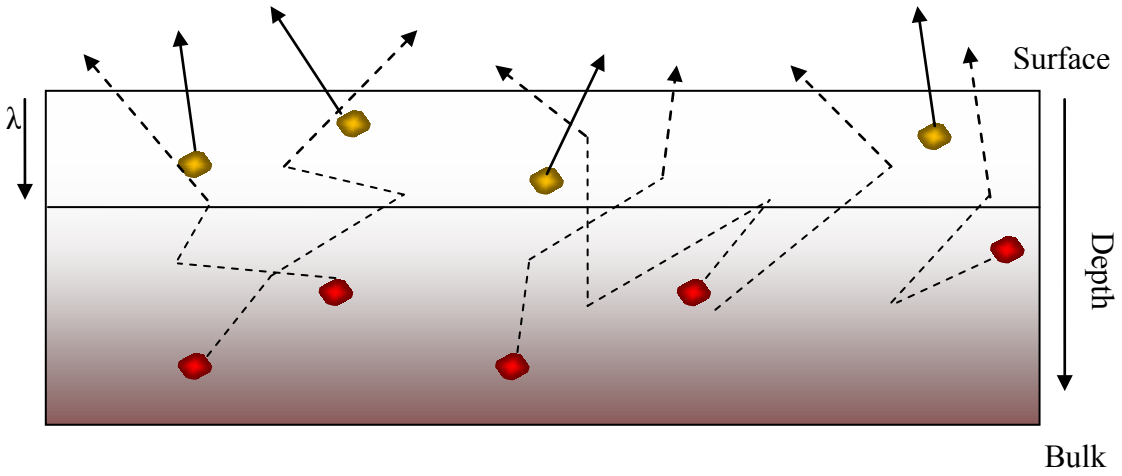

Fig. 2.5.2 XPS ejecting electrons; from the near surface region, without energy loss (yellow), from the bulk, with energy loss (red).

Two XPS systems/machines were used for the study of the iron oxide catalyst in the experiment: a Scienta ESCA 300 high performance X-ray photoelectron spectrometer in The National Centre for Electron Spectroscopy and Surface Analysis (NCESS), Daresbury Laboratory and a Kratos Axis Ultra DLD XPS System at Cardiff University, Fig.2.5.3. The ESCA 300 is a high intensity, high energy-resolution and high spatial resolution system[27]. The main components of the this system are: the X-ray power through a rotating anode, 8 kW maximum power, more than ten times higher than traditionally used 600 W anode source, X-ray source; seven crystals, double focusing monochromator, monochromatised Al K_α/Cr K_β and W L_α X-ray source, lens and analyzer system and detection system with hemispherical analyzer and multichannel detector, which gives 0.30 eV minimum overall resolution.

The Kratos Axis Ultra DLD system has a monochromatic X-ray source with a dual Al-Mg anode, magnetic lenses, and a similarly hemispherical analyzer. In comparison with ESCA 300 the Kratos XPS system has a lower power X-ray source and comparable resolution. The Krotos AXIS Ultra system has a minimum resolution of 15 µm and with the addition of the spherical mirror analyzer, the real time chemical state images can be obtained with a spatial resolution down to 3 µm (minimum overall resolution lower than 0.5 eV) [28.] Both XPS systems are presented in Figure below.

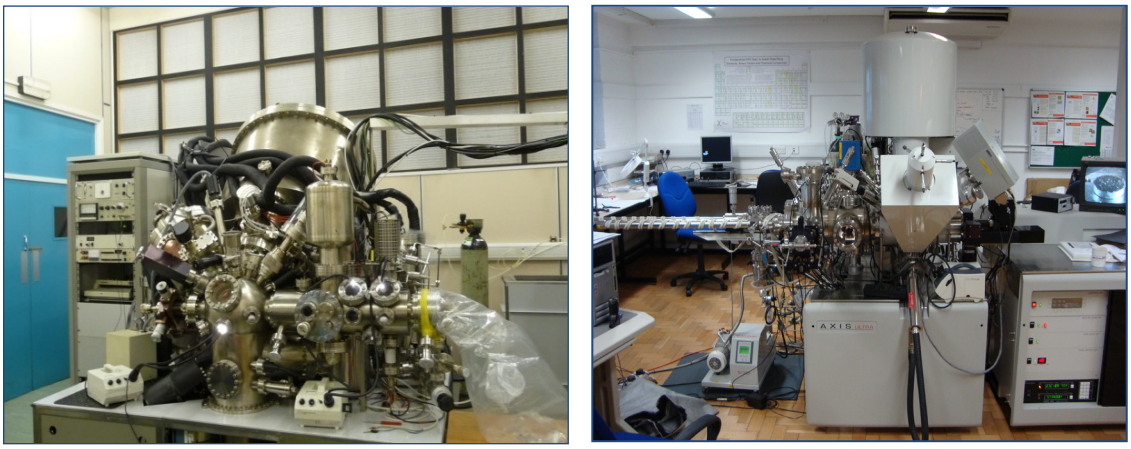

Fig. 2.5.3. Scienta ESCA 300 XPS, NCESS, Daresbury (left), Kratos Axis Ultra DLD XPS, Cardiff University (right).

2.6 X-ray Fluorescence spectroscopy (XRF)

The fundamentals of the XRF technique are the same as for the previously presented analytical methods involving interactions between electron beams and X-rays with samples. The XRF is an analytical technique, which measures characteristic energy or wavelength of the fluorescence X-ray emitted after when the sample is exposed to an X-ray source with required energy[29]. The technique is used for quantitative and qualitative determination of chemical elements and it is used mostly in analyses of solids e.g. minerals, rocks, sediments.

The spot size of XRF is relatively big and the large depth of radiation enables the technique to be used for large fractions of the samples and to be classified as a bulk analytical technique. The penetration and the escape depth depends on the emitted energy which is specific for different analyzing element. Characteristic spectral Kα lines of the interest elements (Na, S, K, Fe, Rb) are respectively: 1041, 2307, 3311, 6403 and 13395eV and for Kβ respectively: 1071, 2464, 3590, 7058 and 14961 eV[30,31]. The lighter elements with lower energy X-Rays have lower X-Ray attenuation length e.g. Na

and S in Fe_2O_3 (density 5.2 g/cm^3)[32] have respectively 0.1µm and 1.5µm length, and the attenuation length of K, Fe and Rb is in a range 5 and 13 µm.

The XRF technique may be employed for bulk chemical analyses of major but also trace elements. In this work it was employed in the qualitative comparison of high concentration of iron and low concentration of alkali metals and sulfur promoters. To obtain information about the elemental composition of an analyzed sample using the XRF technique the radiated electrons require high enough energy to release electrons from the inner shells of an atom, higher than that bonding them to the atom. The irradiation in the experiment was carried in The Philips Magix Pro WD-XRF system where an X-ray source from an X-ray tube was delivered. When the atoms are exposed to the X-rays, the incident radiation causes the ejection of the electrons from inner shells. The electrons from outer shells will fill created vacancies, emitting X-rays at the same time. The released radiation is specific for each atom and information about each element present in radiated region of the sample can be obtained. The X-ray fluorescence process of K shell electron (similar to that fluorescence in XANES) is presented in Figure, 2.6.1, below.

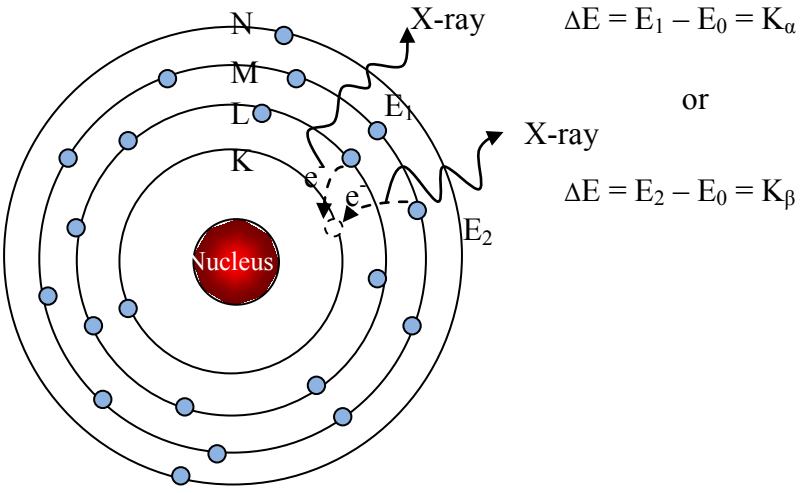

Fig. 2.6.1 The X-ray fluorescence process (Ti), The transition of electrons from the L or M to K shell, to fill the vacancy. The characteristic x-ray unique to this element is emitted[33].

There are two main groups of XRF techniques: Energy Dispersive X-ray Fluorescence Spectroscopy (ED-XRF) and Wavelength Dispersive X-ray Fluorescence Spectroscopy (WD-XRF). The first technique ED-XRF uses a detector able to separate and measure energies of the characteristic radiation emitted from the analyzed sample and determine elements present. In the WD-XRF technique the X-rays of different wavelengths are diffracted in different directions with a system of collimators and diffraction crystals. The WD-XRF system can have a moving or fixed detection system, which allows simultaneous analysis of multiple wavelengths. The moving detector distinguishes intensities of different wavelengths and gives the answer about elements occurring in the sample of interest. The Philips Magix Pro™ WD-XRF system used in this work is equipped with a 4 kW light element Rh-target end-window X-ray tube, analyzer crystals for the analysis of elements in the range of O-U, 3 detectors: Ar-Methane flow and a sealed Xe-filled proportional detector and scintillation detector in parallel, beam filters, collimators[34]. The components of the WD-XRF system are presented in Figure 2.6.2.

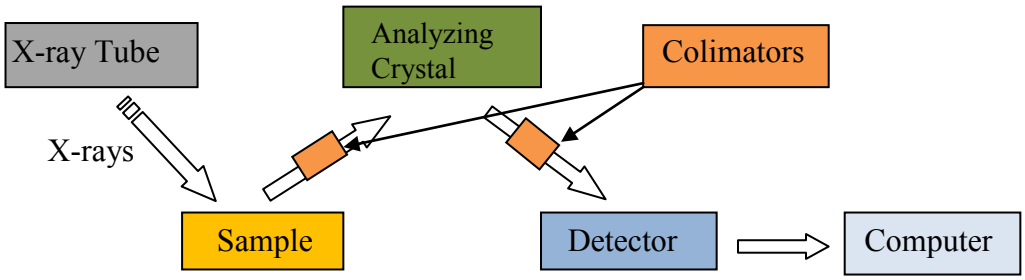

Fig. 2.6.2 The WD-XRF system scheme.

2.7. References

1. Goodhew P. J., Humphreys J., Beanland. R., *Electron Microscopy and Analysis*, 3rd , Taylor & Francis: London and New York, 2001.
2. Zhao R., Sudsakorn K., Goodwin Jr. J.G., Jothimurungesan K., Gangwal S. K., Spivey J.J., *Catal. Today*, 71 (2002) 319.
3. A. Adamson, *Physical Chemistry of Surfaces*, John Wiley & Sons, New York, 1982.
4. Brunauer S., Emmett P.H., Teller E., *J. Am. Chem. Soc.*, 60 (1938) 309.
5. www.particleandsurfacesciences.com
6. Shriver D.F., Atkins P.W., et al., *Inorganic Chemistry*, 4th edition, Oxford University Press, Oxford, 2006.
7. Ladd M.F.C., *Symmetry in Molecules and Crystals*, Ellis Horwood Ltd, New York, 1989.
8. Clegg W., Crystal Structure Determination, Oxford University Press, Oxford, 2005.
9. Newville M., Consortium for Advanced Radiation Sources, University of Chicago, IL, 2004.
10. Bare S.R., *XANES Measurements and Interpretation,* UOP LL, Des Plaines, IL, 2005.
11. Tromp M., *Post Graduate course on XAS data acquisition and analysis,* University of Southampton, 2008.
12. Tromp M., J. A. van Bokhoven, G. P. F. van Strijdonck, P. W. N. M. van Leeuwen, Koningsberger D. C., Ramaker D.E., *J. Am. Chem. Soc.*, 127 (2005) 777.
13. http://xafs.org/XAFS, 2011.
14. Rehr J.J., Alberts R.C., *Rev. Mod. Phys*., 72 (2000) 621.
15. Stern E.A, P.H. Durham S.M. Heald, Koningsberger D.C., ed. Koningsberger and R. Prins, John Willey and sons, *X-Ray Absorption – Principles, Applications, Techniques of EXAFS, SEXAFS and XANES*, North-Holland, 1988.
16. Bunker G., *"Introduction to XAFS: A Practical Guide to X-ray Absorption Fine Structure Spectroscopy"*, Cambridge University Press, Cambridge, 2010.

17. Mihelic A., Kodre A, *XANES spectroscopy*, University of Ljubljana, 2002
18. Sakurai, J. J., *Modern Quantum Mechanics*, Addison Wesley Publishing Company, Los Angeles, 1994.
19. www.p-ng.si/xanes, 2010
20. Erbil A., Cargill G.S., Frahm R., Boehme R.F., *Phys. Rev. B*, 37 (1988) 2450.
21. Flanc A.M., Cauchon G., Lagarde P., Bac S., Janousch M., Watter R., Dubuisson J.-M., Idir M., Langlois F., Moreno T., Vantelon D., *Phys. Res*. B 246 (2006) 269.
22. Evans J., *Graduate School lecture course*, University of Southampton, 2008.
23. www.diamond.ac.uk/Home/Beamlines/I18/specs.html, 2011.
24. Moulder J.F., Stickle W.F., Sobol P.E., and Bomben K.D*., Handbook of X-ray Photoelectron Spectroscopy by Perkin-Elmer Corp*., Eden Prairie, (1992) 10.
25. www.phy.cuhk.edu.hk/course/surfacesci/mod3/m3_s1, 2010.
26. Vickerman J. C., *Surface analysis – the principal techniques,* John Wiley & Sons Chichester, 1997.
27. www.dl.ac.uk/NCESS/xps/esca300.htm, 2011.
28. http://surface.kratos.com/AxisUltraDLD/axisultradld.html, 2011.
29. Janssens K.H.A., Adams, F.C.V., Rindby, A., *Microscopic x-ray fluorescence anal*ysis, John Wiley & Sons, Chichester, 2000.
30. Bearden J.A., "X-Ray Wavelengths", *Rev. Mod. Phys.,* 39 (1967) 86.
31. Brunetti A., Sanchez del Rio M., Golosio B., Simionovici A., Somogyi A., *Spectrochim. Acta Part B*, 59 (2004) 1725.
32. CRC Handbook of Chemistry and Physics, CRC Press, Taylor and Francis Group, 89th Edition, London, UK, 2008.
33. www.amptek.com/xrf.html, 2011.
34. www.noc.soton.ac.uk/geochem/Facilities Links/xrf.htm, 2011.

Chapter 3

The nature of iron in FT catalysts

3.1 Synthesis of the iron catalyst

The method of catalyst preparation plays an important role in its physical properties and catalytic performance. In this work catalysts were synthesized with various additives and in different conditions and methods. The synthesized catalysts were characterized as prepared by means of different bulk and surface sensitive analytical techniques (all the techniques are described in Chapter 2).

In the first stage of the work two synthesis methods were employed: incipient wetness impregnation and co-precipitation. Then the synthesis conditions were optimized, the parameters concerned were:

- the amount of starting components used,
- the process environment (air or an inert gas (N_2)),
- the drying and calcination temperatures and temperature change rates,
- the method of filtration and washing,
- different pH values after titrant addition (pH 5, pH 7, pH 9),
- different rates of titrant addition (8 ml/min, 0.25 ml/min),
- different temperatures at co-precipitation stage (24 °C and 60 °C),
- different promoters used (Na, K and Rb).

After the first characterization (SEM-EDX and P-XRD) from all the possibilities of the synthesis methods of the iron oxide catalyst, the most significant were chosen. The list of the synthesis conditions and preparation methods for the samples with one of the promoters, Rb, are listed in Table 3.1.

Table 3.1 Method of preparation and conditions for the samples exemplified with a Rb promoter

Sample	pH value			Temperature		Titrant addition rate		Method of preparation	
	pH=7	pH=9	pH=5	RT	60°C	8 ml·min^{-1}	0.25 ml·min^{-1}	Co-precipitation	Impregnation
Rb 01, 02, 03	●			●		●		●	
Rb 04, 05, 06	●			●			●	●	
Rb 07, 08, 09	●				●	●		●	
Rb 10, 11, 12		●		●		●		●	
Rb 13, 14, 15			●	●		●		●	
Rb 13, 14, 15	●			●		●			●

The first stage of the synthesis was precipitation using NH_4OH (8 ml/min and 0.25 ml/min titrant addition). The rate of the titrant addition may change the crystallization/crystallinity of Fe_2O_3. It was necessary to control the amount of the base added during precipitation (pH control) to obtain stoichiometric Fe_3O_4 after reduction[1]. After precipitation the iron-slurry was dried and calcined. The alkali promoter was added at different stages depending on the synthesis method. In the co-precipitation method it was added directly after titration, before drying and in impregnation method after drying of the iron slurry and before calcinations. The calcination of the FT Fe-based catalyst cannot be performed at very high temperatures due to sintering and consequent loss of active surface. The temperature should not be lower than 200 ºC in order to effectively remove poisoning nitrates from the catalyst surface. The exact drying and calcinations duration and temperature are noted in subchapters 3.1.1-3, below. The scheme of the iron oxide catalyst synthesis is presented in a Figure 3.1. After calcination the sample was ground using a mortar and pestle, and its physical and chemical properties were examined using various techniques like e.g. XRD or SEM-EDX.

In order to be active in FTS, the iron oxide has to be reduced. After calcination the samples were reduced under 5% H_2/He for 20h (the results for the non-reduced and reduced samples are presented in Chapters 4, 5 and 6). Calcination and reduction conditions (time and temperature) influence the transformation of S species on the surface of the Fe-based catalyst[2].

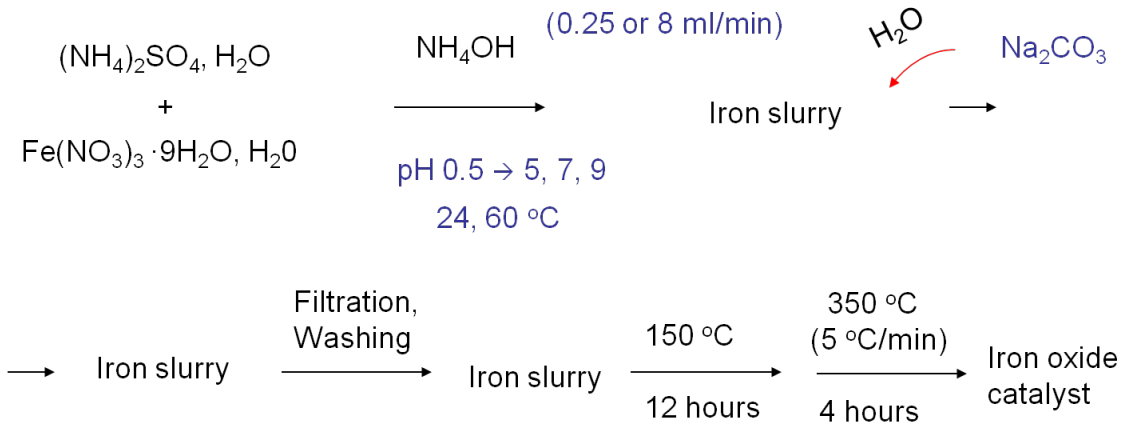

Fig. 3.1. Scheme of the iron oxide catalyst synthesis with Na promoter.

3.1.1 Synthesis of catalyst containing (0.4 g / 100 g Fe) Na_2O and (0.05 g S / 100 g Fe) by co-precipitation

$(NH_4)_2\ SO_4$ (4.2 mg) was dissolved in deionised water (10 ml). $Fe(NO_3)_3 \cdot 9H_2O$ (14.48g) was dissolved in deionised water (30 ml). The $(NH_4)_2SO_4$ and $Fe(NO_3)_3 \cdot 9H_2O$ solutions were mixed and stirred together (total volume 40 ml). NH_4OH (25% NH_3 aqueous solution) was added at a rate of 0.25 ml min^{-1} (or 8 ml min^{-1}) to titration end point (~ 8.5 ml). Solution pH was changed from 0.5 to 7 (or 5, or 9). After increasing the pH value Na_2CO_3 (13.7 mg) dissolved in deionised water (5 ml), was added to the slurry, while it was stirred vigorously and the solution was stirred for another 5 min to allow the pH to stabilize. The above procedure was conducted at 24 or 60 °C. The iron-slurry was dried for 12 hours at 150 ^oC under N_2, and calcined at 350 ^oC for 4 hours (rate 5 ^oC/min) in tube furnace. The sample was ground using a mortar and pestle.

3.1.2 Synthesis of catalyst containing (0.6 g / 100 g Fe) K_2O or (1.2g / 100g Fe Rb_2O and (0.05 S g / 100 g Fe) by co-precipitation

After mixing $(NH_4)_2SO_4$ and $Fe(NO_3)_3 \cdot 9H_2O$ aqueous solutions and increasing the pH value as described above, K_2CO_3 (17.7 mg), or Rb_2CO_3 (29.9 mg) dissolved in deionised water (5 ml) was added to the slurry. The mixture was stirred for another 5 min to allow the pH to stabilize. The procedure was conducted at 24 °C. Drying and calcination were done as above. The calcined sample was ground using a mortar and pestle.

3.1.3 Precipitation of catalyst containing Na and S by incipient wetness Impregnation

After mixing $(NH_4)_2SO_4$ and $Fe(NO_3)_3 \cdot 9H_2O$ aqueous solutions, the pH value was increased to pH 6.8 by titration with an ammonium hydroxide solution (as described above). The iron-slurry was filtered and washed with water. The slurry was dried for 4 hours at 150 ^oC under nitrogen. After drying, Na_2CO_3 (13.7 mg) dissolved in deionised water (5 ml) was added to the reactor with powder by incipient wetness impregnation method. After impregnation the solution was dried once more for 4 hours, ground and calcined at 350 ^oC for 4 hours (rate 5 ^oC/min) in tube furnace. The calcined sample was ground using a mortar and pestle. The same procedure for the samples with K and Rb was carried out.

3.2 Powder X-Ray diffraction (P-XRD) for iron catalyst samples prepared under different conditions

3.2.1 P-XRD for iron catalyst samples prepared under different conditions with a Na promoter

The iron catalysts used in the experiment were synthesized at two pH values: 7 and 9, using a fast (8 ml min^{-1}) and slow (0.25 ml min^{-1}) addition of titrant, at two different temperatures, 60 ^{o}C and room temperature (RT), by the co-precipitation and wetness incipient impregnation methods. Diffractograms were recorded after calcination procedures, before activation. The iron oxide samples with Na promoter are presented in a Figure 3.2.1.

The reflections in all iron catalyst samples correspond to those of the haematite (α-Fe_2O_3), which, according to the literature sources[3-8], has characteristic peaks at 2θ values of 24.2, 33.1, 35.6, 40.8, 49.52, 54.0, 57.6, 62.5 and 64° Miller indices of, respectively, 012, 104, 110, 113, 024, 116, 018, 214, 300[4,5].

The peaks at a 2θ value of 33.1 for all the samples synthesised in various conditions were compared, and presented in Figure 3.2.1 All of the samples were compared to the sample synthesised at pH7, co-precipitated, fast titrant addition at room temperature used as a model/pattern sample presented at the top of the figures. The peaks of the co-precipitated sample with fast titrant addition rate are slightly narrower (FWHM = 0.28) than the sample with slow titrant addition (FWHM = 0.32). The same peaks for the impregnated samples were broader than those of the co-precipitated samples (FWHM = 0.39). The peaks of the samples where titration was applied at 60 ^{o}C were also broader (FWHM = 0.43) than those synthesised at room temperature. They were the broadest of all the samples synthesised in different conditions with Na.
In general the most crystalline sample (lowest FWHM) with Na was obtained under the conditions: pH 7, fast titrant addition in room temperature, while least crystalline was obtained in: pH 7, fast titrant addition in 60 ^{o}C.

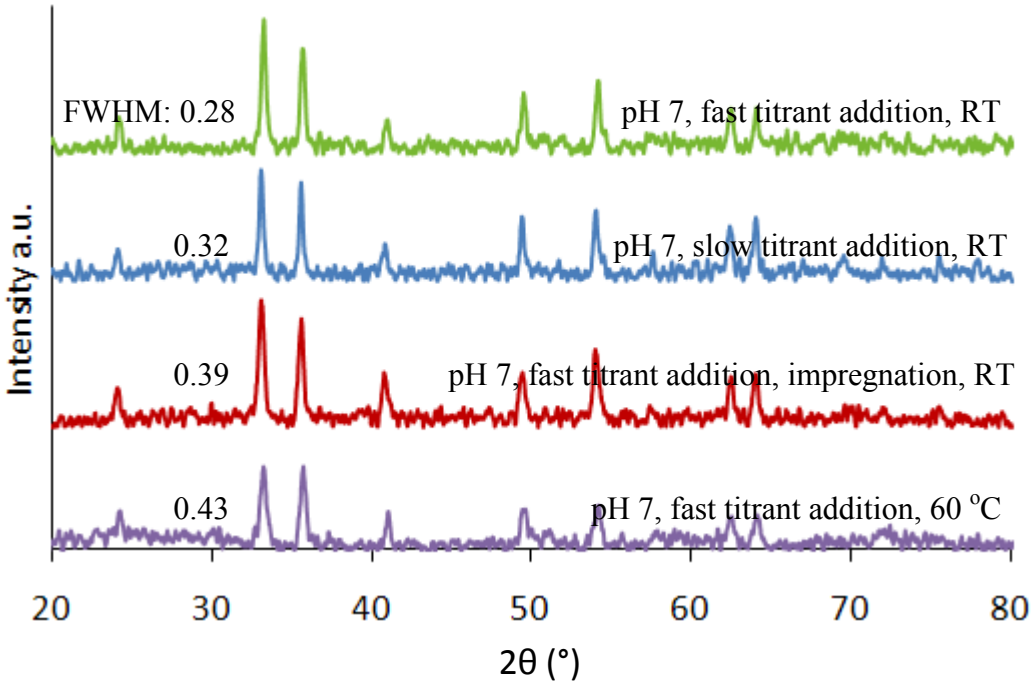

Fig.3.2.1. The P-XRD analysis for the samples with Na promoter: pH 7, co-precipitation, fast titrant addition, RT; pH 7, co-precipitation, slow titrant addition, RT; pH 7, impregnation, fast titrant addition, RT; pH 7, co-precipitation, fast titrant addition, 60 ^{o}C.

3.2.2 P-XRD for iron oxide samples prepared under different conditions with a K promoter

The iron oxide structure of haematite (α-Fe_2O_3) was observed for iron catalyst samples before activation with a K promoter, similar to those with a Na promoter. The FWHM of the peaks at 2θ equal 33.1 for the samples co-precipitated at pH 7 with fast titrant addition was slightly larger (0.34) than the samples with slow titrant addition (0.32), in contrast to the samples with Na promoter. The FWHM for the impregnated samples was larger (0.36) than for those co-precipitated (0.34). It was also observed that the FWHM for the samples where titrant was added at room temperature was lower in comparison to those synthesized in 60 ^{o}C, where FWHM equalled 0.43.

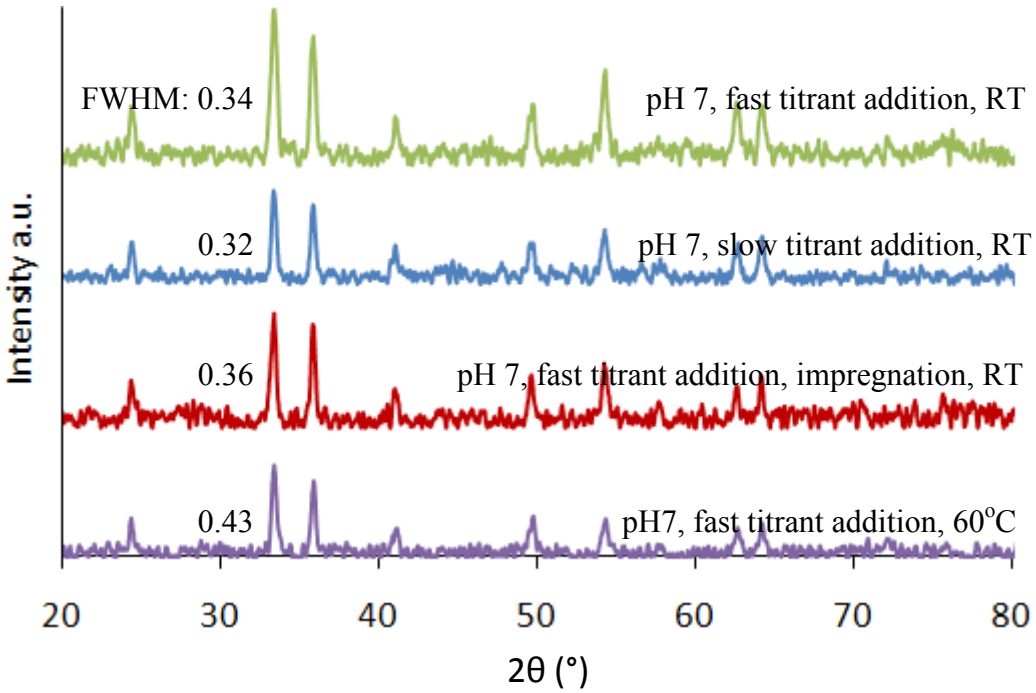

Fig. 3.2.2. The P-XRD analysis for the samples with K: pH 7, co-precipitation, fast titrant addition, RT; pH 7, co-precipitation, slow titrant addition, RT; pH 7, impregnation, fast titrant addition, RT; pH 7, co-precipitation, fast titrant addition, 60 ^{o}C.

The crystallinity of samples with K synthesised at room temperature by three different methods does not vary significantly. The peak for the sample synthesised at 60°C has a much higher FWHM and is less crystalline than the others.

3.2.3 P-XRD for iron oxides samples prepared under different conditions with a Rb promoter

The structure of all samples with rubidium promoter is that of the iron (III) oxide (α-Fe_2O_3)[6-8]. The samples with Rb are presented in Figure 3.2.3. The biggest difference was attributed to the rate of titrant addition and temperature during precipitation. The peaks for the samples for which the titrant was added rapidly are narrower (FWHM = 0.31) than for the samples made with slow titrant addition (FWHM = 0.36). The diffractograms show distinct differences between the co-precipitated samples and those

impregnated, where the FWHM (0.43) for the impregnated sample was the largest among all the samples with Rb. The FWHM for the samples where the titrant was added at room temperature was also much more lower (0.31) in comparison to those synthesized in 60 ^{o}C (FWHM = 0.42).

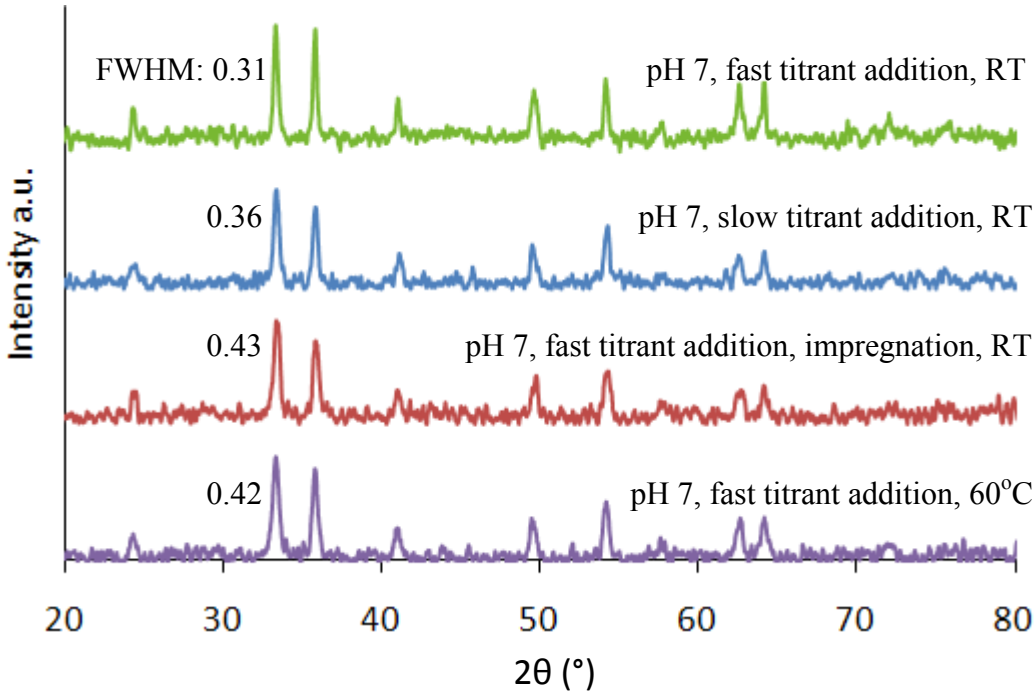

Fig. 3.2.3. The P-XRD analysis for the samples with Rb: pH 7, co-precipitation, fast titrant addition, RT; pH 7, co-precipitation, slow titrant addition, RT; pH 7, impregnation, fast titrant addition, RT; pH 7, co-precipitation, fast titrant addition, 60 ^{o}C.

3.2.4. Particle size for the iron oxide samples synthesised in different conditions

In order to estimate the average particle size in samples, the Scherrer formula[9] was employed (equation below). It involved calculations with the full width at half of the high maximum for the diffraction peak at 2θ equal to 33.1°. The results are listed in Table 3.2.4.

$$t = \frac{0.9\lambda}{B\cos\theta_B}$$

t - particle size,

B - full width at half of the height maximum in radians,

θ_B - Bragg angle

It was found that the size of the particles for all the iron oxide catalyst samples with different promoters was between 19.3 and 29.5 nm. The comparison of the particle size for the samples with two different titrant addition rates does not reveal significant differences. The average (arithmetic mean) size of the particles for the samples with fast and slow titrant addition rate was respectively 26.9 and 24.8 nm. The particle size for the samples with Na and Rb synthesised with fast titrant addition is slightly higher than for those with slow titrant addition rate with the same promoters. However the samples with K reveal the opposite trend.

The difference in particle size for the co-precipitated and impregnated samples (prepared at the same temperature) was more significant. Lower particle size for impregnated samples than co-precipitated was observed for all the catalysts synthesised with three different promoters. The calculated average particle size for the impregnated samples is equal 21.1 nm. The smallest difference was observed for the samples with K promoter (Table 3.2.4).

A significant decrease in particle size was observed for the samples synthesised at 60 ^{o}C in comparison to those synthesised at room temperature. The average particle size for the samples precipitated in 60 ^{o}C with three different promoters was 19.5 nm. The particle size for these samples was the lowest of all the samples. The arithmetic mean for particles size for the samples with different promoters was also compared. The average for Na, K, Rb was respectively 23.9, 23.1 and 22.2 nm. So the type of dopant did not have any significant effect on the particle size. The noticeable changes were influenced by the synthesis method and temperature.

Table 3.2.4. Average particle size in different samples estimated with the use of Scherrer formula

Conditions	Na, FWHM (2θ °)	Na, Particle size, nm	K, FWHM (2θ °)	K, Particle size, nm	Rb, FWHM (2θ °)	Rb, Particle size, nm	Arithmetic mean, nm
pH 7, fast titrant addition	0.28	29.5	0.34	24.5	0.31	26.8	26.9
pH 7, slow titrant addition	0.32	25.8	0.32	25.8	0.36	22.9	24.8
pH 7, impregnation, fast titrant addition	0.39	21.2	0.36	22.9	0.43	19.3	21.1
pH7, fast titrant addition, 60^{o}C	0.43	19.3	0.43	19.3	0.42	19.8	19.5
Arithmetic mean	-	23.9	-	23.1	-	22.2	-

3.3 Structure determination with the use of XPS: comparison of the properties of FT catalysts

First, XPS measurements were performed on the reference samples. Subsequently, the samples were studied with XPS before and after activation. The most significant conditions and methods of preparation were chosen similarly to the previously carried P-XRD experiments. The samples are listed below:

- pH 7, co-precipitation, fast titrant addition, RT,
- pH 7, co-precipitation, slow titrant addition, RT
- pH 7, co-precipitation, fast titrant addition, 60 ^{o}C
- pH 7, impregnation, fast titrant addition, RT
- pH 7, co-precipitation, fast titrant addition, RT, reduced at 400 ^{o}C
- pH 7, co-precipitation, slow titrant addition, RT, reduced at 400 ^{o}C
- pH 7, impregnation, fast titrant addition, RT, reduced at 400 ^{o}C
- pH 7, co-precipitation, fast titrant addition, RT, reduced at 450 ^{o}C
- pH 7, co-precipitation, slow titrant addition, RT, reduced at 450 ^{o}C
- pH 7, impregnation, fast titrant addition, RT, reduced at 450 ^{o}C

3.3.1 The XPS characterization of Fe p peaks of reference samples

The Fe 2p spectrum for the Fe_2O_3 reference sample has two Fe $2p_{3/2}$ and Fe $2p_{1/2}$ main peaks, and satellites for both of the peaks, (Figure 3.3.1).The Fe $2p_{3/2}$ peak at 710.3 eV has a satellite peak about 8.1 eV to the higher energy. The Fe $2p_{1/2}$ peak was at 724.2 eV with the satellite at 733.2 eV. The BE of the Fe 2p peaks and their satellites are similar to those of Fe_2O_3 samples found in the literature[10- 18]. According to the literature sources,[10-18] the Fe 2 $p_{3/2}$ of Fe_2O_3 peaks are in the binding energy range: 709.9 – 711.4 eV, with the satellite at around 8 eV higher energy[10-17].

The Fe $2p_{1/2}$ peaks were observed in the range: 724.0 – 724.5 eV [11,13]. The Fe 3p single peak of Fe_2O_3 reference sample was measured at 55.6 eV without a satellite. The BE of Fe 3p peak is similar to that found in the literature source, with the energy range between: 55.6 – 56.6 eV[14-18]. In the literature, the Fe 2 $p_{3/2}$ peak BE values for the next reference Fe_3O_4 were found in the range between 708.1 and 710.8 eV[11,12,14,17,18], the Fe $2p_{1/2}$ peaks between 723.5 and 724.1 eV[11,19], and Fe 3p between 53.7 and 56.4 eV[14,17,18]. The satellite of Fe 2 $p_{3/2}$ was hidden under Fe $2p_{1/2}$ envelope and not observed in the literature sources[11-19]. The Fe $2p_{3/2}$ peak for the Fe_3O_4 reference sample used in the experiment was noticed at 710.2 eV. The satellite peak for that sample was weakly pronounced at 719.3 eV. The Fe $2p_{1/2}$ peak for the Fe_3O_4 was observed at 723.9 eV without a satellite peak. In the Fe 3p spectrum of Fe_3O_4, a single peak at 55.8 eV was observed, without any satellite peak, similar to the results for Fe_2O_3. The Fe 3p peak was slightly wider than that of Fe_2O_3. The Fe p spectra are comparable to those of the Fe_3O_4 from the literature sources cited above. However the satellite of Fe 2 $p_{3/2}$ was hidden under Fe $2p_{1/2}$ envelope and not observed in the literature sources.

In the Figure 3.3.1, Fe_2O_3, Fe_3O_4, FeS and $FeSO_4$ references are presented. The $Fe2p_{3/2}$ peak position of the FeS reference was at 710.4 eV and Fe $2p_{1/2}$ at 724.4 eV; the satellite was not observed. The $Fe2p_{3/2}$ peak for $FeSO_4$ reference was measured at 710.4 eV and the Fe $2p_{1/2}$ peak at 724.1 eV with the satellite at around 716.5 eV. The references used in the experiment were compared with the references in the literature, to show absence or presence of Fe $2p_{3/2}$ satellite. The satellite was clearly visible for Fe_2O_3 and FeOOH compounds and not observed for the Fe_3O_4, FeO and Fe^0 [10-20] (Figure 3.3.1 b). This information is complementary with the P-XRD results. Using P-XRD it was possible to distinguish between the α-Fe_2O_3 and spinel Fe_3O_4. However, differences between Fe_3O_4 and γ-Fe_2O_3 were more subtle. The presence of the Fe $2p_{3/2}$ satellite of γ-Fe_2O_3 and absence of the satellite for Fe_3O_4 may help distinguish between these two forms of iron oxide. The data from Fe p spectra from all references from literature are compared with the experimental ones obtained in this study in Table 3.3.1.

a)

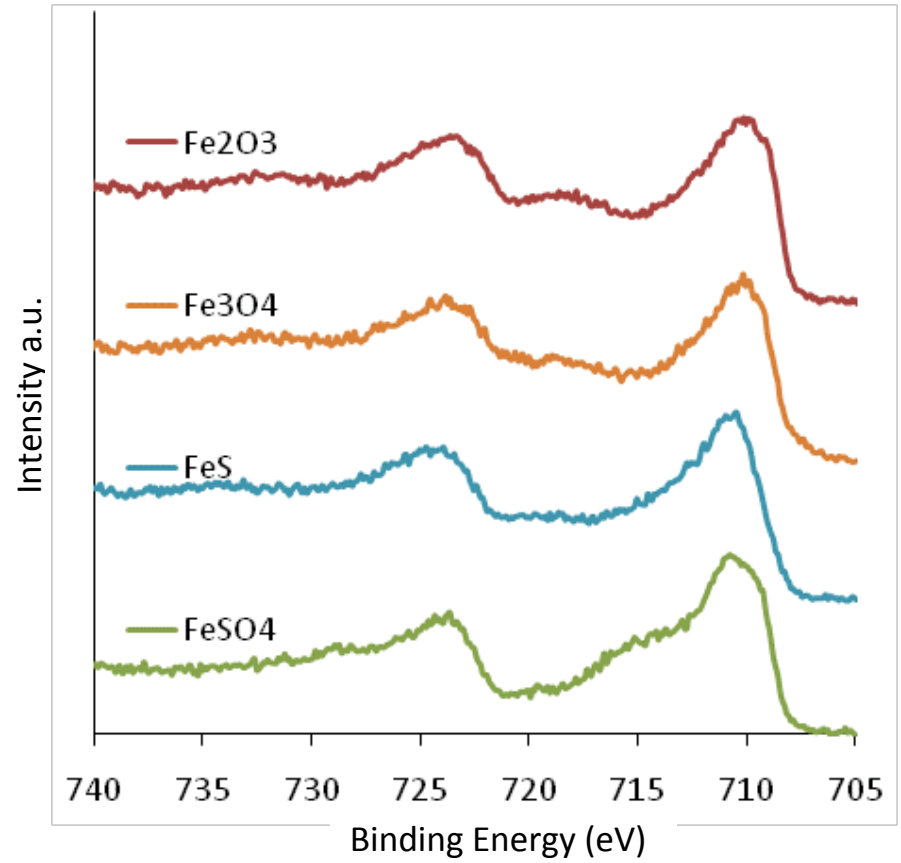

b)

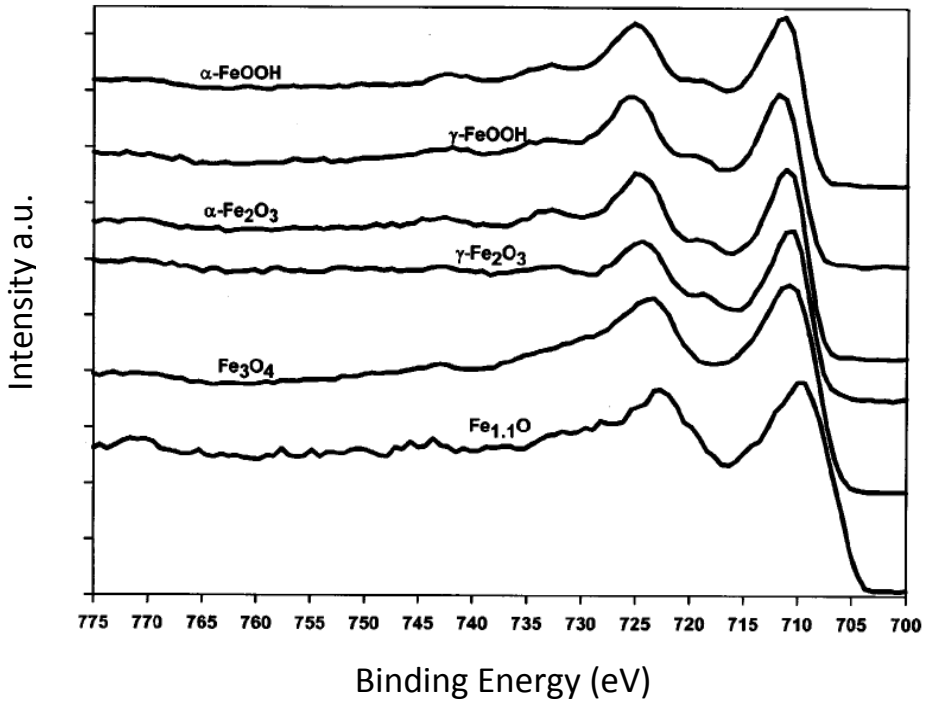

Fig. 3.3.1. XPS Fe(2p) spectra of the reference samples a) used in a experiment b) published in literature.

Tab. 3.3.1 Binding Energies (eV) of Fe p references.

Name	Fe $2p_{3/2}$	Satellite for Fe $2p_{3/2}$	Fe $2p_{1/2}$	Fe 3p
Fe_2O_3	710.3	718.4	724.2	55.6
Fe_3O_4	710.2	719.3	724.2	55.8
FeS	710.4	-	724.4	55.7
$FeSO_4$	710.4	716.5	724.1	55.6
Fe_2O_3[10-17]	709.0-711.4	717.0-719.4	724.0-724.5	55.6-56.6
Fe_3O_4[11-19]	708.1-710.8	-	723.5-724.1	53.7-56.4
FeOOH[11,20]	711.4-711.5	718.4-719.9	724.3-724.5	56.0-56.4
FeO[14,14-18]	709.3-710.7	-	723.1-723.3	54.7-56.0
Fe[14,14,18,]	706.5-708.7	-	720.1-721.0	52.4-53.5

3.3.2 The XPS characterization of iron oxide samples prepared under different conditions with a Na promoter, before activation

The binding energies of Fe $2p_{3/2}$ for all samples with a Na promoter prepared in different conditions were between 710.1 and 710.3 eV, Fig.3.3.2. For all the samples the satellite peak was in the range between 718.3 and 718.6 eV. The binding energies of Fe $2p_{1/2}$ for these samples were observed between 724.1 eV and 724.3 eV. There were also characteristic low intensity satellite peaks for Fe $2p_{1/2}$ spectra with the maxima between 733.0 eV and 733.2 eV for all the samples synthesised in various conditions. The position of the Fe $2p_{3/2}$ and Fe $2p_{1/2}$ peaks for Fe_2O_3 from the experimental data were approximately the same as for the references samples and for those found in the literature[10-18]. In general, there were no significant differences between Na samples synthesised in different conditions.

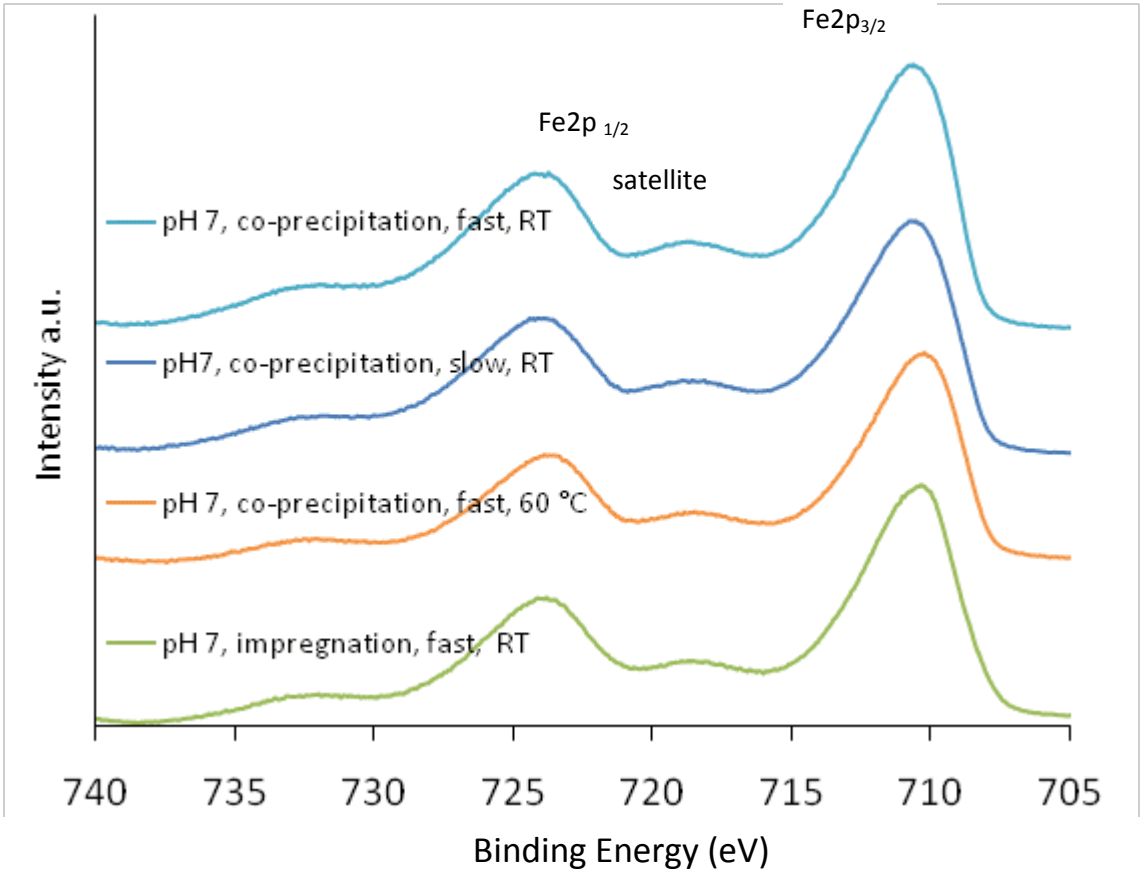

Fig 3.3.2 XPS Fe (2p) spectra of the samples with Na promoter before activation; From the top following: pH 7, co-precipitation, fast titrant addition, RT, pH 7, co-precipitation, slow titrant addition, RT, pH 7, co-precipitation, fast titrant addition, 60 ^{o}C, pH 7, impregnation, fast titrant addition, RT.

3.3.3 The XPS characterization of iron oxides samples prepared under different conditions with K promoter, before activation

The Fe $2p_{3/2}$ spectra for all the samples with K promoter before activation, prepared in various conditions were between 710.2 and 710.3 eV (Fig.3.3.3). The satellite peak position was observed between 718.5 eV and 718.4 eV. The distance between Fe $2p_{3/2}$ and its satellite was on average 8.1 eV for all the samples studied, which is the typical separation for Fe_2O_3 according to literature[10-17]. The Fe 2p spectra for the samples with K are presented in Figure 3.3.3.

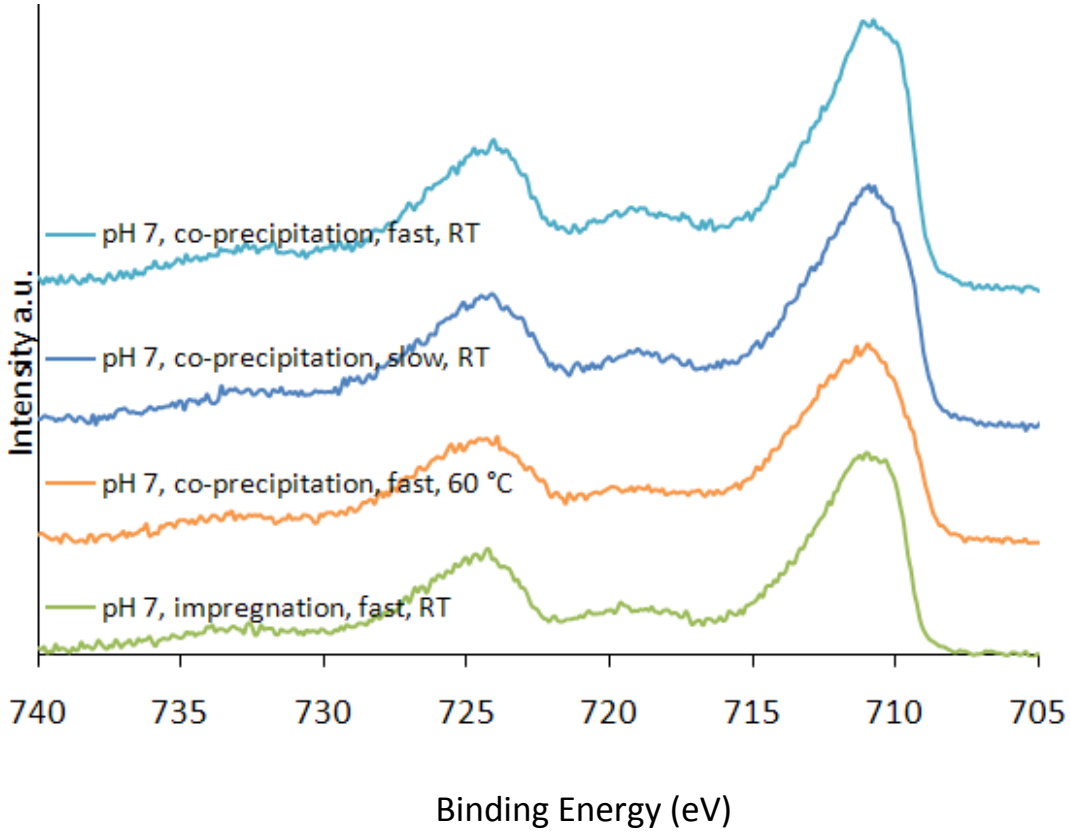

Fig.3.3.3. XPS Fe(2p) spectra of the reference sample and of the samples with K promoter before activation; From the top: Fe_2O_3 reference, pH 7, co-precipitation, fast titrant addition, RT, pH 7, co-precipitation, slow titrant addition, RT, pH 7, co-precipitation, fast titrant addition, 60 ^{o}C, pH 7, impregnation, fast titrant addition, RT.

The peak position of Fe $2p_{1/2}$ for the same samples was between 724.1 eV and 724.5 eV. The low intensity satellite peak for Fe $2p_{1/2}$ was observed in the energy range between 733.1eV and 733.9 eV. As for these samples synthesised with Na, there are no significant differences between samples synthesised with different conditions, with K promoter.

3.3.4 The XPS characterization of samples prepared under different conditions with Rb promoter, before activation

In these experiments the binding energies of Fe $2p_{3/2}$ for samples before activation were observed between 710.1 and 709.9 eV. The Fe $2p_{3/2}$ peak for all the samples has an associated satellite peak located approximately 8 eV higher than the main Fe $2p_{3/2}$ peak. The binding energies of Fe $2p_{1/2}$ for the same samples were between 724.3 eV and 724.6 eV. There are also characteristic satellite peaks for Fe $2p_{1/2}$ spectra in the range between 733.8 eV and 734.2 eV. The satellite peaks of Fe $2p_{3/2}$ and Fe $2p_{1/2}$ for the sample synthesised at pH 7, impregnated, fast titrant addition in room temperature are more pronounced than for the other samples, see Figure 3.3.4. Binding energies data from the analyzed non-reduced samples are contained in Table 3.3.5.

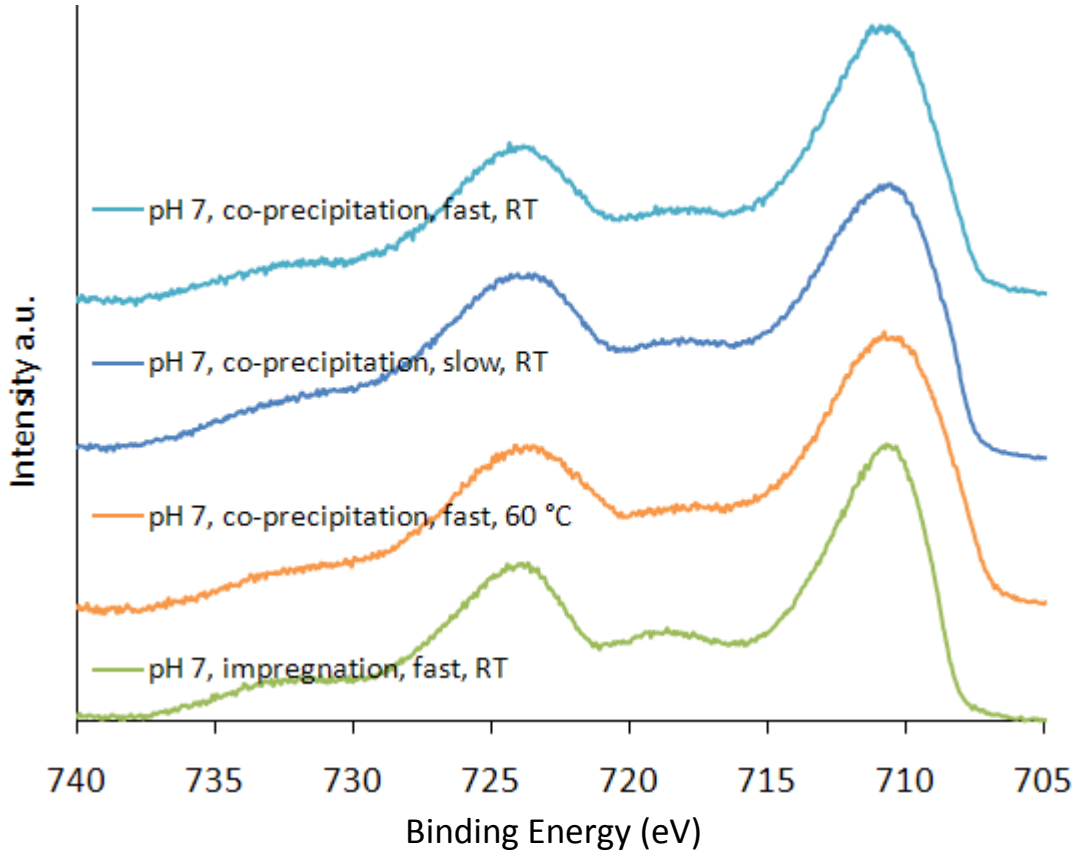

Fig.3.3.4 XPS Fe(2p) spectra of samples with Rb promoter before activation; pH 7, co-precipitation, fast titrant addition, RT, pH 7, co-precipitation, slow titrant addition, RT, pH 7, co-precipitation, fast titrant addition, 60 ^{o}C, pH 7, impregnation, fast titrant addition, RT.

3.3.5 The XPS characterization of samples prepared under different conditions with Rb promoter after activation

The peak positions of iron species Fe $2p_{1/2}$ and Fe $2p_{3/2}$ depend on the ionic states of iron[20,26]. The samples with Rb promoter reduced at 400 ºC, 450 ºC and non-reduced samples are compared below. The binding energy values of Fe $2p_{3/2}$ peaks after activation at 400 °C were in the range between 709.9 and 710.5eV, which is about 0.5 eV lower than non-reduced samples. The Fe $2p_{1/2}$ spectrum was observed in the range 733.7 – 734 eV. The satellites for the Fe $2p_{3/2}$ and Fe $2p_{1/2}$ peaks for the samples reduced at 400 °C were not noticed. The characteristic wider Fe $2p_{3/2}$ peak and the absence of associated satellite peak is typical for the Fe_3O_4 structure, as confirmed by reference samples[12,19,21]. The characteristic width of the Fe $2p_{3/2}$ peak is due to the coexistence of Fe^{2+} and Fe^{3+} peaks under the main peak. The shape and FWHM of Fe $2p_{3/2}$ depends on the ratio Fe^{2+} : Fe $^{3+}$. Therefore, the analysis, such as the fitting of Fe $2p_{3/2}$, the Fe 3p and the Fe^{2+} : Fe $^{3+}$ ratio will be studied below.

For the samples reduced at 450 °C the Fe $2p_{3/2}$ and $2p_{1/2}$ peaks were observed at the same position as for the samples reduced at 400 °C. However, a splitting in the lower energy shoulder for Fe $2p_{3/2}$ was observed. The main peaks were slightly narrower than for the sample reduced at 400 °C. The smaller peak on the lower energy side of the Fe 2p peak at 706.5 eV, in the range typical for metallic Fe, was observed. The activated iron oxide with Rb is presented in Figure 3.3.5.

For the sample reduced at 450 °C with Rb and Na the Fe $2p_{3/2}$ satellite was observed which could be due to the presence α-FeOOH or re-oxidation and occurrence of γ-Fe_2O_3[11-20]. The observed satellite of α-Fe_2O_3 and γ-Fe_2O_3 may be confused. However, the XRD measurement of the experimental samples and different method of synthesis for both compounds exclude the presence of α-Fe_2O_3 in the activated samples. It was noticed in the literature that the α-Fe_2O_3 is converted to the inverse spinel structure Fe_3O_4 by the reduction process and then to γ-Fe_2O_3 structure required re-oxidation (which was not necessary in this work)[22].

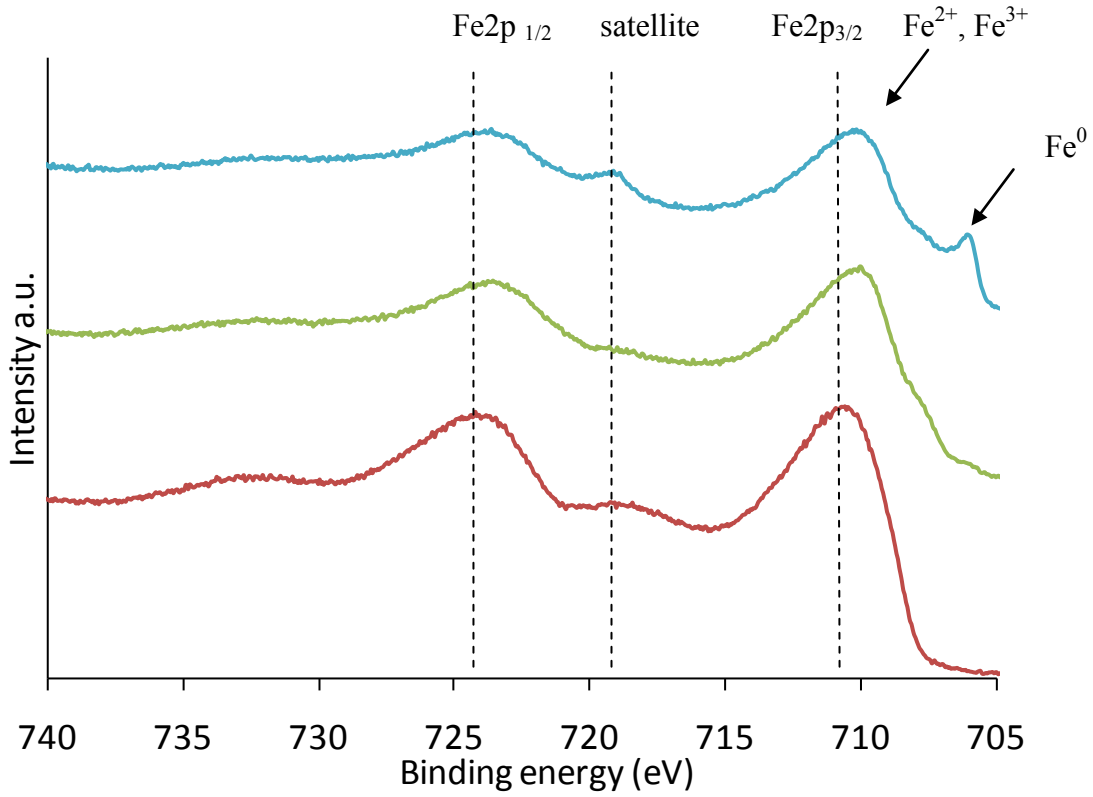

Fig.3.3.5 The Fe(2p) XPS spectra of the samples (from the top): reduced at 450 °C, synthesised at pH 7, co-precipitation, fast titrant addition - blue; reduced at 400 °C, synthesised in the same conditions - green; non-reduced - red.

Tab. 3.3.5 Binding Energies (eV) of Major Core Lines obtained from non-reduced and reduced iron catalyst XPS data.

Name, reduction temperature	Fe $2p_{3/2}$	Satellite for Fe $2p_{3/2}$	Fe 3p
pH7, fast, RT, Na	710.2	718.6	55.4
pH7, slow, RT, Na	710.2	718.4	55.1
pH7, fast, RT, Na, impregnated	710.1	718.3	55.5
pH7, fast, 60 ^{o}C, Na	710.2	718.3	55.8
pH7, fast, RT, K	710.1	718.4	55.6
pH7, slow, RT, K	710.2	718.5	55.1
pH7, fast, 60 ^{o}C, K	710.2	718.5	54.9
pH7, fast, RT, K, impregnated	710.2	718.4	54.8
pH7, fast, RT, Rb	710.1	718.4	54.9
pH7, slow, RT, Rb	710.1	718.2	54.6
pH7, fast, 60 ^{o}C, Rb	710.0	718.2	55.3
pH7, fast, RT, Rb, impregnated	710.1	718.3	55.7
pH7, fast, RT, Rb, 400 ^{o}C	710.3	-	55.8
pH7, fast, RT, Rb, 450 ^{o}C	710.3	719.5	55.8

3.3.6. The XPS spectral analysis. The fitting for the samples with different promoters before and after activation

The Gupta and Sen (GS) [20-25] calculation was used to fit references and samples with different promoters measured before and after activation. The multiplet components information like a FWHM range for high-spin Fe^{3+}, Fe^{2+}, multivalent Fe_3O_4 and Fe^0 is reported in their publications and those of others[14, 26,20-25]. The main peak envelope centre of gravity was determined using the GS multiplets fitting. The envelope, corresponding to GS calculations contains multiplets peaks, high-BE "surface-peak", low-BE "pre-peaks" The Fe (2p) spectra were fitted by a least squares routine.

3.3.7. The XPS spectral analysis. The Fe (2p) peak fitting for the samples with sodium, potassium and rubidium before reduction

The full width at half of the maximum (FWHM) range of the peaks used to fit the Fe $2p_{3/2}$ experimental multiplet spectra for the Fe_2O_3 reference sample was between 1.0 eV and 1.4 eV. The double maximum in the Fe $2p_{3/2}$ spectrum for the reference was fitted by two narrow (FWHM = 1.0 eV and 1.2 eV) peaks of equal intensity, separated by 1.2 eV, which was similar to the published references[14,20].

The multiplets were fitted by starting with the most intense peaks with similar width and shape. The multiplet fitting for the reference sample can be seen in Figure 3.3.7.1. The area under the peak is related to the GS experiment[20,24] and presented in a Table 3.3.8.2. There are significant differences in the shape and FWHM between Fe $2p_{3/2}$ of the α-Fe_2O_3 and γ-Fe_2O_3 described in literature[14,20]. The first and the second peak of the multiplet under Fe $2p_{3/2}$ peak for α- and γ-Fe_2O_3 have different intensities, BE difference and FWHM and this causes a characteristic split in the envelope. The combination of these factors should help distinguish between the α- and γ- structures of the Fe_2O_3. For example, first two of the multiplet peaks of the same intensity may interfere and give a smooth enveloped peak without any splitting. However, a little difference in the BE difference between two multiplet peaks may

cause a small split in the envelope[14,20,23]. Another case when the splitting may occur is when one of the multiplets peak has higher intensity than the other. Distinguishing the difference based only on the FWHM and the distance of the first two multiplet peaks may be also regarded as good procedure (not only the shape of the envelope). The FWHM is always slightly larger under the envelope of the γ-structured samples.

The difference between both structures is explained by the difference in orientation of the Fe^{3+} cations. All of the cations in the α-compound are octahedrally coordinated, while in a γ-compound of spinel-related structure, three quarters of the Fe^{3+} cations are octahedrally and a quarter tetrahedrally coordinated[14,20].The Fe_2O_3 reference sample has equal intensity for both first multiplet peaks. The BE differences between multiplets and FWHM are comparable with those of α-Fe_2O_3 described by GS[14,24,25]. The multiplets, surface-peaks and pre-peaks for Fe $2p_{3/2}$ for the reference sample are given in Table 3.3.7.

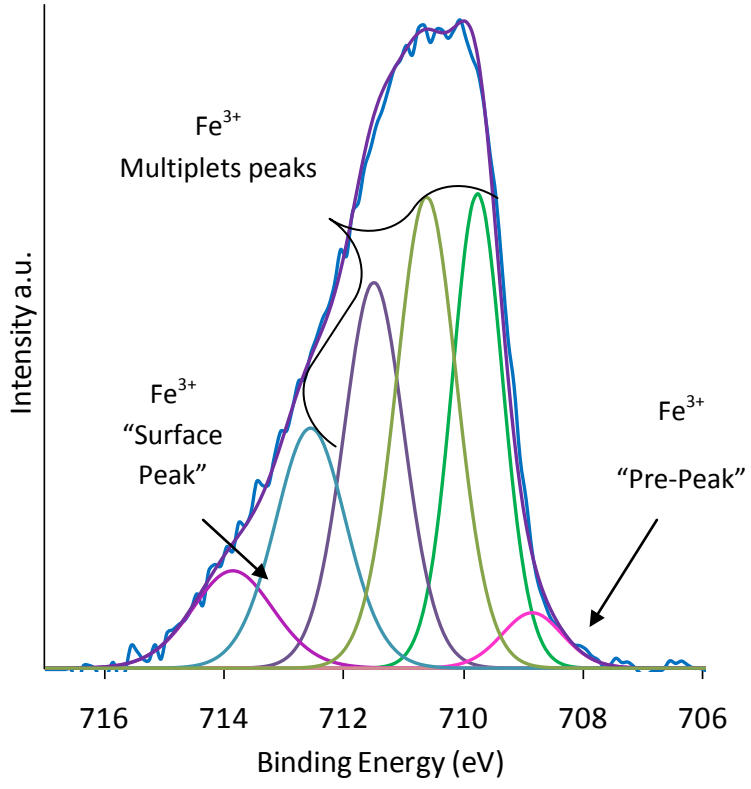

Fig. 3.3.7.1 The XPS Fe $2p_{3/2}$ spectra of Fe_2O_3 reference sample. The multiplet peaks, "surface peak" and "pre-peak" have been assigned on the spectrum.

Differences in the intensity for the first peaks of the multiplets of the samples with different promoters were observed (peaks no 1 and 2, Figure 3.3.7.2 - 3.3.7.4). The low energy peak of the multiplet has a higher intensity for the samples with K and Rb in comparison to the sample with Na, which has equal intensity for both multiplet peaks, see Figure 3.3.7.2 – 3.3.7.4. No significant differences were observed in the width (FWHM) of the multiplet peaks under the Fe $2p_{3/2}$ peak between the non-reduced samples synthesized with different promoters. The above, and the similarity with the fingerprint sample, leads to the conclusion that all of the samples have an α-Fe_2O_3 structure. The multiplets, surface-peaks and pre-peaks for Fe $2p_{3/2}$ for the samples with three different promoters were calculated using the XPS Casa software[27] and are given in Table 3.3.7.

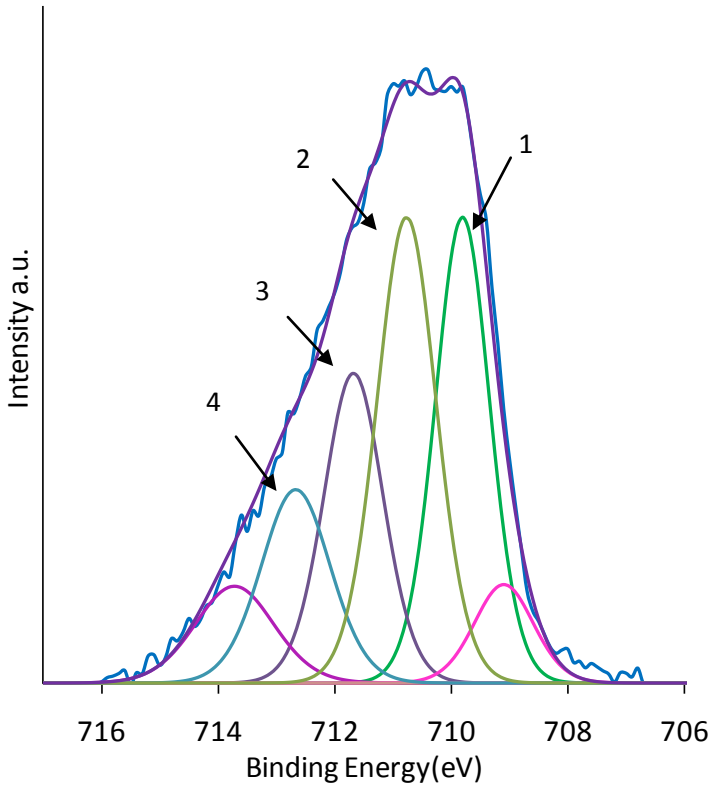

Fig. 3.3.7.2 The XPS Fe $2p_{3/2}$ spectra of iron oxide catalyst synthesised in pH 7, fast titrant addition, RT, with K promoter.

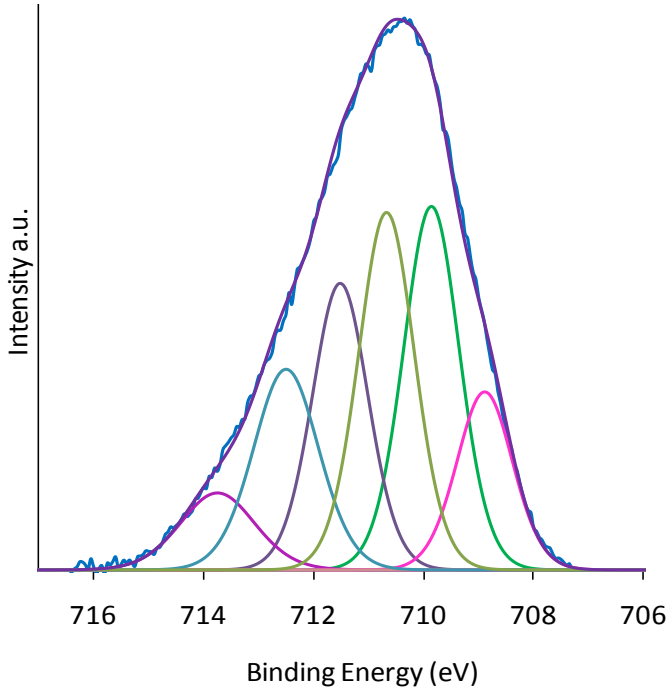

Fig. 3.3.7.3 The XPS Fe $2p_{3/2}$ spectra of iron oxide catalyst synthesised in pH 7, fast titrant addition, RT, with Na promoter.

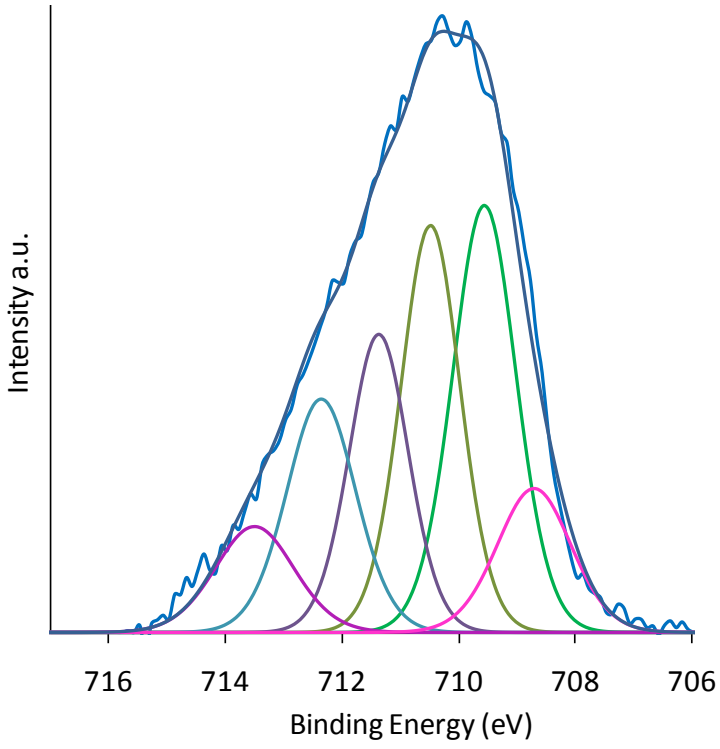

Fig. 3.3.7.4 The XPS Fe $2p_{3/2}$ spectra of iron oxide catalyst synthesised in pH 7, fast titrant addition, RT, with Rb promoter.

Tab. 3.3.7. The Fe ($2p_{3/2}$) multiplet peak positions used to fit the Fe^{2+} and Fe^{3+} compounds, based on Gupta and Sen (GS).

Iron oxide (pH 7, fast, RT)/promoters, reduction temperature	Peak 1 (eV), FWHM	Peak 2 (eV), FWHM	Peak 3 (eV), FWHM	Peak 4 (eV), FWHM	Peak 5 "pre-peak" (eV), FWHM	Peak 6 "surface peak"(eV), FWHM
Fe_2O_3	709.8, 1.0	710.6, 1.2	711.5, 1.2	712.5, 1.4	708.2, 1.2	713.8, 1.6
Na	709.8, 1.0	710.7, 1.2	711.5, 1.2	712.4, 1.4	708.7, 1.2	713.7, 1.6
K	709.8, 1.0	710.6, 1.2	711.4, 1.2	712.4, 1.4	708.8, 1.4	713.7, 1.6
Rb	709.6, 1.1	710.5, 1.2	711.4, 1.2	712.3, 1.4	708.7, 1.4	713.7, 1.6
Fe_3O_4 (Fe^{3+})	710.2 1.4	711.1, 1.4	712.1, 1.4	713,3 1.4	-	714.4, 1.5
Rb, 400 °C	710.2 1.4	711.1,3 1.4	712.1, 1.4	713,4 1.4	-	714.5, 1.6
Na, 400 °C	710,1 1.4	711.1,1 1.4	712.2, 1.4	713,3 1.4	-	714.4, 1.55
Rb, 450 °C	709.8 1.4	710.9 1.4	712.1, 1.4	713,1 1.4	-	714.1, 1.6
Na, 450 °C	709.9 1.4	710.9 1.4	712, 1.4	713,2 1.4	-	714, 1.6
Fe_3O_4 (Fe^{2+})	708.1 1.2	709.1, 1.2	710.9, 1.4	-	707.8, 1.4	714.4, 1.5
Rb, 400 °C	708.8 1.2	709.1, 1.2	710.1, 1.4	-	707, 1.4	714.5, 1.6
Na, 400 °C	708.5 1.2	709.1, 1.2	710.5, 1,4	-	707.5, 1.4	714.4, 1.55
Rb, 450 °C	707.9, 1.2	709.4, 1.2	710.9, 1.4	-	707.3, 1.5	714.1, 1.6
Na, 450 °C	708, 1.2	709.5, 1.2	710.6, 1.4	-	707.2, 1.6	714, 1.6

XPS Standard deviation (SD) for the peak positions: 0.02-0.1

3.3.8. The Fe 2p XPS spectral analysis. The fitting of the Fe_3O_4 reference and the samples with Na and Rb promoters after reduction at 400 °C and 450 °C

The spectrum of the multivalent Fe_3O_4 reference sample significantly varies from the spectra of the Fe_2O_3 reference because of the characteristic broad Fe $2p_{3/2}$ envelope with a shoulder on the low binding energy side. The characteristic width of the Fe $2p_{3/2}$ envelope for the Fe_3O_4 reference sample is due to the fact that both Fe^{2+} and Fe^{3+} components were fitted into the Fe $2p_{3/2}$ spectrum, exactly as described before by Gupta, Sen, McIntyre, Zetaruk and Grosvenor[14,20,24,25]. The Fe^{3+} multiplet peaks for the Fe_3O_4 reference sample are shifted to higher energies from around 0.4 eV to 0.7 eV in comparison to those observed in the Fe_2O_3 reference sample, as was described in the literature[14,20,23,25]. The distinctive peaks used to fit the Fe^{2+} and Fe^{3+} species in Fe_3O_4 have been marked in Figure 3.3.8.The multiplet peaks energies used to fit the Fe^{2+} and Fe^{3+} species are in the Table 3.3.7.

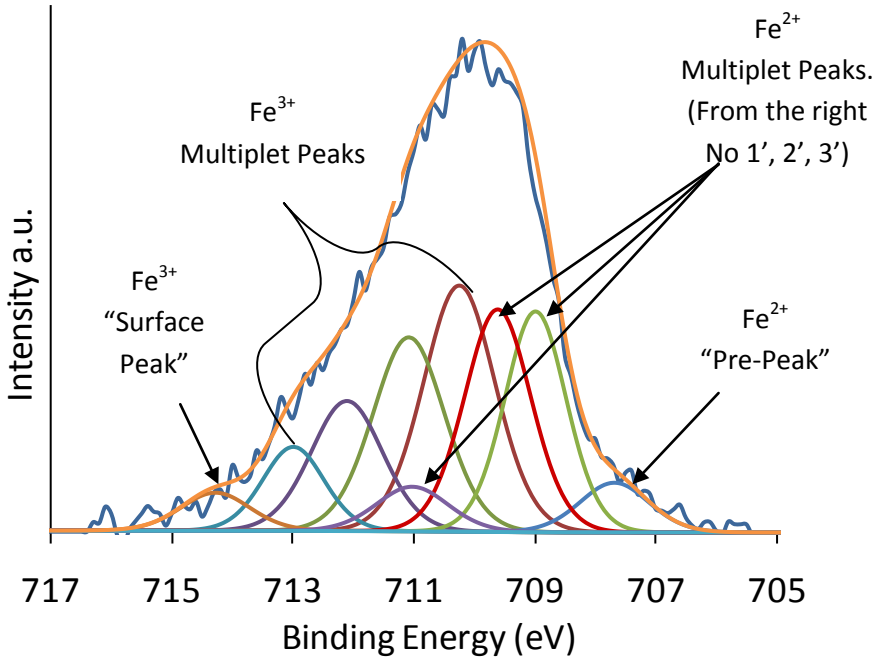

Fig. 3.3.8. GS backround-substracted Fe $2p_{3/2}$ spectrum of Fe_3O_4, reference sample. The multiplet peaks, "surface peak" and "pre-peak" have been labelled on thee spectrum.

3.3.8.1 The Fe $2p_{3/2}$ XPS spectra fitting of samples prepared in pH7, fast titrant addition, RT with Na and Rb after activation in 400 ^{o}C

The Fe^{3+} multiplets peaks for the samples with Na and Rb promoters synthesised in pH7, fast titrant addition, RT, reduced at 400 ^{o}C have similar shapes and binding energy values to the Fe_3O_4 reference sample, Figure 3.3.11 and 3.3.12. Slightly higher binding energy Fe^{2+} multiplet peaks and a visible indent in the lower energy part of the envelope were observed for the sample with Na promoter. The partial oxidation level above Fe_3O_4 could be the reason of lower width of the main Fe $2p_{3/2}$ peak for the samples with Na promoter. The samples reduced at 400 ^{o}C and fitted multiplet peaks are presented in Figure 3.3.8.1 a and 3.3.8.1 b.

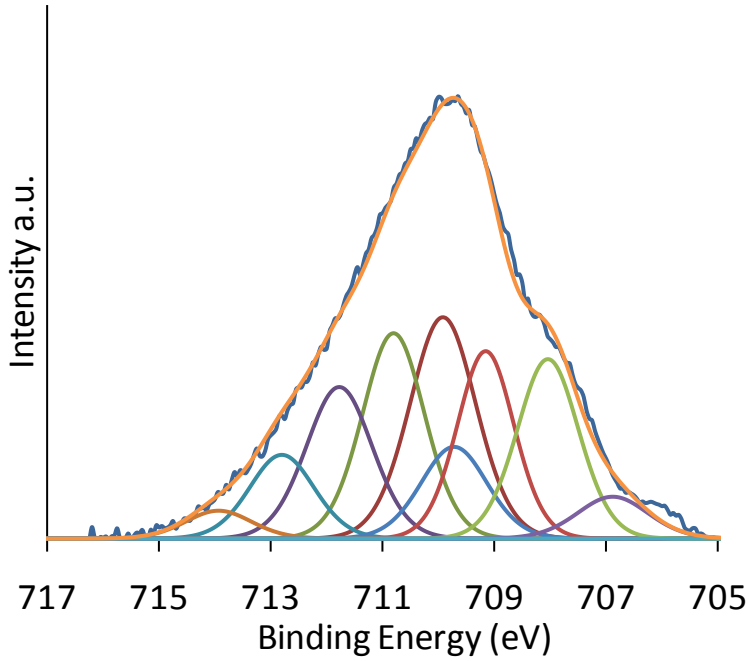

Fig. 3.3.8.1 a The XPS Fe $2p_{3/2}$ spectra of iron oxide catalyst with Na promoter, synthesised in pH7, fast titrant addition, RT and activated in 400 ^{o}C.

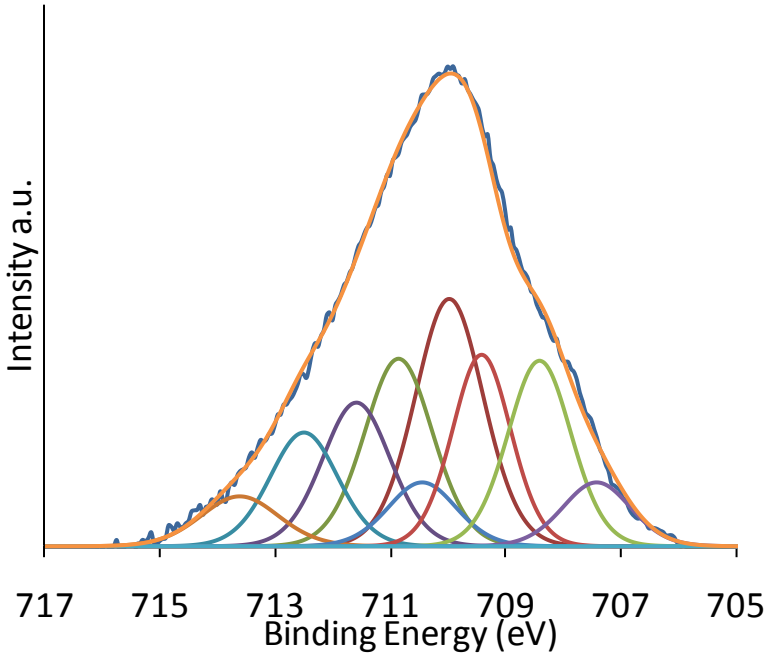

Fig. 3.3.8.1 b The XPS Fe $2p_{3/2}$ spectra of iron oxide catalyst with Rb synthesised in pH7, fast titrant addition, RT, reduced in 400 ^{o}C.

3.3.8.2 The Fe $2p_{3/2}$ XPS spectra fitting of samples prepared in pH7, fast titrant addition, RT with Na and Rb after activation in 450 ^{o}C

The Fe $2p_{3/2}$ spectra for the samples with Na and Rb promoters synthesized in pH7, fast titrant addition, RT, reduced at 450 ^{o}C had the same characteristic Fe^{2+} and Fe^{3+} multiplets as the samples reduced at lower temperatures. Furthermore, similar to the sample synthesised at 400 ºC, the visible indent into the elevation of the lower energy part of the envelope for the sample with Na promoter was observed. The significant difference between samples reduced at 400 ºC and 450 ºC was a distinct peak present in the low binding energy region of the envelope in the same BE region as for the samples with Na and Rb. According to the literature, the peak which occurred at 706.4 eV binding energy after reduction in higher temperature was characteristic for the metallic form of Fe. For the sample with Na promoter, a smaller amount of the metallic form of catalyst was observed. The GS fitting for the iron oxide multiplets with metallic iron under envelope are presented in Fig 3.3.8.2 a and 3.3.8.2 b. The binding energies for all Fe 2p multiplets peaks values for the sample reduced at 450 $^{\circ}$C are tabulated in the Table 3.3.7.

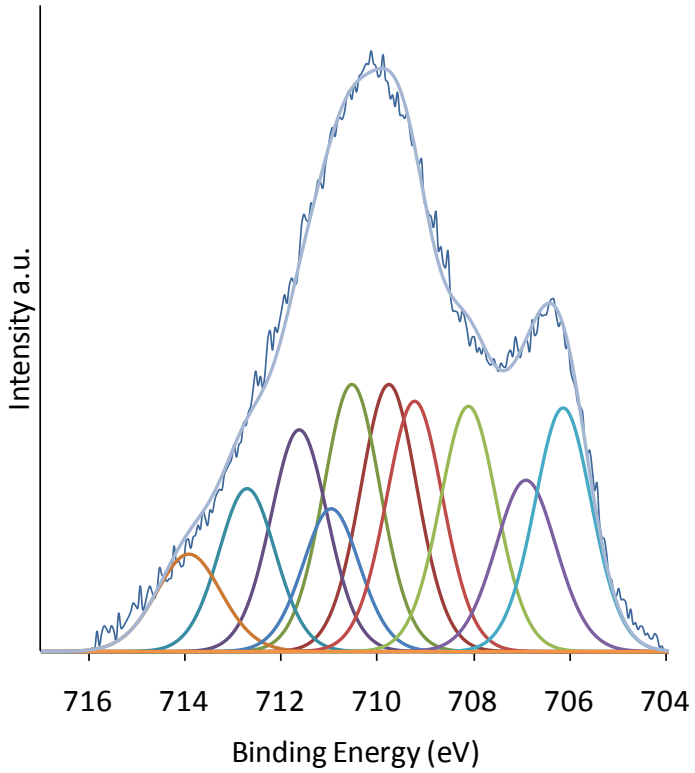

Fig. 3.3.8.2 a The XPS Fe $2p_{3/2}$ spectra of iron oxide catalyst with Na promoter, reduced at 450 °C.

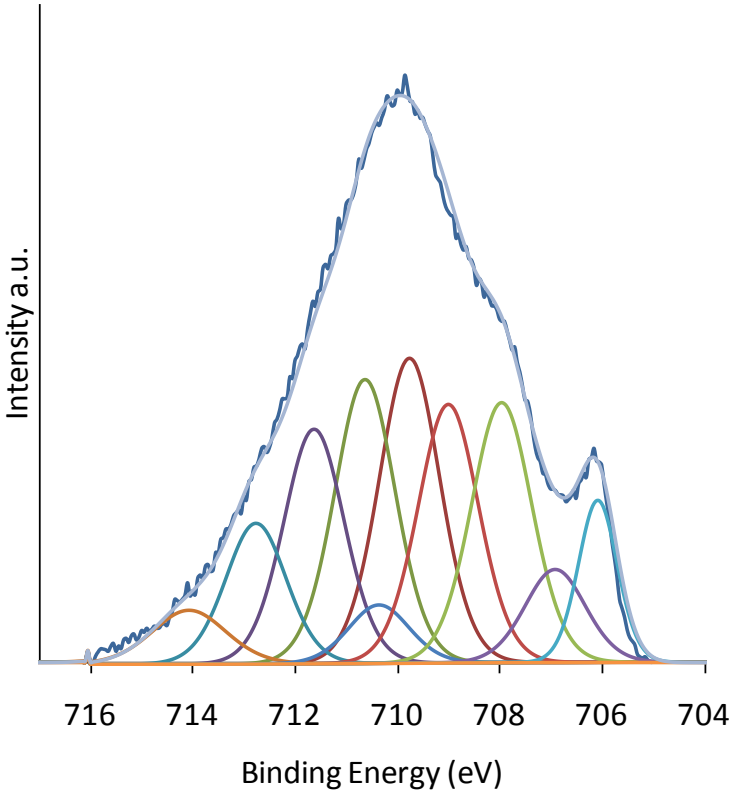

Fig. 3.3.8.2 b The XPS Fe $2p_{3/2}$ spectra of iron oxide catalyst with Rb promoter, reduced at 450 °C.

In the experiment the Fe^{2+}/Fe^{3+} ratio in the Fe_3O_4 structure was also estimated. It was found that in the samples reduced at 400 ^oC with Rb and Na, the Fe^{2+}/Fe^{3+} ratio from Fe $2p_{3/2}$ was 0.52 and 0.51 respectively. For the samples reduced at 450 ^oC with Rb and Na, the Fe^{2+}/Fe^{3+} ratio was 0.60 and 0.54 respectively. The expected the Fe^{2+}/Fe^{3+} ratio in the Fe_3O_4 is 0.5. The Fe^{2+}/Fe^{3+} ratio increased with the reduction temperature which demonstrates transformation of the Fe^{3+} ions into Fe^{2+} with increasing reduction temperature. The ratios for the samples with Rb and Na promoters, reduced at 400 ^oC and 450 ^oC are presented in a Table 3.3.8.2.

The Fe^{2+}/Fe^{3+} ratio was measured for the Fe $2p_{3/2}$ spectra and according to the multiplets overlapping, there is a possibility that the separation of the two phases was not accurate. The error may be related with the overlapping of the first two peaks (No 1, 2) of Fe^{3+} multiplet and the third (No 3) peak of the Fe^{2+} multiplet. Fe 3 p spectra were examined in the next part of that experiment.

Table. 3.3.8.2 The Fe ($2p_{3/2}$) multiplet peak parameters used to fit the Fe^{2+} and Fe^{3+} compounds, based on Gupta and Sen (GS).

Oxidation state of iron oxide	(Fe^{3+})					(Fe^{2+})				Fe^0	Fe^{2+}/Fe^{3+}
Compound[1]/Atomic percent (%), of the GS[2] peak	Peak 1	Peak 2	Peak 3	Peak 4	∑	Peak 1	Peak 2	Peak 3	∑	Peak Fe^0	-
α-Fe_2O_3, reference	33.7	28.1	23.4	14.8	-	-	-	-	-	-	-
Na, RT	29.6	29.1	26.6	14.7	-	-	-	-	-	-	-
K, RT	28.9	28.7	24.3	18.10	-	-	-	-	-	-	-
Rb, RT	30.7	28.4	23.8	17.1	-	-	-	-	-	-	-
Fe_3O_4, reference	21.2	21	14.5	9.2	65.9	14.5	14.2	5.1	33.8	-	0.51
Rb, 400 °C	22.0	21.5	13.8	8.6	65.9	15.0	15.1	4.0	34.1	-	0.52
Rb, 450 °C	18.5	17.2	14.3	8.5	58.5	14.7	14.8	4.5	35.0	7.4	0.60
Na, 400 °C	21.6	20.7	14.1	9.9	66.3	14.5	14.7	4.5	33.7	-	0.51
Na, 450 °C	19.1	17.7	13.6	8.4	58.8	12.7	12.6	6.4	31.7	9.3	0.54

1) Iron oxide (synthesised at pH 7, fast, RT), promoter, reduction temperature.
2) GS - Gupta and Sen peaks. According to Grosvenor (2004), there was chosen 4 peaks Fe^{3+} and 3 significant peaks for Fe^{2+}. The peaks are presented in a Figure 3.3.10

3.3.9 The Fe^{2+} and Fe^{3+} ratio calculation by fitting of the Fe 3p spectra

There is also a good procedure for calculating the Fe^{2+}:Fe^{3+} ratio from the Fe 3p spectrum due to the fairly low complexity of the structure of those spectra[14,19]. The Fe 3p peak, in comparison to 2p peaks, does not have satellite peaks that may partially overlap the 2p main peaks. The Fe 2p peaks are also separated in two peaks which makes it difficult to calculate the Fe^{2+}:Fe^{3+} ratio and to obtain the total contributions of the components, the area under both peaks should be integrated. Moreover, the Fe 3p peak is a single peak without satellites that may interfere with the main peak.

The Fe 3p peak of the Fe_3O_4 reference sample was fitted using Fe^{2+} and Fe^{3+} parameters and peak positions from the Fe 3p of reference sample and literature sources[14,17,18]. The results for deconvoluted peaks for the sample with Na promoter reduced at 400 ^oC gave the Fe^{2+}: Fe^{3+} ratio to be 0.52, slightly higher than expected from the stoichiometry of Fe_3O_4 Fe^{2+}: Fe^{3+} ratio (0.5). The ratio for the samples with Rb promoter reduced at the same temperature was equal 0.50. The results of deconvoluted Fe 3p peaks taking into account the estimated experimental and analysis error, are very similar to those obtained from Fe 2p spectra. S.D. is equal 0.01 for both Fe^{2+} and Fe^{3+}, which is similar to the literature data.The fittings for the Fe 3p of the samples with Na and Rb promoter reduced at 400 ºC are presented in Figure 3.3.9.

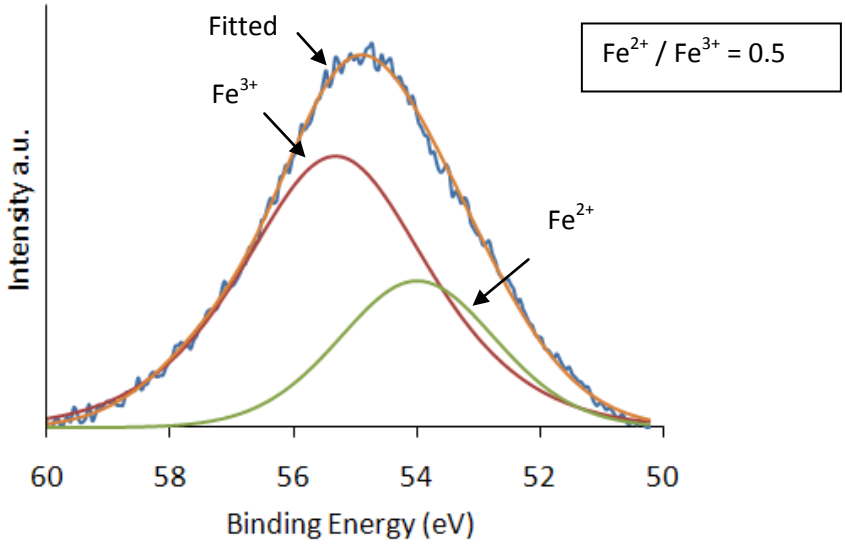

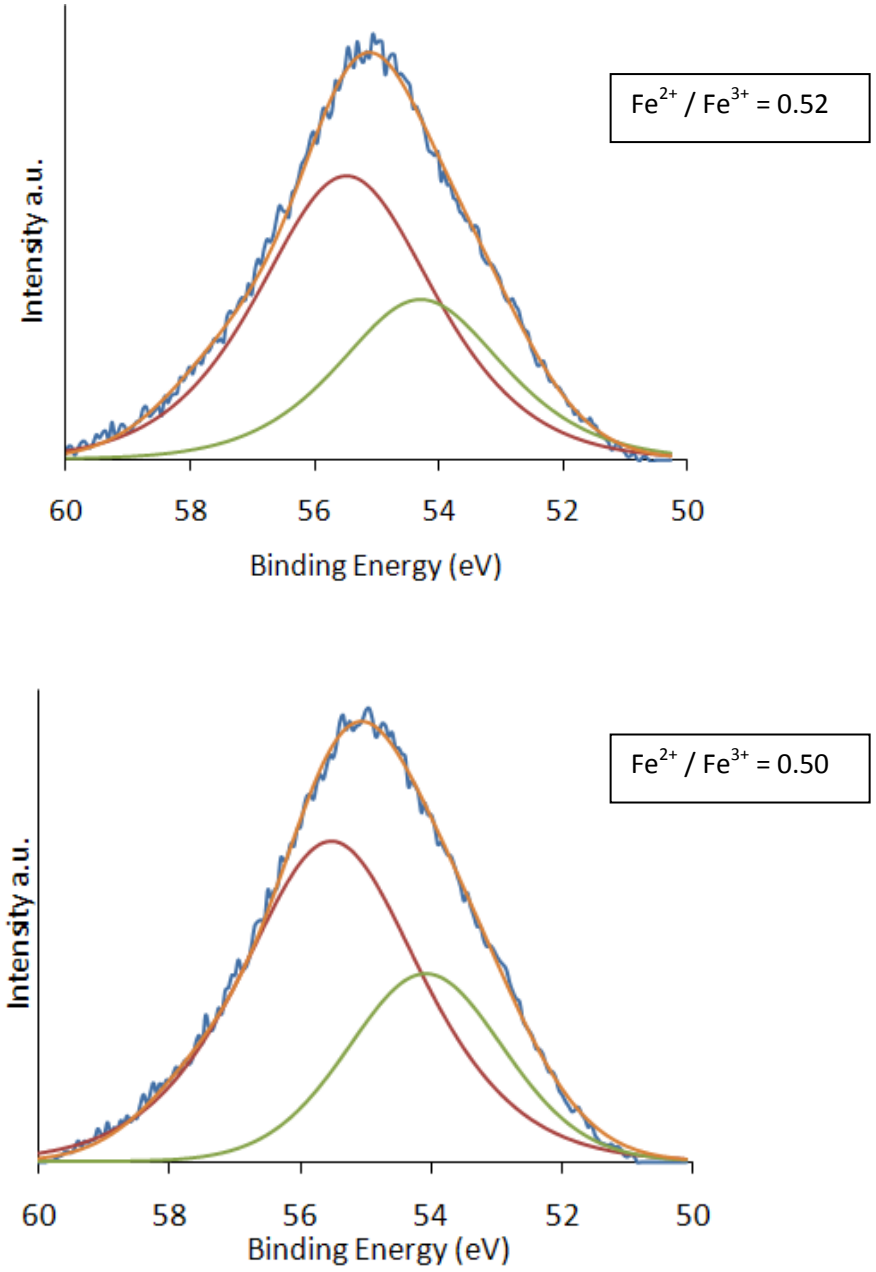

Fig. 3.3.9 The fitting of the Fe 3p line for from the top: Fe_3O_4; pH 7, co-precipitated, fast titrant addition in room temperature, reduced at 400 ^oC, with Na; the same conditions with Rb promoter. The Fe^{2+} : Fe^{3+} ratio have been labelled near to the spectra.

3.3.10 O 1s spectra of samples with alkali promoters

The XPS measurements helped to identify the oxidation state of iron, and the structure of the iron oxide for the samples with different alkali promoters, Na, K, Rb before and after activation. To obtain further information on the type of oxidized iron species present in the samples, the O1s peak was analyzed. The O1s characterization facilitated distinguishing between different forms of iron catalyst surface compounds such as hydroxide and water species. Storage in the air would lead to the formation of hydrates at the surface, and that would influence the performance of the catalyst[28].

3.3.11 O 1s spectra of samples with K promoter for non-activated samples

The measurement of the O1s spectrum for all the samples with K promoter synthesized in different conditions showed main peaks at 530.3 eV, which is comparable with the literature sources[29,30,31]. Every O1s peak had a characteristic shoulder in the higher energy base of the peak, around 2 eV above of the maximum of the peak. The shape and the energy range of the main peak suggested the presence of hydroxides and H_2O species which can appear in small amounts on the surface of the iron oxide catalyst. The slightly larger feature for the samples synthesized at pH 7, impregnated, fast titrant addition in RT was observed. The main O 1s peak and the feature are presented in Figure 3.3.11.

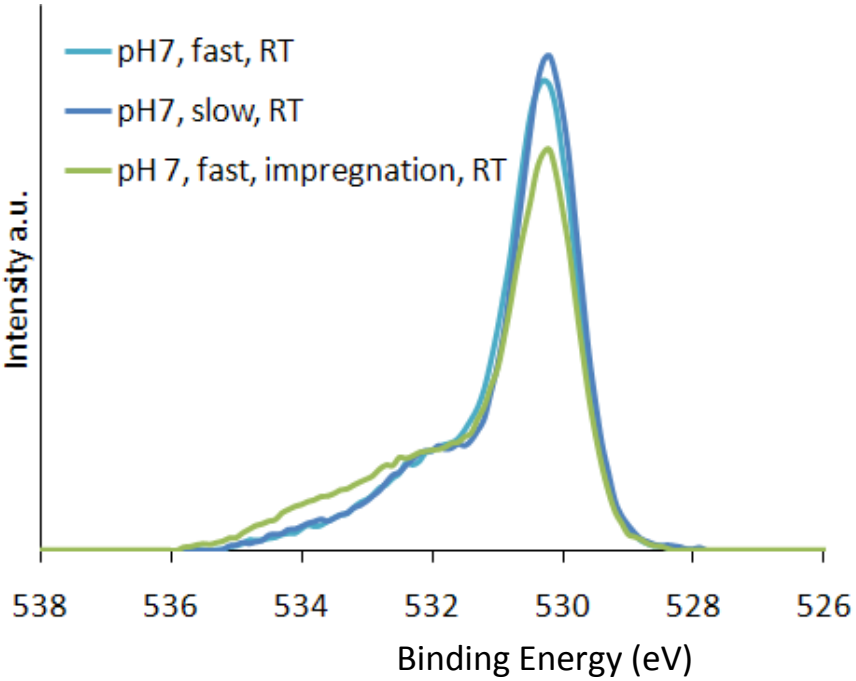

Fig. 3.3.11. The O1s peak for the samples with K promoter (from the top): pH 7, fast titrant addition, RT; pH 7, slow titrant addition, RT; pH 7, fast titrant addition, impregnated, RT

3.3.12 O 1s spectra of samples with Na promoter, before and after activation

For all non-reduced samples with Na promoter synthesized in different conditions a single O1s peak was observed at BE 530.2 eV. The lower gradient of the higher energy shoulder for all the samples was observed. The shape of the O1s peak may suggests presence of hydroxides and H_2O species on the surface of iron oxide catalyst. The O1s peak was slightly broader for the samples synthesised at pH 7, impregnated, fast titrant addition in room temperature, than the rest of the samples. The higher FWHM may suggest the presence of OH^- and H_2O species (higher energy base of the O 1s peak ending at 536 eV). The main O 1s peak is presented in Figure 3.3.12.1.

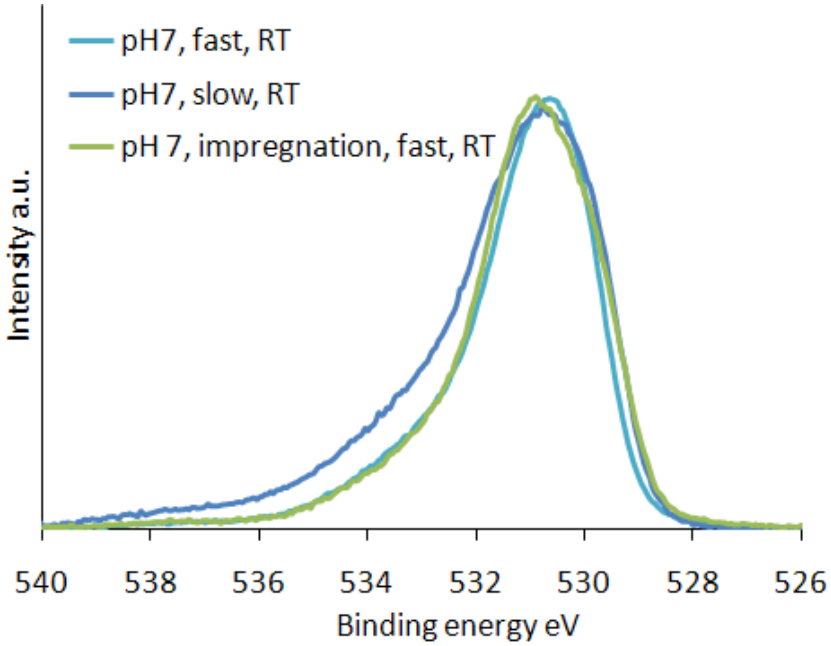

Fig. 3.3.12.1 The O1s peak for the samples with Na, (from the top): pH 7, fast titrant addition, RT; pH7, slow titrant addition, RT; pH 7, fast titrant addition, impregnated, RT

After non-reduced samples with Na promoter, the samples reduced under H_2/He at 400 ºC and 450 ºC samples were recorded, Figure 3.3.12.2. The O 1s spectra for the samples reduced at 400 ^{o}C have one main peak in the area around 530 eV. A small gradient on the higher energy side shoulder of the main peak was visible. The O 1s peaks for the reduced samples are presented in Figure 3.3.12.2. The main O 1s peak for the samples reduced at 450 ^{o}C has nearly the same BE (530.1 eV) as those reduced at the lower temperature. However, a few differences between the samples reduced in the two different temperatures were found. The samples reduced at 400 ºC in comparison to those reduced at 450 ºC have slightly higher intensity and lower FWHM. The feature in the higher energy shoulder (BE in the range 531.0 – 533.5 eV) for the samples synthesized at the higher temperature was still visible.

Higher FWHM for the samples reduced at the lower temperature may suggest presence of the mixture oxides (e.g. Fe_2O_3 and Fe_3O_4) and/or mixture iron oxide and iron hydroxide[29,30,31]. The presence of the feature in the higher energy shoulder for the samples reduces in higher temperature may suggest the presence of hydrates at the surface of the iron oxide. The small prominence (534.5 – 538.0 eV) may be caused by impurities [13,29].

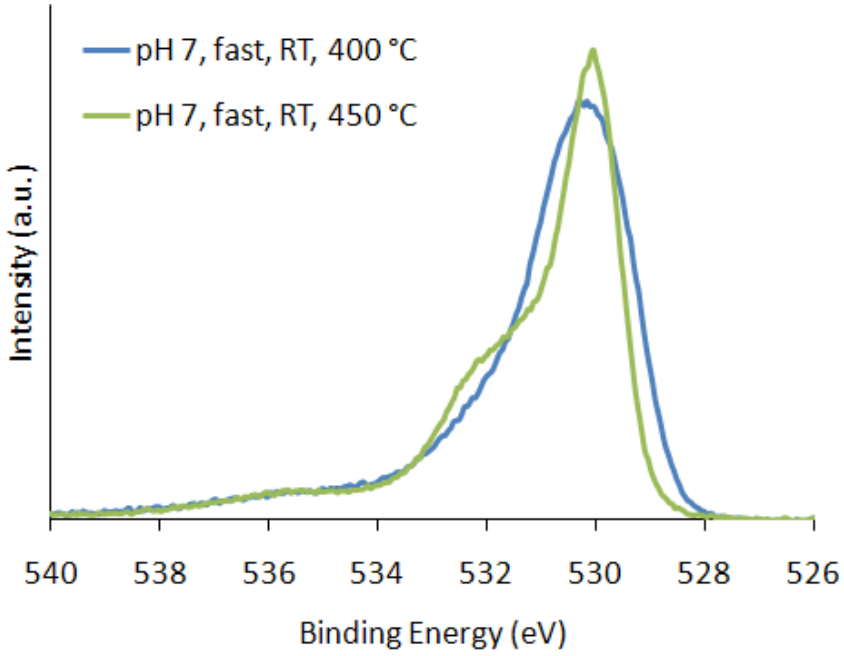

Fig. 3.3.12.2 The O1s peak for the reduced samples with Na: pH 7, fast titrant addition, RT, reduced in 400 ^{o}C; pH 7, fast titrant addition, RT, reduced in 450 ^{o}C

3.3.13 O 1s spectra of samples with Rb promoter before and after activation

The O 1s peaks for the samples with Rb are presented in Figure 3.3.13.1. The O 1s spectrum for the samples with Rb, with slow titrant addition in room temperature, splits into two peaks with BE values 530.0 eV and 532.7 eV. The splitting divides the main O 1s peak into two peaks of nearly equal intensity. The peak splitting may indicate the presence of combined oxides and hydroxides at the surface of the iron catalyst. The hydroxide peak for the sample, synthesized at pH 7 with fast titrant addition rate, has a similar intensity to that synthesized with slow titrant addition rate. However only one broad peak was observed, which may suggest interference of the O^{2-} and OH^{-} species peaks. For the sample synthesized at pH 7, fast titrant addition impregnated the main peak 530.0 eV and minor 532.8 eV were observed. The main peak was two times higher than that of the samples described before. The lower gradient of the peak in a range between 535.0 – 538.5 eV may suggest presence of impurities on the iron oxide surface. It was observed that all the samples with Rb promoter before reduction have more hydroxides and water compared to these with Na and K.

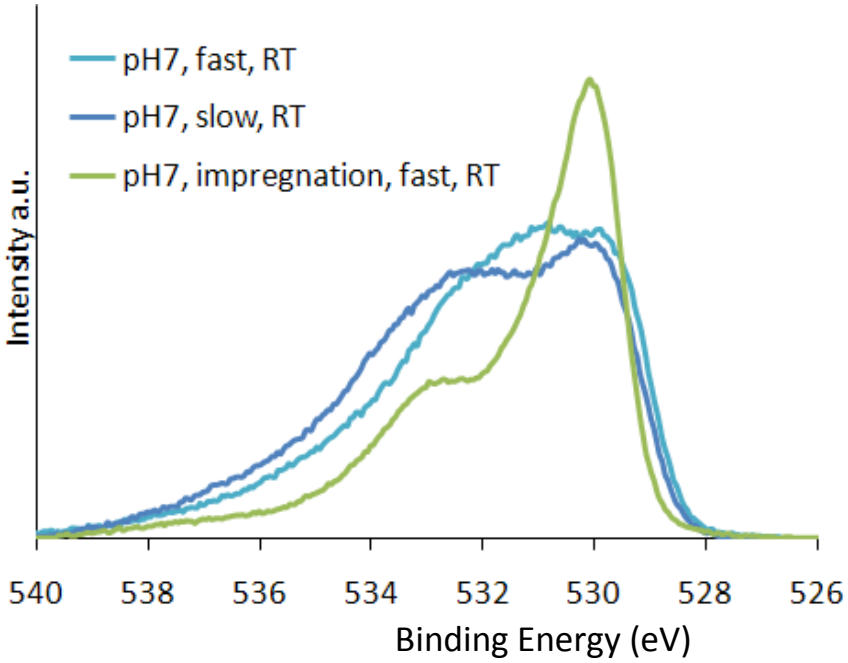

Fig. 3.3.13.1 The O1s peak for the samples with Rb, (from the top): pH 7, fast titrant addition, RT; pH7, slow titrant addition, RT; pH 7, fast titrant addition, impregnated, RT

The O 1s spectrum for the samples reduced under H_2/He at 400 ºC has one main peak localized between 529.8 eV and 530.2 eV. The samples synthesized at pH 7, fast titrant addition rate, reduced at 400 ^{o}C have a lower gradient higher energy shoulder than the rest of the samples. Two other samples synthesised at pH 7 slow titrant addition in room temperature, reduced in 400 ^{o}C and pH 7 fast titrant addition in room temperature, reduced at 450 ^{o}C have a lower gradient higher energy shoulder and clearly visible small feature at BE 532.1 – 534.1 eV. The lower gradient of the higher energy shoulder and the feature can suggest the presence respectively OH^- and H_2O species. The high energy side shoulder for the samples synthesized at pH 7 slow titrant addition in room temperature, reduced in 450 ^{o}C and impregnated samples reduced in two different temperatures have similar gradient as the samples described above however, the feature was not observed. The O 1s spectra for the samples reduced at 400 ºC and 450 ºC are compared in Figure 3.3.13.2.

The lower gradient of the higher energy shoulder may suggest a mixture of OH^- and O^{2-} species. The small concentration of the hydroxides may have big influence on the Fe:O ratio and stoichiometry of iron oxides with different promoters during activation process. The Fe:O atomic percent ratio will be calculated using XPS and bulk sensitive techniques in the next section.

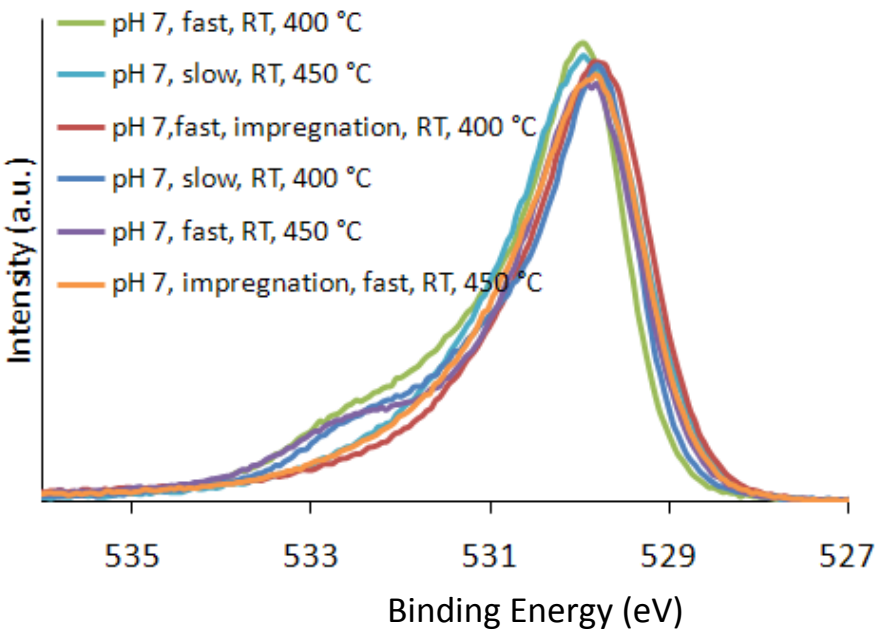

Fig. 3.3.13.2 The O1s peak for the reduced samples with Rb: pH 7, fast titrant addition, RT, reduced in 400 ^oC; pH 7, slow titrant addition, RT, reduced in 450 ^oC; pH 7, fast titrant addition, impregnation, RT, reduced in 400 ^oC; pH 7, slow titrant addition, RT, reduced in 400 ^oC; pH 7, fast titrant addition, RT, reduced in 450 ^oC; pH 7, fast titrant addition, impregnation, RT, reduced in 450 ^oC.

3.4 Elemental analysis techniques (XRF, EDX, XPS) and the determination of the iron oxide stoichiometry

The elemental analysis of the iron and oxygen content was carried out using both bulk and surface sensitive techniques. The EDX, XRF and surface sensitive XPS facilitated the comparison of Fe:O atomic percent ratio for the non-activated and activated iron oxide catalysts. The atomic percentage of Fe and O of the samples synthesised in three different conditions with three different promoters: Na, K and Rb are compared and presented in the Table 3.4.1.

The surface sensitive XPS analysis of the non-activated iron oxide samples, synthesised under various conditions with Na indicate Fe:O ratios in the range 0.58 – 0.65. The sample synthesised at pH 7, slow titrant addition at room temperature has the lowest Fe:O ratio (0.59), which is lower than experimental α-Fe_2O_3 reference (0.63) and the theoretical Fe_2O_3 (0.67). The slightly higher amount of oxygen noticed may be caused by the hydroxides and H_2O presented on the surface, which was observed using XPS O 1s spectra analysis.

Two of the samples synthesised at pH 7, slow titrant addition at room temperature and at pH 7, fast titrant addition in 60 ^oC with K have the amount of oxygen higher then theoretical, a Fe:O ratio of respectively 0.69 and 0.75. The sample synthesised at pH 7, fast titrant addition at room temperature has a ratio comparable to the theoretical α-Fe_2O_3 Fe:O ratio (0.67).

The catalyst synthesised at pH 7, slow titrant addition at room temperature with Rb has lower than theoretical Fe:O ratio 0.61 (61.9 at % of O). The Fe:O ratio for the two other samples was between 0.67 – 0.7 (58.9-59.7 at % of O), which is in a range between theoretical α-Fe_2O_3 and Fe_3O_4 (57 - 60 at% of O).

The XRF bulk technique for non-reduced samples with three different promoters indicated Fe:O ratio in a range (0.62 – 0.69) and reveals the presence of oxygen in a range between (59.06 – 61.59 %). The lowest Fe : O ratio was noticed for the samples synthesised in pH 7, slow titrant addition in room temperature with Na (0.62 and 61.59 at % of O). The highest Fe:O (0.69) was also observed for the sample with Na, synthesised in pH 7, fast titrant addition in room temperature.

The EDX technique shows similar data to these XRF. The Fe:O ratio measured by that technique is in the range between 0.52 - 0.69 and oxygen atomic percent in the range 59.2 - 65.9. The lowest Fe:O ratio was noticed for the sample synthesised at pH7, fast titrant addition in 60 ^{o}C, with K. The highest ratio was noticed for the sample synthesised at pH7, slow titrant addition in room temperature, with Rb. The increase of the Fe:O ratio with the reduction temperature was observed using XRF bulk elemental analysis. Both bulk and surface techniques confirmed results obtained using P-XRD. The higher amount of oxygen recorded for some of the samples may be caused by the presence of H_2O and hydroxides on the surface. The difference in stoichiometry between non-reduced samples synthesized with different promoters was not significant. The average Fe:O ratios for the samples analysed by surface and bulk techniques before reduction, with Na, K and Rb were: 0.62, 0.65, 0.66, respectively. The results for both surface and bulk sensitive techniques are presented in Table 3.4.1.

Tab. 3.4.1 The EDX, XPS, XRF elemental analysis of Fe and O (at %) for non-reduced iron oxide samples synthesized in various conditions with different promoters

Conditions	**Atomic % of Fe, EDX**		**Fe : O Ratio**	**Atomic % of Fe, XRF**		**Fe : O ratio**	**Atomic % of Fe, XPS**		**Fe : O Ratio**
Sample/Element analysed	**Fe**	O	Fe_nO[1]	**Fe**	O	Fe_nO	**Fe**	O	Fe_nO
α-Fe_2O_3	**38.6**[2]	61.4	0.63	**39.41**[3]	60.52	0.65	**38.5**[4]	61.5	0.63
pH7, fast, RT, Na	**37.9**	62.1	0.61	**40.73**	59.06	0.69	**37.1**	62.6	0.59
pH7, slow, RT, Na	**38.0**	62.0	0.61	**38.08**	61.59	0.62	**39.2**	60.5	0.65
pH7, fast, 60 ^oC, Na	**37.3**	62.7	0.59	**39.45**	60.20	0.65	**36.5**	63.2	0.58
pH7, fast, RT, K	**38.9**	60.1	0.65	**41.21**	59.70	0.69	**40.2**	59.8	0.67
pH7, slow, RT, K	**39.9**	60.0	0.66	**39.80**	60.10	0.66	**40.8**	59.1	0.69
pH7, fast, 60 ^oC, K	**34.1**	65.9	0.52	**38.90**	61.0	0.64	**43.0**	57.0	0.75
pH7, fast, RT, Rb	**40.6**	59.4	0.68	**40.48**	59.47	0.68	**38.1**	61.9	0.61
pH7, slow, RT, Rb	**40.8**	59.2	0.69	**38.59**	61.37	0.63	**40.3**	59.7	0.67
pH7, fast, 60 ^oC, Rb	**39.9**	60.1	0.66	**39.87**	60.08	0.66	**41.1**	58.9	0.70

1. **at% theoretical**: Fe = 40 %, O = 60 %; $Fe_2O_3 = Fe_{0.67}O$
2. **EDX Standard deviation (SD):** Fe(1.3-1.5); O(1.2-1.5)
3. **XRF Standard deviation (SD) for Fe and O:** (0.05- 0.5)
4. **XPS Standard deviation (SD):** Fe(1.0 - 1,4); O(0.9 – 1.1)

The surface XPS analysis for the samples with Na and Rb promoters after reduction in 400 ^oC and 450 ^oC H_2/He for 20 h was carried out. The changes of Fe:O ratio due to the changes in oxygen concentration caused by increasing reduction temperature are

observed. The results for all activated samples are presented in the Table 3.4.2. The samples reduced at 400 ^{o}C with Na promoter according to the PXRD experiment reveal the presence of the cubic magnetite Fe_3O_4 structure, theoretically of 43 at % of Fe and 57 at % of O ($Fe_{0.75}O$). The samples with the same promoter reduced at 450 ^{o}C according to the PXRD reveal the presence of the cubic crystal structure of metallic iron Fe^0. For the sample with Rb mixtures of Fe_3O_4 and Fe^0 after reduction at 400 and 450 ^{o}C were observed.

The quantitative XPS analysis for the samples with Na after reduction at 400 ^{o}C showed a lower Fe:O ratio (0.69) than the theoretical Fe:O ratio for Fe_3O_4. The Fe:O ratio for the samples with Rb reduced in the same temperature was 0.72, (the atomic percent of oxygen in a range 58.1 – 58.2). The XPS elemental analysis for the samples with Na reduced in 450 ^{o}C showed a slightly higher Fe:O ratio (0.72) and lower 58.1 atomic percent of oxygen which may be due to metallic iron occurring on the surface. The Fe:O ratio for the samples with Rb reduced in 450 ^{o}C was in the range between (0.67 – 0.70), which is between theoretical Fe_2O_3 and Fe_3O_4 (0.67 – 0.75). The XPS surface elemental analysis was compared to the XRF bulk analyses. The results for the activated samples with Na and Rb are presented in Table 3.4.2.

The Fe:O ratio measured by the XRF technique for the samples with Na promoter reduced in 400 ^{o}C is 0.67 and is lower than those of the samples reduced in a higher temperature 450 ^{o}C, Fe : O (0.70) . The samples with Rb reduced in 400 ^{o}C have the Fe:O ratio in the range 0.70 – 0.76 and for the samples reduced 450 ^{o}C was 0.76 - 0.84.

Tab. 3.4.2 The EDX, XPS, XRF elemental analysis Fe and O in iron oxide samples synthesized in different conditions with Rb and Na promoter after reduction in 400 ^{o}C and 450 ^{o}C

Conditions before reduction	**Atomic % of Fe, XRF**		**Fe : O ratio**	**Atomic % of Fe, XPS**		**Fe : O Ratio**
Sample/Element analysed	**Fe**	O	Fe_nO	**Fe**	O	Fe_nO
Fe_3O_4	**43.0**[1]	57.0	0.75	**41.9**	59.1	0.71
pH7, fast, RT, Na, 400 ^{o}C	**40.1**[2]	59.4	0.67	**41.0**[3]	59.0	0.69
pH, fast, RT, Na, 450 ^{o}C	**41.0**	58.2	0.70	**41.9**	58.1	0.72
pH7, fast, RT, Rb, 400 ^{o}C	**43.4**	56.9	0.76	**41.9**	58.1	0.72
pH7, slow, RT, Rb, 400 ^{o}C	**42.4**	57.8	0.73	**41.8**	58.2	0.72
pH7, fast, 60 ^{o}C, Rb, 400 ^{o}C	**42.1**	56.8	0.74	**41.9**	58.1	0.72
pH7, fast, RT, Rb, 450 ^{o}C	**45.2**	55.4	0.81	**40.2**	59.8	0.67
pH7, slow, RT, Rb, 450 ^{o}C	**43.2**	57.0	0.76	**40.3**	59.7	0.68
pH7, fast, 60 ^{o}C, Rb, 450 ^{o}C	**45.6**	54.3	0.84	**41.2**	58.8	0.7

1. **at% theoretical**: Fe = 40 %, O = 60 %; $Fe_2O_3 = Fe_{\mathbf{0.67}}O$
2. **at% theoretical**: Fe = 43 %, O = 57 %; $Fe_3O_4 = Fe_{\mathbf{0.75}}O$
3. **at% theoretical**: Fe = 50 %, O = 50 %; FeO = $Fe_{\mathbf{1.0}}O$
4. **XRF Standard deviation (SD) for Fe and O:** (0.05- 0.5);
5. **XPS Standard deviation (SD):** Fe(1.2-1.5); O(0.9-1.0)

3.5 Surface determination by nitrogen adsorption measurement

Nitrogen adsorption-desorption isotherms of all the samples synthesised with different promoters in various conditions are Type IV, Figure 3.5.1 according to the IUPAC definition[32,33]. Characteristic features of the Type IV isotherm are its hysteresis loop, which is associated with capillary condensation taking place in mesopores, and the limiting uptake over a range of high p/p° . The beginning of the isotherm is recognized as a monolayer-multilayer adsorption. The linear section of the branch after inflection point is observed. The inflection point called the "B" point[32] is attributed to the stage at which monolayer coverage is finished and multilayer adsorption is beginning.

The majority of the isotherms had similar nearly vertical steep adsorption and desorption branches, and belong to the H1 type[34,35]. Type H1 is often associated with porous materials known, from other evidence, to consist of compact agglomerates of approximately uniform spheres in a fairly regular array, and hence to have narrow distributions of pore size[,36].

The pore size distribution (PSD) was measured using the adsorption branch. The adsorption branch, as opposed to the desorption branch, is hardly affected by any tensile strength effect (TSE) phenomenon. Moreover, applying adsorption branches allows avoiding the influence of pore network effect.

3.5.1 Surface determination by nitrogen adsorption measurement; comparison of the properties of FTS catalysts with Na promoter

The samples with Na promoter synthesised in various conditions have the characteristics of a Type IV hysteresis loop. The shape of the hysteresis, nearly-parallel vertical adsorption and desorption branches of the sample synthesised in pH 7, fast titrant addition, RT, was typical for the H1 type.

The samples synthesised in pH 7, impregnated, fast titrant addition, RT and with slow titrant addition had a hysteresis loop and limiting uptake over a range of high p/p^o characteristic also for the H1 type. The samples with Na promoter synthesised at 60 ºC have a slope with smaller gradient for the adsorption and desorption branches, and the beginning of hysteresis loop point is lower than in the samples described above.

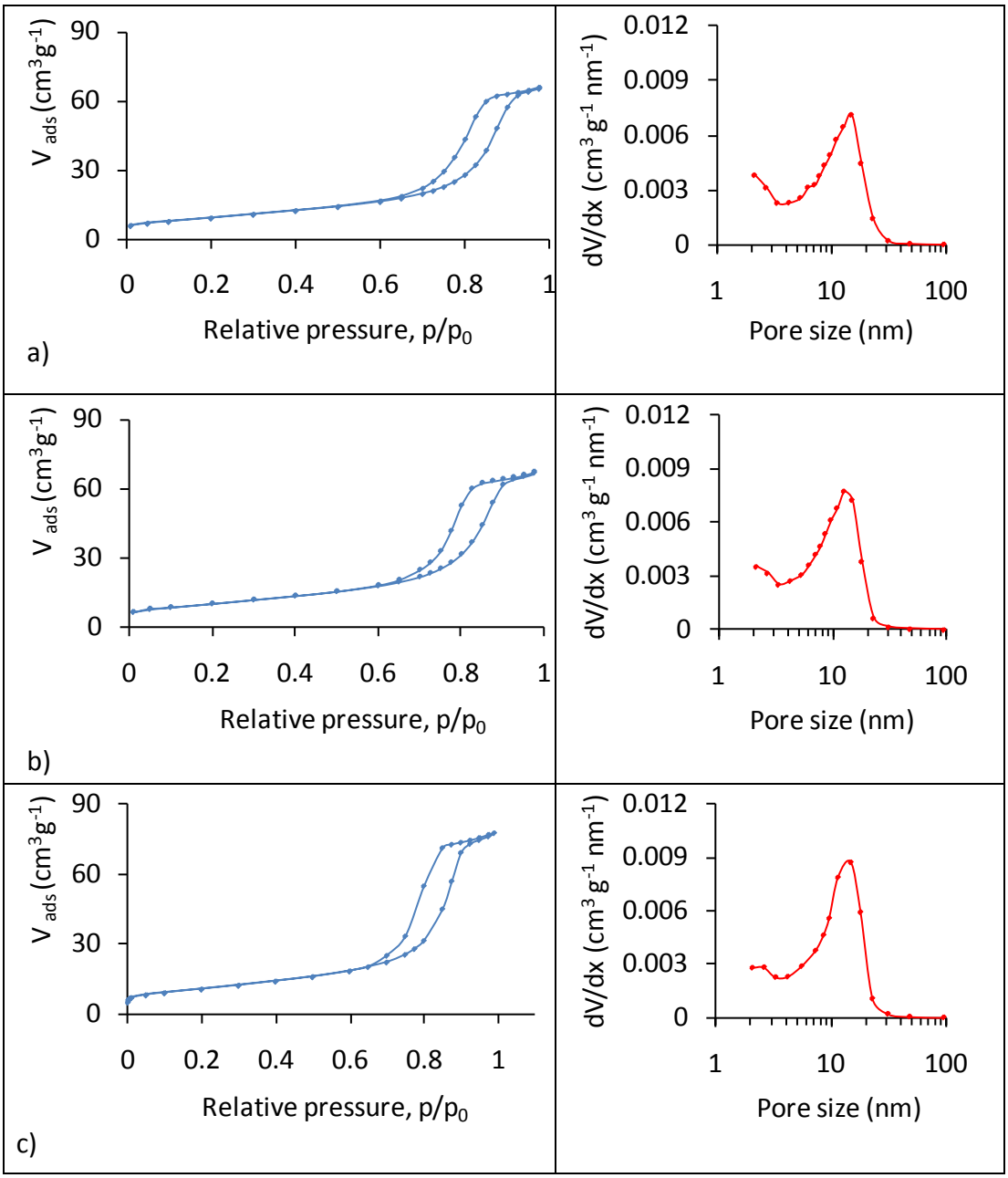

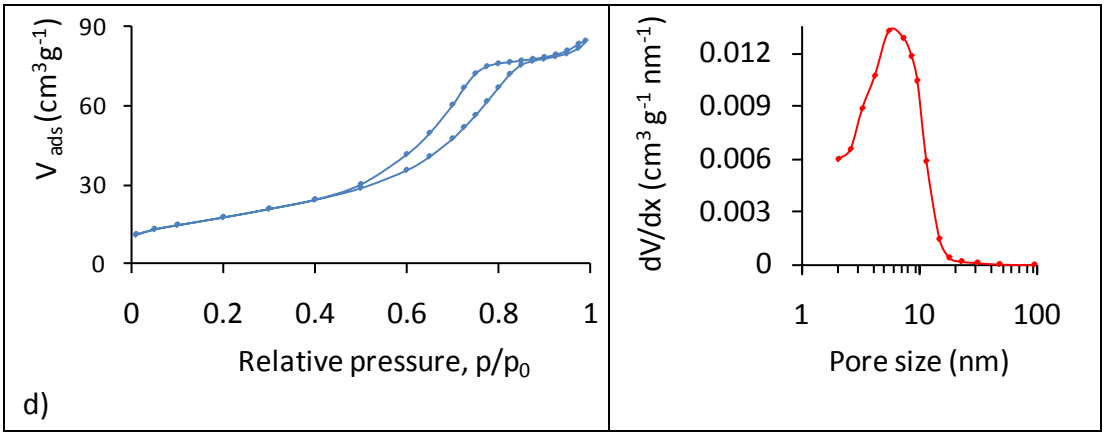

Fig. 3.5.1 Nitrogen adsorption and desorption isotherms (left), and corresponding PSD as derived from BJH model (right), for samples with Na promoter, from the top: a) synthesised at pH 7, co-precipitation, fast titrant addition, RT b) synthesised at pH 7, co-precipitation, slow titrant addition, RT c) synthesised at pH 7, impregnation, fast titrant addition, RT d) pH 7, co-precipitation, fast titrant addition, 60 ^{o}C

The samples synthesised in various conditions with Na promoter exhibited relatively narrow PSD values. Only the samples synthesised in pH 7, fast titrant addition at 60 ^{o}C have a slightly broader PSD peak, which may suggest a less homogenous surface.
The sample synthesised at 60 ºC has the smallest average PSD 5.6 nm. The PSD of the rest of the samples have values between 12.6 and 14.7 nm. It is the highest average PSD in comparison to the catalyst with K and Rb promoters shown below. Nitrogen adsorption and desorption isotherms and corresponding PSD are presented in a Figure 3.5.1.

The total pore volume (TPV) for the sample synthesised at 60 ºC is higher than for the rest of the samples (0.013 cm^2 g^{-1}). The TPV for the rest of the samples is between 0.009 and 0.011 cm^2 g^{-1}. All the values for pore volumes and pore size distribution are presented in Table 3.5.3.

The BET surface area was observed to be between 33 and 37 m^2 g^{-1} for the samples synthesised under different conditions with a Na promoter. The highest surface area was that of sample synthesised at 60 ºC and the lowest for sample synthesised with a slow titrant addition, and this is related with the crystallinity of these samples. Lower surface

area was related with higher crystallinity, as shown in the powder-XRD experiments. Surface area values are presented in Table 3.5.3.

3.5.2 Surface determination by nitrogen adsorption measurement: comparison of the properties of FT catalysts with K promoter

The hysteresis loop characteristic for type IV according to IUPAC definition for all the samples with K promoter was observed, Figure 3.5.2. The samples synthesised at pH7 and slow titrant addition rate had typical for H1 type with nearly-parallel vertical adsorption and desorption branches. The sample synthesised at pH 7, fast titrant addition in 60 ºC, pH7, fast titrant addition in RT, impregnated had a smaller gradient of adsorption branches and the lower adsorption at high p/p^o than the rest of the samples. These characteristics suggest that the sample belongs to the H2 . A distribution of various sized cavities but with the same entrance diameter would give this type of hysteresis loop. Differences between condensation (adsorption branch) and evaporation (desorption branch) are attributed to narrow neck and wide bodies, so called "inc-body shape", or more commonly the role of the network effects are considered[37].

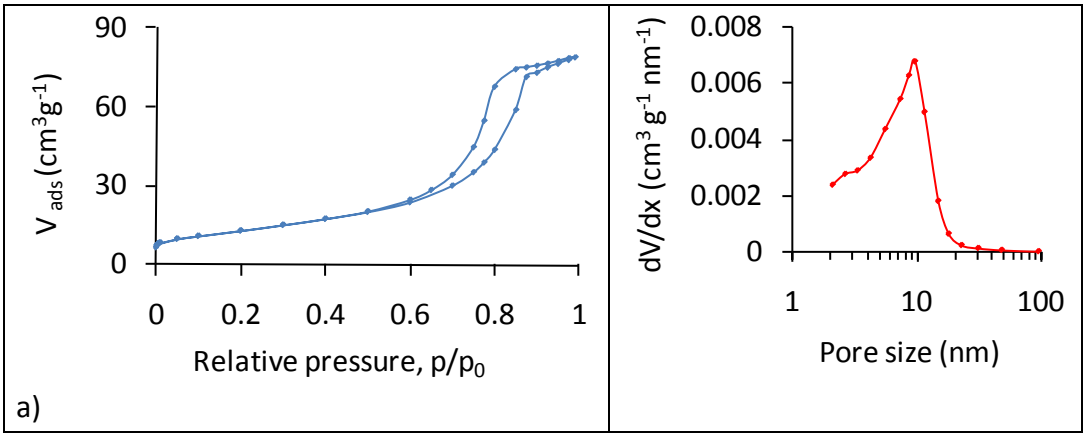

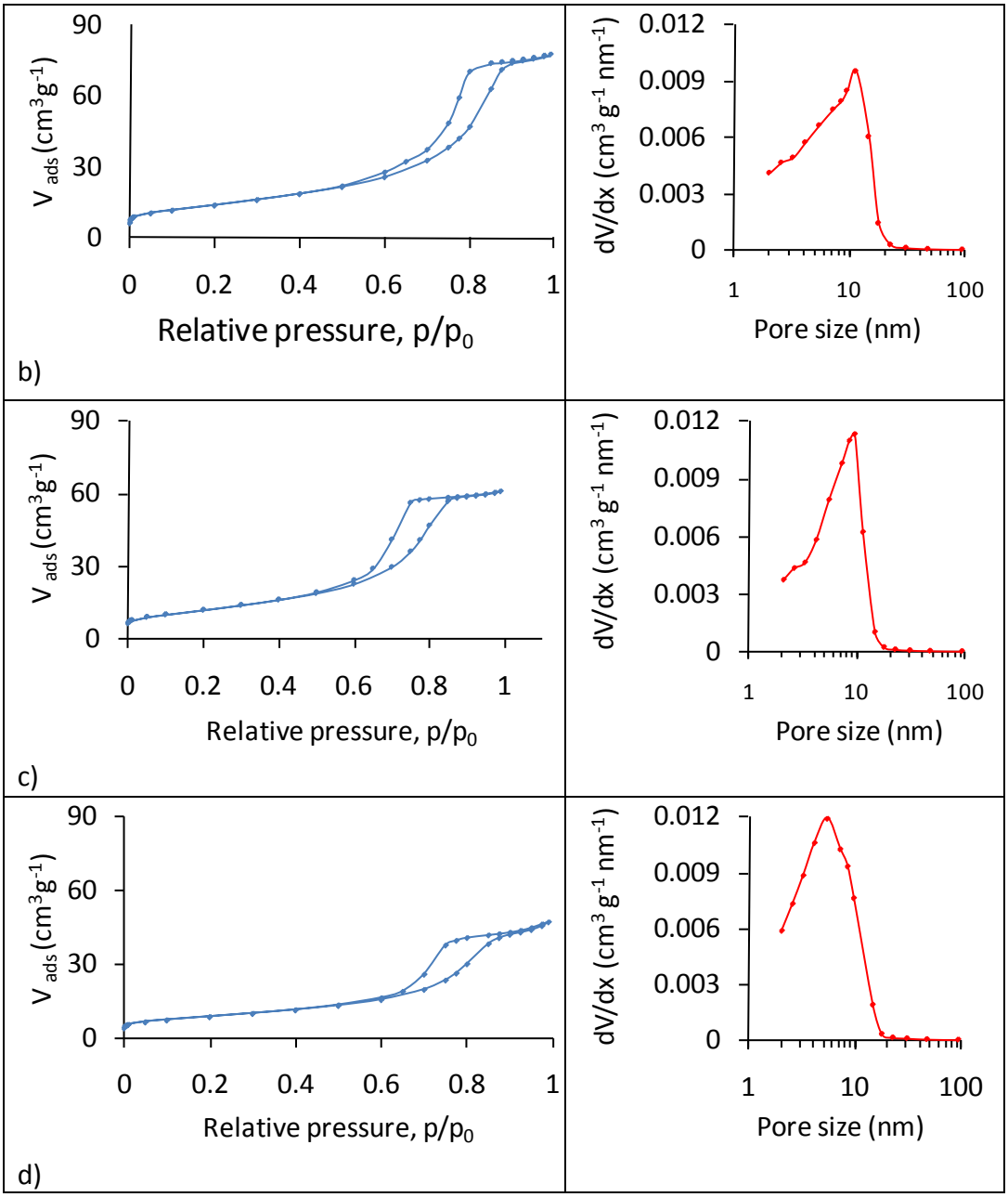

Fig. 3.5.2. Nitrogen adsorption and desorption isotherms (left), and corresponding PSD as derived from BJH model (right), for samples with K, from the top: a) synthesised at pH 7, co-precipitation, fast titrant addition, RT b) synthesised at pH 7, co-precipitation, slow titrant addition, RT c) synthesised at pH 7, impregnation, fast titrant addition, RT d) pH 7, co-precipitation, fast titrant addition, 60 ^{o}C.

All of the samples synthesised in various conditions with K promoter presented a narrow pore size distribution (PSD). The samples, except 60 ^{o}C, have a comparable average pore size between 9.7 and 11.3 nm. The sample synthesised at pH 7, fast titrant

addition in 60 ^{o}C, has a lower average pore size equal 5.6 nm. The adsorption and desorption isotherms and corresponding PSD for the samples with K are presented in a Figure 3.5.2.

The TPV for all the samples with K promoter was between 0.007 cm^3 g^{-1} for sample precipitated at pH 7, fast titrant addition in RT and 0.012 cm^3 g^{-1} for the sample synthesised at pH 7, fast titrant addition in 60 ^{o}C.

The BET surface areas for the samples with K are between 45 and 61 m^2g^{-1} and are higher by approximately 10 m^2g^{-1} than the samples with Na. The highest observed surface area was for the sample synthesised at pH7, fast titrant addition in room temperature. The values for surface area, pore volumes and pore size distribution are presented in Table 3.5.3.

3.5.3 Surface determination by nitrogen adsorption measurement; comparison of the properties of FT catalysts with Rb promoter

The samples synthesised under various conditions have characteristics like those of the last two promoters, Type IV hysteresis loop[32,33]. The shape of the hysteresis and the limiting uptake over a range of high p/p^o for the samples synthesised at pH 7, fast titrant addition in RT with Rb and pH 7, slow titrant addition in RT with the same promoter is typical for the H1 type. Some of the samples synthesised at pH 7, fast titrant addition in 60 ^{o}C and synthesised at pH 7, fast titrant addition in RT, impregnated with Rb, as it was observed in the samples with other promoters, have adsorption and desorption branches with a smaller gradient than the rest of the samples, Figure 3.5.3. The adsorption at high p/p^o was similar to the rest of the samples and hysteresis loop was not as wide as for the samples with H2 type as occurred in the catalyst with promoter previously described.

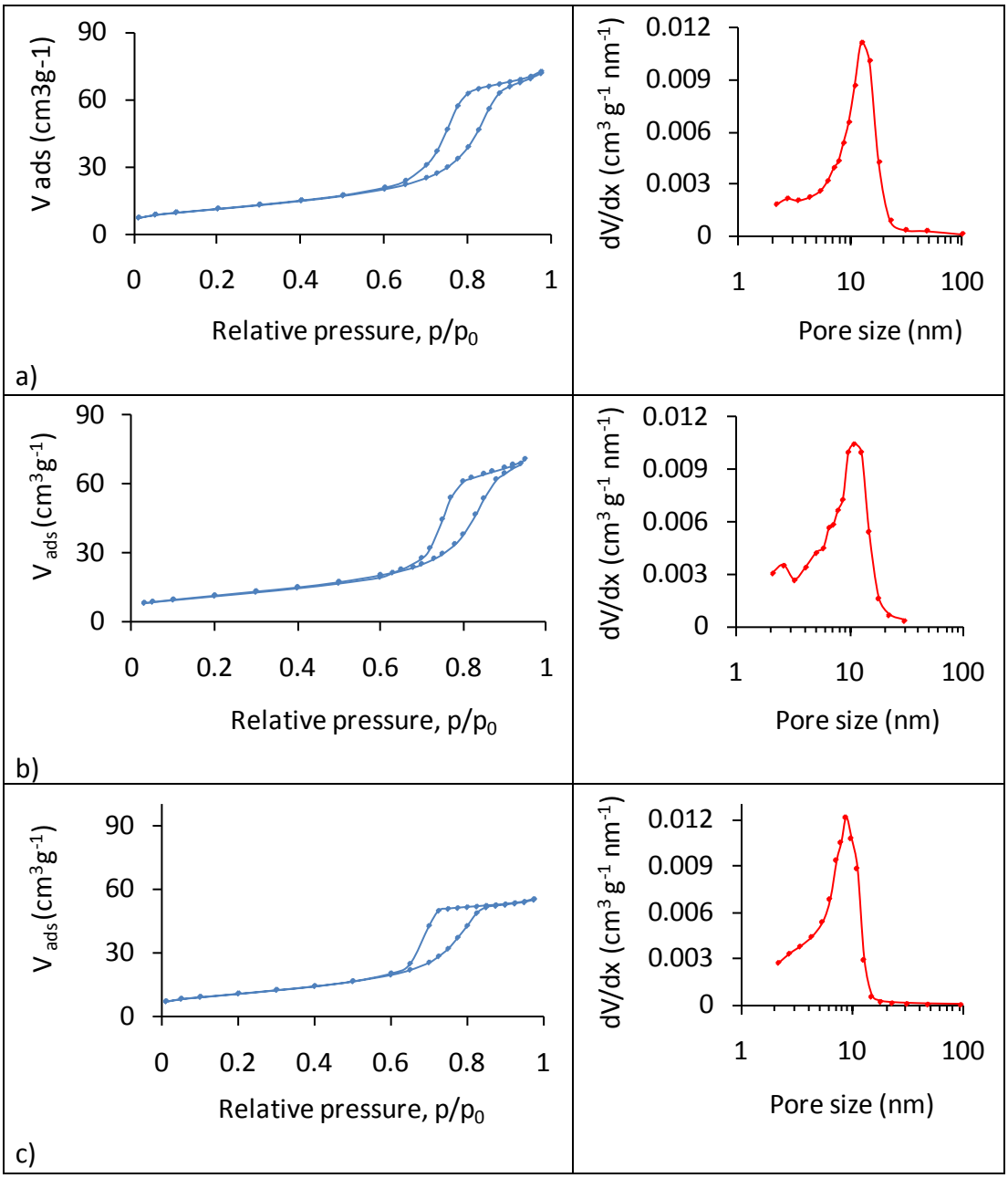
V ads (cm3g-1)
90
60
30
0
0
0.2
0.4
0.6
0.8
1
Relative pressure, p/p0
a)
dV/dx (cm3 g-1 nm-1)
0.012
0.009
0.006
0.003
0
1
10
100
Pore size (nm)
V ads (cm3g-1)
Relative pressure, p/p0
b)
Pore size (nm)
V ads (cm3g-1)
Relative pressure, p/p0
c)
Pore size (nm)

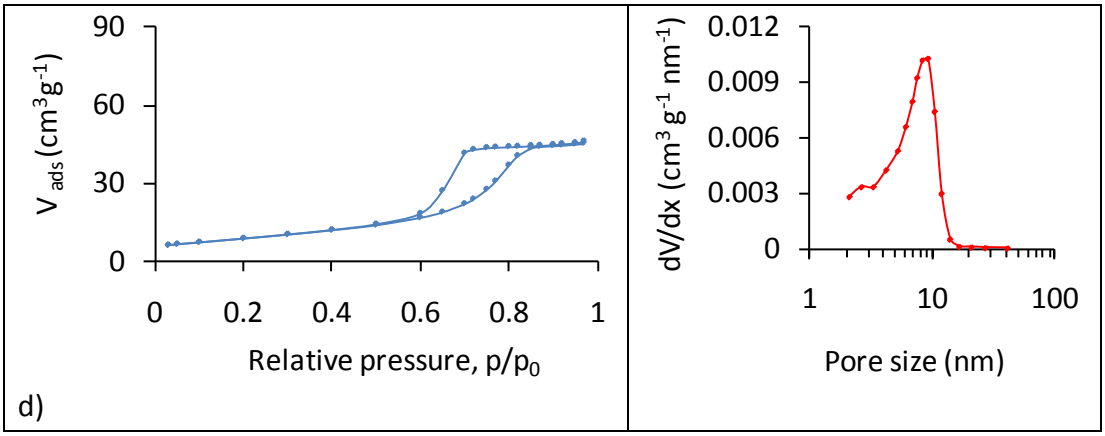

Fig. 3.5.3 Nitrogen adsorption and desorption isotherms (left), and corresponding PSD as derived from BJH model (right), for samples with Rb, from the top: a) synthesised at pH 7, co-precipitation, fast titrant addition, RT b) synthesised at pH 7, co-precipitation, slow titrant addition, RT c) pH 7, co-precipitation, fast titrant addition, 60 ^{o}C, d) synthesised at pH 7, impregnation, fast titrant addition, RT.

The PSD graphs for the samples with Rb exhibited narrow distributions, which may suggest that they have a uniform surface like the previous samples. The size of the pores may differ depending on synthesis conditions. The lowest average pore size 8.7 nm was for the sample synthesised at pH 7, impregnation, fast titrant addition in RT and the highest 12.5 nm for the sample synthesized at pH 7, fast titrant addition in RT, with Rb. Nitrogen adsorption and desorption isotherms and corresponding PSD for the samples with Rb promoter are presented in a Figure 3.5.3.

The TPV for the samples with Rb was fairly comparable for all the samples synthesised in various conditions. The values between 0.010 and 0.012 nm for the samples synthesised at 60 ^{o}C and slow titrant addition respectively. The BET surface area for the samples with Rb was observed to be between 37 m^2g^{-1} and 41 m^2g^{-1}. The sample synthesised at pH 7, fast titrant addition in RT, has the lowest surface area and sample synthesised at 60 ^{o}C the highest. The decrease of the surface area is related similarly like for the previously described samples with increase of the crystallinity, as XRD experiment proved. The PSD, TPV and the surface areas are presented in Table 3.5.1.

Tab. 3.5.3 Structural characteristics of the iron oxide catalyst samples

Sample name	Surface area (m^2 g^{-1})	Total pore volume (cm^2 g^{-1})	The pore size distribution (nm)
pH7, fast, RT, **Na**	36	0.007	14.7
pH7, slow, RT, **Na**	33	0.008	12.6
pH7, fast, RT, **Na**, impregnated	35	0.009	14.6
pH7, fast, 60 ^{o}C, **Na**	37	0.013	5.6
pH7, fast, RT, **K**	61	0.007	9.7
pH7, slow, RT, **K**	45	0.009	11.3
pH7, fast, RT, **K**, impregnated	48	0.011	9.7
pH7, fast, 60 ^{o}C, **K**	46	0.012	5.6
pH7, fast, RT, **Rb**	37	0.011	12.5
pH7, slow, RT, **Rb**	38	0.010	10.9
pH7, fast, RT, **Rb**, impregnated	38	0.012	8.7
pH7, fast, 60 ^{o}C, **Rb**	41	0.010	9.2

3.6 Discussion and Conclusions

The crystallinity and elemental composition of the product is influenced by the method in which the synthesis process is performed, the parameters and conditions applied. X-ray diffractograms of all samples before activation showed peaks that correspond to those of the haematite structure of iron oxide (α-Fe_2O_3). The samples of the iron oxide catalyst synthesised at pH 7, fast titrant addition in room temperature exhibit a more crystalline structure in comparison to the rest of the samples. The samples with slow titrant addition in comparison to those where titrant was added spontaneously have similar or slightly lower crystallinity. Lower crystallinity (smaller particle size and higher FWHM) was observed for impregnated samples than the co-precipitated ones for all the catalysts synthesised with three different promoters. The crystallinity of the samples precipitated at 60 ^{o}C in comparison to those reduced at room temperature was clearly lower. The significant decrease in particle size for those samples was observed.

In general, the highest crystallinity was observed for the samples synthesised at pH7, fast titrant addition rate, at room temperature. The trend in which the crystallinity decreased: after the most crystalline samples mentioned above were the samples synthesised with slow titrant addition rate, then those impregnated and at the end (the lowest) those synthesised at 60 ^{o}C. The exceptions were the samples synthesised with K, with slow titrant addition at room temperature, which exhibited slightly higher crystallinity than those where the titrant was added quickly. The crystallinity of the impregnated samples with Rb, was only slightly higher than those co-precipitated at 60 ^{o}C.

The crystallinity of the samples synthesised at pH7, fast titrant addition rate, at room temperature, after activation at different temperatures will be presented in Chapter 5. The iron oxide catalyst samples synthesized in various conditions with different promoters, before and after activation, were examined by XPS. The binding energies (BEs) of the mean core lines of the references with the non-activated iron oxide catalyst synthesized with Na, K and Rb promoters were compared. The BEs, shape of the

spectra and the distance between the Fe $2p_{3/2}$ peak and its satellite (~ 8eV) of all of the samples were the same as α-Fe_2O_3 reference and the literature sources.

The samples reduced at 400°C have a clearly broader Fe $2p_{3/2}$ peak. The typical width is a result of both Fe^{2+} and Fe^{3+} ions being fitted into the Fe $2p_{3/2}$ spectrum. The fitting done under the Fe $2p_{3/2}$ peak proves that the samples reduced at 400 ^oC, have the spinel Fe_3O_4 form of iron oxide. Additional proof for the Fe_3O_4 form of iron oxide is the absence of Fe $2p_{3/2}$ peak's satellite.

For the sample reduced at higher temperature (450 ^oC), the Fe $2p_{3/2}$ peak has similar properties to those reduced in 400 ^oC, however, the satellite which appears in the sample reduced at the more elevated temperature may suggest the occurrence of γ-Fe_2O_3 or α-FeOOH on the surface of the catalyst, but insufficient to be observable by PXRD[38]. Additionally, the splitting of the lower energy arm of the Fe $2p_{3/2}$ peak and clearly visible additional peak suggested the occurrence of Fe^o for the samples reduced at the higher temperature. The XPS characterization of O 1s spectra indicated that there can be small amounts of OH^- and H_2O species on the surface of the catalyst.

The Fe^{2+}/Fe^{3+} ratios calculated for Fe2p and 3p peaks for reduced at 400 ^oC samples were similar to the theoretical 0.5. The Fe^{2+}/Fe^{3+} ratios calculated for the activated at 450 ^oC samples was higher than these reduced in 400 ^oC. The elemental analysis of the iron and oxygen concentration using both bulk and surface sensitive techniques helped identify the stoichiometry of the non-reduced and reduced iron oxide samples. Both bulk and surface techniques confirmed results obtained before using P-XRD. The Fe:O ratio of Fe_2O_3 is close to the theoretical (0.67).

A higher amount of oxygen was discovered for some of the samples, which may be caused by the presence of H_2O and hydroxides. The difference in stoichiometry between

non-reduced samples synthesized with different promoters was not significant.

The quantitative XPS surface and XRF bulk analysis for activated samples revealed the occurrence of a mixture of oxides (400 ^oC) and iron oxides with metallic iron (450 ^oC), which was also confirmed by P-XRD results. The Fe:O ratio for all activated samples

was higher than the non-activated. The Fe:O ratio increased with rising reduction temperature for the samples with Na and Rb. A slight difference was observed in the stoichiometry of the samples with Na and Rb. The samples with Na promoter had a lower Fe:O ratio after reduction than those containing Rb.

The adsorption and desorption isotherms for all the iron oxide samples with different promoters exhibited type IV hysteresis loop that confirms the occurrence of mesopores in the pore structure of the catalyst. Most of the samples synthesised with different promoters belong to H1 type, which is a typical for closed packed agglomerates of homogeneous spheres, with narrow distributions of pore size.

The majority of the samples reveal narrow PSD, which indicates a homogenous character of the surface of the catalysts. The samples synthesized at 60 ºC have shown a slightly broader PSD, which may suggest a less homogenous surface. The TPV is higher for the samples synthesized at 60 ºC than the rest of the samples. The higher TPV and the lower PSD parameter for these samples may suggest increasing volume of the cavities with the same pore entrance. The surface area for those samples is a little higher in comparison to other samples which additionally may be a proof for the higher cavities volume. The TPV is increasing with PSD for the rest of the samples synthesized. That behaviour may suggest that the entrance diameter is proportionally bigger with the cavities sizes. The BET surface area for the same samples synthesized at 60 ºC is higher than the rest of the samples. The surface area of the samples synthesized at pH7 and slow titrant addition rate is relatively small between 33 and 45 m^2 g^{-1}. The samples synthesised at pH7, fast titrant addition at room temperature had the lowest surface area and highest crystallinity.

The determination of the structure type may be useful information for further catalysis stages in the Fischer-Tropsch process. The mesoporous iron oxide has higher catalytic activity than the micro and macroporous materials[39].

3.7. References

1. Khollam Y. B., Dhage S.R, Podtar H.S., Deshpande S.B., Bakare P.P., Kulkarni S.D., Date S.K., *Mater. Lett*., 56 (2002) 571.
2. Bromfield T., Coville N., *App. Surf. Sci.,* 119 (1997) 19.
3. Yang Y., Xiang H.-W., Xu Y.-Y., Bai L., Li Y.-W., *Appl. Catal. A: General* 266 (2004) 181.
2. Sadykov V.A., Isupova L.A, Tsybulya S.V., Cherepenova S.V., Litvak G.S., Burgina E.B., Kustova G.N., Lolomiichuk V.N., Ivanov V.P., Paukshtis E.A., Golovin A.V., Avvakumov E.G., *J. Solid State Chem.*, 123 (1996) 191.
5. Yu S.-C., Lee J.-S., Tung S.-F., Lan C.-L., *J. Geol. Soc., China*, 42 (1999) 349.
6. Baron V.; Gutzmer J.; Rundloef H.; Tellgren R.; *Solid State Sci.,* 7 (2005) 753.
7. Kelm K., Mader W., *Z. Anorg. Allg. Chem.,* 631 (2005) 2383.
8. Rozenberg G.Kh., Dubrovinskii L.S., Pasternak M.P., Naaman O., Le Bihan T., Ahuja R., *J. Phys. Condens. Matter.,* 65 (2002) 064112.
9. Cheetham, A.K., Day, P., *Solid State Chemistry Techniques*, Oxford University Press, Oxford, 1987
10. Langevoort J.C., Sutherland I., Hanekamp L.J., Gellings P.J., *Appl. Surf. Sci.*, 28 (1987) 167.
11. Tan B.J., Klabunde K.J., Sherwood P.M., *Chem. Mater.,* 2 (1990) 186.
12. Hawn D.D., DeKoven B.M., *Surf. Interf. Anal*., 10 (1987) 63.
13. Moulder J.F., Stickle W.F, Sobol P.E., Bomben K.D., *Handbook of X-ray Photoelectron Spectroscopy,* published by Perkin-Elmer Corp., 1992, MN, USA
14. McIntyre N.S., Zetaruk D.G., *Anal. Chem.,* 49 (1977) 1521.
15. Paparazzo E., *J. Phys. D*., 20 (1987) 1091.
16. Konno H., Nagayama M., *J. Electron Spectrosc. Relat. Phenom.* 18,(1980) 341.
17. Brion D., *Appl. Surf. Sci.,* 5 (1980) 133.
18. Mills P., Sullivan J.L., *J. Phys. D*., 16 (1983) 723.
19. Yamashita T., Hayes P., *Appl. Surf. Sci*., 1 (2007) 1.
20. Grosvenor A. P., Kobe B. A., Biesinger M. C., McIntyre N. S., *Surf. Interf. Anal.,* 36 (2004) 1564.
21. Muhler M., Schlogl R., Ertl G., *J. Catal.,* 138 (1992) 413.

22. Feng Jiao F., Jumas J.-C., Womes M., Chadwick A.V., Harrison A., Bruce P.G., *J. Am. Chem. Soc.,* 128 (2006) 1290.
23. Aronniemi M., Sainio J., Lahtinen J.*, Surf. Sci*., 578 (2005) 108.
24. Gupta R.P., Sen S.K.,*Phys. Rev. B.,* 10 (1974) 71.
25. Gupta R.P., Sen S.K.,*Phys. Rev. B.,* 12 (1975) 15.
26. Yamashita T., Hayes P., *J. Electron Spectrosc.,* 152 (2006) 6.
27. www.casaxps.com, 2011.
28. Shchukarev A.V., Korolkov D.V., *Cent. Eur. J. Chem.,* 2 (2004) 347.
29. Pirlot C., Delhalle J., Pireaux J.J., Mekhalif Z., *Surf. Coat. Tech.,* 138 (2001) 166.
30. Mohlala P.J., Strydom C.A*., Int. J. Adhes. Adhes.*, 29 (2009) 240.
31. Mullet M., Khare V., Ruby C*., Surf. Interface Anal*., 40 (2008) 323.
32. Sing K.S., Everett D.H., Haul R.A., Moscou L., Pierotti R.A., Rouquerol J., Siemieniewska T., *Pure Appl. Chem*., 57 (1985) 603.
33. Rouquero J., Avinr D., Fairbridge C. W., Everett D.H., Haynes J. H., Pernicone N., Ramsay J. D., Sing K.S. and Unger K. K., *Pure Appl. Chem*., 66 (1994) 1739.
34. Yuan Z. –Y., Ren T.-Z., Su B.-L., *Catal. Today,* 93–95 (2004) 743.
35. Liu Z., Fan T., Zhang W., Zhang D., *Micropor. Mesopor. Mater.,* 85 (2005) 82.
36. Groen J.C., Peffer L.A., Perez-Ramırez J., *Micropor. Mesopor. Mater*., 60 (2003) 1.
37. Groen J.C., Pérez-Ramirez J., *Appl. Catal*., A 268 (2004) 121.
38. Xiang B., Xu H., Li W.,*Chin. J. Catal.*, 28 (2007) 841.
39. Liu Q., Cui Z. M., Ma Z., Bian S. W., Song W. G., *Nanotechnology*, 18 (2007) 385605.

Chapter 4

The promoter action of alkali metals in Fischer-Tropsch synthesis

4.1 Introduction

The most important promoters for the chemical industry as well as in Fischer-Tropsch synthesis (FTS) are alkalis. Alkali promoters have a very significant role because of their chemical and physical properties. Application of the alkali metals in iron oxide catalysts leads to activity enhancement due to their electrostatic field. The role of alkalis in general, as presented in the introduction, is to increase the catalytic activity for FTS and WGS reactions, enhance the CO dissociation, reduce methane selectivity and shift the selectivity to higher hydrocarbons[1- 9.]

The alkali metals most commonly used for iron oxide catalyst in FTS are Na and K. In spite of the recognized importance of the alkali promoter, data to document their relative influence are not abundant. The objective of this study was to obtain information about Na, K and Rb promoters. The observation of chemical differences in the iron oxide catalyst samples influenced by different conditions and synthesis methods was also an aspect of study.

Reduction of iron oxide under hydrogen results in the evolution of different iron species. It also influences the alkali metals speciation and migration abilities (both in the bulk and on the surface). It was also mentioned in the introduction that alkali promoters have significant influence on the activation process, especially the reduction temperature of the FT catalysts. Potassium for examples is well known as a promoter which facilitate the reduction of iron oxide to metallic iron during hydrogen activation[1,2,7- 13].

Altogether, the synthesis conditions, methods of preparation of the iron oxide catalyst, the type of alkali metal used may have a significant influence on the iron catalyst surface species.

4.2 Powder X-Ray diffraction (P-XRD) for iron oxides samples with alkali promoters

The powder X-Ray diffraction (P-XRD) method was used to determine the crystallinity of the samples and the structure of iron oxide catalysts containing low concentrations of alkali metals and sulfur. It was reported that, the peak intensities of α-Fe_2O_3 in non-activated catalyst with alkali promoters are larger than that of the unpromoted catalyst. This implies that alkali addition promotes the aggregation or increase of domain size of α-Fe_2O_3 crystallites.

Alkali promoters are believed to act a significant role during the reduction process. It was reported[1,6,7,10,14-16] that the K promoter in the iron catalysts used for the Fischer-Tropsch reaction facilitates the reduction of iron oxide to metallic iron during hydrogen activations. In these experiments the behaviour of the catalyst during activation under hydrogen with two other alkali promoters (Na and Rb) is studied. Diffractograms for three different promoters and their influence on the reduction temperature will be compared.

4.2.1 Powder X-Ray diffraction (P-XRD) for iron oxides samples prepared in different conditions with a Na promoter before and after activation

The catalyst synthesized at pH 7, room temperature, by the co-precipitation method and a titration rate 8 ml min^{-1} was examined. Diffractograms were measured before and after activation. The reduction was carried out under H_2/He for 20 h at different temperatures (100 °C, 300 °C, 350 °C, 400 °C, and 450 °C). Prior to reduction the structure of the sample was that of rhombohedral haematite (α-Fe_2O_3), which has characteristic peaks at 2θ values of: 24.2 °, 33.15 °, 35.6 °, 40.8 °, 49.52 °, 54.0 °, 57.6 °, 62.5 ° and 64°[17-21]. Each peak corresponds to a different set of Miller indices, presented respectively: 012, 104, 110, 113, 024, 116, 018, 214, 300[17,18]. The reflections in samples reduced at 100 ^oC, Figure 4.2.1, correspond also to those of the rhombohedral haematite α-Fe_2O_3 structure of iron oxide. After reduction at 300 °C for 20 h, the structure changed to that

of cubic magnetite (Fe_3O_4) [22,23], see Figure 4.2.1. The characteristic peaks for Fe_3O_4 were observed at 2θ = 30.4 °, 35.8 °, 43.4 °, 53.5 °, 57.3 °, 62.9 °, 89.9 ° and respectively Miller indices: 220, 311, 400, 422, 511, 440, 731 [24-27]. After reduction at 350 °C, peaks corresponded to the literature values for Fe_3O_4. Reduction at 400 °C also resulted in a cubic magnetite structure. The peaks at 2θ = 30.4 °, 35.8 °, 43.4 °, 53.5 °, 57.3 °, 62.0 ° had a higher intensity than those of samples treated at 300 °C and 350 °C which may be explained by the development of more crystalline cubic magnetite at higher temperature. The appearance of distinct peaks at 2θ = 37.4 °, 74.3 °, 75.2 °, 87.0 ° and the Miller indices 222, 533, 622, 642, further confirmed the presence of the cubic magnetite structure of Fe_3O_4 of the analysed catalyst. After reduction at 450°C, the iron in the sample changed oxidation state from $Fe^{2+/3+}$ to Fe^0. Well resolved peaks of high intensity were registered at 2θ = 45.1 °, 65.4 °, 82.7 ° and characteristic Miller indices: 110, 220, 211, 220, which correspond to the body centred cubic crystal structure of metallic iron[28-31]. However, a mixture of Fe_3O_4 and Fe^0 on the surface of the samples with Na and Rb promoters reduced at 450 °C, was observed using the XPS technique (Chapter 3.3.8.2).

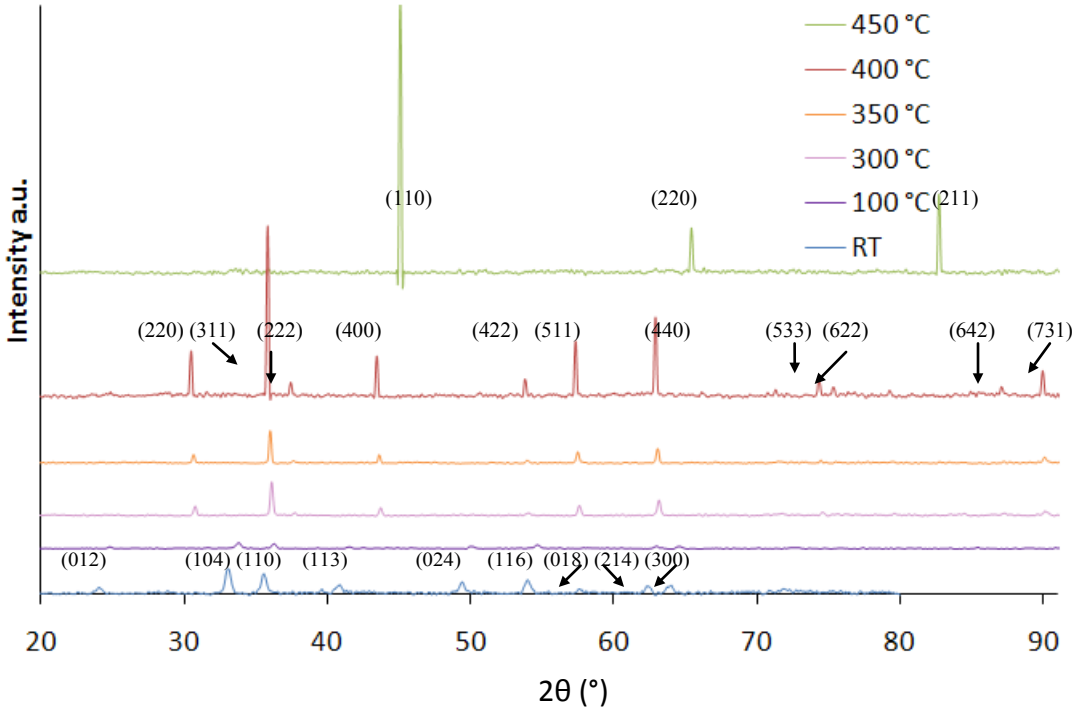

Fig.4.2.1 The PXRD of the samples prepared at room temperature, pH 7, co-precipitation, Na promoter. The samples were calcined at 350 °C and reduced at different temperatures for 20h. Reduction temperatures from the top: 450 °C, 400 °C, 350 °C, 300 °C, 100 °C, non-reduced.

4.2.2 Powder X-Ray diffraction (P-XRD) for iron oxides samples prepared in different conditions with K promoter before and after activation

After examination of the iron catalyst samples with Na promoter, the samples with K promoter were also studied. The iron catalysts synthesized in the same conditions as the samples with Na (pH 7, room temperature, by the co-precipitation method and at titration rate 8 ml min^{-1}) were examined.

The reduction was carried out under 5% H_2/He for 20 h at different temperatures (400 °C, 450 °C, and 500 °C). Prior to reduction the structure of the sample was that of rhombohedral iron (III) oxide (α-Fe_2O_3)[17-21]. After reduction at 400 ^oC, peaks corresponding to the literature values for Fe_3O_4[24-27] were observed and, unlike the case for catalyst with Na at the temperature, a characteristic peak for metallic iron was also visible. The reflections in samples reduced at 450 ^oC for 20 hours, correspond to iron (II, III) oxide (Fe_3O_4), and metallic iron (Fe^0). The intensity of the Fe_3O_4 peak is much weaker than at 400 °C. Lower intensity peaks characteristic for Fe_3O_4 were observed at 2θ = 35.8^o, 63.0^o. Well resolved peaks of high intensity at 2θ = 45.1^o, 65.3^o, 82.7^o, 99.3^o and Miller indices were registered, which correspond to cubic Fe^0 [28-31]. After reduction at 500°C, the iron in the sample changed oxidation state from $Fe^{2+/3+}$ to Fe^0 Figure 4.2.2.1.

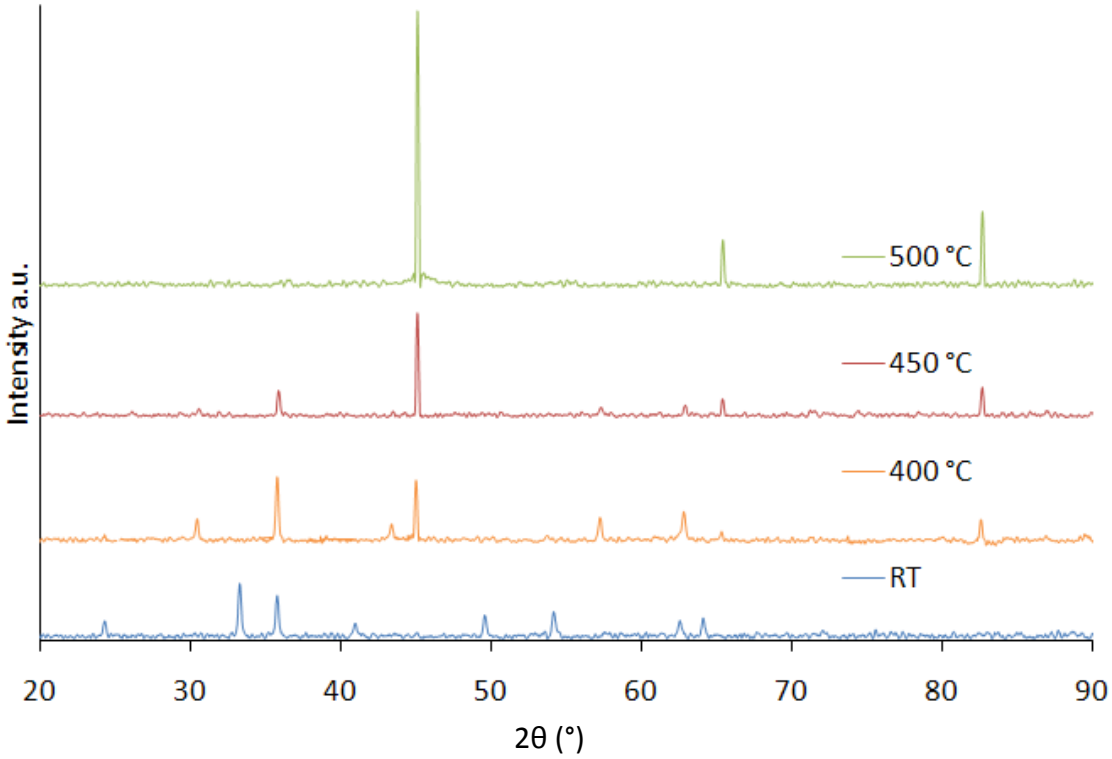

Fig.4.2.2.1 The PXRD of the samples prepared at room temperature, pH 7, fast titrant addition, K promoter. The samples were reduced at different temperatures for 20 h. Reduction temperatures from the top: 500 ^{o}C, 450 ^{o}C, 400 ^{o}C, non-reduced.

Additionally further reduction at elevated temperatures (600 °C, 700 °C, and 800 °C) under 5% H_2/He for 1h was carried out. For the sample reduced at 600 °C for 1 h, the characteristic peaks for cubic Fe_3O_4 were observed at 2θ = 30.8^{o}, 35.8^{o}, 43.5^{o}, 63.0^{o}. The peaks at 2θ = 36.3^{o}, 42.1^{o}, 61.0^{o}, 72.8^{o}, 76.7 ^{o} and Miller indices 111, 200, 220, 331, 222, characteristic for cubic FeO and/or $Fe_{0.925}O$ or $Fe_{0.74}O$, were also noted[28,32,33] as well as low intensity peaks characteristic for Fe^0 at 2θ = 45.1^{o}, 65.4 ^{o}, 82.7^{o}, 99.3^{o}. This indicates the presence of a mixture of oxides and metallic iron. After reduction carried out at 700 ^{o}C for 1 h, the peaks corresponded to the literature values for FeO and Fe^0 [28-31]. Reduction at 800°C for 1 h resulted in a Fe^0 structure. The peaks at 2θ = 45.1^{o}, 65.4^{o}, 82.7^{o}, 99.3^{o} due to metallic Fe were sharper and had a higher intensity with the increase in temperature and were more visible for samples reduced at 800 ^{o}C for 1 h. The structures were the same as in the catalyst reduced at 500 ^{o}C for 20 h, however, the physical properties of the powders were different. The grains of powder reduced at higher temperatures attracted each other and formed aggregates. These powders were also attracted by a magnetic stirrer, their grains 'jumped' onto the stirrer

placed above the sample. The samples reduced in different temperatures for 1h in elevates temperatures with K promoter are shown on Figure 4.2.2.2.

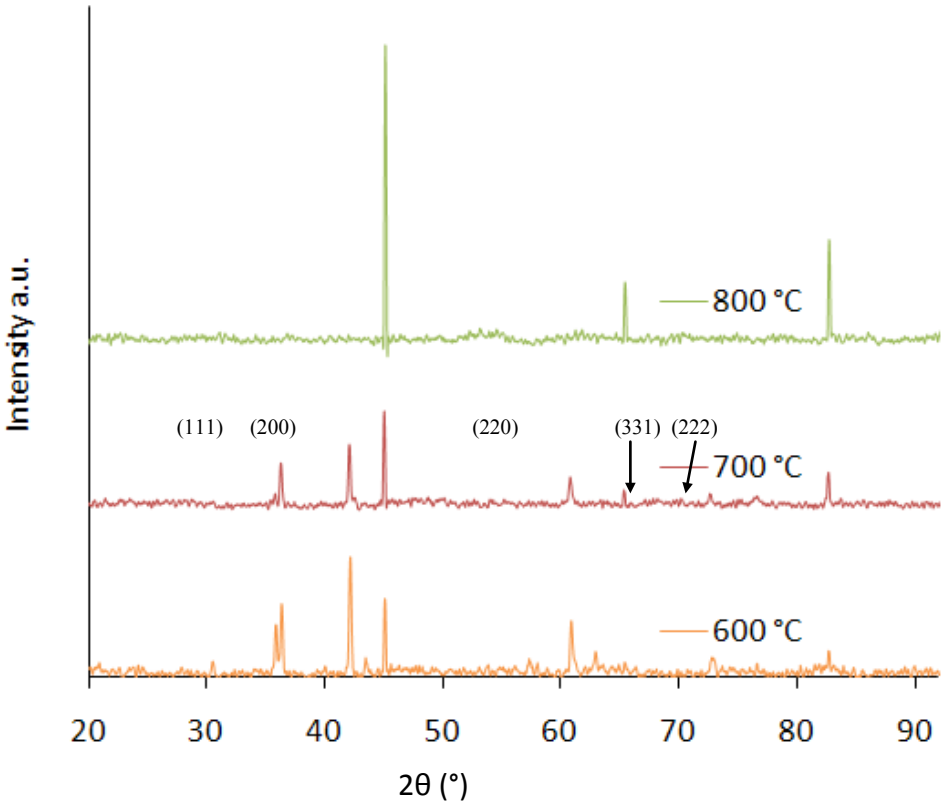

Fig.4.2.2.2 The PXRD of the samples prepared at room temperature, pH 7, fast titrant addition, K promoter. The samples were reduced at different temperatures for 1 h. Reduction temperatures from the top: 800 ^{o}C, 700 ^{o}C, 600 ^{o}C.

4.2.3 Powder X-Ray diffraction (P-XRD) for iron oxide samples prepared in different conditions with Rb promoter before and after activation

These iron catalysts with rubidium promoter were synthesized in the same conditions as the previous samples (pH 7, room temperature, titration rate 8 ml min^{-1}). The reduction was carried out under 5% H_2/He for 20 h at different temperatures (400 °C, 450 °C, and 500°C). The P-XRD carried out for non-reduced samples registered the structure of rhombohedral iron (III) oxide. After reduction at 400 ^{o}C, peaks corresponding to the literature values for Fe_3O_4[24-27] and characteristic for metallic iron were visible (similar

to the sample with K promoter). The reflections in samples reduced at 450 °C for 20 hours, correspond to iron (II, III) oxide, and metallic iron. The Fe_3O_4 peaks have lower intensity than the sample reduced at 400 °C and were observed at 2θ = 35.8°, 63.0°. After reduction at 500 °C, the reflections characteristic for iron (III, II) oxide nearly disappear and well resolved peaks of high intensity at 2θ = 45.1°, 65.3°, 82.7°, 99.3° characteristic for metallic iron[28-31] were observed Fig.4.2.3.

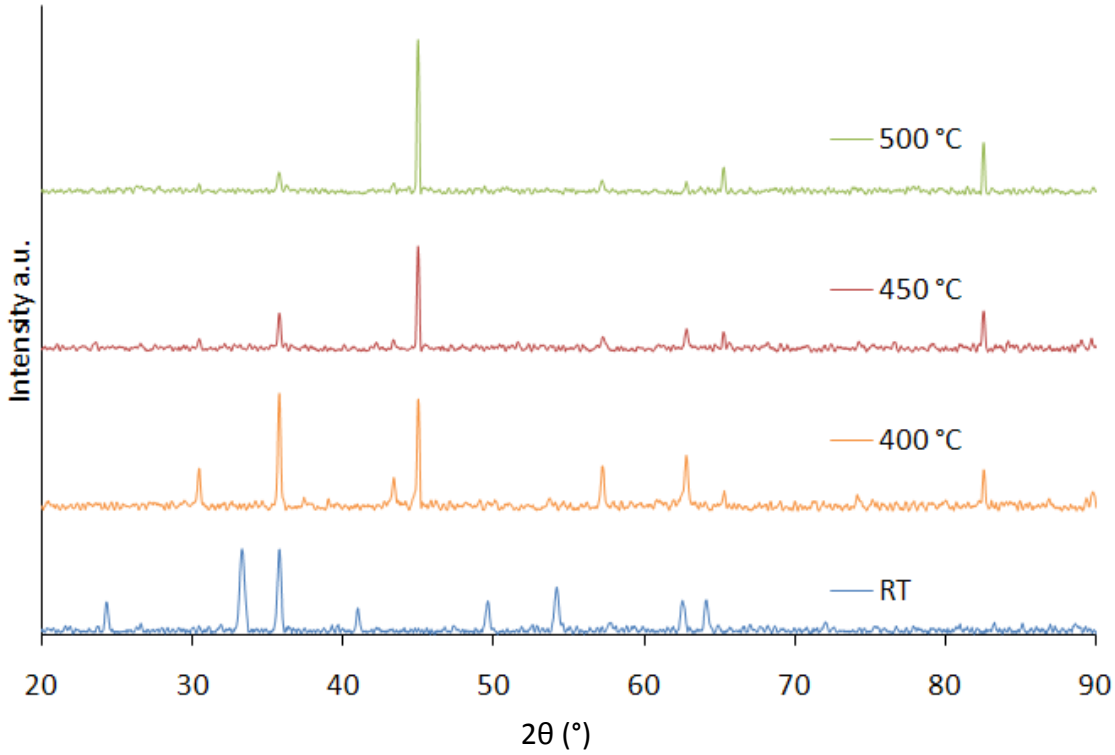

Fig.4.2.3 The PXRD of the samples prepared at room temperature, pH 7, fast titrant addition, Rb promoter, after reduction. Reduction temperatures from the top: 500 °C, 450 °C, 400 °C, non-reduced.

4.2.4 Influence of reduction temperature on iron species in FTS iron oxide catalysts with different alkali metals (Na, K, Rb)

The dependence of the oxidation state of iron on the reduction temperature for three different promoters is shown in Figure 4.2.4. It was observed in the literature[1,6,7,10,14-16] that a K promoter decreases the temperature required for reduction, i.e. facilitates the reduction of iron oxide. In this study the behaviour of the Na, K and Rb was compared. The iron oxide catalysts with Rb and K have similar behaviour during reduction. For both of them the phase transformation from Fe_3O_4 to Fe was at around 50 ^oC lower temperature than for the samples with Na promoter. For all the alkali cations which may occur with carbonates after calcination and reduction this behaviour can be connected with the decrease in the first ionisation potential (I_1) of alkali metal atoms and ionicity of the metal-carbonate bonds[34]. The dependence of the alkali metals used in experiment on the reduction temperature and theoretical binding energy (BE) of C_{1s}, and the dependence on first ionization potential of alkali metal carbonates and hydrocarbonates are presented in Figure 4.2.4 a, b respectively.

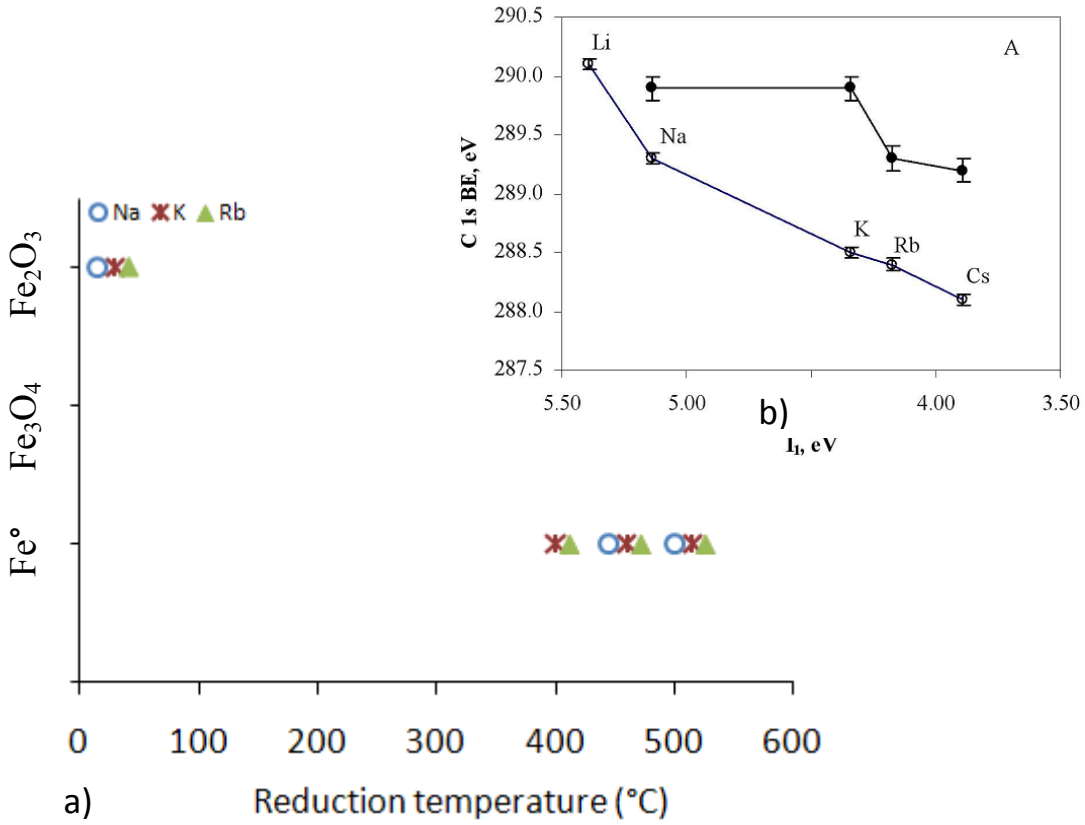

Fig.4.2.4 a) Influence of reduction temperature on iron species in FTS iron oxide catalysts with different alkali metal (Na, K, Rb) promoters used in the experiment. **b)** theoretical binding energy (BE) of C1s, and the dependence on first ionization potential of alkali metals ◦ –carbonates and • – hydrocarbonates.

4.3 SEM analysis of the iron oxide catalyst samples with the alkali promoters

The SEM technique was used to observe the influence of different alkalis and synthesis conditions on the surface morphology, the size of the particles and the shape of the observed agglomerates.

In Figures 4.3.1 - 4.3.3 SEM images of iron oxide catalyst with three different alkali promoters Na, K, Rb synthesised at pH 7, fast titrant addition at room temperature were compared. The catalyst with the Na promoter synthesised in the same conditions had two different kinds of surfaces. One kind of surface had irregularly shaped agglomerates with smaller round edged particles attached to their surface, (Figure 4.3.1) and the other contained more homogenous agglomerates with sharp edges (Figure 4.3.1 b). The majority of the irregularly shaped agglomerates were observed in general for the samples with Na. For the samples with the K and Rb promoters, two different shapes were also observed (Fig. 4.3.2 a, b and Fig. 4.3.3 a, b). The agglomerates for the samples with K were in general bigger than those with the Rb and Na promoters. The samples with a Rb promoter seemed more homogenous: the surface was flat and had a more faceted morphology. However, the small particles were also attached to the agglomerates' surface, Figure 4.3.3 a.

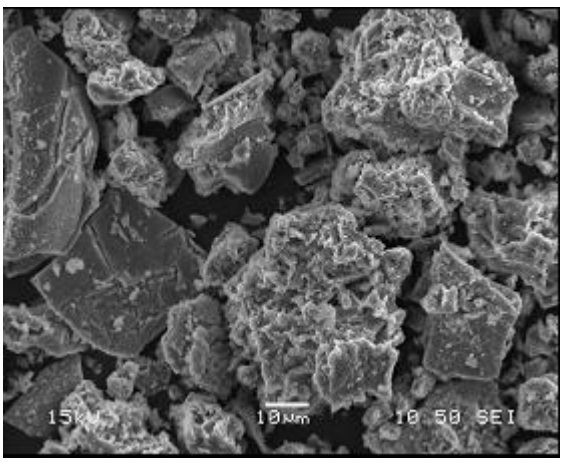

a)

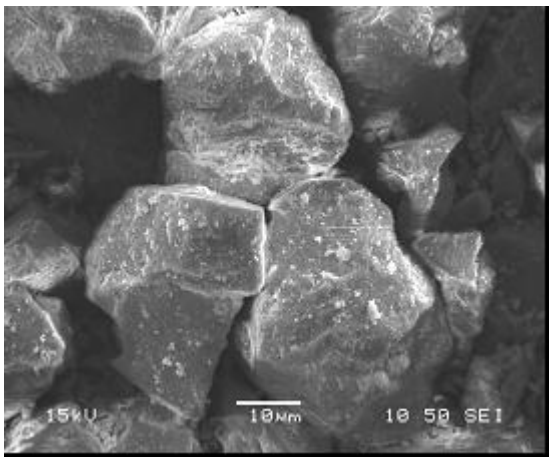

b)

Fig.4.3.1 The SEM images at magnification 1000, 15 kV, of the catalyst with the Na promoter synthesised at pH 7, fast titrant addition, room temperature **a)** Irregularly shaped aggregates with smaller round edged particles attached to the surface **b)** more homogenous surfaces with sharp edges.

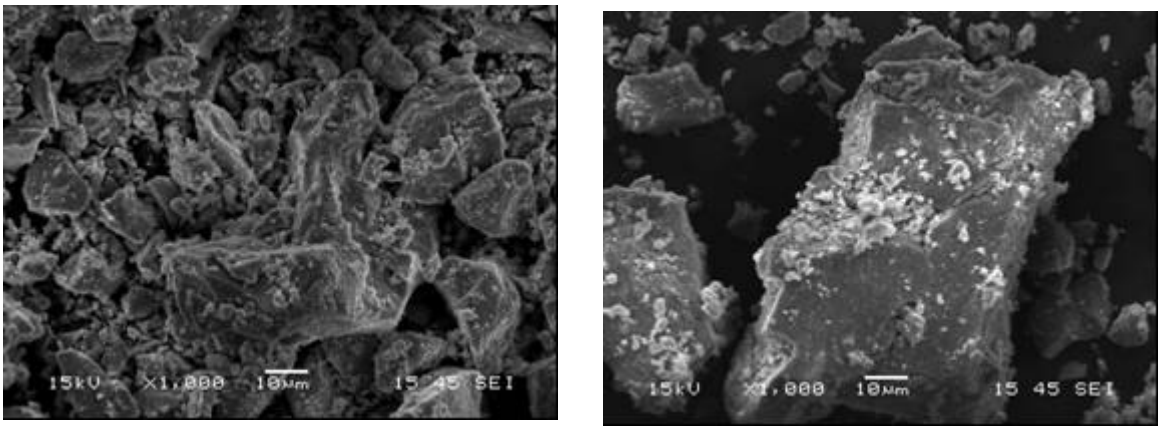

a) b)

Fig.4.3.2. The catalyst with the K promoter synthesised at pH 7, fast titrant addition at room temperature **a)** Irregularly shaped aggregates with smaller round edged particles attached to the surface **b)** homogenous surfaces of the same catalyst (The SEM images at magnification 1000, 15 kV)

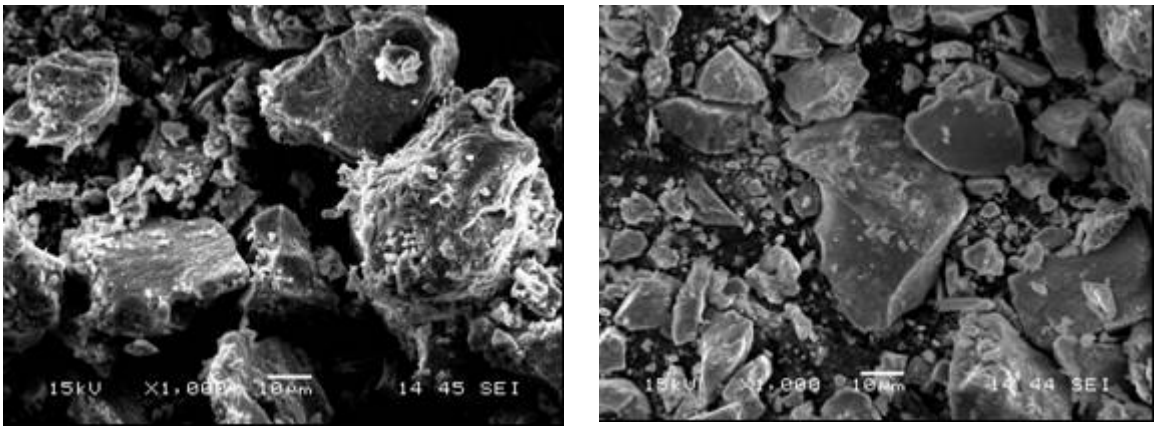

a) b)

Fig.4.3.3 The SEM images at magnification 1000 (15 kV) of the catalyst with the Rb promoter synthesised at pH 7, fast titrant addition, room temperature **a)** Irregularly aggregates with smaller particles attached to the surface **b)** homogenous surfaces with sharp edges.

Differences in the morphology of the samples at higher magnification were also observed. At higher magnification it was possible to distinguish different features of samples with different promoters more clearly. Similarities for all the samples at magnification 10,000 and 15 kV were found. Small particles or smaller agglomerates on the surface of the large particles were observed for all the samples. Two of the examples for iron oxide catalyst samples with Na and Rb promoters are shown in Figures 4.3.4 a, b.

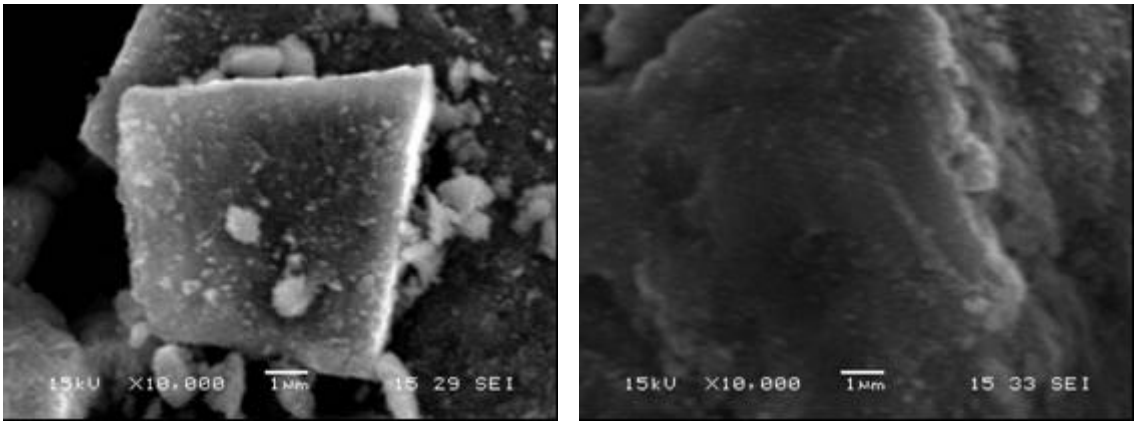

a) b)

Fig 4.3.4 The SEM images for the iron oxide catalyst samples with **a)** Na and **b)** Rb promoters synthesised at pH 7, fast titrant addition, room temperature, compared at magnification 10,000 and 15 kV.

The use of SEM exposed the differences in morphology, particle and agglomerate size in catalysts synthesized in different conditions. The smallest single agglomerates attached to the surface of the bigger agglomerates were observed for the catalyst synthesised with the K promoter at 60 ºC. For comparison, the sample synthesised at 60 ^{o}C is presented together with the sample prepared at room temperature in Figures 4.3.5 a and b respectively.

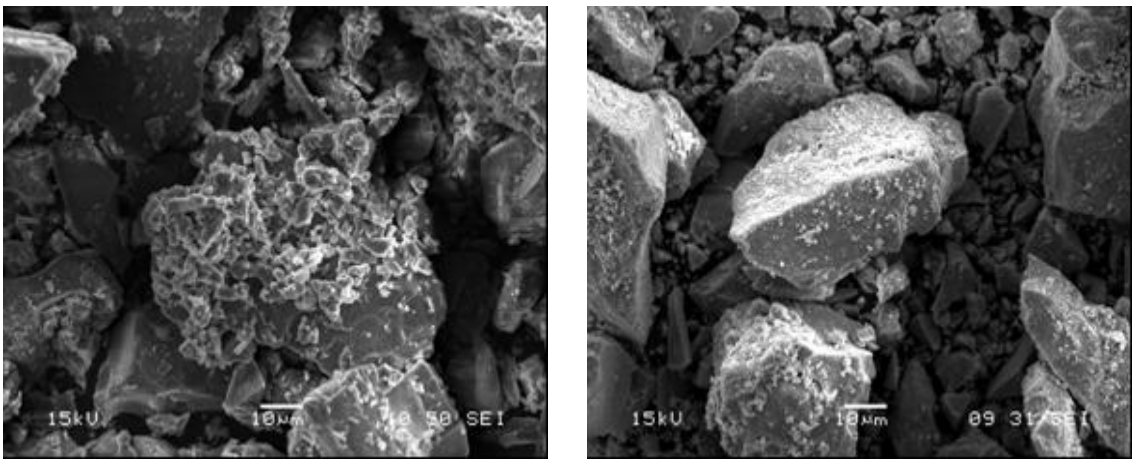

a) b)

Fig.4.3.5 The SEM at magnification 1000, 15 kV for the catalyst samples with K promoter synthesised at pH 7, fast titrant addition, room temperature were compared **a)** precipitated at 60 ºC, **b)** precipitated at room temperature

Single agglomerates under magnification 10,000 on the surface for all of the agglomerates for the samples synthesized different conditions with the K promoter were observed (Figure 4.3.6 a, b).

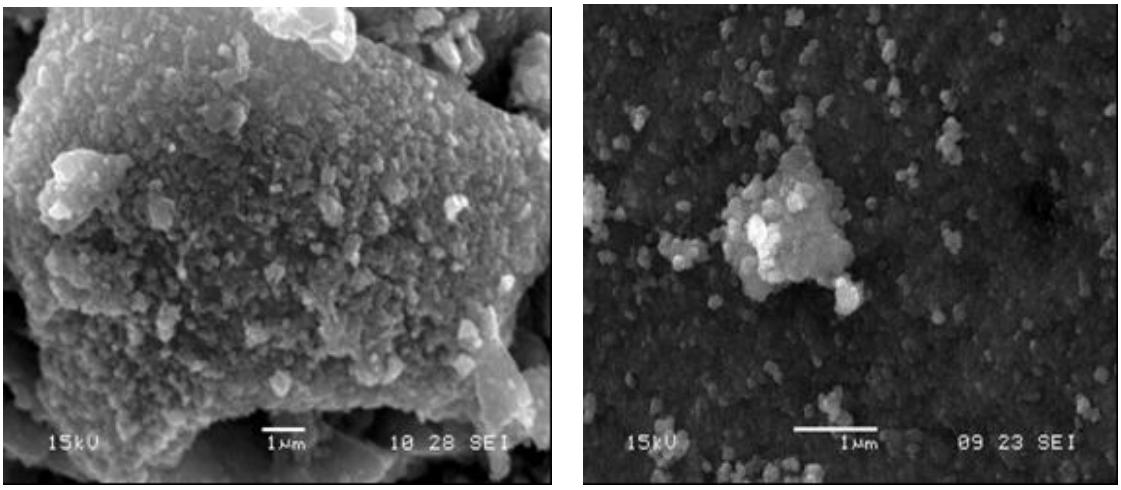

a) b)

Fig. 4.3.6 The SEM , magnification 10, 000, 15 kV for the catalyst sample with K synthesised at pH 7, fast titrant addition, room temperature were compared promoter **a)** precipitated at 60 ºC **b)** the sample precipitated at room temperature.

It was also observed that the samples with a Rb, synthesized at pH 7, fast titrant addition, at room temperature had the most homogenous, flat shaped agglomerates with sharp edges, but again also with small agglomerates attached. The image of the sample is presented below in a Figure 4.3.7.

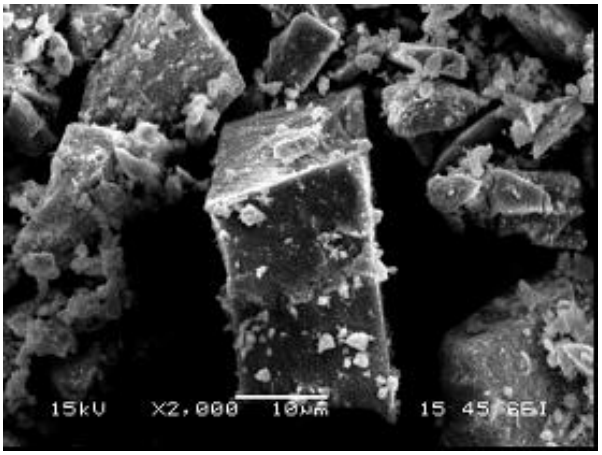

Fig. 4.3.7 The SEM images of Rb synthesised at pH 7, fast titrant addition, room temperature homogenous surface with attached smaller particles. SEM image magnification 2000, 15 kV.

4.4 XPS of the alkali metals in the iron oxide samples prepared in different conditions

The XPS technique was employed to examine the effect of the three different alkali metals Na, K, Rb on the synthesised iron oxide catalysts. For each of the alkali promoter, samples synthesised in different conditions were compared:

- pH 7, fast titrant addition, room temperature
- pH 7, slow titrant addition, room temperature
- pH 7, fast titrant addition, 60 ºC

The XPS for two of the alkali promoters Na and Rb were carried out before and after reduction in 5% H_2/He at 400^{o}C, 450 ºC and 500 ºC. The Na, K and Rb alkali metals references binding energies have been summarized and are listed in a Table 4.4. The published references[35-40] for Na promoters NaCl, Na_2SO_4, Na_2CO_3 give spectra from Na (1s) XPS in the binding energy range from 1071.2 - 1072.8 eV. The reported peaks of K2$p_{3/2}$ and K2$p_{1/2}$ from the K_2SO_4, $KClO_4$, $KClO_3$, KNO_3, K_3PO_4, K_2SO_3, K_2CO_3, K_3PdF_6, references were centred in the range and 292.0 - 293.7 eV (K 2$p_{3/2}$) and 294.7 - 296.4 (K 2$p_{1/2}$)[37,38]. The Rb 3d (3$d_{3/2}$ and Rb 3$d_{5/2}$) and Rb 3p (3$p_{1/2}$ and 3$p_{3/2}$) spectra of RbC_8, RbC_{60}, Rb_2SO_4, Rb_3PO_4, Rb_2CO_3, and RbCl, references were in the range 109.7-110.4 (Rb 3$d_{5/2}$), 111.4 (Rb 3$d_{3/2}$) eV, 238.1 – 238.9 eV (Rb 3$p_{3/2}$) and 247.1 – 247.9 (Rb 3$p_{1/2}$) have been reported[37,41,-43].

Tab. 4.4 The alkali metals published and experimental references XPS binding energies

Compound with the alkali metal	Alkali metal transitions spectra (eV)	Published references
Na_2CO_3	Na (1s): 1071.5 – 1071.7	[35], [36], [37]
Na_2SO_4	Na (1s): 1071.2 - 1072.50	[35], [37], [38]
NaCl	Na (1s): 1071.5-1072.8	[35], [37], [39], [40]
K_2SO_4	K ($2p_{3/2}$): 293.3	[38]
K_2SO_3	K ($2p_{3/2}$): 293.5	[38]
KCl	K ($2p_{3/2}$): 292.9, K ($2p_{1/2}$): 295.7	[38]
$KClO_3$	K ($2p_{3/2}$): 292.0-292.5	[37]
$KClO_4$	K ($2p_{3/2}$): 293.3- 293.6	[37]
KNO_3	K ($2p_{3/2}$): 292.6 - 293.7	[37]
K_3PO_4	K ($2p_{3/2}$): 293.2-293.6	[37]
RbCl	Rb ($3d_{5/2}$): 109.7-110.4, Rb ($3d_{3/2}$): 111.4	[37]
Rb_3PO_4	Rb ($3d_{5/2}$): 109.8-110.3	[37]
RbC_8	Rb ($3p_{3/2}$): 239.7, 239.8	[41], [42]
RbC_{60}	Rb ($3p_{3/2}$): 238.1 – 238.9, Rb ($3p_{1/2}$): 247.1 – 247.9	[37], [43],
Na_2CO_3	Na (1s): 1071.9	Experimental
K_2CO_3	K (2p): 292.8	Experimental
Rb_2CO_3	Rb (3d)110.2, Rb ($3p_{3/2}$): 238.7, Rb ($3p_{1/2}$): 247.4	Experimental

4.4.1 XPS of the K (2p) core-level spectrum for iron oxide samples prepared in different conditions with K promoter, before activation

Two peaks were observed in the K (2p) spectrum of the iron oxide samples synthesised under various conditions. The spectra for the samples with K, synthesised in the three different conditions are shown in Figure 4.4.1, below. The binding energies for the lower energy peaks of the three samples synthesised in different conditions are between 292.6 eV and 293.2 eV, and the higher energy peaks are between 295.5 eV and 296.2eV. The difference between these peaks was about 2.8 eV. The binding energies for all the samples synthesised in different conditions are similar and they are compared in Table 4.4.2.1.a. Although the K spectra were fairly noisy, they were clear enough to distinguish the distance between peaks and the energy ranges characteristic for the spin-orbit split doublet K($2p_{3/2}$) and K($2p_{1/2}$) of the potassium oxides[37,44,45].

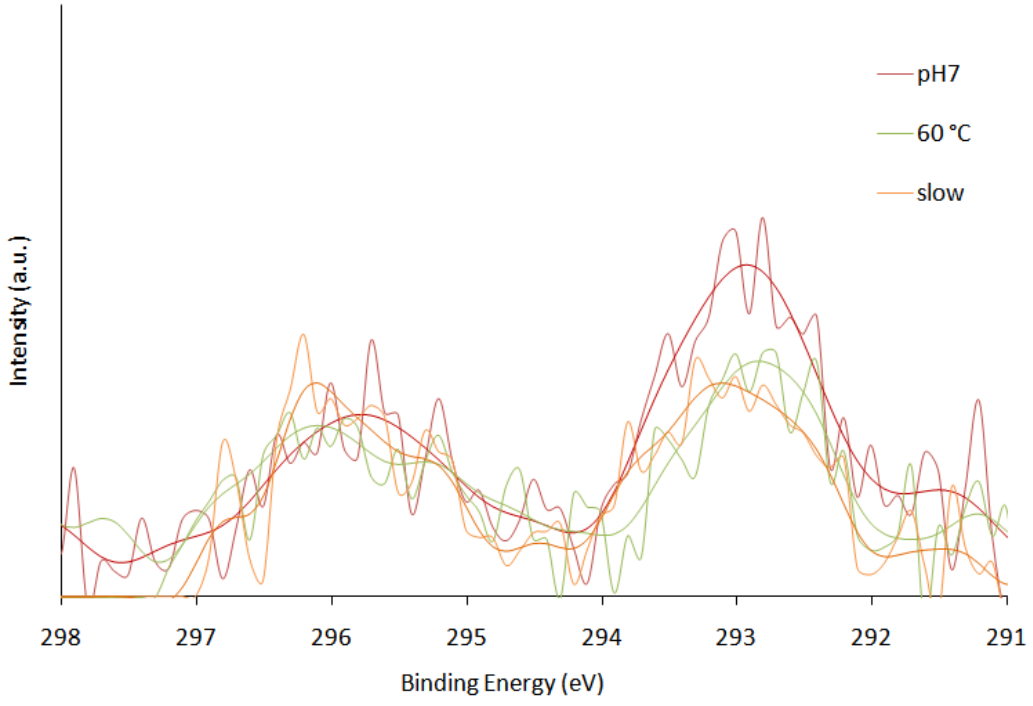

Fig. 4.4.1 XPS K (2p) spectra of samples with K promoter before activation; From the top: pH 7, fast titrant addition, RT; pH 7, fast titrant addition, 60 ^{o}C; pH 7, slow titrant addition, RT

4.4.2 XPS of the Na (1s) core-level spectrum for iron oxide samples prepared in different conditions with Na promoter, before activation

The XPS measurements produced spectra for samples synthesized in different conditions with Na promoter. The Na (1s) peak was observed between 1071.5 eV and 1071.9 eV for all the samples and indicated the presence of sodium ion (Na^+) [35-40]. The Na (1s) spectra for all the samples synthesised in various conditions are presented in Figure 4.4.2. The binding energy shift is presented in Table 4.4.2.1.a.

There were differences in intensity between samples with Na synthesized in different conditions observed. The peak with the highest intensity belonged to the sample prepared at pH 7, fast titrant addition rate, room temperature and the smallest intensity was recorded for the sample prepared at pH 7, slow titrant addition rate, room temperature. The differences in intensity were not so significant and they could be attributed to differences in Na concentration or particle size.

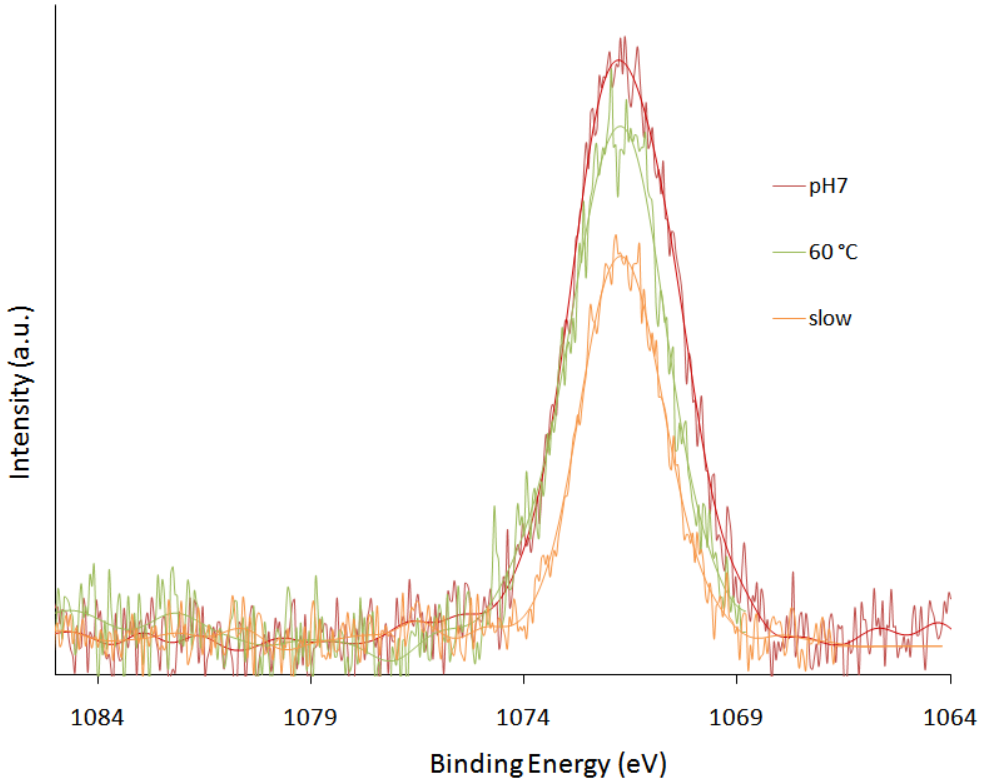

Fig. 4.4.2 XPS Na (1s) spectra of samples with Na promoter before activation; From the top: pH 7, fast titrant addition, RT, pH 7, fast titrant addition, 60 °C; pH 7, slow titrant addition, RT.

4.4.2.1 XPS of the Na (1s) spectrum for iron oxide samples prepared in different conditions with Na promoter, after activation

The Na (1s) XPS spectra for the sample synthesised in pH 7, fast titrant addition, at room temperature before and after activation in 400 ^{o}C and 450 ^{o}C were compared in Figure 4.4.2.1. The Na (1s) peaks are between 1071.5 eV and 1071.3 eV, which indicates the presence of Na^{+}. A slight shift in a binding energy to a lower energy for the reduced samples in comparison to the non-activated ones was observed. The energies are listed in Table 4.4.2.1.a. The differences in Na (1s) spectra intensity between non-reduced and activated samples are significant. The samples reduced at 450 ºC have higher intensity compared to those reduced at 400 ºC. The above can lead to the conclusion that high temperature reduction treatment increases mobility and migration of Na to the surface.

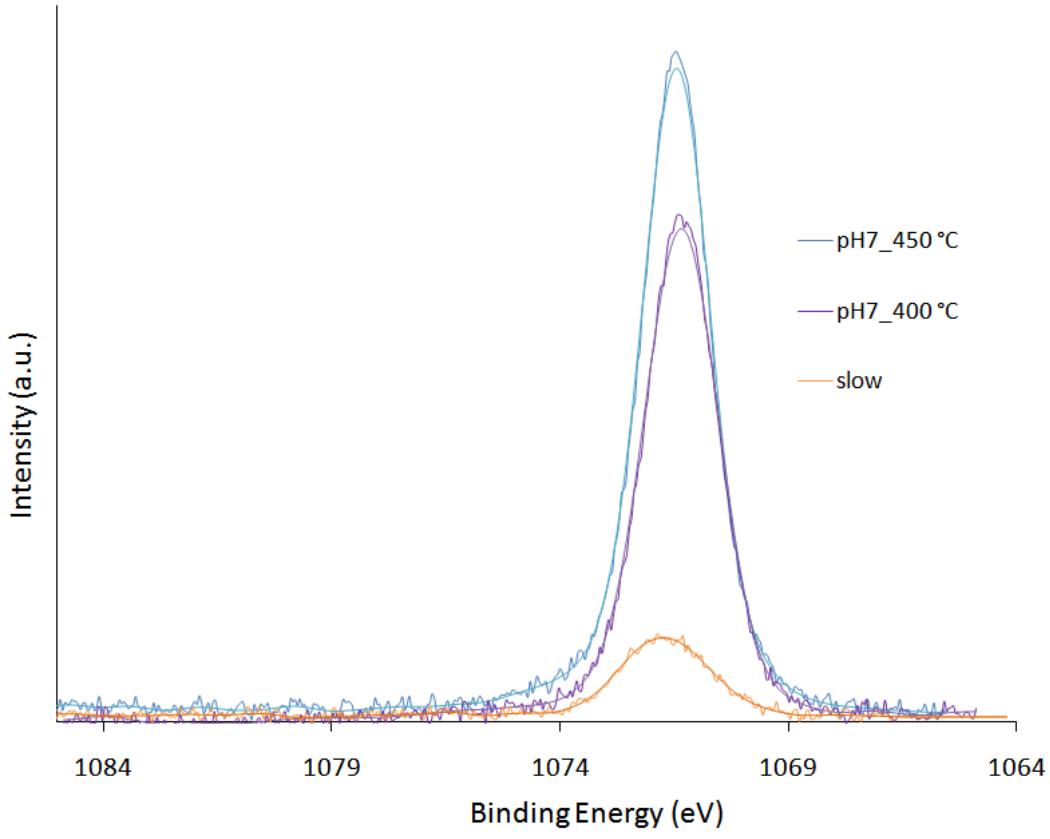

Fig. 4.4.2.1 The XPS Na (1s) spectra of sample synthesised at pH 7, slow, RT; before and after activation at 400 ^{o}C and 450 ^{o}C for the sample

Tab. 4.4.2.1.a The XPS spectra of iron oxide catalyst for non-reduced samples with different promoters

Conditions	**Peak Position, eV**	**Conditions**	**Peak Position, eV**
pH 7, fast, RT, **K**	293.9	pH 7, fast, RT, **Rb(3d)**	110.7
pH 7, fast, 60^{o}C, **K**	292.9	pH 7, fast, 60 ^{o}C, **Rb(3d)**	110.3
pH 7, slow, RT, **K**	292.1	pH 7, slow, RT, **Rb(3d)**	110.1
pH 7, fast, RT, **Na**	1071.9	pH 7, fast, RT, **Rb(3p)**	238.7[1], 247.4[2]
pH 7, fast, 60 ^{o}C, **Na**	1071.9	pH 7, fast, 60 ^{o}C, **Rb(3p)**	238.7, 247.4
pH 7, slow, RT, **Na**	1071.8	pH 7, slow, RT, **Rb(3p)**	238.7, 247.4

1 - Rb $3p_{3/2}$, **2 -** Rb $3p_{1/2}$

Tab. 4.4.2.1.b The XPS peak positions of the samples prepared in different conditions after reduction

Conditions	**Peak Position, eV**	**Conditions**	**Peak Position, eV**
pH 7, fast, RT, 400 ^{o}C, Na	1071.5	pH 7, fast, RT,450 ^{o}C, Na	1071.6
pH 7, fast, RT, 400 ^{o}C, Rb	109.9[1],111.1[2]	pH 7, fast, RT, 400 ^{o}C, Rb	238.1[3], 247.1[4]
pH 7, fast, 60C, 400 ^{o}C, Rb	109.9,111.1	pH 7, fast, 60C, 400 ^{o}C, Rb	238.2, 247.2
pH 7, slow, RT, 400 ^{o}C, Rb	109.9,111.1	pH 7, slow, RT, 400 ^{o}C, Rb	238.2, 247.2
pH 7, fast, RT, 450 ^{o}C, Rb	110.1,111.2	pH 7, fast, RT, 450 ^{o}C, Rb	238.4, 247.3
pH 7, fast, 60C, 450 ^{o}C, Rb	109.9,111.2	pH 7, fast, 60C, 450 ^{o}C, Rb	238.4, 247.3
pH 7, slow, RT, 450 ^{o}C, Rb	110.1,111.2	pH 7, slow, RT, 450 ^{o}C, Rb	238.4, 247.3

1 - Rb $3d_{5/2}$, **2 -** Rb $3d_{3/2}$, **3 -** Rb $3p_{3/2}$, **4 -** Rb $3p_{1/2}$

4.4.3 XPS of the Rb (3d) core-level spectrum for iron oxide samples prepared in different conditions with a Rb promoter, before activation

For the samples with Rb promoter synthesised in different conditions a Rb (3d) peak in a binding energy range between 110.3eV and 110.2eV was observed, Figure 4.4.3. Samples synthesised at pH 7, fast titrant addition rate, room temperature and pH 7, fast titrant addition rate, 60 ºC conditions have very similar intensities. For the sample synthesised in pH 7, fast titrant addition rate, room temperature had a slightly higher intensity. Two other peaks were observed, one between 93.9 eV and 92.8 eV, and the other between 100.3 and 98.2 eV, which correspond to Fe (3s) and Fe(3s) satellite peaks. The Rb (3d) peak did not reveal the characteristic[37,46,47] Rb $3d_{5/2}$ and $3d_{3/2}$ doublet, which will be explained below.

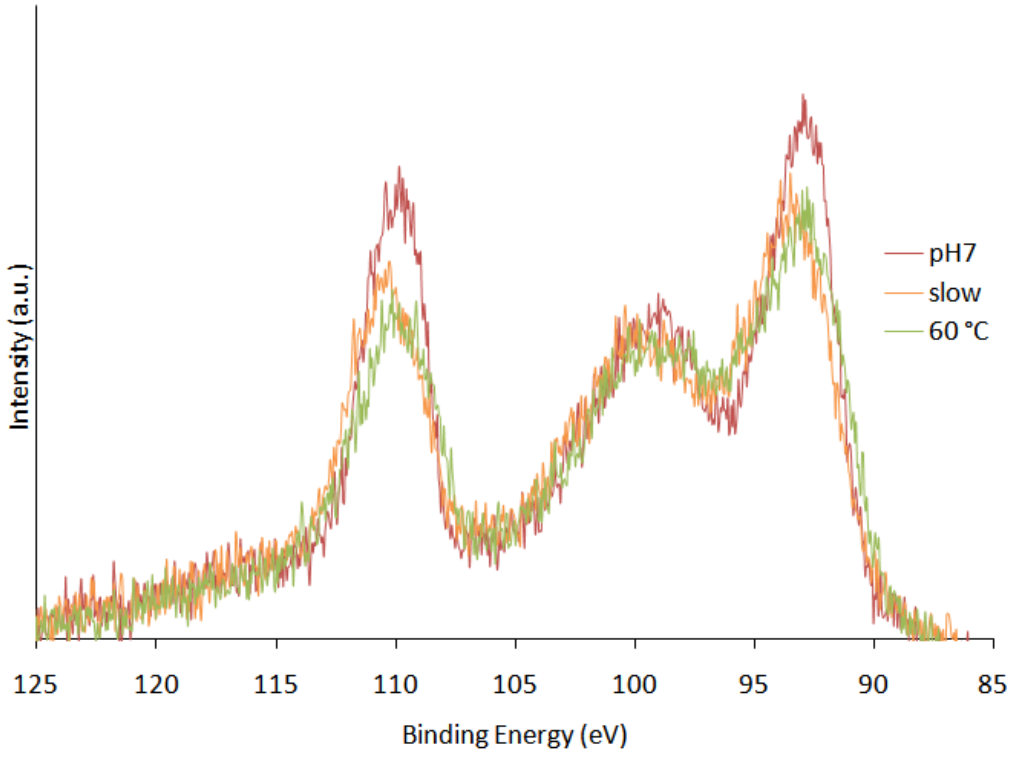

Fig. 4.4.3 XPS Rb (3d) spectra of samples with Rb promoter before activation; from the top: pH 7, fast titrant addition, RT, pH 7, slow titrant addition, RT; pH 7, fast titrant addition, 60 °C.

4.4.3.1 XPS of the Rb (3d) core-level spectrum for iron oxide samples prepared in different conditions with Rb promoter, after activation

The Rb (3d) XPS spectrum for the samples with Rb promoter after reduction under H_2/He in 400 ^oC in the region between 110.2 eV and 111.3 eV was observed. The peaks are presented in Figure 4.4.3.1 a. For all the samples reduced at 400 ºC spin-orbit split doublet ($3d_{5/2}$ and $3d_{3/2}$) was evident, which was not visible for the non-reduced samples. The peaks in doublet have a characteristic for the rubidium oxides 1.5 eV split and ratio of the area under the doublet peaks is 0.67 [37,46]. The intensity of the Rb (3d) peak of the samples after reduction was much higher than for the non-reduced samples. Results suggest, similarly like for the Na, the possible migration of Rb to the surface and its enrichment with the alkali metal. Higher concentration of the alkali metals affects the intensity of the signal, thus, making the doublet more visible.

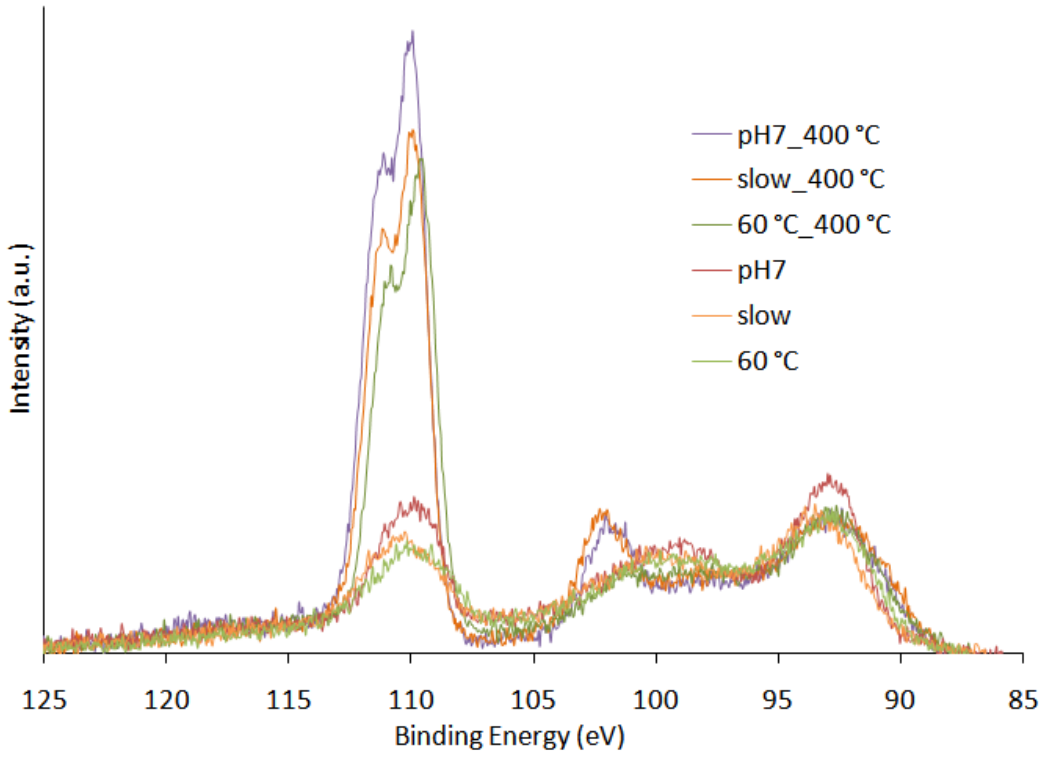

Fig.4.4.3.1.a XPS Rb(3d) spectra of samples with Rb promoter before and after reduction; From the top: pH 7, fast titrant addition, RT, reduced at 400 ^oC; pH 7, slow titrant addition, RT, reduced at 400 ^oC; pH 7, fast titrant addition, 60 ^oC, reduced at 400 ^oC; pH 7, fast titrant addition, RT; pH 7, slow titrant addition, RT; pH 7, fast titrant addition, 60 ^oC.

The characteristic 1.5 eV split (separation), occurred due the spin-orbit coupling energy difference between the two *j* states for the samples reduced in 450 ^{o}C. A doublet for the samples with Rb promoter synthesised in different conditions analysed after reduction under H_2/He at 450 ^{o}C was observed in the region between 111.2 eV and 110 eV (see Figure 4.4.3.1 b, c. As it was observed before for the samples reduced at 400 ºC, the 3d split doublet areas ratio is 2/3. The $3d_{5/2}$ and $3d_{3/2}$ areas under the peak ratios are presented in Table 4.4.3.1. The intensity of the $3d_{5/2}$ peak for the samples reduced at 450 ºC is slightly higher in comparison with the sample reduced at 400 ºC. The exception was the sample synthesised at pH 7, fast, RT, reduced at 400 ºC, which has the highest intensity among the reduced samples. Samples reduced in both temperatures have much higher intensity than non-reduced samples.

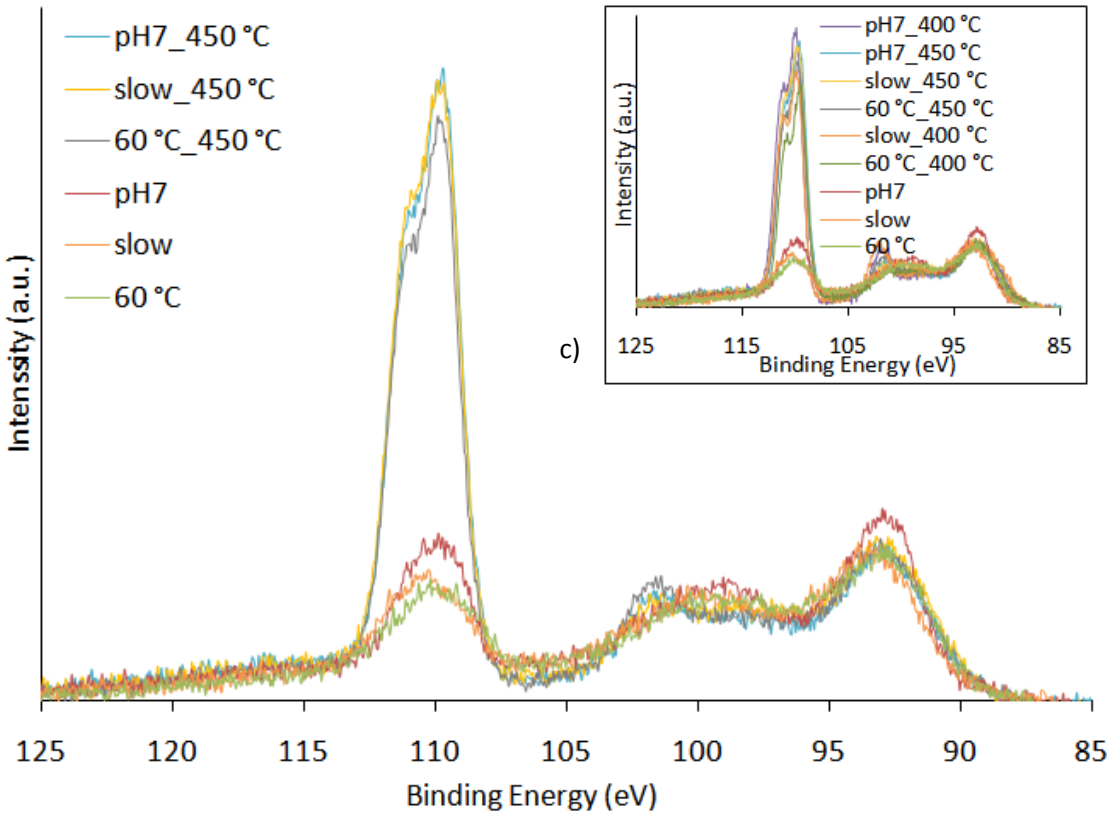

Fig. 4.4.3.1 b) XPS Rb (3d) spectra of samples with Rb promoter before and after reduction; From the top: pH 7, fast titrant addition, RT, reduced at 450 ^{o}C; pH 7, slow titrant addition, RT, reduced at 450 ^{o}C; pH 7, fast titrant addition, 60 ^{o}C, RT reduced at 450 ^{o}C; pH 7, fast titrant addition, RT; pH 7, slow titrant addition, RT; pH 7, fast titrant addition, 60 ^{o}C, **c)** comparison with the samples reduced at 400 ^{o}C; right side top corner.

Tab. 4.4.3.1 The XPS measurement of the area under the Rb $3d_{3/2}$ and Rb $3d_{5/2}$peaks for the reduced samples.

Conditions	**Area under the peaks: Rb $3d_{3/2}$ and Rb $3d_{5/2}$**	**The ratio of the Rb $3d_{3/2}$ and Rb $3d_{5/2}$ peaks**
pH 7, fast, RT, 400 ^{o}C	39.1; 60.1	0.65
pH 7, fast, 60 ^{o}C, 400 ^{o}C	39.7; 60.3	0.66
pH 7, slow, RT, 400 ^{o}C	40.6; 59.4	0.68
pH 7, fast, RT, 450 ^{o}C	40.2; 59.8	0.67
pH 7, fast, 60 ^{o}C, 450 ^{o}C	41.9; 58.1	0.72
pH 7, slow, RT, 450 ^{o}C	41.0; 60.0	0.68

4.4.4 XPS of the Rb (3p) core-level spectrum for iron oxide samples prepared in different conditions with Rb promoter, before activation

There were two different intensity peaks separated by approximately 9 eV for all the samples. The maximum of the higher energy Rb $3p_{1/2}$ peak for the samples synthesised in various conditions was observed in the range between 247.3 eV and 247.1 eV and the lower energy peak $3p_{3/2}$ between 239.3 eV and 238 eV, Figure 4.4.4. The intensities for all the samples were comparable. Slightly higher intensity was observed for the sample synthesised at pH 7, fast titrant addition rate, room temperature.

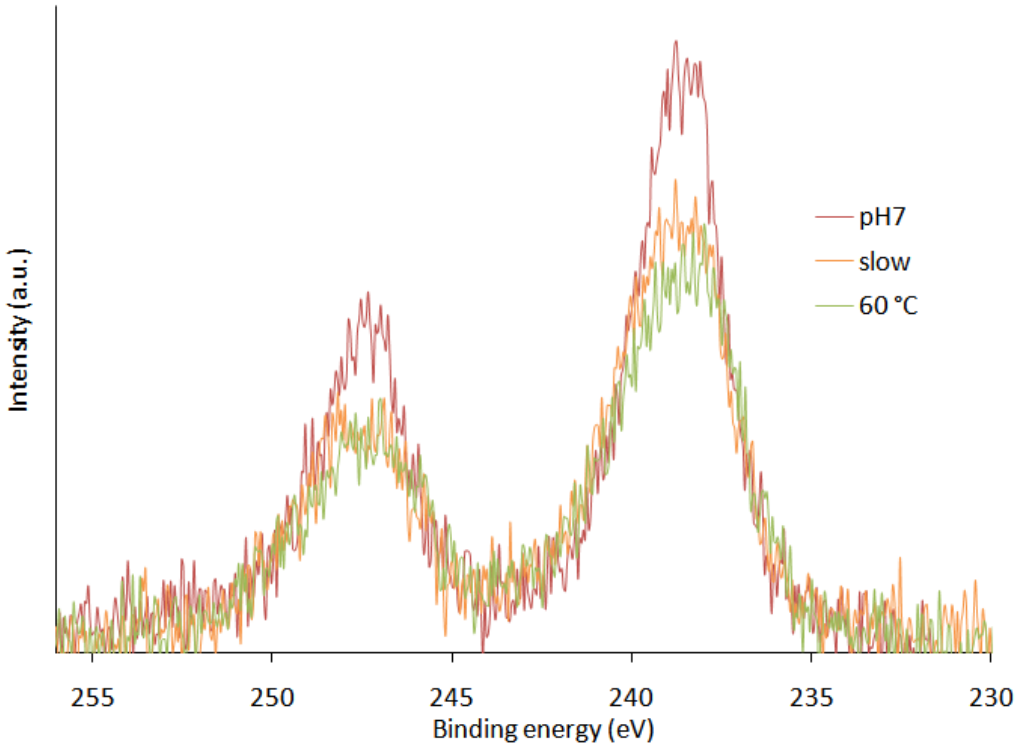

Fig.4.4.4 XPS Rb (3p) spectra of samples with Rb promoter before activation; from the top: pH 7, fast titrant addition, RT; pH 7, slow titrant addition, RT; pH 7, fast titrant addition, 60 ^{o}C.

4.4.4.1 XPS of the Rb (3p) core-level spectrum for iron oxides samples prepared in different conditions with a Rb promoter, after activation

The characteristic Rb 3p spectrum doublet separated by 9 eV energy, as for non-reduced samples, was observed. The $3p_{1/2}$ peak was observed in the range 247.5 eV to 247 eV, and the $3p_{3/2}$ peak between 238.5 eV and 238.2 eV, Figure 4.4.4.1 a. Only a minor shift towards lower energies was noticed for all reduced samples in comparison to the non-reduced ones. The binding energy values are presented Table 4.4.2.1.b.

The higher intensity of the Rb (3p) peaks after reduction is consistent with migration of Rb to the surface as was observed for the samples with a Na promoter.

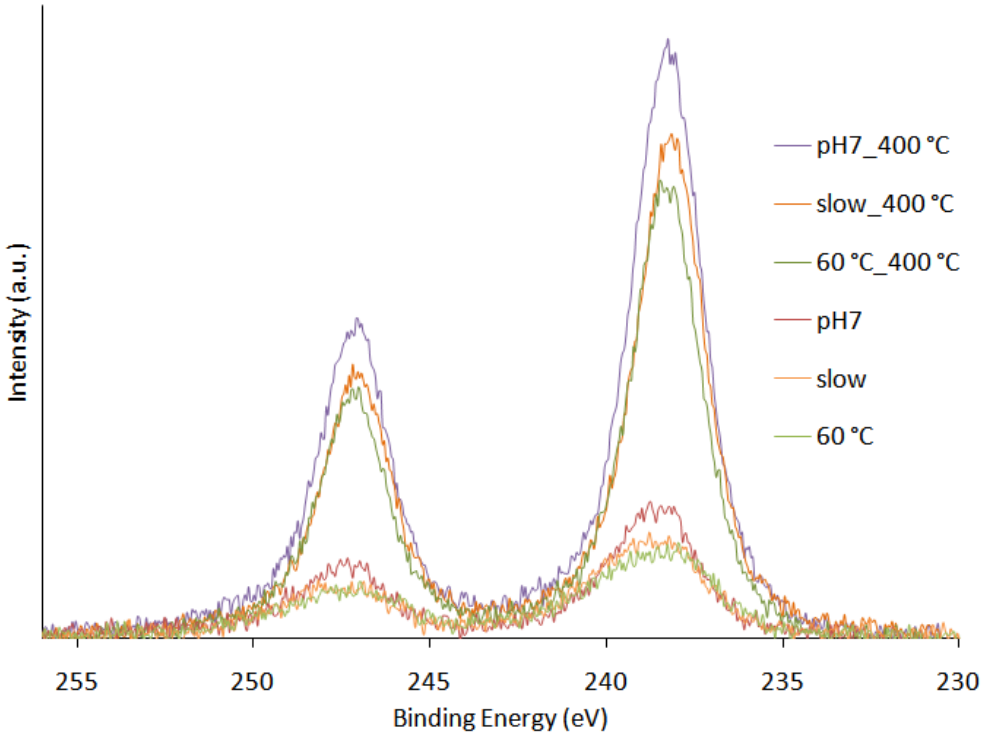

Fig. 4.4.4.1 a XPS Rb (3p) spectra of samples with a Rb promoter before and after reduction; From the top: pH 7, fast titrant addition, RT, reduced at 400 ^{o}C; pH 7, slow titrant addition, RT, reduced at 400 ^{o}C; pH 7, fast titrant addition, 60 ^{o}C, RT reduced at 400 ^{o}C; pH 7, fast titrant addition, RT; pH 7, slow titrant addition, RT; pH 7, fast titrant addition, 60 ^{o}C.

For the samples reduced at 450 ºC the $3p_{1/2}$ and $3p_{3/2}$ doublet was observed in the same binding energy area as for samples reduced at 400 ^{o}C. The difference between two of the peaks in the doublet was also (like previously) around 9 eV for the samples synthesised in different conditions. All of the samples activated in the higher temperature have the same energy shift like those synthesised in 400 ^{o}C. The difference in intensity for non-reduced samples and samples reduced at 450 ºC are shown in Figure 4.4.4.1 b, c. The peaks of the samples reduced at 450 ºC had a slightly higher intensity than those reduced at 400 ºC. The exception, as it also was for Rb (3d), was the sample synthesised in pH 7, fast, RT, and reduced in 400 ºC, Figure 4.4.4.1 b, c. The peak positions for all the samples are tabulated in Table 4.4.2.1 a and 4.4.2.1 b.

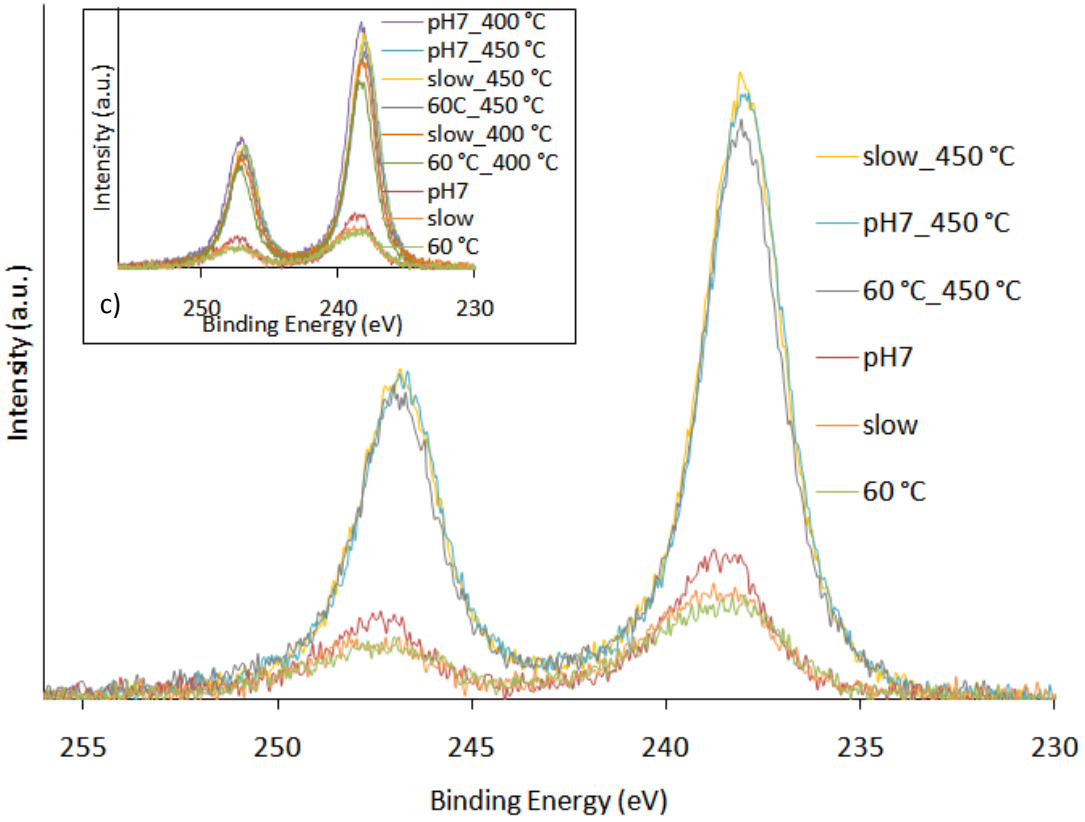

Fig.4.4.4.1 b XPS Rb(3p) spectra of samples with Rb promoter before and after reduction; From the top: pH 7, slow titrant addition, RT, reduced at 450 ^{o}C; pH 7, fast titrant addition, RT, reduced at 450 ^{o}C; pH 7, fast titrant addition, 60 ^{o}C, reduced at 450 ^{o}C; pH 7, fast titrant addition, RT; pH 7, slow titrant addition, RT; pH 7, fast titrant addition, 60 ^{o}C, **c)** comparison with the samples reduced at 400 ^{o}C; top corner.

The comparison of the surface elemental analysis XPS and bulk techniques like EDX and XRF confirmed the possibility of migration of alkali metals to the surface as the reduction temperature was increased. The elemental composition of the alkali metals on the surface and in the bulk will be presented later in the chapter. The XPS elemental analysis results for all the samples are tabulated in Table 4.4.2.1.a and 4.4.2.1.b. Such a migration of alkali metals to the surface and increased concentration on the surface with increasing reduction temperature may have influence on the effective reduction temperature depending on the alkali metal used as promoter. Different reduction temperatures required for change of the iron oxide phase were observed for different alkali promoters used (PXRD experiment 4.3.3).

4.5 Alkali XANES for iron oxide samples prepared in different conditions before and after activation

4.5.1 Na K-edge XANES for iron oxide samples prepared in different conditions

The energy of the K-edge spectrum at 1070.8 eV for sodium is relatively low. The incident photons have low energy, necessary to observe the K-edge of these elements, consequently the X-ray photons do not penetrate deeply into the sample (100–1000 Å maximum)[48]. Therefore, the different shapes for all of the XAFS spectra will be decidedly dependent on the structure of the catalyst surface. Moreover, the interaction with atmosphere (H_2O, CO_2) may create precipitates such as hydroxides, carbonates etc., which influence the shape of the spectra[49].

The Na K-edge XANES spectra for the reference compounds (Na_2SO_4, Na_2SO_3, Na_2CO_3) and for the iron oxide catalyst sample synthesized in pH 7, fast titrant addition, room temperature, are presented in Figures 4.5.1 and 4.5.2. For all of the presented reference samples Na_2SO_4, Na_2SO_3 and Na_2CO_3 there were small pre-edge and two good developed peaks visible. The higher peak from the doublet in the lower energy area for the Na_2SO_3 sample was split in two, i.e. a lower intensity peak at 1074.4 eV and a more developed peak at 1074.8 eV. The second higher energy peak in the doublet at 1080.7 eV was observed. The small pre-edge peak at 1071.0 eV may indicate that $s \rightarrow p$ transition is partially allowed.

For the Na_2CO_3 reference, the split for the first peak in the doublet was difficult to notice. The first, lower energy peak was not developed like that in Na_2SO_3. However, the distortion in the same area as in lower energy peak of Na_2SO_3, at 1074.4 eV, was observed. The second higher energy peak of the doublet has the same characteristic as the previous sample. It was slightly shifted to a higher energy (around 0.2 eV). The split for the lower energy peak in the doublet with the maximum at 1074.5 eV for Na_2SO_4 was not observed. The maximum of the second higher energy peak for that sample was observed at 1080.6 eV. The peak has very similar energy shift, but higher intensity in

comparison to the second peak of Na_2SO_3 sample. The edge position at 1074.1 eV for all the references was observed.

In a similar to manner to the reference samples, the Na K-edge XANES spectrum for the experimental iron oxide catalyst sample was also recorded. The position of the lower energy peak was approximately between 1074.6 and 1075.4 eV. The characteristic shape of Na K-edge XANES spectrum is in the same energy range like the fingerprint samples and literature references[50-53], which suggests presence of the Na^+, see Figure 4.5.2. The noisy data did not allow resolution of the doublet splitting in the catalyst sample. The quality of the Na K-edge XANES signal could not be improved by longer acquisition due to the degradation of the beryl monochromator used in the experiment by the X-ray beam. Therefore, it was also difficult to determine the environment of the sodium ion. The peak positions for the references and iron catalyst sample compounds are listed in Table 4.5.1.

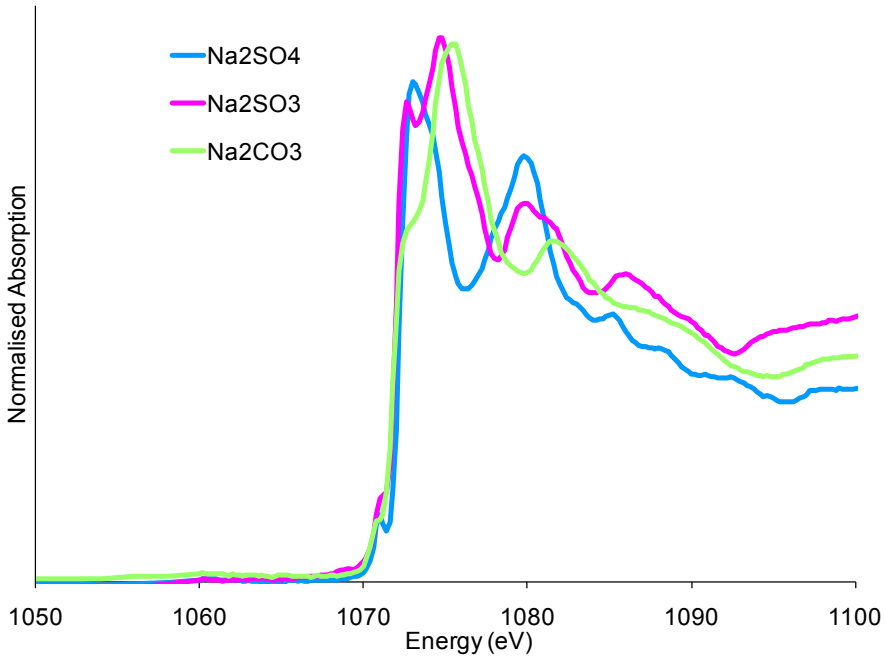

Fig. 4.5.1 Na K-edge XANES spectra of references Na_2SO_4, Na_2SO_3, Na_2CO_3.

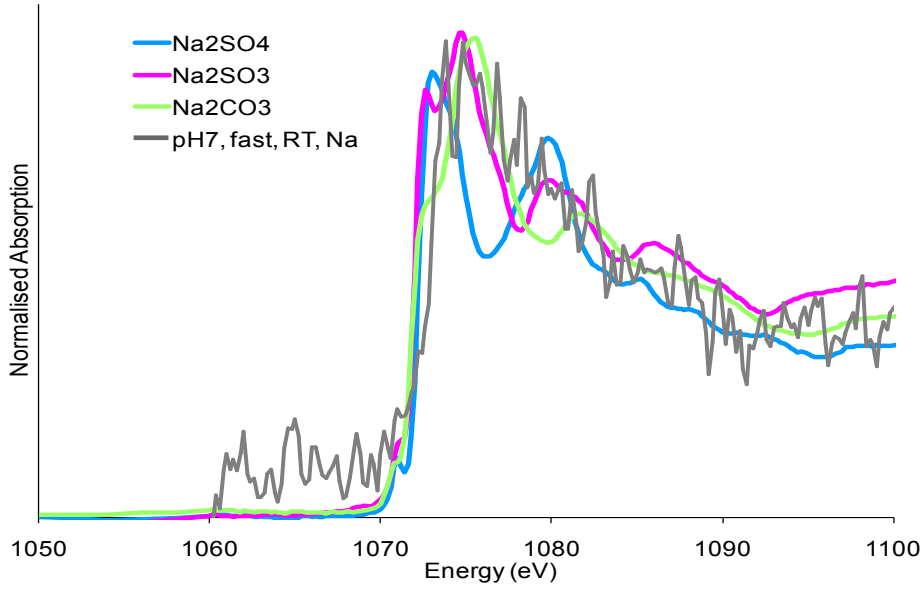

Fig. 4.5.2 Na K-edge XANES spectra of sample synthesized at room temperature, pH 7, fast titrant addition, compared with references Na_2SO_4, Na_2SO_3, Na_2CO_3.

Table 4.5.1 Sodium K-edge XANES spectra peak positions for sample synthesized at room temperature, pH 7, fast titrant addition and for reference samples Na_2SO_4, Na_2SO_3, Na_2CO_3.

Standard /Sample	**Chemical Formula**	**Peak Position, eV**
Sodium sulfate	Na_2SO_4	1074.2
		1080.8
		1084
Sodium sulfite	Na_2SO_3	1074.1, 1074.5
		1080.7
		1085.2
Sodium carbonate	Na_2CO_3	1075.6
		1081.6
Iron catalyst sample	unknown	~ 1075

4.5.2 Potassium K-edge XANES for iron oxide samples prepared in different conditions

Spectral changes and the shape of the absorption edge depend on changes in the oxidation state and the local geometry of the absorbing metal atom. However, for potassium, which is present as K^+, changes may be caused by variations of the local structural environment of K^+ and the number and kind of atoms in its vicinity[54].

Due to the higher binding energy as compared to Na, (Chapter 2), giving a higher penetration depth and thus a stronger signal of the XANES region, the K K-edge samples were easier to record and analyse than the Na K-edge spectra.

4.5.2.1 Potassium K-edge XANES for iron oxide samples prepared at room temperature

The K-edge spectra for potassium for the samples before activation synthesised in various conditions have a broad peak between 3615.4 eV and 3617.7 eV. For the sample synthesised at pH5, fast titrant addition rate, room temperature, the K-edge peak 3616 eV was narrower than for the rest of the samples. All of the samples were compared with the reference K_2CO_3, which was used as a "fingerprint". For all of the samples the main peak was in the same energy region as for the reference K-edge spectrum. The spectrum of the reference, as given in the literature[55-57], was split in two closely spaced peaks at 3614.3 eV and 3620.7 eV (Table 4.5.2).

The structure, of potassium carbonate can be described as a slightly distorted hexagonal close packed array of carbonate ions, where potassium ions occupy both octahedral and trigonal bipyramidal sites[58]. The octahedral site (K2) has K-O interatomic distances between 2.62 and 2.80 Å (average 2.68 Å) and the trigonal site (K1), has a very disordered structure with 6 K-O distances between 2.82 and 2.94 Å and a further three in the range 3.1 - 3.2 Å (average 2.98 Ă).

The K-O distances for the samples and references used in the experiment will be presented below, in Table 4.5.2.2. The overall average of 2.85 Å is much longer than

the experimental value of 2.70 Å. However, after the very long distances were excluded the average drops to 2.77 Å. The complexity of the K-O distances makes K_2CO_3 a difficult reference e.g. problems with the coordination number due to a wide distribution of distances.

The changes of multiple-scattering (MS) region and single-scattering (SS) of KCl and micas references found in the literature are described here.The changes of the intensities of maxima of the first two peaks of K K-edge in KCl with different number of atomic shells in the cluster were reported by Lavrentyev et al. In their simulations, the main features of the XANES arise for clusters with only two atomic shells (19 atoms in the cluster) (Figure 4.5.2.1 a). Increasing in the numbers of atomic shells up to six (81 atoms) did not change the energy positions of the spectra, however, it led to the increase of the intensities of the maxima. The XANES features did not change for the samples with number of atomic shells beyond six.

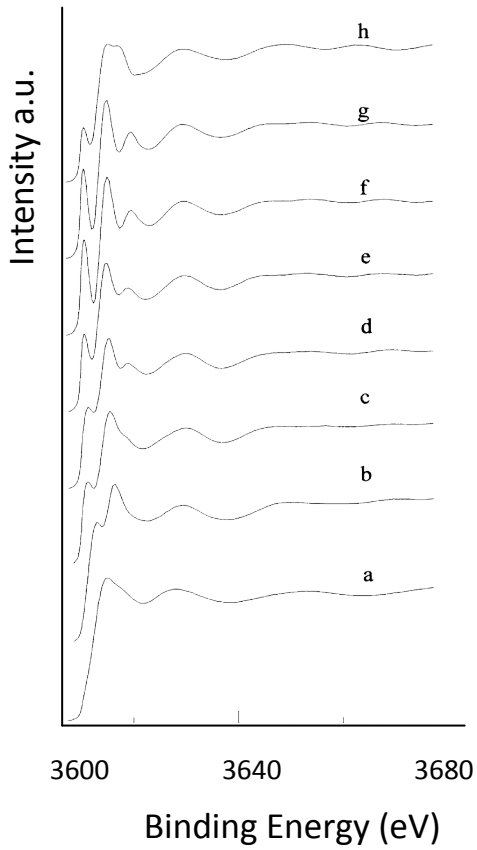

Fig. 4.5.2.1 a K K-edge for KCl, calculated with different numbers of atomic shells in the cluster. a-g spectra of the compounds with 1-7 atomic shells respectively) single scattering approximation, 7 atomic shells in the cluster.

In the report by Cibin et al., changes in K K-edges for the samples with different coordination number (CN) were observed. A linear trend was observed between the CN of K and the changes in energy between the high-energy peak E_1 from the single-scattering region of EXAFS and the absorption edge energy E_0, (E_1- E_0), for anhydrous silicates (leucite, with CN = 6, microcline with CN = 7, sanidine with CN = 9 and silivite (HCl) with CN = 6. The (E- E_0) energy difference decreased with increasing CN. Only silivite deviated from the trend with very small energy differences, due to significant differences in the ligand anion. However, the mica samples presented further in the experiment by Cibin et al. , have threshold absorption edge energies much higher than references presented above and did not fit the observed trend due to small E-E_0 differences, which gave unrealistic coordination numbers (CN = 14 to 16). Moreover, there were similarities in the MS region between 3630 – 3650 eV for all the samples presented in Cibin et al. the local structure around the K was the same in all mica interlayers.

The shape of the maxima of the K K-edge XANES spectrum, as explained by Parratt and Jossem (in their experiment potassium chloride was used),[59,60] is due to the transitions of the K-electron into the exited states. The first peak may be as the result of 1s → 4p transition in the ion K^+, and the following into 5p. However, according to Yang[54] this interpretation of the spectral changes may be complicated due to the fact that it is not appropriate to assign separate spectral features to particular transitions for K spectra, as for other low Z atoms like C or O. It was observed in Figure 4.5.2.1 b that the splitting was not developed for the samples before reduction, which may be caused by the mixture of sites with overlapping spectra. The peak positions for all the samples and reference are in Table 4.5.2.

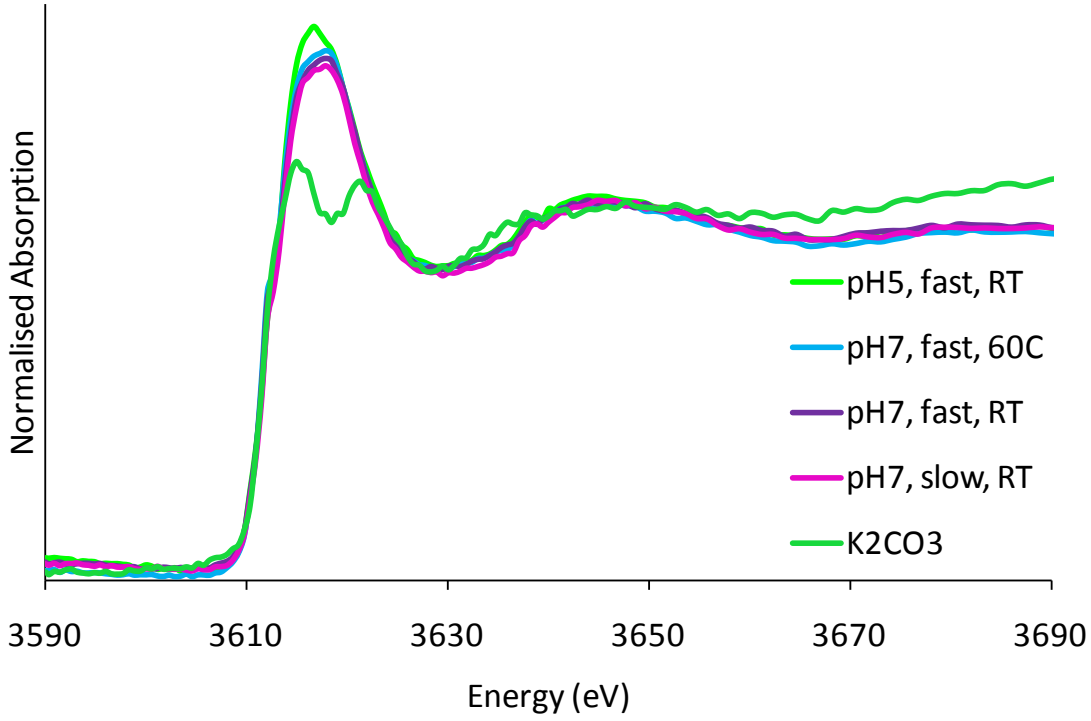

Fig. 4.5.2.1 b K K-edge XANES spectra of iron oxide catalyst sample before reduction; From the top: pH 5, fast titrant addition, RT; pH 7, fast titrant addition, 60 ^{o}C; pH 7, fast titrant addition, RT; pH 7, slow titrant addition, RT; K_2CO_3 reference

4.5.2.2 Potassium K-edge XANES for iron oxide samples after reduction

The potassium K-edge for the samples synthesised in different conditions after reduction in 450 ^{o}C were split into a characteristic doublet. Two closely spaced peaks between 3614.4 eV and 3618.3 eV were observed (Table 4.5.2), similar to K_2CO_3 (Figure 4.5.2.2 a). The same was observed for the samples with K promoter synthesised in different conditions after reduction at 500 ºC, Figure, 4.5.2.2 b. The K K-edge spectrum was also split for the fingerprint. However, the peaks after reduction at the higher temperature were more distinct than those for samples reduced at 450 ºC,

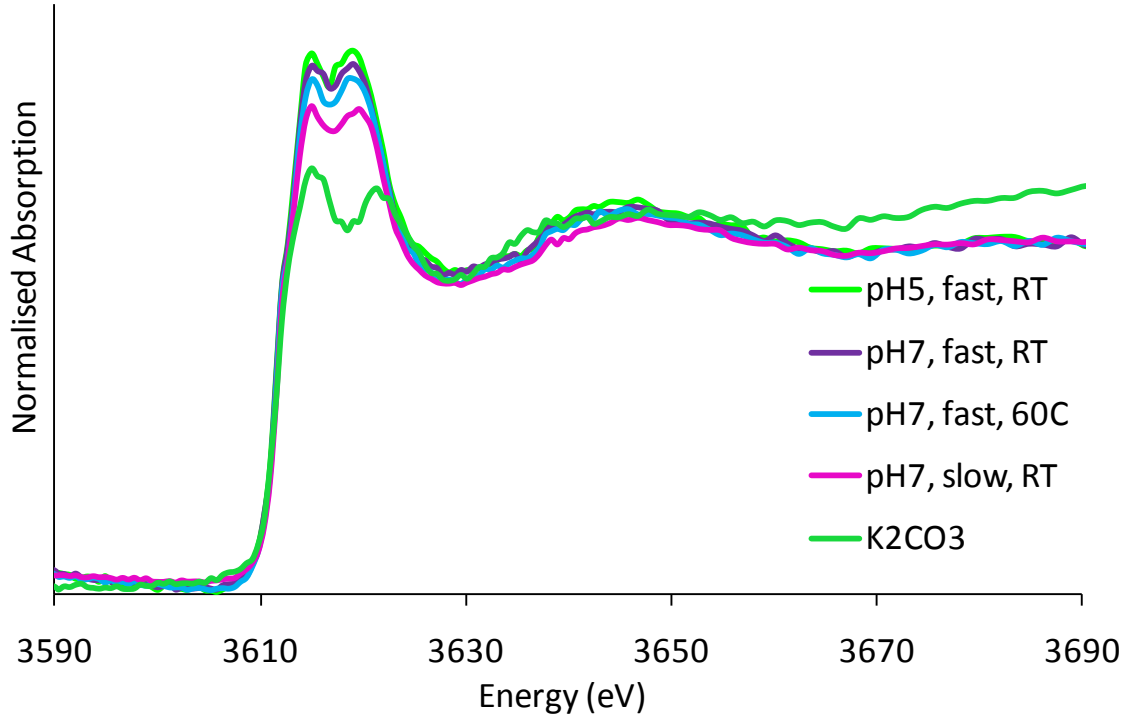

Fig. 4.5.2.2 a K K-edge XANES spectra of iron oxide catalyst sample after reduction at 450 ^{o}C; From the top: pH 5, fast titrant addition, RT; pH 7, fast titrant addition, RT; pH 7, fast titrant addition, 60 ^{o}C; pH 7, slow fast titrant addition, RT; K_2CO_3 reference

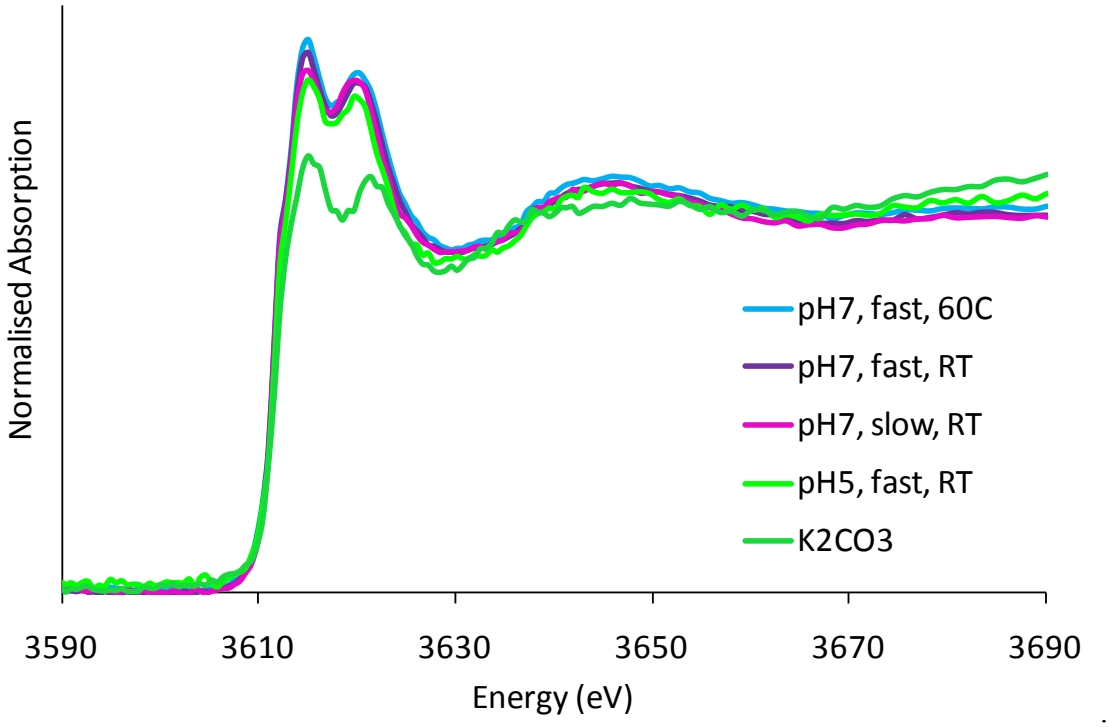

Fig. 4.5.2.2 b K K-edge XANES spectra of iron oxide catalyst sample after reduction at 500 ^{o}C; From the top: pH 7, fast titrant addition, 60 ^{o}C; pH 7, fast titrant addition, RT; pH 7, slow titrant addition, RT; pH 5, fast titrant addition, RT, K_2CO_3 reference

The coordination numbers of K and K-O distances were measured using the Athena software, for chosen samples synthesised in pH 7, fast titrant addition in room temperature, prior to activation, reduced under H_2/He at 450 ^{o}C and H_2/He at 500 ^{o}C and for the K_2CO_3 reference sample. The results are presented in Table 4.5.2.3.

Table 4.5.2.2 The coordination numbers, K - O distance with estimated standard deviations and $E_1 - E_0$ difference for the iron oxide samples synthesised at pH = 7, fast titrant addition at room temperature, before and after reduction at two different temperatures, and for the reference sample K_2CO_3.

Sample	Coordination number of K	K – O distance (Å)	Energies differences between $E_1 - E_0$
RT, α-Fe_2O_3	6(2)	2.72(2)	-
450 ^oC, Fe_3O_4	6 (1)	2.72(3)	31.5
500 ^oC, Fe_3O_4/Fe^0	6 (5)	2.70(1)	31.5
K_2CO_3	8 (6)	2.70(1)	29.0

It was not possible to observe a similar trend as was evident for references in Cibin et al., experiment (above, 4.5.2.1) due to the high standard deviation of the coordination number. The E_1-E_0 difference was similar for all the samples reduced at 450 and 500 ^oC. The energy difference for the reference K_2CO_3 sample was significantly lower than rest of the samples.

Prior to reduction, the XANES region of the spectra showed one single peak which may indicate that a K^+ ion is embedded in the structure, either on or in the iron oxide (α-Fe_2O_3), which octahedrally coordinates Fe^{3+} ions. After the samples were activated, the second feature of the double white line started to be visible. It was found after P-XRD experiment, that the α-Fe_2O_3 form of non-reduced catalysts, at 400 ^oC is reduced to Fe_3O_4, where ¾ of cations are coordinated octahedrally and ¼ tetrahedrally; and in 500 ^oC to the mixture of Fe_3O_4 and metallic iron. Thus, the more extended structure may give the rise to multiple scattering, showing double features.

The K–O distances calculated from the EXAFS data for all the samples were nearly the same around 2.7 Å (Table. 4.5.2.2. According to Gatehouse, references and data calculated in the experiment, similar K-O distances, large Debye-Waller factor for all the samples, it may be concluded that the K^+ ions retain an O environment and do not migrate to Fe^0, prior to and after reduction in higher temperature, where metallic iron appeared in the catalyst.

Both of the promoters (Na and K) have many differences like different radii, first ionisation energy etc. (chapter 1, Table 1.4.1) However, the promoters used in the experiment also have some similarities like for example the same charge which distinguishes them as a group from different promoters. Thus, the study of potassium, which is the easier to analyse, may facilitate understanding the properties of the sodium. The information about changes in the local structural environment of K^+ may be similar to the changes for the samples with Na but it was not possible to observe them due to the noisy spectrum of the Na K-edge.

Tab. 4.5.2.3 Potassium K-edge XANES spectra peak positions for sample synthesized at different conditions and for K_2CO_3 used as a reference

Iron catalyst with K promoter samples condition	**Peak position, eV**
Reference: K_2CO_3	3614.3, 3620.7
pH 7, fast, RT,	3616
pH 7, slow, RT	3615.4, 3617.7
pH 7, fast, 60 °C	3615.4, 3617.7
pH 5, fast, RT,	3615.4, 3617.7
pH 7, fast, RT, 450 °C	3614.6, 3618.1
pH 7, slow, RT, 450 °C	3614.4, 3618.3
pH 7, fast, 60 °C, 450 °C	3614.6, 3618
pH 5, fast, RT, 450 °C	3614.6, 3618.1
pH 7, fast, RT, 500 °C	3614.3, 3619.5
pH 7, slow, RT, 500°C	3614.3, 3619.5
pH 7, fast, 60 °C, 500°C	3614.3, 3619.5
pH 5, fast, RT, 500 °C	3614.3, 3619.5

4.6. Elemental analysis of the FT catalyst with alkali metal promoters

Bulk analysis and surface elemental analysis for examination of the alkali promoters in iron oxide catalyst was performed. The bulk elemental analysis: XRF, SEM-EDX and surface analysis XPS have been used in the experiment.
The atomic percentages of the alkali metals for the iron oxide samples, before and after activation, were measured. The elemental analysis results are compared and presented in Tables 4.6.1 and 4.6.2.

The bulk EDX analysis for the iron oxide samples before reduction indicated the presence of Na in a range between 0.1 and 0.3 at%. The same analysis indicated between 0.1 at% and 0.2 atomic % of K promoter. For the samples with Rb between 0.4 at% and 0.5 at% of promoter was found, which was slightly higher than theoretical (0.3 at %).

The XRF experiment indicated the presence of alkali promoters in the bulk of the iron oxide samples before reduction. For the samples with Na and K promoters between 0.2 at% and 0.3 at% of alkali metals was found; and 0.2 at% for the samples with a Rb promoter. The XRF elemental characterization results were similar to the EDX and may confirm the results obtained by that technique. The results for both EDX and XRF techniques are presented in Table 4.6.1.

The surface XPS characterization for non-reduced iron oxide samples indicated the presence of Na in a range between 0.5 and 2.0 at% at the surface, which was higher than the theoretical data for bulk and the surface (0.3 at%). The XPS for samples with K promoter, synthesized in various conditions showed the presence of promoter for all the samples between 1.6 and 2.6 at%. The XPS for samples with Rb promoter, synthesized in various conditions proved the presence between 0.8 at% and 1 at%, which was also higher than the theoretical concentration.

The highest concentration (0.5 at%) of the alkali promoters in the bulk before activation was observed for the sample prepared at pH 7, fast titrant addition, 60 ^{o}C and for sample

synthesized at pH 7, fast titrant addition in room temperature with a Rb. The highest concentration of the alkali promoters on the surface (2.6 at %) was observed for the samples prepared in pH 7, slow titrant addition at room temperature with K.

The bulk and a surface elemental analysis for reduced samples were also carried out. The results for the samples reduced at different temperatures with Rb and Na promoter are listed in a Table 4.6.2. The XRF characterisation indicated similar to the theoretical concentration of the alkali metals in an iron oxide catalyst in a range between 0.2 and 0.4 at%. The highest concentration was noticed for the samples synthesised at pH 7, slow titrant addition in a room temperature after reduction in 400 ^{o}C.

The XPS analysis for reduced samples showed a visible increase in the concentration of alkalis in comparison to the non-reduced. The increase or the same concentration of alkalis with increase of the reduction temperatures was also observed. The atomic % for samples with Na and Rb reduced under hydrogen at 400 ^{o}C was between 3.5 and 4.6 at%. The iron oxide samples with Na and Rb reduced at 450 ^{o}C presented a higher concentration of alkali metals, between 3.6 at% and 5.0 at %. The exception was the sample synthesised at pH 7, fast titrant addition in room temperature with a Rb, which has slightly higher concentration of the Rb (3.8 at%) on reduction at 400 ^{o}C in comparison to the samples reduced at 450 ^{o}C with the same promoter, (maximum 3.7 at%).

Tab. 4.6.1 The EDX, XPS, XRF elemental analysis (at %) for non-reduced iron oxide samples synthesized in various conditions with different promoters

Conditions	**Atomic % of alkali metal, EDX**	**Atomic % of alkali metal, XRF**	**Atomic % of alkali metal, XPS**
at% theoretical	**0.3**	**0.3**	**0.3**
pH 7, fast, RT, **Na**	0.1[1]	0.2[2]	0.8[3]
pH 7, slow, RT, **Na**	0.3	0.3	2.0
pH 7, fast, 60 ^{o}C, **Na**	0.2	0.3	0.5
pH 7, fast, RT, **K**	0.2	0.2	1.6
pH 7, slow, RT, **K**	0.1	0.2	2.6
pH 7, fast, 60 ^{o}C, **K**	0.1	0.3	1.8
pH 7, fast, RT, **Rb**	0.5	0.2	1.0
pH 7, slow, RT, **Rb**	0.4	0.2	0.8
pH 7, fast, 60 ^{o}C, **Rb**	0.5	0.2	0.8

1. **EDX Standard deviation (S.D.) for Na, K and Rb promoters:** (0.1 - 0.3)
2. **XRF S.D for Na, K and Rb:** (0.03 - 0.1)
3. **XPS S.D for Na, K and Rb:** (0.05 - 1.3)

Tab. 4.6.2 The EDX, XPS, XRF elemental analysis for alkali promoters in iron oxide samples synthesized in different conditions with Rb and Na promoter after reduction in 400 ^{o}C and 450 ^{o}C

Conditions	Atomic %, XRF	Atomic %, XPS
pH 7, fast, RT, **Na**, 400 ^{o}C	0.2	4.6
pH 7, fast, RT, **Na**, 450 ^{o}C	0.2	5
pH 7, fast, RT, **Rb**, 400 ^{o}C	0.3	3.8
pH 7, fast, 60 ^{o}C, **Rb**,400 ^{o}C	0.3	3.5
pH 7, slow, RT,**Rb**,400 ^{o}C	0.4	3.6
pH 7, fast, RT, **Rb**, 450 ^{o}C	0.2	3.7
pH 7, fast, 60 ^{o}C, **Rb**,450 ^{o}C	0.2	3.6
pH 7, slow, RT,**Rb**,450 ^{o}C	0.3	3.7

In general, using bulk and surface sensitive quantitative analysis the surface enrichment of promoter depending on conditions and kind of promoter added was observed. The highest increase of the promoter on the surface was observed for the samples synthesised at pH 7, slow titrant addition in room temperature. The highest increase was observed for the samples with K promoter. There is a further enhancement of the promoter species on the surface due to the reduction process. The discrepancies which depend on conditions and kind of promoter were not as noticeable as for the non-reduced samples.

4.7 Conclusions

In this chapter, it was seen that the type of alkali metal used, the synthesis conditions, and methods of preparation of the iron oxide catalyst have a significant influence on the catalyst species. It was also discovered that reduction of iron oxide under hydrogen results in the development of different iron oxide species, (Chapter 4.2) and the migration of alkali metals to the surface. The alkali promoters influenced the activation process and especially the change of the reduction temperature of the FT catalysts. Two of them, K and Rb, cause a lowering, in comparison to Na, in the effective reduction temperature. For the iron oxide samples with Na promoter reduced at 400 ^{o}C for 20 h the Fe_3O_4 cubic phase was observed. For the samples with the same promoter transformation from Fe_3O_4 to Fe occurred at 450 ^{o}C. For the samples with K and Rb promoters the mixture of Fe_3O_4 and metallic iron after reduction at 400 °C was found. After further reduction at 450 ^{o}C, negligible Fe_3O_4 and predominant Fe were observed. The reduction process at 500 °C resulted in the further reduction of Fe_3O_4 to metallic iron and no presence of Fe_3O_4 was indicated.

After the reduction carried out at elevated temperatures (600 °C, 700 °C, and 800 °C) under 5% H_2/He for shorter time (1 hour), the FeO and/or $FeO_{(1-x)}$ phase were observed. The occurrence of other iron oxide species during the experiment carried out in higher reduction temperature for shorter periods in that part of the experiment was also discovered. The PXRD characterisation of the samples reduced for 1 hour at 600 ^{o}C yielded a mixture of cubic Fe_3O_4, FeO and Fe; at 700 ^{o}C showed cubic magnetite Fe_3O_4 and FeO; and at 800 ^{o}C only reflections characteristic for the metallic form of iron were observed, (Chapter 4.2). The alkali metals influence on the reduction temperature is significant not only on the iron oxide phase but also on the sulfur phase (behaviour of the sulfide promoters) as it is presented in Chapter 5.

The discrepancies in concentration of the alkali promoters due to the different conditions and synthesis methods prior to reduction were not significant. The largest alkali metal surface concentration was observed for the samples synthesised at pH 7, fast titrant addition at room temperature. However, the differences in intensity of the XPS spectra between non-activated samples prepared in different conditions with the same promoter were minor, (Chapters 4.3, 4.4).

The significant differences in XPS spectra intensity between non-reduced and reduced samples with different alkali promoters synthesized in different conditions were observed. The concentration of the promoters on the surface was substantially higher after reduction. The largest differences in surface concentrations were observed between non- reduced and reduced samples with the Na promoter. In general, the concentration of the alkalis at the surface increased with the reduction temperature.

The possibility of migration of the promoters to the surface during reduction was further confirmed using other bulk sensitive elemental analysis techniques like EDX and XRF and comparison with XPS. The EDX analysis for all the samples indicated amounts of alkali promoters close to the theoretical concentration (0.3 atomic %). The XPS analysis indicated higher concentration than theoretical by up to 2.8 atomic %. The bulk sensitive XRF analysis carried out for the non-reduced samples indicated between 0.2 and 0.3 atomic %, very similar to the theoretical concentration. The XRF analysis for all reduced samples similar concentration of alkali metals to these non-reduced indicated (between 0.2 and 0.4 atomic %).

The XANES technique was used to analyse properties of Na and K promoters (~0.3%) in the non-activated and activated iron oxide catalysts. The Na K-edge signal was difficult to analyse, because of the low energy, low concentration of sodium, and relatively short acquisition time (due to the degradation of the beryl monochromator). The amount of the K promoter was exactly the same as in the sample with Na promoter, but higher energy and longer acquisition facilitated the XANES experiment. The shape of the K K-edge XANES spectra was different prior to reduction and after, and changed with the increase of the reduction temperature. The splitting of K K-edge spectra was observed only for the activated catalyst and was more pronounced for the catalyst samples reduced at 450 ºC than those activated at 400 ºC. This indicates possible changes in the local environment during the increase of reduction temperature, like for example changes in the oxygen coordination number around the K^+ during the reduction process.

The SEM technique was employed to observe the influence of different alkali promoters and synthesis conditions on the surface morphology of the catalyst samples. The agglomerates for the samples with K were larger than those with Rb and Na promoters. The samples with Rb were had the most smooth surfaces. All catalyst samples had particles attached to the surface of larger agglomerates. The smallest particles were observed for the catalyst synthesized with the K promoter at 60 ºC.

4.8. References

1. Ngantsoue-Hoc W., Zhang Y., J. O'Brien R., Luo M., Davis H. *Appl. Catal. A-Gen.* 236 (2002) 77.
2. Kolbel H.,Giehring H., *Brennstoff-Chem.* 44 (1963) 343.
3. Dry M.E., Shingles T., Boshoff L.J. and Osthuizen G.J., *J. Catal.,* 15 (1969) 190.
4. Luo M., O'Brien R.J., Bao S., Davis B.H*., Appl. Catal. A-Gen.,* 239 (2003) 111.
5. Lee E.H., *Catal. Rev*. 8 (1973) 285.
6. Yang Y., Xiang H-W., Xu Y-Y., Bai L., Li Y-W., *Appl. Catal. A-Gen.,* 266 (2004) 181.
7. Bukur D. B., Mukesh D., Patel S,A., *Ind. Eng. Chem. Res.,* 29 (1990) 194.
8. Benzel H.P., Kerbs H.J., *Surf. Sci.*, 109 (1981) 527.
9. Miller D. G., Moskovits M., *J. Phys. Chem. Process Des. Dev.,* 22 (1983) 97.
10. Yang T., Wen X-D., Li Y-W., Wang J., Jiao H., *Surf. Sci.*, 603 (2009) 78.
11. Rankin J.L., Bartholomew C. H., *J. Catal.,* 100 (1986) 533.
12. Jiang M., Koizumi N., Yamada M., *Appl. Catal*. *A*., 204 (2000) 895.
13. Ndlela S. C., Shanks B. H., *Ind. Eng. Chem.,* Res.42 (2003) 2112.
14. Gaube J., Klein H.-F., *Appl. Catal. A- Gen. 1(2008)1*
15. An X., Wu B., Wan H.-J., Li T.-Z., Tao Z.-C., Xiang H.-W., Li Y.-W., *Catal. Commun.*,1 (2007) 1.
16. Li S., Krishnamoorthy S., Li A., Meitzner G. D., Iglesia E. *, J. Catal.,* 206 (2002) 202.
17. Sadykov V.A., Isupova L.A, Tsybulya S.V., Cherepenova S.V., Litvak G.S., Burgina E.B., Kustova G.N., Lolomiichuk V.N., Ivanov V.P., Paukshtis E.A., Golovin A.V., Avvakumov E.G., *J.Solid State Chem.*, 123 (1996) 191.
18. Yu S.-C., Lee J.-S., Tung S.-F., Lan C.-L., *J. Geol. Soc.,* China, 42 (1999) 349.
19. Baron V.; Gutzmer J.; Rundloef H.; Tellgren R.; *Solid State Sci.,* 7 (2005) 753.
20. Kelm K., Mader W., *Z. Anorg. Allog. Chem.,* 631 (2005) 2383.
21. Rozenberg G.Kh., Dubrovinskii L.S., Pasternak M.P., Naaman O., Le Bihan T., Ahuja R.,*Phys. Rev.B.Condens. Matter.,* 65 (2002) 064112.

22. Diego Gatta G., Kantor I., Boffa Ballaran T., Dubrovinsky L., McCammon C., *Phys. Chem. Miner.* 34 (2007) 627.
23. Kuriki A., Moritomo Y., Ohishi Y., Kato K., Nishibori E., Takata M., Sakata M., Hamada N., Todo S., Mori N., Shimomura O., Nakamura A., *J. Phys. Soc. Jap.* 71 (2002) 3092.
24. Basta E.Z., *Mineral. Mag.,* 31 (1957) 431.
25. O'Neill H.C., Dollase W.A., *Phys. Chem. Miner.,* 20 (1994) 541.
26. Tombs N., *Acta Crystallogr*., 4 (1951) 474.
27. Fleet M.E., *J. Solid State Chem.,* 62 (1986) 75.
28. Hanawelt et al., *Anal. Chem*. 10 (1938) 475.
29. Gorton A.T., Bitsianes G., Joseph T.L., *Trans. Met. Soc*. , 233 (1965) 1519.
30. Davey W.P., *Phys.Rev*., 25 (1925) 753.
31. Hull A.W., *Phys.Rev*., 10 (1917) 661.
32. Fjellvag H., Gronvold F., Stolen S., Hauback B., *J. Solid State Chem*., 124 (1996) 52.
33. Willis B.T., Rooksby H.P*., Acta Crystallogr*., 6 (1953) 827.
34. Shchukarev A.V., Korolkov D.V., *Centr. Eur. J. Chem.,*, 2 (2004) 347.
35. Siriwardene R. V., Cook J. M., *J. Colloid Interface Sci*. 104 (1985) 250.
36. Hammond J.S., Holubka J.W., Devries J.E., Duckie R.A., *Corros. Sci.* 21, (1981) 239.
37. Moulder J.F., Stickle W.F, Sobol P.E., Bomben K.D., *Handbook of X-ray Photoelectron Spectroscopy,* published by Perkin-Elmer Corp., 1992, MN, USA
38. Turner N.H., Murday J.S., Ramaker D.E., *Anal. Chem.,* 52 (1980) 84.
39. Seyama H., Soma, M., J. *Chem. Soc*. *Faraday Trans*., 81 (1985) 485.
40. Kohiki S., Ohmura T., Kusao K., *J. Electron Spectrosc. Relat. Phenom.,* 31 (1983) 85.
41. Schlogl R., Geiser V., Oelhafen P., Guntherodt H.-J., *Phys. Rev. B*., 35, (1987) 6414.
42. Estrade-Szwarckopf H., Rousseau B., *Synthetic Metals*., 23, (1988) 191.
43. Danno T., Shiozawa K., Haluska M., Kuzmany H., *Carbon Vol.,* 36 (1998) 617.
44. Li S., Kang E.T., Neoh K.G., Ma Z.H., Tan K.L., Huang W., *Appl. Surf. Sci.*, 181, (2001) 201.

45. Blass P. M., Zhou X.-L., White J. M., *J. Phys. Chem., 94 (I990) 1*
46. Jain H., Kamitsos E.I., Yiannopoulos Y.D., Chryssikos G.D., Huang W.C., Kichler R., Kanert O., *J. Non-Crystalline Solids,* 203 (1996) 320.
47. Garbout A., Bouattour S., Botelho do Rego A.M., Ferraria A., Kolsi A.W., *J., Cryst. Growth,* 304 (2007) 374.
48. Jun K., Hirohiko A., Shinjiro H., Song Y.Z., Kazuo K., Yohichi G., Kuniko M., Yoshinori K., *Spectrochim. Acta, Part B: Atom. Spectrosc*., 49 (1994) 739.
49. Weiss W., Ranke W., *Prog. Surf. Sci.,* 70 (2002) 1
50. Wispelaere S., Cabaret D., Levelut C., Rossano S., Flank A.-M., Parent P., Farges F., *Chem. Geol.,* 313 (2004) 63.
51. Castro A. R., Kolmakov A., Lofken J. O., Nowak C., Soldatov A. V., Wark A., Yalovega G., Moller T., *J. Chem. Phys*., 115 (2001) 1319.
52. Prado R.J., Flank A.M., *Phys. Scripta,* 115 (2005) 165.
53. Yamasha H., Yoshida S., Tomita A., *Ind. Eng. Chem. Res*., 30 (1991)1651.
54. Yang X.Q., Chen J.M., *Phys. Rev. B.,* 40 (1989) 7948.
55. Marcelli A.,. Cibina G, Cinquea G., Mottanaa A., Brigattic M. F., *Radiat. Phys. Chem.*, 75 (2006) 1596.
56. Lavrentyev A.A., Gabrelian B.V., Nikiforov I.Y., Rehr J.J., *J. Phys. Chem. Solids*, 60 (1999) 787.
57. Cibin G., Mottana A., Marcelli A., Brigatti M. F., *Mineral. Petrol.,* 85 (2005) 67.
58. Gatehouse B.M., Lloyd D.J, *J. Chem. Soc., Dalton Trans.*, 1 (1973) 70.
59. Parratt L.G., *Rev. Mod. Phys*., 31 (1959) 616.
60. Parratt L.G., Jossem E.L., *J. Phys. Chem. Solids,* 2 (1957) 67.

Chapter 5

Sulfur in FT iron-based catalysts

5.1 Sulfur in FT iron-based catalysts

The study of the role of different sulfur species and their transformations is very important in industry, especially in the field of catalysis. As was mentioned above in the introduction chapter, sulfur containing compounds are well known to exert an inhibiting or poisoning effect in catalysts. Sulfur structures may decrease or even suppress the reactivity of the metal catalyst.

Bromfield and Coville[1] suggested that reduction to metallic iron in the presence of sulfur led to the formation of poisonous sulfide species. Higher temperatures affected the conversion of sulfate (SO_4^{2-}) to sulfide. Catalysts with sulfide species at the surface showed effects of poisoning, while catalysts with the sulfates exhibited an enhancement in activity. The catalysts with higher sulfide concentration will be most likely poisoned[1-7]. However, it has been proven that catalysts with very low amount of sulfide (up to 500 ppm) can be more active in the Fischer–Tropsch reaction than a sulfur-free catalyst[4-7]. Baoshan et al. (2004) also reported[6] that a small amount of sulfate species may promote the catalyst by increasing activity and improving the heavier hydrocarbon selectivity. Thus that is also very important the strict control of sulfur levels in the feedstock gases. The amount of allowable sulfur in the FTS is in the order of a few ppb (less than 5 ppb)[7]. Thus, examination of the concentration and oxidation state of sulfur can be a very important source of information in a study of the nature of the catalyst used in FTS. Moreover, it helps distinguish different molecular species of the element and understand electron transfers during reaction progressions[8]. Most of these transformations of S effect changes in oxidation states in the range from -2 to +6. The determination of the oxidation state of sulfur in the catalyst should help indicate the possibility of a poisoning effect or promoting properties of the sulfur additive.

The synthesis conditions, the methods of preparation of the iron oxide catalysts, and the amount of sulfur added in the pre-treatment[9,10] may have a significant influence on the sulfur and iron oxide species existing in the catalyst[11]. The nature of these species may affect the catalyst behaviour[5,12,13].

The main aim of this stage of the study was to investigate the existence and the proportion of sulfur ions and their specific nature in an iron oxide catalyst. The sulfate was added during the precipitation step in catalyst preparation. The precipitation was conducted in different conditions: different temperatures, slow and fast titrant addition rates and different pH values. The sulfur species in the iron oxide catalysts were determined by the use of XPS, XANES, SEM-EDX, XRF, before and after activation.

5.2 X-Ray photoelectron spectroscopy examination (XPS) of the S (2p) core-level spectrum for iron oxide samples

PXRD analysis of iron oxide samples with alkali promoters before activation was carried out previously and indicated haematite, an iron III oxide structure (Fig.2, chapter 4). The small concentration of sulfur (0.05 ppm), which was co-precipitated with the catalyst as a promoter, was examined by XPS. The aim of this part of the experiment was to show how different synthesis methods and conditions significantly affected the nature and concentration of the sulfur species present before and after reduction.

5.2.1 XPS results of the S (2p) core-level spectrum for iron oxide samples with Na promoter, before activation

The sulfur bonding states have been summarized from published references and are listed in Table 5.2.1. The S $2p_{3/2}$ binding energies presented covered an energy range from 160.8 to 170.7 eV. The peak observed in the range 160.8-162.9 eV was assigned to sulfides (S^{2-} monomers or S_2^{2-} dimers)[14-20] and that in the range 163.8 - 164.35 eV to elemental sulfur[21-23]. The reported peak of sulfites[14,24-26] is centred within the range of 166.4 - 167 eV. The binding energies of sulfates[14,24,25,27] was centred within the range of 168.0 - 168.8 eV and these of thiosulfates in the range 167.0 - 168.8 eV. Reference samples ($FeSO_4$, Rb_2SO_4 and FeS) were also analyzed, the binding energies of which are noted in the table below (5.2.1).

Tab. 5.2.1. Binding energies of the S 2p $_{3/2}$ eV core level in relation to the sulfur bonding

Material	Species	BE S 2p $_{3/2}$ eV	Reference no.
Iron (II) sulfide (FeS)	S^{2-}	160.8 – 161.4	[14-16]
Iron (II) sulfide (FeS_2)	S^{2-}, S_2^{2-}	162.4 - 162.9	[17-20]
Sulfur S_8	S^0	163.8 – 164.35	[21-23]
Sodium sulfite (Na_2SO_3)	SO_3^{2-}	166.4 - 167	[14, 24-26]
Sodium Thiosulfate ($Na_2S_2O_3$)	$S_2O_3^{2-}$	167.0 – 168.8	[14, 24, 25]
Iron (II) sulfate ($FeSO_4$)	SO_4^{2-}	168.6 – 168.8	27
Sodium Sulfate (Na_2SO_4)	SO_4^{2-}	168.6 – 168.8	[14, 24, 25]
Ammonium Sulfate $(NH_4)_2(SO_4)$	SO_4^{2-}	168.0 – 168.2	14
$FeSO_4$	SO_4^{2-}	168.8	this study
Rb_2SO_4	SO_4^{2-}	168.7	this study
FeS	S^{2-}	162.1	this study

The XPS for all the samples with Na promoter were synthesized in different conditions are presented in Fig.5.2.1. The S (2p) binding energies for all Na promoted samples are observed between 169.0 eV and 169.3 eV, the region typical for sulfates[14-27]. The sample synthesized at pH 7, fast titrant addition at 60^{o}C, and pH 7, fast titrant addition in room temperature has the highest binding energy. Quantification of the amount of sulfur present for the different samples shows the smallest amount of 0.1 at% S for the sample with slow titrant addition rate and the highest amount of 0.3 at% for the sample synthesized at pH 9, fast titrant addition rate in RT. The sulfur concentration for all the samples was higher than the expected theoretical value of 0.05 at%. All results are summarised in Table 5.2.3.

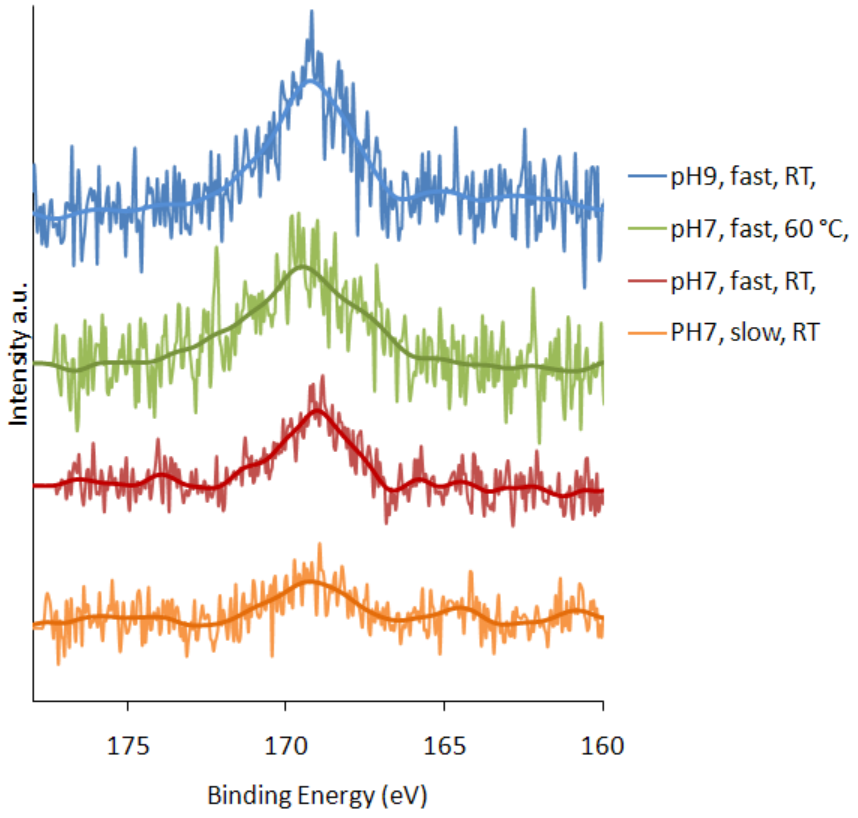

Fig.5.2.1. The S(2p) XPS spectra of samples with Na promoter before activation; from the top: pH 9, fast titrant addition, RT (blue line, experiment and fit), pH 7, fast titrant addition, 60 ^{o}C (green), pH 7, fast titrant addition, RT (red), pH 7, slow titrant addition, RT (orange).

5.2.2 The S (2p) XPS characterization for iron oxide samples with K promoter, before activation

The S (2p) spectra signal was also noisy like for the samples with Na promoter. However it can be observed in Figure 5.2.2 that the binding energies of S (2p) for iron oxide samples with K promoter before activation are between 168.7 eV and 168.8 eV, indicating sulfates. There was also observed small peak in BE 163.5 eV, which may indicate presence of elemental sulfur. A small shift to a higher energy was observed for the samples synthesised at pH 7, prepared with slow and fast titrant addition rate in room temperature.

The area under the S (2p) peak for the sample with slow titrant addition, was smaller in comparison to the rest of the samples, i.e. the atomic percentage of the sulfur observed was 0.1 at%, whereas for the rest an amount of 0.2 at% was determined.

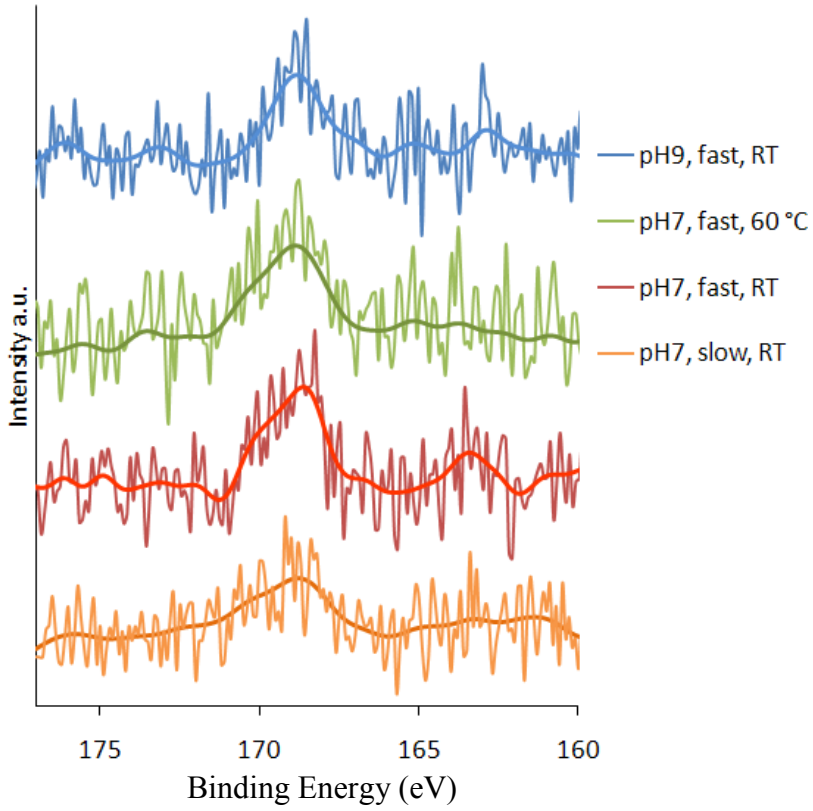

Fig. 5.2.2 XPS S(2p) spectra of samples with K promoter before activation; from the top: pH 9, fast titrant addition, RT (blue), pH 7, fast titrant addition, 60 ^{o}C (green), pH 7, fast titrant addition, RT (red), pH 7, slow titrant addition, RT (orange).

5.2.3 The S (2p) XPS characterization for iron oxide samples with Rb promoter, before activation

The binding energies of S (2p) for the samples with a Rb promoter before activation prepared under various conditions are between 168.7 eV and 168.8 eV, i.e. sulfates region, as can be seen in Fig. 5.2.3. The area under the S (2p) peak for the sample synthesised at pH 7, co-precipitation temperature 60 ^{o}C, was smaller than for the rest of the samples synthesized with the same promoter. The atomic percent for that sample was less than 0.1 %. The differences between binding energies of S (2p) for the iron

oxide samples with Rb promoter, prepared in different conditions are difficult to determine owing to the small signals with noise, (S.D. = 0.08 – 0.15).

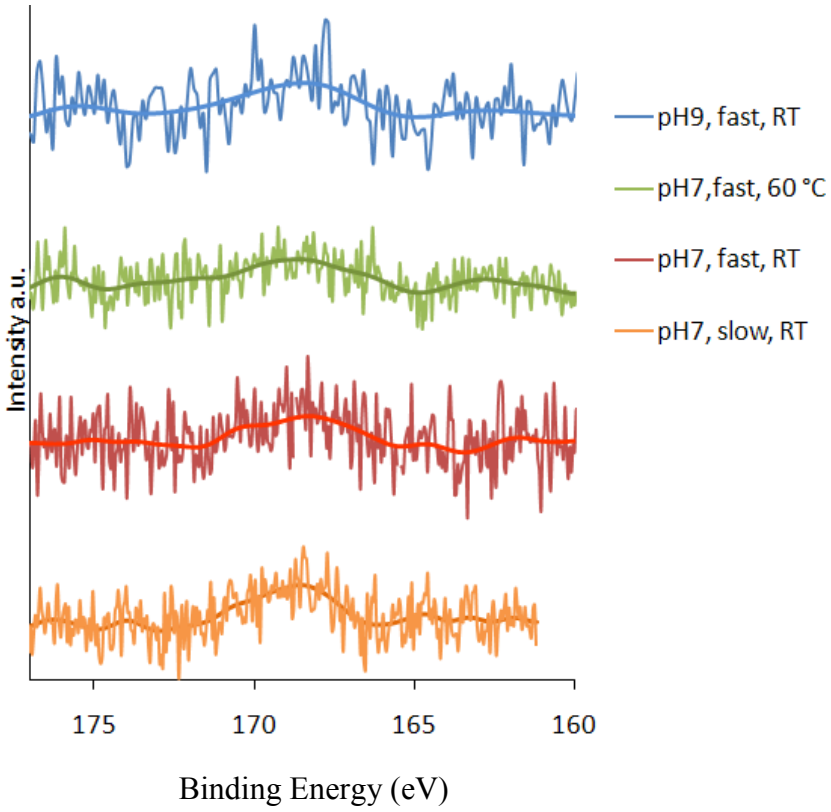

Fig. 5.2.3 XPS S(2p) spectra of samples with a Rb promoter before activation; from the top: pH 9, fast titrant addition, RT (blue), pH 7, fast titrant addition, 60 ^{o}C (green), pH 7, fast titrant addition, RT (red), pH 7, slow titrant addition, RT (orange).

Tab. 5.2.3. The XPS peak positions for iron oxide catalyst non-reduced samples with different promoters, prepared in different conditions

Conditions	Peak Position, eV	Atomic %, XPS
pH 9, fast, RT, Na	169.1	0.3[1]
pH 7, fast, 60C, Na	169.2	0.2
pH 7, fast, RT, Na	169.0	0.2
pH 7, slow, RT, Na	169.1	0.1
pH 9, fast, RT, K	168.8	0.2
pH 7, fast, 60C, K	168.8	0.2
pH 7, fast, RT, K	163.5, 168.7	0.05, 0.2
pH 7, slow, RT, K	168.7	0.1
pH 9, fast, RT, Rb	168.8	0.1
pH 7, fast, 60C, Rb	168.8	0.05
pH 7, fast, RT, Rb	168.8	0.1
pH 7, slow, RT, Rb	168.7	0.1

1. **XPS S.D. for the Na, K:** (0.08 – 0.15)

All of the samples were loaded with an amount of 0.05 at% sulfur. The XPS analysis of Na promoted samples before activation revealed the presence of that element in a range between 0.1 and 0.3 at% of sulfur. For samples promoted with K the presence of the sulfate in the range 0.1 - 0.2 at% was derived for all the samples. Rb promoted samples showed 0.1at% of sulfur for most of the samples with exception for the sample synthesised at pH 7, fast titrant addition at 60 ^{o}C where sulfate was not detected.

For all the samples prepared with K and Rb promoters there is a small shift of the range 0.1 -0.6 eV to a lower binding energy in comparison to the iron oxide samples prepared with Na promoter. The same shift between samples with K and Rb promoter was not observed which may be explained by smaller differences in ionic radius between K and Rb, than between Na and K. It could be observed that the binding energies of S 2p for sulfate (SO_4^{2-}) ion decreased down the alkali group as influenced by the inter-atomic effect (the ionicity of $M^+ SO_4^{2-}$)[28].

5.2.4.1 The S (2p) XPS characterization for iron oxide samples with Rb and Na promoter, after reduction in 400 ^oC (H_2/He)

In the next stage of the experiment the changes in the sulfur speciation during the activation process were examined with XPS. The characterisation of the S (2p) for the iron oxide catalysts with Rb promoter activated under 5% H_2/He at 400 ^oC and 450 ^oC were performed. As for non-reduced samples, as can be seen in Fig.5.2.4.1, the binding energies of S (2p) were observed between 168.0 eV and 168.7 eV, in the region typical for sulfates[14,24-27]. Moreover, for all the samples except that prepared at pH 7, co-precipitated at 60 ºC, a significant second peak at 162.2-162.3 eV was observed. The peak position suggested that for samples reduced at 400 ^oC sulfides[14-20] species are also present on the surface, which were not observed before for non-reduced samples.

The amount of sulfur and sulphate differs between samples from different synthesis procedures. As a comparison to the samples with Rb, a Na promoted sample synthesised in pH 7, fast titrant addition rate, room temperature reduced at the same temperature is also shown in Figure 5.2.4.1 For the sample prepared with Na promoter both a sulfate peak (168.3eV), and a sulfide one (162.5 eV) were also observed. The area under the sulfide peak for that sample was slightly larger than for the samples with Rb promoter, i.e. a lower sulfate/sulfide ratio. The peak positions and sulfate/sulfide ratios for all activated samples are presented in Table 5.2.4.

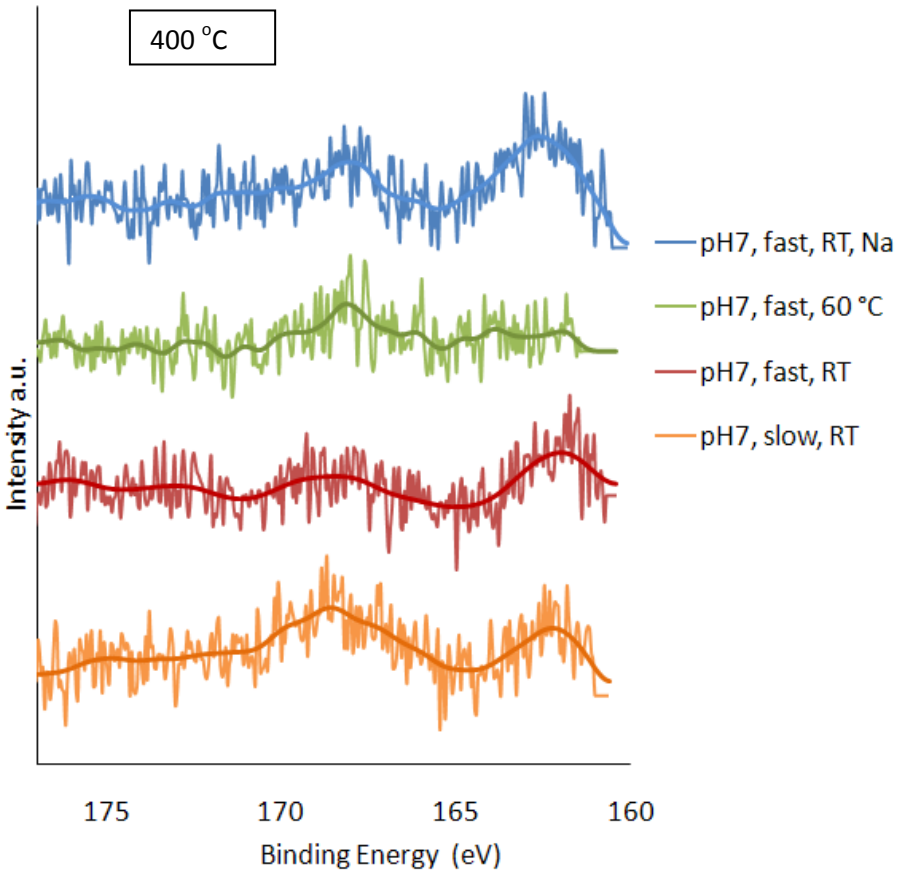

Fig. 5.2.4.1 XPS S(2p) spectra of samples with Rb promoter after activation in 400 °C; from the top: Na, pH 7, fast titrant addition, RT (blue); Rb, pH 7, fast titrant addition, 60 °C (green); Rb, pH 7, fast titrant addition, RT, (red), Rb, pH 7, slow titrant addition, RT(orange).

5.2.4.2 The S (2p) XPS characterization for iron oxide samples with Rb promoter, after reduction in 450 °C (H_2/He)

For the samples prepared under various conditions with Rb promoter, reduced at 450 ºC, sulfate peaks between 168.1 and 168.8 eV were still observed, Figure 5.2.4.2 but also all the samples showed a sulfide peak at 162.0-162.5 eV. The lowest area under the sulfate peak was observed for the sample prepared at pH 7, fast titrant addition rate, room temperature as was the case for the samples prepared in the same conditions and reduced at 400 °C. For the same sample the highest amount of sulfide was observed. For the sample with Na promoter reduced at 450 °C, a broad sulfate peak and even bigger area under the sulfide peak compared to the samples with Rb was observed. The sulfate peak for the samples with Na was not shifted in comparison to the samples with Rb, Figure 5.2.4.2.

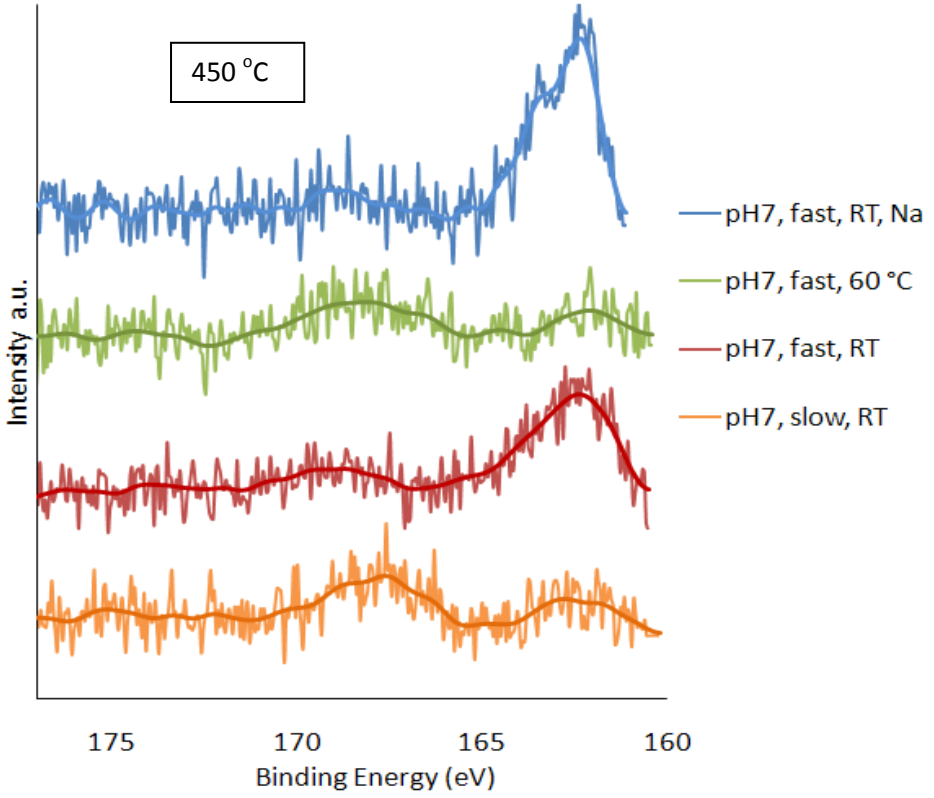

Fig. 5.2.4.2. XPS S(2p) spectra of samples with Rb promoter after activation in 450 °C; from the top: Na, pH 7, fast titrant addition, RT (blue); Rb, pH 7, fast titrant addition, 60 °C (green); Rb, pH 7, fast titrant addition, RT, (red), Rb, pH 7, slow titrant addition, RT(orange).

There was a bigger sulfate/sulfide area ratio for samples prepared in different conditions and reduced at 400 ^{o}C with Rb in comparison with the samples reduced at 450 ^{o}C. For all the samples with Rb promoter reduced at 400 ^{o}C the average ratio of areas under the sulfate/sulfide peaks was 1.6, and for those reduced at 450 ^{o}C it was 1.2.

The XPS analysis for reduced samples showed an increase in the concentration of sulfur in comparison to these non-reduced. There were no observed discrepancies in atomic percent for the samples activated in two different temperatures. The atomic % for samples reduced under hydrogen at 400 ^{o}C was between 0.1 and 0.4 at% and in the same range for the samples reduced in 450 ^{o}C was observed. A slightly smaller overall concentration of sulfur species was observed for the sample with slow titrant addition at the room temperature reduced in higher temperature than for the rest of the samples with Rb. The atomic percentages of sulfur species are presented in the Table 5.2.4.2.

Tab. 5.2.4.2. The XPS elemental analysis of S (overall sulfate and sulfide) in iron oxide samples synthesized in different conditions with Rb promoter after reduction in 400 ^{o}C and 450 ^{o}C

Conditions	Atomic %, XPS, after reduction in 400 ^{o}C	Atomic %, XPS, after reduction in 450 ^{o}C
pH 7, fast, RT, Na	0.4	0.4
pH 7, fast, 60 ^{o}C, Rb	0.1	0.1
pH 9, fast, RT, Rb	0.4	0.4
pH 7, slow, RT, Rb	0.4	0.3

1. **XPS S.D for the Na, K and Rb (reduced samples):** (0.08 – 0.15)

In general, this part of the experiment showed that two main phenomena may occur. The full transformation for the samples synthesised at pH7, fast titrant addition in room temperature with Na and Rb, reduced at 450 ^{o}C or partial transformation of sulfate species into sulfides upon in H_2/He for two another samples was observed. Only small decrease of sulfide species for the samples precipitated with slow titrant addition was noticed which can be explained by a partial release of sulfur as gaseous H_2S. However, a further changes of sulfide species concentration for samples reduced at 450 ºC compared to 400 ºC was not noticed. The ratios for all the samples are tabulated in below in the Table 5.2.4.3.

Tab.5.2.4.3 The peak positions, area under the peak sulfate/sulfide ratio and oxidation state for samples with Na and Rb promoters reduced at 400 ^{o}C and 450 ^{o}C.

Conditions	Peak Position, eV	Area under the peak, sulfate/sulfide ratio	Formal Oxidation State
pH 7, fast, RT, 400 ^{o}C, Na	168.3, 162.5	0.6	+6, -2
pH 7, fast, 60 ^{o}C, 400 ^{o}C, Rb	168.0 -	-	+6
pH 7, fast, RT, 400 ^{o}C, Rb	168.6, 162.2	0.5	+6, -2
pH 7, slow, RT, 400 ^{o}C, Rb	168.7, 162.3	2.9	+6, -2
pH 7, fast, RT, 450 ^{o}C, Na	- 162.0	-	+6, -2
pH 7, fast, 60 ^{o}C, 450 ^{o}C, Rb	168.2 162.2	2.0	-2
pH 7, fast, RT, 450 ^{o}C, Rb	168.8, 162.0	0.2	+6, -2
pH 7,slow, RT, 450 ^{o}C, Rb	168.1, 162.5	2.1	+6, -2

5.3. Sulfur X-ray absorption near-edge structure (XANES) spectroscopy

X-ray absorption near-edge structure (XANES) spectroscopy provides a significant non-destructive tool for the investigation of oxidation states and chemical speciation. In this part of experiment, the sulfur oxidation states in different iron-oxide catalysts were derived from S K-edge XANES. The near-edge region of the S K-edge spectrum is dominated by dipole-allowed bound-state transitions of the 1*s* electron to vacant molecular p-orbitals. The near-edge spectrum thus provides a sensitive probe of electronic structure and hence of chemical form[29].

For the S K-edge of the sulfur species in the analysed catalysts there is a clearly visible shift of the absorption edge to the higher energy with increasing oxidation state[30,31]. For these studies the samples were reduced up to 400°C.

XANES spectra were measured at the LUCIA beamline, Swiss Light Source (SLS), Villigen, Switzerland and I18 at the Diamond Light Source in Oxfordshire, England.

5.3.1 Sulfur XANES for samples with Na promoter before and after activation

5.3.1.1 The iron oxide phase determination by P-XRD before XANES experiment

The powder X-Ray diffraction method was used to determine the crystallinity of the samples as well as the structure of the iron oxides containing low concentrations of sodium and sulfur. The reflections in all samples, before reduction, correspond to those of the haematite structure of iron oxide (Fe_2O_3), Fig.5.3.1.1. After reduction at 100 °C for 12 h, no structural changes in the sample were found (it remained as Fe_2O_3). After subsequent reduction from 300 °C, the structure of iron oxide changed to Fe_3O_4. After

the reduction at 350 and 400 ^{o}C the crystallinity of Fe_3O_4 was higher and at 450 ^{o}C the iron oxide catalyst was transformed to the metallic iron. The changes during activation of the catalyst are shown in Figure 5.3.1.1.

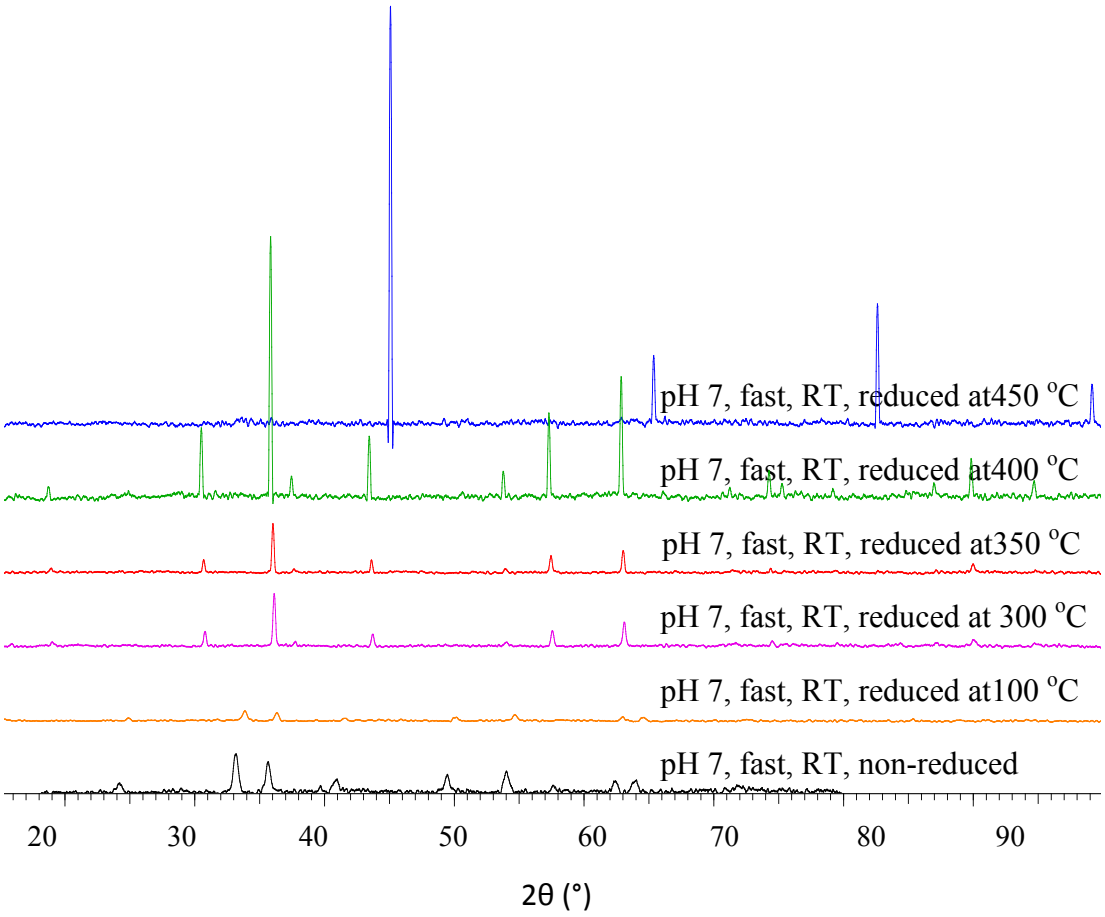

Fig. 5.3.1.1. Powder X-ray diffraction of iron catalysts with Na promoter, prepared with the use of different methods, after and before reduction.

5.3.1.2 The S K-edge XANES

Sulfur exhibits particularly rich XANES spectra, due to the relatively sharp line widths (good experimental resolution) and the large chemical shift range (of some 13 eV) over its range of oxidation states (−2 to +6)[32-35]. The S K-edge XANES spectra enabled empirical determination of the sulfur oxidation state by comparison of the analyzed iron-oxide catalyst samples with model compounds. The fingerprint reference compounds used were: Na_2SO_4, $FeSO_4$, Na_2SO_3, FeS, and S_8. All XANES spectra of reference samples are presented in Figure 5.3.1.2. The peak positions and oxidation state for reference samples are tabulated in Table 5.3.1.2.

Na_2SO_4 has a characteristic main peak at 2483.4 eV (indicative of S^{6+})[29-35]. The $FeSO_4$ reference sample has its main peak in the same region as Na_2SO_4 as expected since this is also S^{6+}. A small feature at 2480.5 eV was also observed, which suggest amount of reduced S being present (S^{4+}). Na_2SO_3 had characteristic peaks at 2479.2 eV and 2482.8 and a small peak between at 2480.8 eV. The peaks at 2479.2 eV and 2482.8 eV correspond to the SO_3^{2-} and SO_4^{2-} ions respectively, i.e. S^{4+} and S^{6+}[29]. The S_8 and FeS have S K-edge spectra at 2473.2 eV and 2472.0 eV, characteristic for S^{2-} and S^0, as was confirmed in the literature sources[29-35]. The differences in the shape and the position of S K-edge references used in a experiment was observed, prooving that the technique is sensitive for different oxidation states of sulfur[34,35].

The shift in binding energies of the spectrum is determined by effective nuclear charge Z_{eff} of the ions of analysed catalyst with the sulfur additives. The oxidation state changes are directly related with Z_{eff}, thus an increase in edge energy with to increasing oxidation state from S^{2-} for FeS, S^0 (S_8) up to SO_4^{2-} (S^{6+}) is observed. There is a different intensity and the shape of the S K-edge XANES differs for the different references samples, which is related to dipole allowed core-valence transitions 1s → 3p. The occupation of the p orbital varies for Na_2SO_4, $FeSO_4$, Na_2SO_3, FeS, and S_8. There is a different number of p orbital holes for sulfur compounds presented above: S^{2-} $3s^23p^6$,(0 holes); S^0 $3s^23p^4$, (2 holes); S^{4+} $3s^23p^0$,(6 holes); S^{6+} $3s^03p^0$(6 holes), Figure 5.3.1.2.

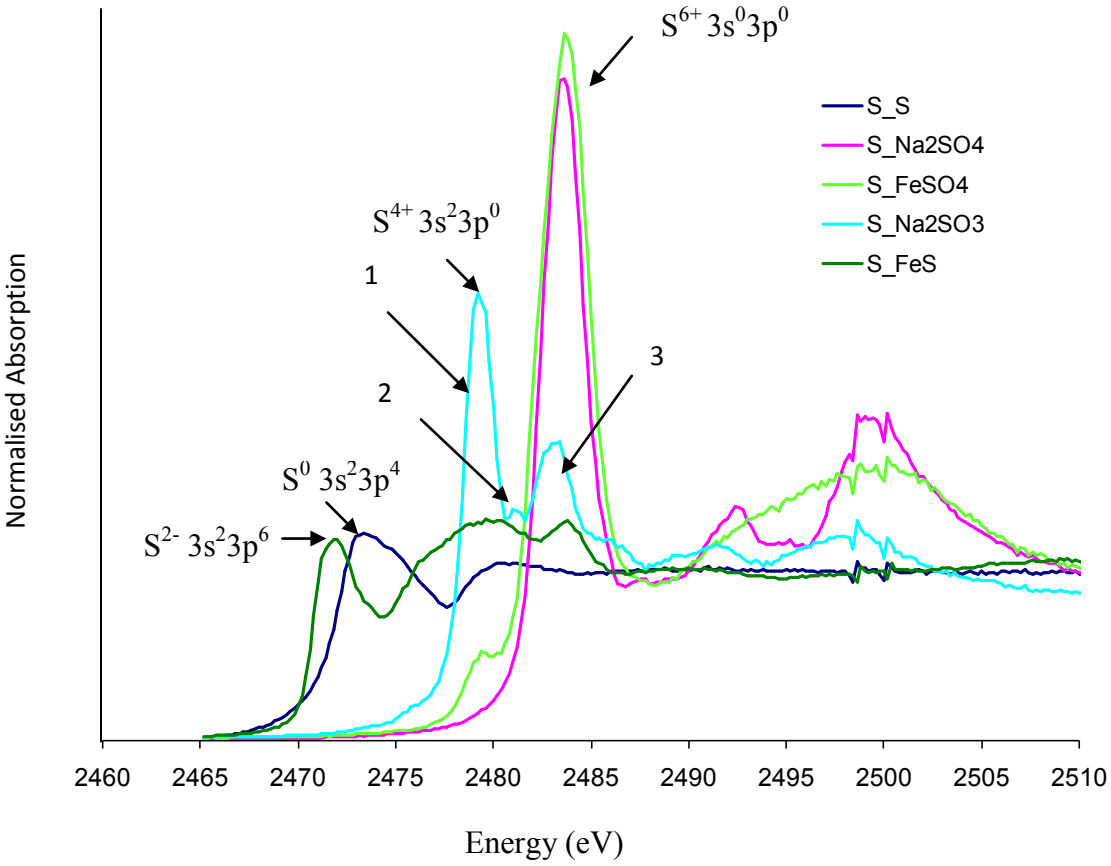

Fig.5.3.1.2. The S K-edge XANES spectra for reference compounds (FeS, S_8, Na_2SO_3, Na_2SO_4, $FeSO_4$).

Tab. 5.3.1.2 Sulfur containing reference compounds, their peak positions and oxidation state.

Standard	Compound	Chemical Formula	Peak Position, eV	Formal Oxidation State
Troilite	Iron sulfide	FeS	2472.0	-2
Sulfur	Elemental Sulfur	S_8	2473.2	0
Sulfite	Sodium sulfite	Na_2SO_3	**2479.2**	+4
			2482.8	
Sulfate	Sodium sulfate	Na_2SO_4	**2483.4**	+6
Sulfate	Iron (II) sulfate	$FeSO_4$	2479.4	+4, +6
			2483.6	

Bold – main peak

5.3.1.3 The S K-edge XANES analysis for non-reduced samples with Na promoter

The first S K-edge XANES experiment was carried out at the Lucia of Swiss Light Source station. The samples synthesized in various conditions were examined to study the S oxidation state as a function of method of preparation. Figure 5.3.1.3 a displays the S K-edge XANES spectra for all the samples prepared under different conditions.

The main, high intensity peak position for all the synthesized samples, before reduction, was registered in the range between 2483.3 eV and 2483.5 eV, Fig.5.3.1.3 a, corresponding to that of the SO_4^{2-}, Table 5.3.1. There was also a smaller peak at 2473.5

eV which corresponded to that of sulfur in the "0" oxidation state, observed. In the spectra of the sample synthesized at pH 7, fast titrant addition rate, room temperature, was most pronounced. A small hump was also observed for all the samples at 2480.5 eV, which indicates a small amount of reduced sulfur species in the "+4" oxidation state. The peak positions of samples synthesized at different conditions for non-reduced samples are in the Table 5.3.1.5 a.

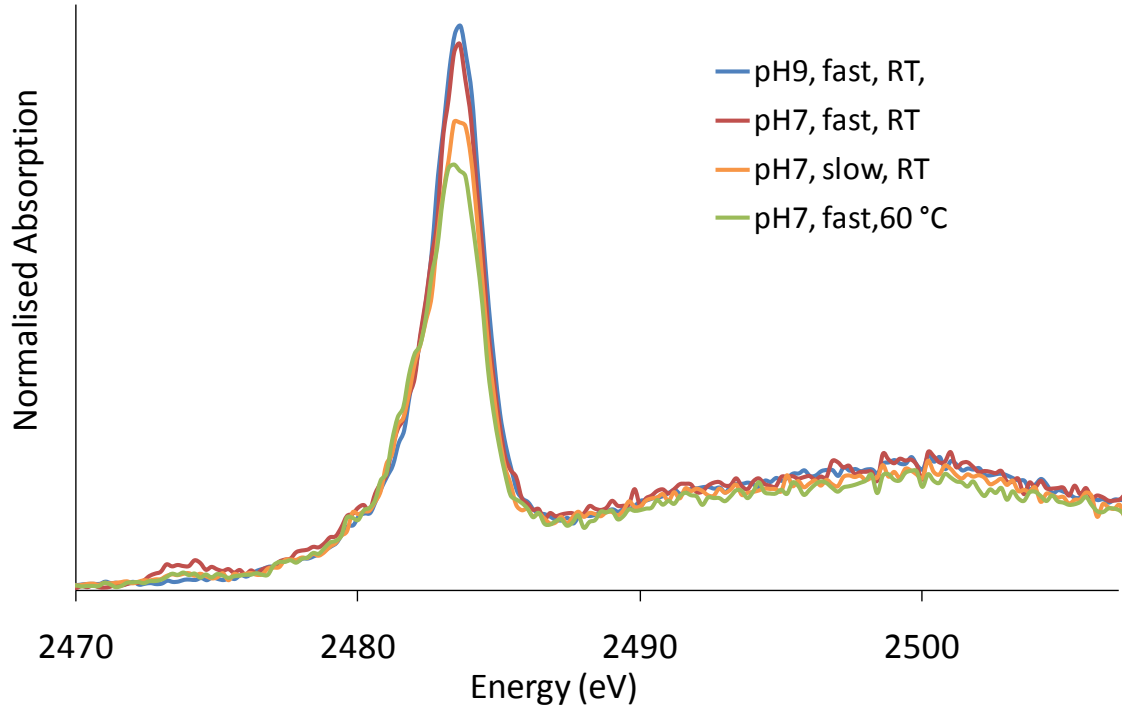

Fig.5.3.1.3 a Comparison of S K-edge XANES spectra for samples prepared with Na promoter, before reduction, in different conditions.

In Figures 5.3.1.3 b and c samples synthesised at pH 7 and pH 9 with fast titrant addition in room temperature are compared to $FeSO_4$, Na_2SO_4 and S references. The main peak at 2483.4 eV and a broad peak between 2489 eV and 2505 eV characteristic for sulfates

were observed for both iron catalyst samples. There is also a clearly visible small hump at 2480.5 eV (typical for S^{4+}) and a peak at 2473.5 eV characteristic for sulfur "0" for

the sample synthesized at pH 9, fast titrant addition rate, room temperature. There was a slight reduction observed in the beam (experiment done in time in the beam) of the $FeSO_4$, which was not observed for the Na_2SO_4 reference. The same was noticed for the experimental samples. This might be an indication that S is associated directly to Fe. The XANES is the only technique with which this phenomenon was noticed.

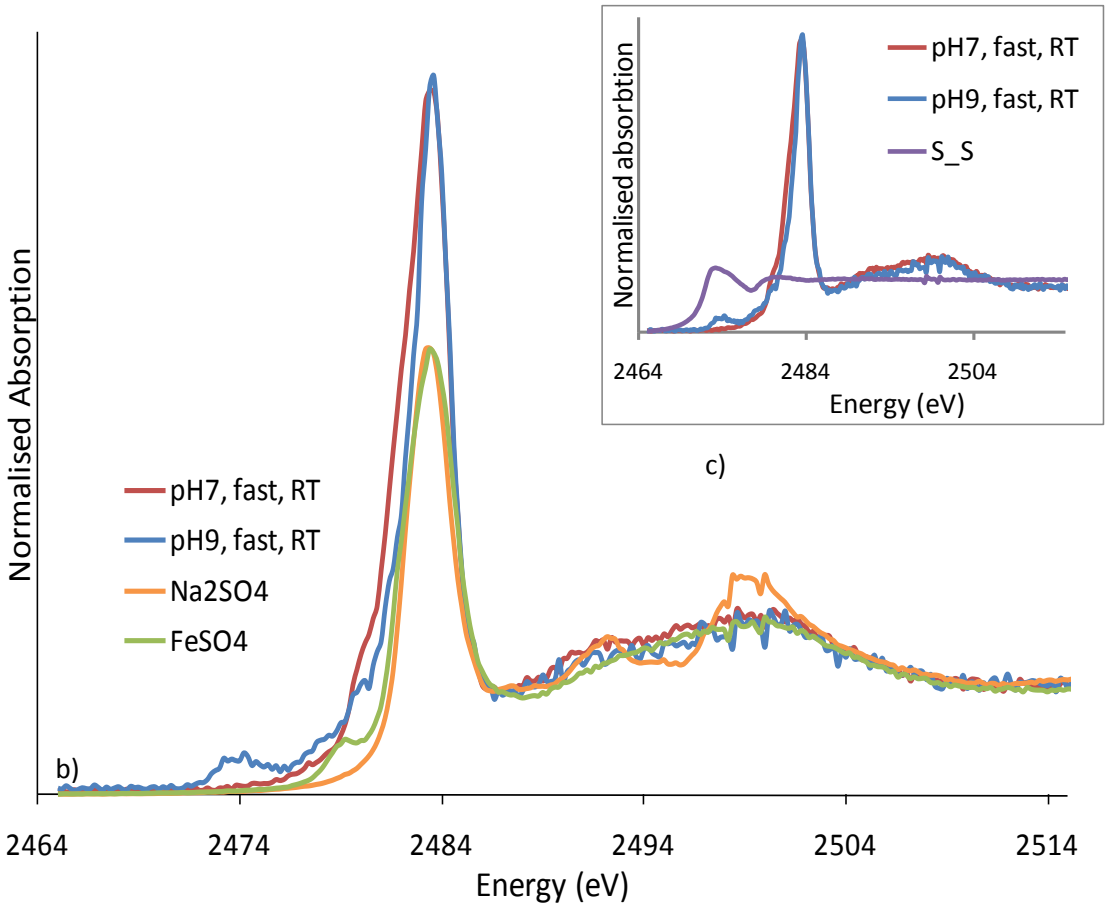

Fig. 5.3.1.3 b Comparison of S K-edge XANES spectra for samples with Na, before reduction and prepared in different conditions with b) Na_2SO_4 reference, $FeSO_4$ reference, **c)** Sulfur reference (upper right corner)

5.3.1.4. The S K-edge XANES analysis for samples with Na promoter reduced at 100 °C

The S K-edge XANES spectra for the samples synthesized at pH 7 and pH 9, fast titrant addition rate in room temperature with Na promoter reduced at 100 °C have similar characteristics, like those of non-reduced samples. The samples were compared with $FeSO_4$ and Na_2SO_4 and are presented in Fig.5.3.1.4. For both of the samples there was a visible main peak at 2483.4 eV indicating mainly S^{6+} and a small hump observed at 2480.2 (small amount of reduced S^{4+}) at the base of the peak as was noted before for the non-reduced samples. For the sample synthesized at pH 9 the S K-edge of the S^0 peak is not visible, while it was present before activation.

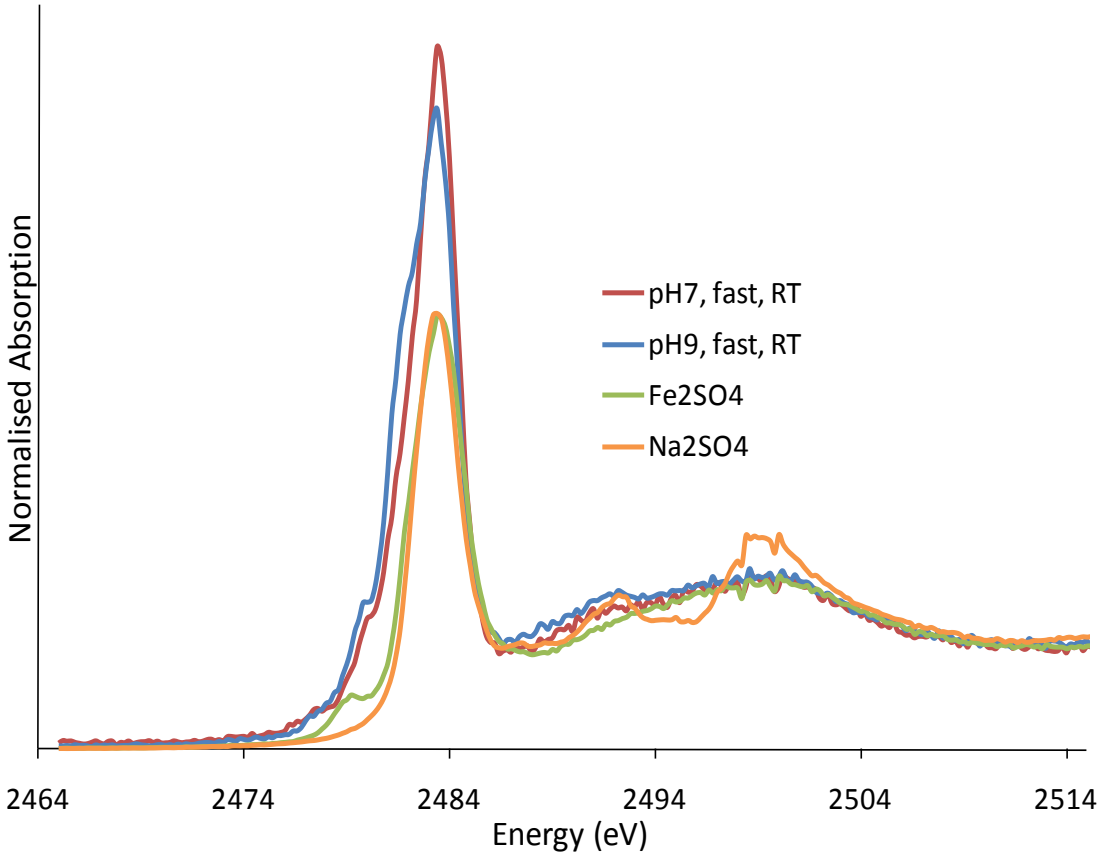

Fig. 5.3.1.4. Comparison of XANES S K-edge spectra for samples with Na, after reduction in 100 ºC, synthesised in various conditions with the Na_2SO_4 and $FeSO_4$ references.

5.3.1.5 The S-K-edge XANES analysis for samples with Na promoter reduced at 300 °C

In the spectra of the samples reduced at 300 °C two main peaks of high intensity were observed, Fig.5.3.1.5 a. The first at 2479.6 eV and the second at 2482.0 eV for the sample synthesized at pH 9, and at 2479.4 and 2482.0 eV for the sample synthesized at pH 7, fast titrant addition rate, room temperature. The peaks positions and oxidation states for samples reduced at 100 ^{o}C and 300 ^{o}C are listed in Table 5.3.1.5 b. At lower binding energies two convoluted low intensity peaks at 2473.2 and 2470.6 eV for both samples, were observed. The references FeS and S were used as a fingerprint for both of the peaks, Fig.5.3.1.5 b. The low intensity peaks are at the same positions as those recorded for S^{-2} and S^{0} and the two high intensity peaks are at positions corresponding to those for SO_3^{2-} and SO_4^{2-}. To show the mixture, the $FeSO_4$ and Na_2SO_3 references were used. The spectra suggest that sulfur is present in the samples mainly as a mixture of sulfur in the oxidation states +4 and +6 with small amounts of 0 and -2.

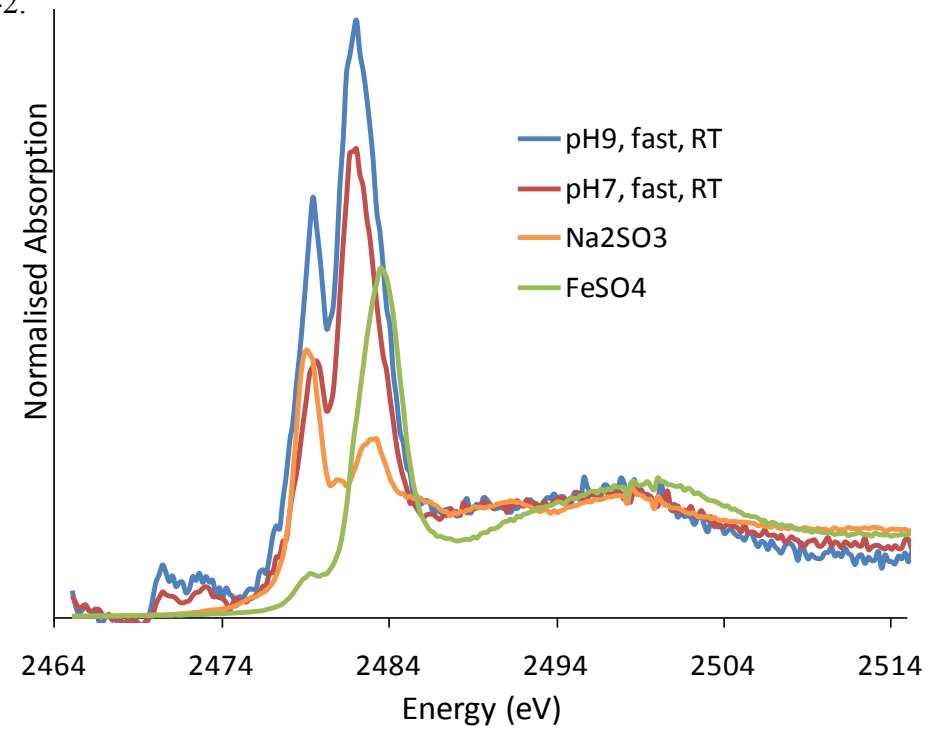

Fig. 5.3.1.5 a Comparison of S K-edge XANES spectra for the samples prepared in different conditions, with Na, after reduction at 300 ^{o}C, with Na_2SO_3 and $FeSO_4$ reference.

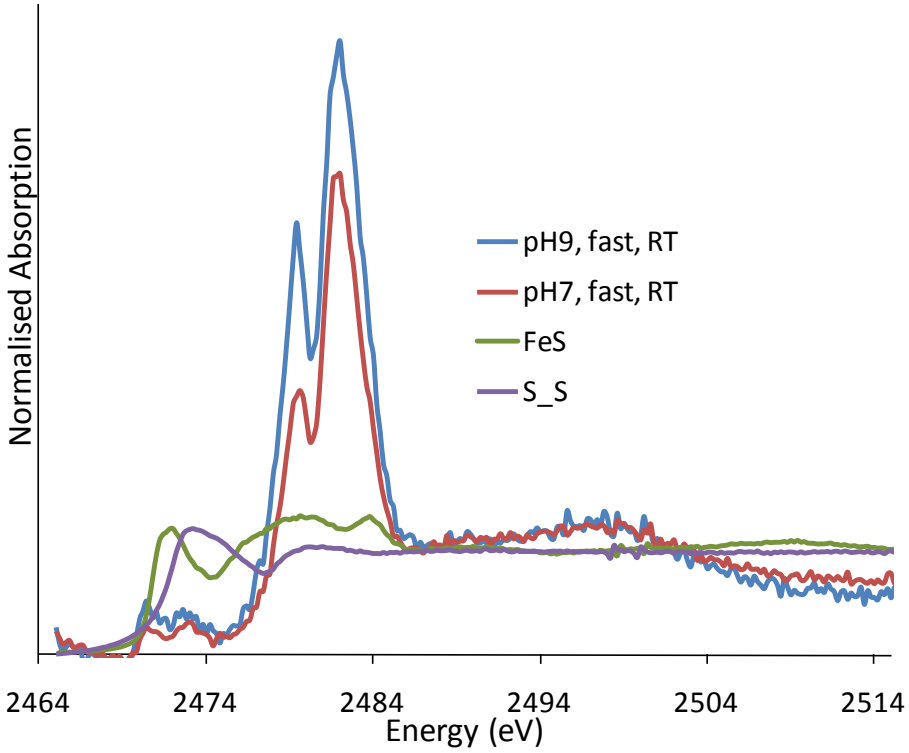

Fig.5.3.1.5 b Comparison of S K-edge XANES spectres for the samples prepared in two different conditions, with Na promoter, after reduction in 300 ^{o}C, with S and FeS reference.

Tab. 5.3.1.5 a The XANES S K-edge peak positions and oxidation state of samples with Na synthesized at different conditions.

Reduction conditions	**Peak position, eV**	**'Oxidation State'**
pH 9, fast, RT,	2480.5 2483.4	+4,+6
pH 7, fast, RT,	2473.5, 2480.0 2483.4,	0, +4, +6,
pH 7, slow, RT	2480.5 2483.5,	+4,+6
pH 7, fast, 60 ^{o}C	2480.5 2483.3	+4,+6

Tab. 5.3.1.5 b Sulfur K-edge XANES spectra peak positions for iron oxide catalyst with Na, reduced at 100 °C and 300 °C .

Reduction conditions	Sample	Peak position, eV	'Oxidation State'
As synthesized	pH 7, fast, RT	2483.4	+6
	pH 9, fast, RT	2483.4	+6
Reduced at 100 °C	pH 7, fast, RT	2483.6	+6
	pH 9, fast, RT	2483.4	+6
Reduced at 300 °C	pH 7, fast, RT	2482.0	+4, +6
		2479.6	
		2473.2	0
		2470.6	(-2)
	pH 9, fast, RT	2482.0	+4, +6
		2479.4	
		2472.6	0
		2470.4	(-2)

5.3.2. Sulfur K-edge XANES for samples with K promoter

5.3.2.1. Sulfur K-edge XANES for samples with K promoter before activation

The X-Ray absorption spectra of the S K-edges of iron oxide samples with K promoter were studied on I18 at the Diamond Light Source in Oxford.

In the previous experiment when the S K-edge for the samples with Na promoter were measured, a significant high intensity peak characteristic for S^{6+} [29-35] for non-reduced synthesized in different conditions samples was noticed. The same S K-edge position during XANES measurement for the samples with K promoter was observed, Fig.5.3.2.1.

In the experiment the Fe_2SO_4 reference sample was used as a fingerprint. The S K-edges for all the samples with K promoter after comparison with $FeSO_4$ suggest presence of the sulfate SO_4^{2-} species, below Fig.5.3.2.1.

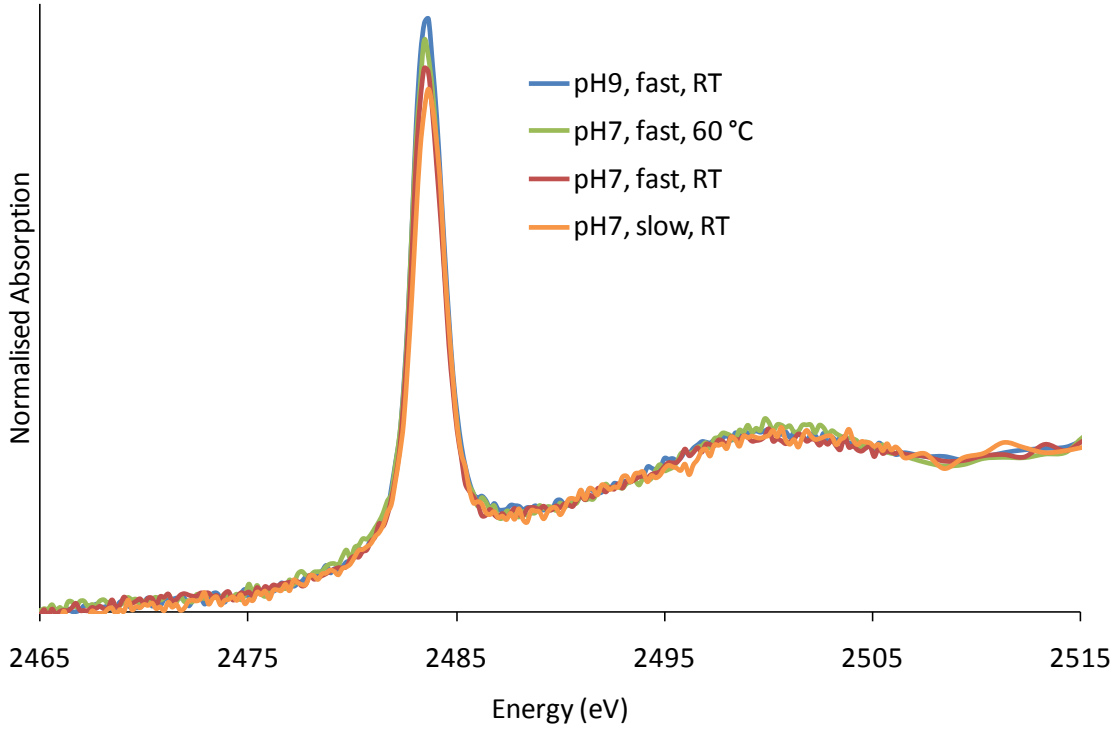

Fig.5.3.2.1. Comparison of S K-edge XANES spectra for iron catalyst samples with K promoter, before reduction, prepared in different conditions.

5.3.2.2 Sulfur XANES for samples with K promoter after activation

In comparison with samples reduced at 100 ºC and 300 ºC with Na promoter, iron oxide samples with K reduced at the higher temperature of 400 ºC did not show a significant amount of sulfur and its speciation was therefore impossible to derive, Fig.5.3.2.2. A very low intensity peak for two of the samples in the S K-edge area was visible. This can indicate that the sulfates were present on the surface. The weak signal may be due to a lower level of sulfur after reduction at high temperature. However, any other sulfur species (like e.g. sulfides) were not detected.

Previous examinations using powder XRD analysis verified the presence of the iron oxide speciation after reduction at different temperatures. The synthesized iron oxide catalyst with Na promoter changed from Fe_3O_4 to Fe after reduction at 450 ºC. For the iron oxide catalyst with K promoter transformation from Fe_3O_4 to Fe started to be visible after reduction at 400 ºC. Changes both in the speciation of sulfur and in the structure of the iron oxide, take place during activation at different temperatures[1,,36]. When the catalyst is reduced under H_2 in high temperatures, the sulfate species may be transformed into sulfides and eventually H_2S is released as a gas phase.

$$M^{n+}SO_4 + 4H_2 \rightarrow M^{n+}O + H_2S + 3H_2O$$

The total decomposition of $M^{n+}SO_4$ is only possible in high temperatures35[,37,38] due to the large thermal stability of SO_4^{2-} on metal-oxides. Thus, the transformation of the SO_4^{2-} to the S^{2-}on the surface may be observed at rising reduction temperatures lower than the temperature of thermal decomposition.

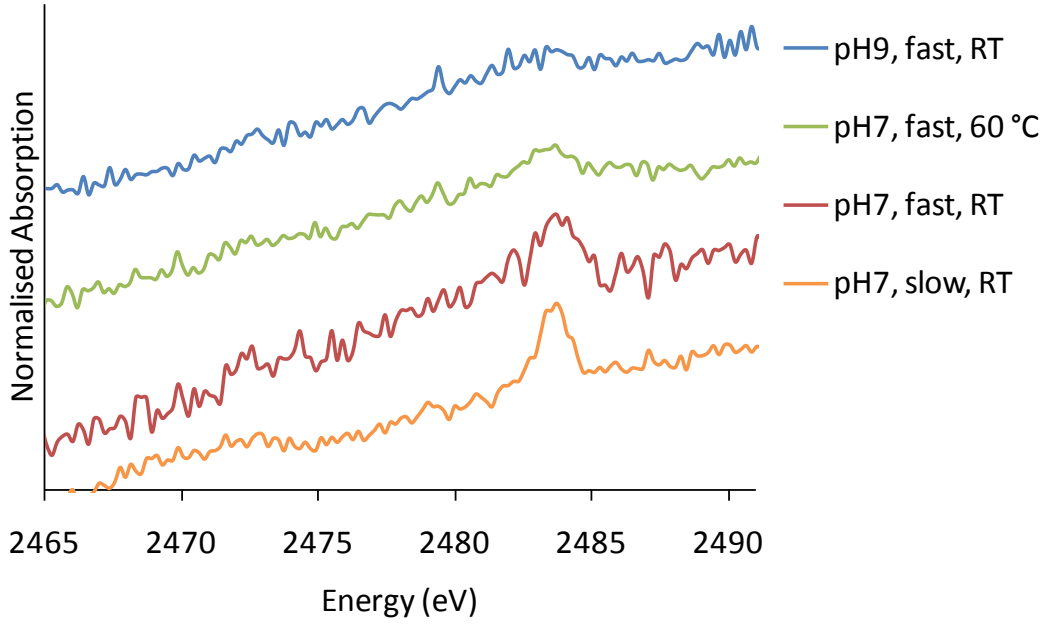

Fig.5.3.2.2. Comparison of XANES S K-edge spectra for the catalysts with K promoter prepared in different conditions after reduction in 400 ºC.

5.4 Elemental analysis of sulfur species in the bulk and on the surface of catalyst using, SEM-EDX, XRF and XPS techniques

The elemental analysis of the sulfur species using various techniques was carried out. The surface analysis and bulk elemental analysis like XPS, SEM-EDX, like XRF have been used in the project.

Sulfur containing catalyst samples were impregnated in epoxy resin prior to SEM/EDX analysis. Hence, the analyzed surfaces had a low roughness, Figure.5.4.

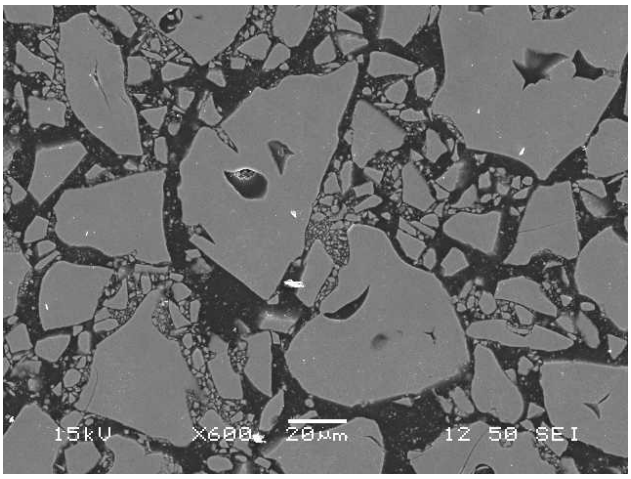

Fig.5.4. The example of the SEM image for sample with prepared at pH 7, fast titrant addition, room temperature, with S and Na promoters.

5.4.1. The SEM-EDX elemental analysis of sulfur in iron oxide catalyst

The SEM-EDX analyses were performed on a JSM 5910 SEM at the Electron Microscopy Centre, University of Southampton. The EDX with comparison to XPS and XRF elemental analysis for the iron oxide samples with different promoters are listed in Table 5.4.3. The EDX analysis for samples with Na promoter, synthesized in various conditions indicated the presence of approximately 0.1 at%. All of the samples were loaded with an amount of 0.05 at% sulfur. The lower detection limit of the EDX

technique is 0.1 at%, (S.D. = 0.07), so any content below this value is not observable in the data. The atomic percent of sulfur in non-reduced samples using XPS technique was slightly higher in a range 0.1 – 0.3 at%. The S.D. for XPS was between 0.08 and 0.15.

The EDX for samples with K promoter, synthesized in different conditions showed the presence of sulfur for all the samples between 0.1 and 0.2 at%, higher than the loaded amount. Samples synthesised in pH 7, slow titrant addition in the room temperature and pH 9, fast titrant addition in room temperature, have lower amounts of sulfur in comparison to the rest of the samples with Na promoter. The amount of sulfur for the non-reduced samples with K was in the same range 0.1 – 0.2 at%. The elemental analysis for the samples with Rb promoter indicated 0.1 at% of sulfur. The exception is the sample synthesized in pH 7, fast titrant addition, and temperature 60 ^{o}C during precipitation, where nu sulfur was detected. Presented before atomic percent of sulfur for the samples with Rb promoter noticed by XPS indicated the same amount of sulfur.

5.4.2. The XRF analyses of sulfur in iron oxide catalyst

The XRF elemental analyses were performed on a Philips MagiX-Pro WD-XRF spectrometer, National Oceanography Centre, Southampton. The XRF experiment indicated presence of sulfur in the bulk of all the iron oxide samples with different promoters. The maximum of the observed S was 0.1 at%. For the iron oxide sample with Na and K promoters synthesized at pH 9 no sulfur was indicated. There was also no sulfur in the iron oxide sample with Rb promoter precipitated at 60 ^{o}C. The same for this sample was noticed using EDX analysis. The accuracy of XRF technique was higher in comparison to presented above EDX and XPS techniques, S.D. = 0.05 - 0.08.

5.4.3. The elemental analysis of the sulfur species in the catalyst after activation

The XRF elemental analysis of the reduced iron oxide samples was also carried out. The analysis indicated the absence of sulfur for most of the samples. Only for the sample with slow titrant addition rate, reduced at 400 ºC the same amount of sulfur 0.1at% as before reduction was noted.

Presented before the XPS elemental analysis of the reduced samples with Rb indicated 0.1 – 0.4 at% for the samples reduced at 400 ^{o}C and 450 ^{o}C. However the experimental error related mainly with highly noise signal was high S.D = 0.08 - 0.15.

The comparison of the bulk elemental analysis (XRF and EDX) of sulfur with the surface sensitive technique (XPS) shows discrepancies in concentration of the element before and after activation in the bulk and surface of the catalyst. There was a lower amount of sulfur species in the non-reduced catalyst observed in the bulk (up to 0.1 at%, XRF and EDX technique) than on the surface (maximum 0.3 at%, XPS technique). As for non-reduced samples, concentration of sulfur for activated samples in the bulk was lower than on the surface. The surface XPS analysis for the activated samples revealed concentrations up to 0.4 at%. The results for the samples reduced in increased temperatures (400 ^{o}C and 450 ^{o}C), are noticed in a subchapter 5.2.4.2, Table 5.2.4.2.

There are many factors that may influence on the quantitative characterization of the non-activated and activated catalysts. All of the presented techniques may reveal different accuracy, precision, sensitivity, resolution, and detection limit. The discrepancies caused by some of these factors may have influence on the observed results. The example may different detection limit for XPS and XRF technique. The detection limit can be related to for example the instrument (instrumental detection limit) or the method of analysis (method detection limit), calibration error, or noise contribution. It was observed that the S.D. calculated for XPS technique is strongly related (proportional) with the noise, (and higher than the S.D. of XRF).

Tab. 5.4.3. The EDX, XPS, XRF elemental analysis (at %) for non-reduced iron oxide samples synthesized in various conditions with different promoters

Conditions	Atomic %, EDX	Atomic %, XPS	Atomic %, XRF
pH 9, fast, RT, Na	0.1	0.3	-
pH 7, fast, 60 ^{o}C, Na	0.1	0.2	0.1
pH 7, fast, RT, Na	0.1	0.2	0.1
pH 7, slow, RT, Na	0.1	0.1	0.1
pH 9, fast, RT, K	0.1	0.2	-
pH 7, fast, 60 ^{o}C, K	0.2	0.2	0.1
pH 7, fast, RT, K	0.1	0.2	0.1
pH 7, slow, RT, K	0.2	0.1	0.1
pH 9, fast, RT, Rb	0.1	0.1	0.1
pH 7, fast, 60 ^{o}C, Rb	-	-	-
pH 7, fast, RT, Rb	0.1	0.1	0.1
pH 7, slow, RT, Rb	0.1	0.1	0.1

1. **EDX Standard deviation (S.D.) for Na, K and Rb promoters:** (0.07 – 0.18)
2. **XRF S.D for Na, K and Rb:** (0.05 - 0.08)
3. **XPS S.D for Na, K and Rb:** (0.08 – 0.15)

S at% theoretical : 0.05

5.5 Conclusions

In this chapter the sulfur speciation in iron oxide catalyst before and after activation was studied. There were differences in the sulfur structure and concentration in the catalysts related to the synthesis conditions and activation temperature. The examined samples were reduced under H_2/He at 100 ^oC, 300 ^oC, 400 ºC and 450 ºC. The nature of sulfur in the iron oxide was determined by XPS, XANES, SEM-EDX, and XRF. Firstly, the oxidation state, electronic and molecular structure using XPS and XANES techniques were studied. Then SEM-EDX, XRF surface and bulk sensitive techniques were applied for examination of sulfur species concentration in the catalyst.

The binding energy measured by XPS technique for all the samples synthesised in various conditions, with different alkali metals Na, K, Rb before activation shows mainly the presence of the sulfate (SO_4^{2-}) form of sulfur species in the catalyst. For all the samples examined by XPS before activation around 0.3 eV shift in binding energy was observed between samples with Na promoter and those with K, Rb promoters.

The peak positions for S (2p) for most of the samples with Rb and Na promoter after activation under H_2/He at 400 ºC were in the BE ranges which indicate a mixture of sulfate and sulfide species. For the sample precipitated at 60 ºC, with Rb, only the sulfate peak was observed. The presence of both sulfate and sulfide ions after activation under H_2/He at 450 ^oC, was also observed. However the sulfate/sulfide ratio was higher for the samples reduced at 400 ^oC in comparison to the samples reduced at 450 ^oC, which may prove the partial conversion of sulfate to sulfide with the increase of reduction temperature. The small decrease of the overall sulfur species concentration for the samples with slow titrant addition, with Rb promoter in comparison to those reduced at 400°C may suggest the partial release of sulfur as gaseous H_2S at the highest experimental reduction temperatures.

The XANES analysis which notices differences in 1s → 3p bound state transitions, also proved that before reduction sulfur was present in all iron catalyst samples in the form of sulfate ions with sulfur in the +6 oxidation state. Minute amounts of sulfur ‘0’ were

also discovered in the sample synthesized at pH 9. The samples reduced at 100 °C reveal the presence of the sulfur at the oxidation state +6 like non-reduced samples. After reduction at 300 °C there was a mixture of sulfur in the +6 and +4 oxidation states and smaller amounts of sulfur in the 0 and -2 oxidation states. The XANES analysis for the iron catalyst samples with K promoter reduced under H_2/He in elevated temperatures of 400 ºC and 450 ºC showed absence of sulfur.

The bulk quantitative analysis XRF and EDX for the catalyst before activation indicated lower or the same amount (0.1at% for Na, Rb and 0.1 - 0.2at% for K) of sulfur species than the concentration of sulfur species indicated by surface sensitive XPS (0.1- 0.3at% for Na, 0.2at% and 0.1at% or less for Rb).

The comparison of the XPS analysis of the sulfur species for the samples with Rb and Na promoter before and after activation prove the increase of the sulfite species on the surface. The concentration of sulfur in the activated catalyst examined by bulk sensitive techniques indicated lower amount of sulfur or even absence of sulfur species (sample precipitated at 60 ^{o}C) in comparison to those non-reduced. The surface sensitive XPS showed the same or higher concentration of sulfur on the surface (0.1-0.4 at %).

It was shown that the relative proportions of S species can be controlled by manipulation of the method and conditions of the catalyst synthesis. The higher reduction temperatures promoted the transformation of SO_4^{2-} into a mixture of SO_4^{2-} and S^{2-}. The reduction carried in elevated temperatures caused migration of sulfate species to the surface and in the highest temperature sulfur may have been released as gaseous H_2S from the surface of the catalyst. These observations prove that using small amounts of sulfate as a promoter is only possible in a certain range of activation temperatures.

5.6 References

1. Bromfield T., Coville N., *App. Surf. Sci.*, 119 (1997) 19.
2. Cornils B., Herrmann W., Schlogl R., Wong C.H., *Catalysis from A to Z*, Wiley-VCH GmbH & Co. KGaA Weinheim 2nd edition, 2003.
3. Curulla-Ferré D., Govender A., Bromfield T.C., Niemantsverdriet J.V., *J. Phys. Chem. B,* 110 (2006) 13897.
4. Li T., Yang Y., Tao Z., Wan H., An X., Zhang C., Xiang H, Li Y., *J. Nat. Gas Chem.,* 16 (2007) 354.
5. Bromfield T., Coville N., *App. Catal. A-Gen.*, 186 (1999) 297.
6. Baoshan W., Bai L., Xiang H., Li Y.-W., Zhang Z., Zhong B., *Fuel,* 83 (2004) 205..
7. Kritzinger J. A. *Catal. Today,* 71 (2002) 307.
8. Vairavamurthy A., *Spectrochim. Acta, Part A,* 54 (1998) 2009.
9. Anderson B. B., Karn F. S., Kelly R. E., Shultz I. F., *Bur. Mines. Bull*. 62, US Government Printing Office, Washington DC, 1965.
10. Bartholomew C., Bowman R*., Appl.Catal.,* 15(1985) 59.
11. Smith G., Hinkley, Zahraa C.O., Nishizawa T., Saporoschenko M., Shiley R*., J.Catal.,*78(1982)262.
12. W.L.van Dijk, Niemantsverdriet J., A.M.van der Kraan, H.S. van der Baan*, Appl. Catal.,* 2 (1982) 273.
13. Paal Z., *Spectroscopy in Catalysis - An Introduction*, VCH, Weinheim, 1995.
14. Cai Y., Pan Y., Xue J., Sun Q., Su G., Li X., *Appl. Surf. Sci.,* 255 (2009) 8750.
15. Yu X.-R., Liu F., Wang Z.-Y., Chen Y.J*., Electron Spectrosc. Relat. Phemon.,* 50 (1990) 159.
16. Jones C.F., Lecount S., Smart R. St, C., White T., *Appl. Surf. Sci.,* 55 (1992) 65.
17. Leiro J.A., Mattila S.S., Laajalehto K., *Surf. Sci*., 547 (2003) 157.
18. Kendelewicz T., Doyle C.S., Bostick B.C., Brown G.E. Jr., *Surf. Sci*., 558 (2004) 80.

19. G.U. von Oertzen, Skinner W.M., Nesbitt H.W., *Phys. Rev. B*, 72 (2005) 235427.
20. Mattila S., Leiro J.A., Laajalehto K., *Appl. Surf. Sci*., 97 (2003) 212.
21. Sasaki K., Tsunekawa M., Ohtsuk T., Konno H., *Geochim. Cosmochim., Acta.,* 59 (1995) 3155.
22. Pratt A.R., Muir I.J., Nesbitt H.W., *Geochim. Cosmochim. Acta*., 58 (1994) 827.
23. Wittstock G., Kartio I., Hirsch D., Kunze S., Szargan R., *Langmuir,* 12 (1996) 5709.
24. Siriwardane R.V., Cook J.M., *J. Colloid Interface Sci.*, 525 (1986) 114.
25. Abraham K.M., Chaudri S.M., *J. Electrochem. Soc.,* 133 (1986) 1307.
26. Wagner C.D., Taylor J.A., *J. Electron Spectrosc. Relat. Phenom.,* 211 (1982) 28.
27. Siriwardene R. V., Cook J. M., *J. Colloid Interface Sci.,* 414 (1985) 108.
28. Wahlqvist M., Shchukarev A., *J. Electron Spectrosc.,* 156 (2007) 310.
29. Sekiyama H., Kosugi N., Kuroda H., Ohta T., *Bull. Chem. Soc. Jpn.,* 59 (1986) 575.
30. Vairavamurthy A., *Spectrochim. Acta Part A*, 54 (1998) 2009.
31. Wetherall K.M., Moss R.M., Jones A.M., Smith A.D., Skinner T., Pickup D.M., Goatham S.W., Chadwick A.V., Newport R.J., *J.Archaeol.Sci.,* 35 (2008) 1317.
32. George G., Gorbaty M., *J. Am. Chem. Soc.,* 111 (1989) 3182.
33. Prietzel J., Thieme J., Salome M., Knicker H., *Soil Biol. Biochem.,* 39 (2007) 877.
34. Chaturvedi S., Rodriguez J.A., Brito J.L., *Catal. Lett.,* 51 (1998) 85.
35. Rodriguez J. A., Jirsak T., Freitag A., Hanson J. C., Larese J. Z. and Chaturvedi S., *Catal. Letters* 62 (1999) 113.
36. Ngantsoue-Hoc W., Zhang Y., J. O'Brien R., Luo M., Davis H. *Appl. Catal. A-Gen.* 236 (2002) 77.
37. Górski A., *Polish J. Chem*., 75 (2001) 159.
38. Jaszczak-Figiel B., Gontarz Z*., J. Therm. Anal. Calorim.,* 96 (2009) 147.

Chapter 6
Conclusions

6.1 Conclusions

In this work, the influence of different types of alkali metals and sulfur on the structural properties of the FT catalyst was investigated. It was also a study of the influence of synthesis parameters and preparation method on the catalyst properties. After the iron oxide catalyst was synthesised, information was collected about the catalytically-active material, i.e. iron oxide and dopants (alkali metals and sulfur). The information was collected in many different stages of the process of creation of the catalyst, Figure 6.1, beginning with the visual observation of the texture and colour of the iron slurry during the precipitation process to the characterisation by highly developed analytical techniques like XPS or XAFS.

The complete information about synthesis, before and after calcinations, before and after the reduction process gives a description that may be used in the next stage of catalyst design (Future work). It is very important to deliver the catalyst with the information package before checking its ability to convert feedstock to various products (activity), the ability to provide the desire product out of all possible products (selectivity)[1] and its life time (which will be a subject of future work).

At the beginning, the changes of the catalytically-active material influenced by different conditions, method of synthesis and activation process were investigated. Information about the iron oxide structure, particle size, morphology, pore size, oxidation state and stoichiometry was collected using techniques like: P-XRD, SEM, EDX, XPS, XANES, XRF.

X-ray diffractograms of all samples before activation showed data characteristic of the haematite structure of iron oxide (α-Fe_2O_3). The highest crystallinity (the highest particle size) was observed for the sample synthesised at pH 7, fast titrant addition at room temperature, then with slow titrant addition, followed by samples which were impregnated and at the and those synthesised at 60 ^{o}C.

Fig. 6.1 Scheme of investigating the influence of the dopants on properties of iron oxide catalysts for the Fischer-Tropsch process. Catalyst before analysis – white. Samples after first characterization – light gray. Catalyst after second characterization, and selection – dark gray. Selected iron oxide FT catalyst – rust.

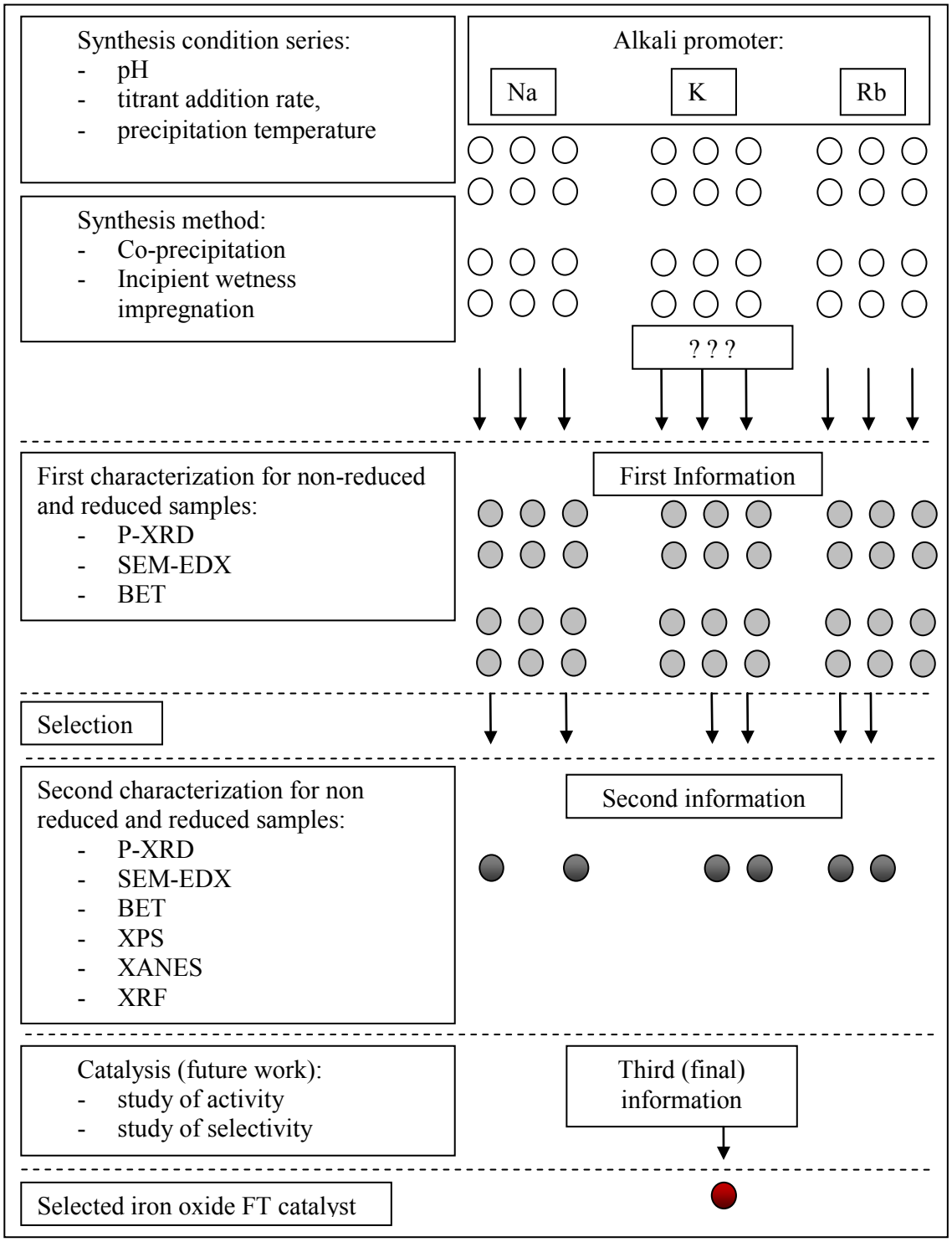

After the activation process in 5% H_2/He, different species of iron oxide were observed, depending on reduction temperature and type of alkali metal used. It was discovered that alkali metals influenced the activation process by changing the reduction temperature of the iron oxide catalyst. The transformation of haematite (α-Fe_2O_3) to magnetite (Fe_3O_4) and Fe_3O_4 to Fe^0 occurred at different temperatures for the iron oxide catalyst doped with Na as compared with K and Rb. For the samples with Na and reduced at 400 ^oC the Fe_3O_4 cubic phase was observed, whilst at 450 ^oC transformation from magnetite Fe_3O_4 to metallic iron Fe occurred. For the samples with K and Rb the mixture of magnetite and metallic iron was found at 400 ^oC and predominantly metallic Fe at 450 ^oC.

The α-Fe_2O_3 form of iron oxide for non-reduced samples was also confirmed using the XPS technique. The binding energies, shape of the peak and presence of the satellite were the same as those of examined references and α-Fe_2O_3 from the literature sources. The characteristic width for the Fe $2p_{3/2}$ spectrum of the samples reduced at 400 ^oC and absence of Fe $2p_{3/2}$ peak's satellite were observed. The differences between Fe_3O_4 and γ-Fe_2O_3 are subtle, when the P-XRD technique is used, thus further XPS study, which could show the absence of the satellite for Fe_3O_4 or the presence of the Fe $2p_{3/2}$ satellite of γ-Fe_2O_3 was needed to help distinguish between the two forms of iron oxide. The most visible difference between the samples reduced at 400 ^oC and at 450 ^oC was the presence of the Fe $2p_{3/2}$ peak's satellite for the samples reduced in the higher temperature which suggests the presence of γ-Fe_2O_3 and/or α-FeOOH. The presence of a peak in the lower energy arm of the Fe $2p_{3/2}$ spectrum proved the occurrence of the Fe^0 in the sample reduced in higher temperature. The XPS technique was also used to measure O 1s spectra. The presence of small amount of OH^- and H_2O species was detected on the surface of all the samples.

The XPS, EDX and XRF quantitative analysis and study of the stoichiometry of the iron oxides additionally proved previous observations. The Fe : O ratio at the surface and in the bulk of all of the non-reduced samples was close to the theoretical ratio for Fe_2O_3 (0.67) and was not influenced by the kind of the alkali promoter used. The higher amount of oxygen discovered for some of the samples could be due to the presence of H_2O and hydroxides. The elemental analysis of the activated samples also confirmed

what was presented previously, i.e. the characteristic Fe : O ratio for the mixture of Fe^{2+} and Fe^{3+} oxides for the samples reduced at 400 ^{o}C and the mixture of oxide and metallic iron for those reduced at 450 ^{o}C. For the samples with Na and Rb promoters the Fe : O ratio increased with the rising reduction temperature.

A comparison of the samples synthesised with different procedures by SEM showed that there are two different types of surface: the irregularly shaped agglomerates with smaller round edged particles attached to their surface and homogenous agglomerates surfaces with sharp edges. The samples with Rb were the most homogenous, i.e. their surface was flat and had a more faceted morphology. The agglomerates for the samples with K were in general bigger than those with Rb and Na promoters. The catalysts' surfaces did not vary with the different conditions of synthesis.

The physisorption isotherms for all the iron oxide samples with different promoters exhibited type IV hysteresis loop, which is characteristic of materials with a mesoporous structure. The hysteresis loops were of the H1 type, which is typical for close packed agglomerates of homogeneous spheres with a narrow PSD. The majority of the catalyst samples revealed a narrow PSD, which indicates a homogenous surface structure. The TPV was higher for the samples synthesized at 60 ºC than the rest of the samples. The higher TPV and the lower PSD parameter for these samples may suggest increasing volume of the cavities with the same pore entrance. The TPV increased with PSD for the rest of the samples, which indicates that the entrance diameter increased proportionally to the cavities sizes. The BET surface area for the same samples synthesized at 60 ºC was higher than the rest of the samples. The samples synthesised at pH 7, fast titrant addition at room temperature had the lowest surface area and highest crystallinity.

The differences in concentration of the alkali metals on the surface of non-reduced samples synthesised in different conditions and by different methods of preparation were not significant. However, noteworthy discrepancies between non-activated and activated catalyst samples with different alkali promoters were discovered. A significant enhancement of alkalis on the surface for the reduced samples was observed using the XPS technique. The largest concentration of alkali promoter was observed for the samples with Na. Moreover, the concentration of the alkali promoters on the surface

increased with increasing reduction temperature. The migration of the alkalis to the surface caused by reduction was also confirmed by quantitative EDX and XRF analysis. The highest increase was noticed for the samples synthesised at pH 7, slow titrant addition at room temperature. The transformation of the haematite (α-Fe_2O_3) to magnetite (Fe_3O_4) and Fe_3O_4 to Fe^0, and the migration of the alkali metal (Rb^+) to the surface in iron oxide catalyst doped with Rb is presented in Figure 6.1.1.

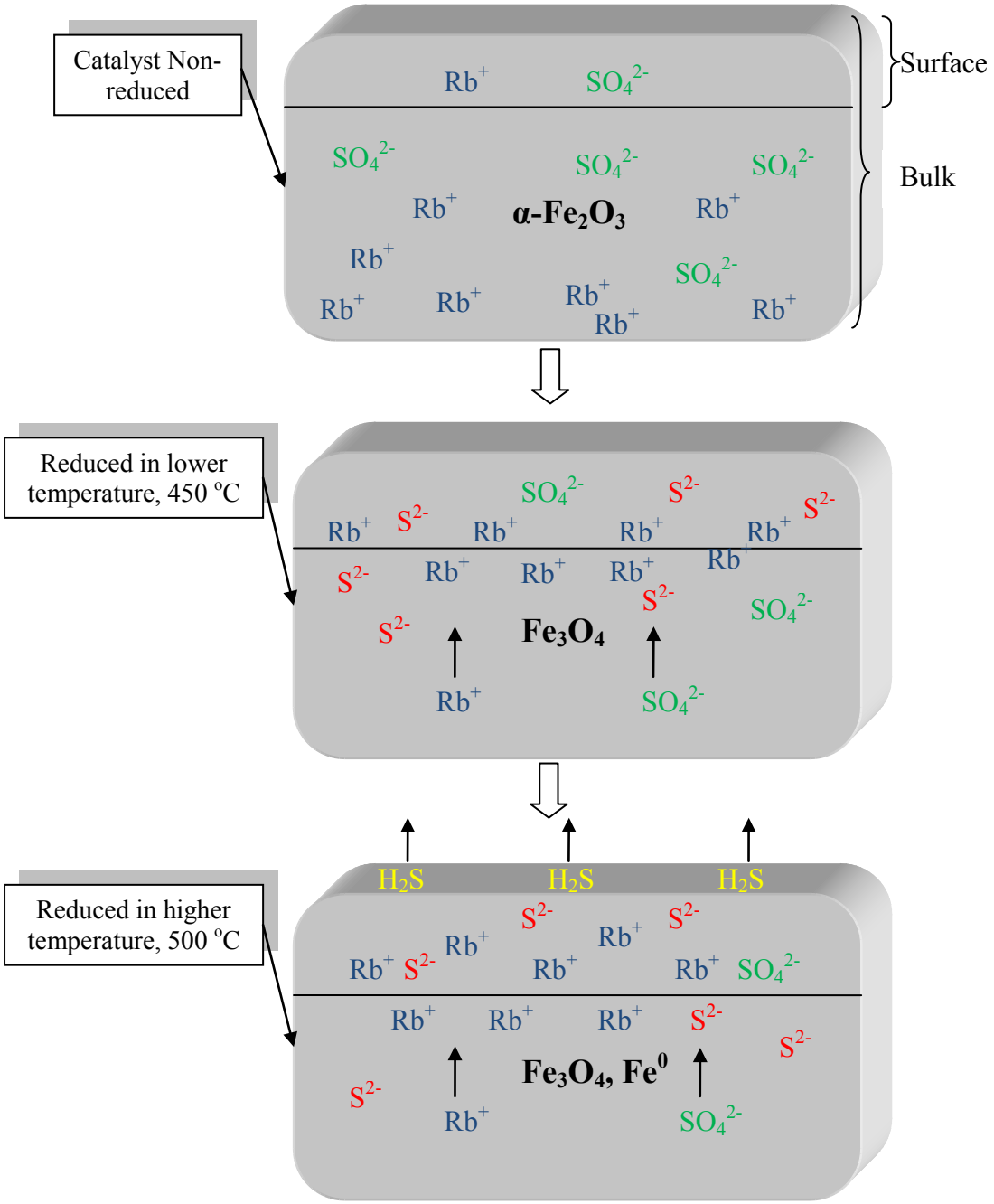

Fig. 6.1.1. Schematic view of the transformation of iron oxide, migration of Rb^+, conversion of the sulfate to sulfide, and release of sulfur as a gaseous H_2S, caused by reduction of the iron oxide catalyst.

The structural properties of K and Na promoters were also studied using the XANES technique. The relatively short acquisition time (degradation of the beryl monochromator), the low loading and low energy of sodium did not permit collection of informative Na K-edge data. The higher absorption edge energy and longer possible acquisition times facilitated the XANES measurement of potassium K-edge. The changes (shape and splitting) in the K-edge spectrum indicated variations in the local environment (e.g. alteration of the coordination number around K^+) during the reduction process, which may have occurred also during the reduction of the sample with Na but could not be observed.

The alkali promoters may have influence not only on the iron oxide phase but also on the local environment around sulfur. It was observed that the kind of alkali metal used as a promoter and the inter-atomic effect (M^+–SO_4^{2-}) may have influenced the energy shift in the XPS spectra. (The samples with Na was shifted 0.3 eV towards higher energy). A slight reduction of sulfur in the X-ray beam was observed during XANES experiment with the model compound $FeSO_4$ and was not observed for the Na_2SO_4 reference. The same behaviour was also noticed for the experimental samples. This might be an indication that SO_4^{2-} is associated directly to Fe. The XANES is the only technique with which this phenomenon was noticed.

The study of the oxidation state, electronic and molecular structure using XPS and XANES techniques shows that all the samples synthesised in various conditions, with different alkali promoters contained the sulfate (SO_4^{2-}) form of sulfur. Most of the samples activated under H_2/He at 400 ^oC characterised using the XPS technique showed S 2p peaks typical for the mixture of both sulfate and sulfide species. The same mixture for the same samples after reduction in higher (450 ^oC) temperature was observed, however the sulfate/sulfide ratio was lower, which showed a correlation between increasing temperature and conversion of sulfate to sulfide. The decrease of the total of sulfur species for the samples with Rb in higher reduction temperature may suggest the release of sulfur as a gaseous H_2S, (schematic view, Figure 6.1.1).

The characterization of sulfur species using the XANES technique for the samples activated at 100 ^oC with Na promoter showed the environment of sulfur to be similar to that in non-reduced samples (oxidation state +6). The analysis of S K-edge of the

samples activated at 300 ^{o}C revealed differences in 1s → 3p bound state transitions indicating a mixture of sulfur in the +6 and +4 oxidation states and smaller concentrations of sulfur in the 0 and -2 oxidation states. The XANES technique performed for S K-edge of the samples with K promoter reduced in H_2/He at 400 ^{o}C and 450 ^{o}C did not reveal the presence of any sulfur species.

After quantitative surface XPS analysis and comparison of sulfur species concentration for the non-reduced and reduced samples with Na and Rb showed an increase of the sulfite species on the surface. The decrease of sulfur species in the bulk of activated samples was also observed using (XRF and EDX) in comparison to the non-activated ones. In general, it was proved that the reduction process at elevated temperatures caused migration of sulfate species to surface.

6.2. Future work

In this work, non-activated and activated iron oxide catalysts were analyzed using various techniques. Careful characterization in many different stages of catalyst production provided information which could be compared with that obtained after catalysis carried out under standard FTS conditions. The influence of the synthesis conditions, i.e. the methods of preparation and the physical and chemical properties of the catalyst e.g. crystallinity, size of the particles, surface area, pore size distribution, distribution of sulfide/sulfate ions and alkali metals in the catalyst on the FTS catalyst activity and higher hydrocarbons selectivity, could be examined. Moreover, the influence of these structural factors on properties like the enhancement of CO and the decrease of H_2 adsorption, favouring formation of unsaturated products, or suppressing hydrogenation of olefins, should be studied. The WGS activity should also be examined with catalysts synthesized in this work, due to the high demand of H_2 in a process where syngas is obtained from coal or gasification of heavy oils (low H_2/CO).

A suitable procedure for further examination of alkali promoters should be established, which would include the XPS and quantification techniques such as EDX and XRF. Observation of the changes of properties of chosen catalysts using in-situ XPS or XAFS during the activation process will be valuable. The transformation of iron oxide, alkali

metals and sulfur promoters simultaneously would be examined in such an experiment. The in-situ XAFS gives more information on chemical speciation. The crystallinity and structure of the iron oxide species should be examined using P-XRD or XPS and the stoichiometry by the use of EDX or XRF. The nitrogen absorption BET analysis, could be a good and simple way to check pore size distribution and surface area, after catalysis, to check for life time of the catalyst. For further analysis of low concentration of sulfur species XPS and XANES would be recommended.

After examination of the influence of the physico-chemical properties of the catalysts on the properties of the final products and overall efficiency of FTS, the optimal catalyst synthesis conditions, method of preparation and activation conditions will be chosen.

6.3 References

1. *Catalyst handbook*, edited M. Twigg, second edition, Manson Publishing, London, 1998.